Quantum Coherence in Laser and Micromaser Systems

by

Pál Bogár

A dissertation submitted to the Graduate Faculty in Physics in partial fulfillment of the requirements for the degree of Doctor of Philosophy, The City University of New York.

1995

This manuscript has been read and accepted for the Graduate Faculty in Physics in satisfaction of the dissertation requirement for the degree of Doctor of Philosophy.

6/16/95
Date

Professor János A. Bergou,
Chair of Examining Committee

7/12/95
Date

Professor Joseph B. Krieger,
Executive Officer

Professor Ying-chih Chen,

Professor Leon Cohen,

Professor Daniel Greenberger,

Professor Mark Hillery,

Supervisory Committee

THE CITY UNIVERSITY OF NEW YORK

ABSTRACT

Quantum Coherence in Laser and Micromaser Systems

by

Pál Bogár

Adviser: Professor János A. Bergou

Quantum coherence effects in lasers and micromasers are studied theoretically. First, we investigate the laser operation when coherences between various levels of the pumping three-level atoms are introduced by some external means. We find that, in the case of closely spaced lower levels (Λ-configuration), zero-threshold lasing without inversion can be achieved with quantum noise reduced to the level of that of an ideal coherent state. Multistable regimes, phase locking, and controlled competition between the modes are found when the, thus far, single-mode operation is extended to a two-mode one.

In the second line of research, we consider two micromasers coupled in series by sharing a common pumping atomic beam. Significant modifications in the behavior of the second field are found due to the atomic coherence prepared in the first cavity, together with the build-up of correlation and phase locking between the two fields. We also study the evolution of the quantum state of the nonlocal two-field system in the two schemes where the final states of the atoms are measured conditionally or nonselectively. It is found that arbitrary steady state entanglement of the two nonlocal fields can be engineered in the form of entangled trapping states. These quantum states are experimentally feasible in the short-time transient regime when dissipation does not exceed a certain threshold.

We also show that the correlation between the nonlocal fields can be translated into a correlation between spatially separated atomic beams. These entangled atoms can have several applications such as studying the effect of interatomic correlations in lasers and micromasers, quantum computing, teleportation, or tests of the local realistic theories.

However, we specifically discuss here their use in experimentally feasible tests of complementarity applying Ramsey's atomic interferometry. We find that the correlation between the atoms provides us with "Welcher Weg" information resulting in a destruction of the interference fringes without leading to Heisenberg's uncertainty principle. Manipulation of information results in a generalized version of the "quantum eraser."

ACKNOWLEDGEMENTS

I want to express my gratitude to my thesis adviser, Professor János A. Bergou, for originally suggesting this study and for his guidance throughout the work. A special note of thanks goes to Professor Mark Hillery for his contributions and concern in this research.

Special thanks go to Professors Ying-chih Chen, Leon Cohen and Daniel Greenberger for their help as members of my thesis committee.

I thank the Research Foundation of the City University of New York, the Office of Naval Research, and the National Science Foundation for their financial support.

Finally, I wish to thank my wife, Adrien, for her infinite patience and invaluable encouragement, my parents and my family for their encouragement and support. I dedicate this work to them.

TABLE OF CONTENTS

LIST OF FIGURES viii

1. INTRODUCTION 1

2. ATOMIC COHERENCE IN LASER SYSTEMS 3

2.1 Studies on Lasing Without Inversion 3

2.1.1 Quantum Theory of a Noninversion Laser with Injected Atomic Coherence 3

2.1.2 Two-Mode Lasing Without Inversion with Injected Atomic Coherence 34

3. QUANTUM COHERENCE IN PUMP-COUPLED MICROMASERS ...66

3.1 The Micromaser 66

3.1.1 Phase Structures in the Micromaser Photon Statistics 66

3.1.2 Quantum Island States in the Micromaser 95

3.2 Pump-coupled Micromasers 122

3.2.1 Pump-coupled Micromasers: Coherent and Incoherent Coupling 122

3.2.2 Pump-coupled High-Q Micromasers with Conditional Measurements of Atoms: Transient and Steady State Entanglement of Nonlocal Fields 195

3.2.3 Pump-coupled Micromasers: Entangled Trapping States of Nonlocal Fields 234

3.2.4 Entanglement of Atomic Beams: Tests of Complementarity and Other Applications 275

4. SUMMARY 286

APPENDIX 288

BIBLIOGRAPHY 293

LIST OF FIGURES

Chapter 2.1.1

Figure 1 33

Chapter 2.1.2

Figures 1-5 ..... 61 - 65

Chapter 3.1.1

Figures 1-13 ..... 82 - 94

Chapter 3.1.2

Figures 1-9 ..... 113 - 121

Chapter 3.2.1

Figures 1-28 ..... 163 - 194

Chapter 3.2.2

Figures 1-14 ..... 218 - 233

Chapter 3.2.3

Figures 1-14 ..... 260 - 274

Chapter 3.2.4

Figures 1-3 ..... 283 - 285

1. INTRODUCTION

In quantum mechanics, any linear combination of states of a physical system determines a proper new state satisfying Schrödinger's equation. This is the principle of superposition, an inherent property of wave-like phenomena. Its quantum mechanical generalization to any physical system, however, directly implies the dual wave-particle character of matter and, hence, lies at the core of the irreconcilable differences between classical and quantum physics. As Richard Feynman notes discussing Young's two-slit experiment in his introduction to quantum mechanics, "We [choose to] examine a phenomenon which is impossible, *absolutely* impossible, to explain in any classical way, and which has in it the heart of quantum mechanics. In reality, it contains the *only* mystery". [1]

Does the superposition principle operate on macroscopic scales? What consequences do we have to face when considering superposition states of a composite system of two correlated subsystems separated by a macroscopically large distance? The famous Schrödinger-cat argument highlights problems of interpretation where macroscopic superposition states are allowed, while the Einstein-Podolsky-Rosen (EPR-) paradox [2] marks the questions concerning nonlocality. On the other hand, what effects do microscopic quantum superposition states make on the behavior of macroscopic physical systems, and can these be employed in practical devices? In quantum optics, it has been of great interest to tackle these questions: to prepare and detect quantum superpositions, and to study their effects and their implications in an optical context. Coherent superpositions of states lead to interference effects such as those in the Young's experiment, while their classical ("incoherent" or "statistical") mixtures do not. Hence, in order to demonstrate coherent superpositions and other quantum coherence phenomena one needs to look for the implications of quantum interferences. As we shall see in the following chapters later on and the references therein, quantum interferences can modify the behavior of quantum optical systems in a crucial way. These effects are experimentally feasible and may have

far reaching practical consequences.

Here, we consider two such examples where quantum coherences make significant effects on the behavior of a quantum optical system. First, we consider laser systems with atomic coherences and look for coherence effects in the laser operation; such as noninversion lasing and quantum-noise reduction. We are using three-level pumping atoms in the Λ-configuration, where the lower two atomic levels are closely spaced. Coherences between the atomic levels are introduced by some external means. They are taken as initial conditions or generated by an external field between the lower two closely spaced levels ("quantum-beat" laser). One- and two-mode laser operations are considered.

Secondly, we consider two micromasers coupled in series by sharing a common pumping beam of two-level atoms. It has become well-known by now that the micromaser is a genuine quantum system. Therefore, one may want to look at the composite system of two and study the quantum effects of the complete system as a consequence of the coupling. In particular, the behavior of the second micromaser is investigated as a function of the atomic coherence prepared by the first one. On the other hand, we also look at the possibilities of generating correlation between the two fields as atomic coherence is transferred from the first to the second cavity. The build-up of correlation, i. e., coherence between the fields is reminiscent of Young's two-slit experiment for having two indistinguishable paths to reach the same final state. Preparation of pure entangled quantum states of the two macroscopically separated fields makes the problem relevant in the context of the EPR-paradox and the Schrödinger-cat argument. Finally, we also study how nonlocal entangled states of two fields can be used to generate entangled states of two distinct atomic beams. Such beams can have several possible applications. Here, we apply them in an experimentally feasible proposal for tests of the complementary character of wave-like and particle-like behaviors.

The thesis is organized as follows. In Chapter 2 we discuss the above outlined aspects of the laser problem with atomic coherence. Chapter 3 is devoted to the pump-coupled micromasers, except 3.1 where some special quantum features of the photon statistics of a single micromaser are studied. Chapter 4 briefly summarizes the main results of the thesis.

2. ATOMIC COHERENCE IN LASER SYSTEMS

2.1 Studies on Lasing Without Inversion

2.1.1 Quantum Theory of a Noninversion Laser with Injected Atomic Coherence†

ABSTRACT

A quantum theory of a Λ-type three-level single-mode quantum-beat laser with injected atomic coherences and with an external microwave field, which coherently drives the lower two nearly degenerate levels, is studied. A master equation for the field-density operator and the photon statistics is derived. The laser operation is analyzed in terms of the coefficients of the Fokker-Planck equation of the laser field. Noninversion lasing is found in both cases: without and with injected atomic coherences. At the same time, in the latter case large quantum-noise reduction is found, and for particular initial parameter choices the laser field is very near to a coherent state with exactly Poissonian photon-number distribution and near-Poissonian phase distribution.

I. INTRODUCTION

The semiclassical and quantum theories of the laser were developed more than 20 years ago and subsequently reached a very high level of sophistication [1-3]. The underlying physics is now believed to be well understood. Some of the key concepts of the theoretical description are population inversion and laser threshold. In the models considered in all of the above theories it is vital to establish population inversion since the gain is proportional to the population difference between the upper and lower levels of the lasing transition. The interpretation is obvious: emission is proportional to the upper-level population,

whereas absorption is proportional to the lower-level population. The net effect of these two elementary processes is the gain. On the other hand, the cavity losses determine the laser threshold: obviously, in order to establish steady-state oscillation, the gain has to balance the loss.

Recent studies, however, on the possibility of amplification in a noninverted medium with very closely spaced upper (lower) levels and a single lower (upper) level pointed to the crucial role of the atomic coherence in the lasing process, especially when compared to conventional laser theory which involves incoherent pumping. Kocharovskaya and Khanin [4] predicted amplification of ultrashort pulses in an active medium consisting of three-level atoms with two nearly degenerate lower levels. Arkhipkin and Heller [5] showed the possibility of amplification in the case in which a single upper level is submerged in a continuum of field-induced autoionizing states (which act as a second degenerate upper level). In closely related works, Harris considered cw amplification with nearly degenerate upper autoionizing levels decaying to the same continuum [6(a)], and also investigated the effect of transient response on the dynamics [6(b)]. A more quantitative study was presented by Lyras et al [7]. Other related works have recently appeared concerning different systems, transient effects, and novel methods to produce nonabsorbing resonances [8(a)], as well as a novel interpretation based on dressed atomic states [8(b)]. Scully, Zhu, and Gavrielides [9] pointed to the crucial role played by atomic coherence between the degenerate levels. The source of noninversion lasing is that in the case of upper-level degeneracy the emissions from the two levels add coherently (constructive interference), whereas with degenerate lower levels the absorption amplitudes from the two levels subtract coherently (destructive interference). That is, nonreciprocity between absorption and emission takes place in such a way that emission dominates over absorption. In this context, it should be noted that a similar effect due to recoil splitting of Doppler-broadened emission and absorption spectra was suggested [10] some time ago. Scully, Zhu, and Gavrielides [9] suggested microwave coupling of the nearly degenerate levels in order to introduce the necessary coherence into the system. In closely related

works noninversion laser with atomic coherences has recently been studied [11] even in the collision dominated regime [12]. In fact, such coherences have long since been investigated in Raman-type processes [13-15], and experimentally demonstrated [16] in connection with studies on optical pumping. It should also be mentioned at this point that the noninversion lasing effect may have far reaching practical consequences. It is increasingly difficult to establish inversion on transitions in the high-frequency part of the spectrum (e.g., vuv, x ray, etc.). A similar difficulty is encountered in two-photon lasers. Instead of trying to pump the system harder to reach inversion it may be more practical to create appropriate coherence between nearly degenerate levels.

We have already mentioned that the concept of inversion plays a central role in incoherently pumped lasers. It is, however, not the inversion that drives the laser but the atomic dipole moment, associated with the lasing transition, which is the source of radiation. In incoherently pumped lasers the laser field itself induces a dipole moment and it turns out to be proportional to the population difference between the levels. In coherently pumped devices, however, the active atoms are prepared in a coherent superposition of the lasing levels and have a finite dipole moment even without the field (injected coherence versus the induced coherence of incoherently pumped lasers). The gain expression of such devices is very different from that of incoherently pumped lasers. Indeed, in closely related studies on correlated-emission laser schemes (coherently pumped lasers or lasers with injected coherence) [17-19] aimed at the reduction of quantum noise it was found, as a by-product, that noninversion lasing was possible, e.g., in the two-photon correlated-emission laser [18] and even in a single-photon laser with injected atomic coherence [19]. In these cases, however, it is not the coherence between closely spaced upper or lower levels that leads to noninversion gain but rather the atomic coherence between upper and lower levels of the lasing transition. It should be noted that the main feature of these correlated-emission laser schemes is the significant amount of quantum-noise quenching and even squeezing under appropriate conditions.

Motivated by the above arguments that point to the crucial role of atomic coherence in achieving noninversion lasing and quantum-noise quenching, in this paper we suggest a

new type of single-mode laser where the active medium consists of three-level atoms in Λ configuration with atomic coherence between all levels. In the special case when there is coherence only between the two nearly degenerate lower levels, our system reduces to previously suggested noninversion laser schemes [9] and the present theory proves that noninversion lasing persists in an all order treatment. Previous studies were limited to linear treatment only. In the other special case when there is coherence between the upper and one lower lasing level this system reproduces the noise-quenching features of the single-photon laser with injected coherence in the highly nonlinear regime [19]. The introduction of split lower levels into this latter system, with coherence between them, gives the flexibility of simultaneously optimizing the gain that arises from the coherences between the upper and lower lasing level (long coherences) and suppressing the loss due to absorption by the lower levels via the coherence between split lower levels (short coherence). This optimization requires a fine balance between the coherences but the payoffs are twofold. Firstly, it turns out that under optimum conditions, the gain of the present system is so high that it immediately enters the nonlinear regime or, in other words, the effective threshold for laser operation is zero and the system does not even have a linear regime. Secondly, the conditions for maximum gain coincide with those of minimum noise and the generated field is very near to an ideal pure coherent state. The effect, in fact, is a striking manifestation for an active system of the Fano-type interferences [20].

The paper is organized as follows. In Sec. II we present the Hamiltonian model of the Λ-type system, in Sec. III the solution of the corresponding Schrödinger equation is provided. In Sec. IV we derive the master equation of the previously described model. In Sec. V by converting the master equation into a Fokker-Planck equation we obtain the diffusion and drift coefficients for the photon number and phase, and study the steady-state operation [21]. We show here that noninversion lasing is accompanied with reduced photon number and phase noise due to the coherent superposition of atomic states and the laser field is very near to an ideal coherent state at the threshold. Section VI is concerned with the discussion of the results.

II. THE MODEL

In this section we derive the interaction Hamiltonian of the coupled atom-field system after two transformations in a second interaction picture. Introducing particular assumptions concerning the cavity modes and the detunings between the frequencies of the modes and transitions, the obtained interaction matrix will be used in Sec. III for the investigation of the time evolution of the physical problem under consideration.

We consider a system of Λ-type three-level atoms as shown in Fig. 1, having one upper level $|a\rangle$ with energy $\hbar\omega_a$, and two lower ones $|b\rangle$ and $|c\rangle$ with energies $\hbar\omega_b$ and $\hbar\omega_c$, respectively. The $|a\rangle \Rightarrow |b\rangle$, and $|a\rangle \Rightarrow |c\rangle$ transitions are assumed to be dipole allowed. The two lower levels $|b\rangle$ and $|c\rangle$, are strongly coupled by a (classical) external microwave field, characterized by a Rabi frequency $\mathcal{V}$ and phase ϕ. Also, the upper level $|a\rangle$ and lower levels $|b\rangle$ and $|c\rangle$ are assumed to be in a coherent superposition due to injected coherence, so that the ρ_{ab} and ρ_{ac} elements of the atomic density matrix are different from zero.

The Hamiltonian for the field and one active atom is given in the Schrödinger picture as

$$H = H_0 + V \quad , \tag{1}$$

where

$$H_0 = \sum_{i=a,b,c} \hbar\omega_i |i\rangle\langle i| + \hbar\Omega_1\left(a_1^\dagger a_1 + \frac{1}{2}\right) + \hbar\Omega_2\left(a_2^\dagger a_2 + \frac{1}{2}\right) \tag{2}$$

and

$$V = \hbar g_1 a_1 |a\rangle\langle b| + \hbar g_2 a_2 |a\rangle\langle c| - \frac{1}{2}\hbar\mathcal{V}e^{i(\Omega_3 t+\phi)}|b\rangle\langle c| + H.c. \quad . \tag{3}$$

Here Ω_1, Ω_2 are the cavity-mode frequencies, a_1 ($a_1^\dagger$), a_2 ($a_2^\dagger$) are the annihilation (creation) operators in these modes, respectively, g_1, g_2 are the coupling constants for the transitions $|a\rangle \Rightarrow |b\rangle$, and $|a\rangle \Rightarrow |c\rangle$. Ω_3 and ϕ are the frequency and phase of the external microwave field, driving the $|b\rangle \Rightarrow |c\rangle$ transition, which is treated semiclassically. It is convenient to work in the interaction picture, defined as

$$V_I = \exp\left(\frac{i}{\hbar}H_0 t\right) V \exp\left(-\frac{i}{\hbar}H_0 t\right) \quad . \tag{4}$$

It can be shown that

$$V_I = V_1 + V_2 \quad , \tag{5}$$

where

$$V_1 = -\frac{1}{2}\hbar\mathcal{V}\begin{bmatrix} 0 & 0 & 0 \\ 0 & 0 & \exp(i\Delta_3 t - i\phi) \\ 0 & \exp(-i\Delta_3 t + i\phi) & 0 \end{bmatrix} \tag{6}$$

and

$$V_2 = \hbar\begin{bmatrix} 0 & g_1 a_1 \exp(i\Delta_1 t) & g_2 a_2 \exp(i\Delta_2 t) \\ g_1 a_1^\dagger \exp(-i\Delta_1 t) & 0 & 0 \\ g_2 a_2^\dagger \exp(-i\Delta_2 t) & 0 & 0 \end{bmatrix} \quad . \tag{7}$$

Here

$$\Delta_1 = \omega_{ab} - \Omega_1 = \omega_a - \omega_b - \Omega_1 \quad ,$$

$$\Delta_2 = \omega_{ac} - \Omega_2 = \omega_a - \omega_c - \Omega_2 \quad ,$$

$$\Delta_3 = \omega_{bc} - \Omega_3 = \omega_b - \omega_c - \Omega_3$$

are the detunings. We assume that the driving field is resonant,

$$\Delta_3 = 0, \text{ and furthermore, } \Delta_1 = -\Delta_2 = \frac{1}{2}\mathcal{V} \quad , \tag{8}$$

and

$$a_1 = a_2 =: a, \quad g_1 = g_2 =: g \quad . \tag{9}$$

Using a second interaction picture defined as

$$V_{II} = \exp\left(\frac{i}{\hbar} V_1 t\right) V_2 \exp\left(-\frac{i}{\hbar} V_1 t\right) \quad , \tag{10}$$

and applying a rotating-wave approximation, where we neglect the rapidly varying terms, $exp[i(\Delta_1 + \frac{1}{2}\mathcal{V})t]$ and $exp[i(\Delta_2 - \frac{1}{2}\mathcal{V})t]$, and retain the slowly varying ones, $exp[i(\Delta_1 - \frac{1}{2}\mathcal{V})t]$ and $exp[i(\Delta_2 + \frac{1}{2}\mathcal{V})t]$, the interaction matrix has the following form:

$$V_{II} = \hbar g \begin{bmatrix} 0 & -i\exp\left(i\frac{\phi}{2}\right)\sin\frac{\phi}{2}a & \exp\left(-i\frac{\phi}{2}\right)\cos\frac{\phi}{2}a \\ i\exp\left(-i\frac{\phi}{2}\right)\sin\frac{\phi}{2}a^{\dagger} & 0 & 0 \\ \exp\left(i\frac{\phi}{2}\right)\cos\frac{\phi}{2}a^{\dagger} & 0 & 0 \end{bmatrix} . \tag{11}$$

III. SOLUTION OF THE MODEL

Based on the obtained Hamiltonian (11) we proceed further with the investigation of the time evolution of the Λ system coupled to a single cavity mode under the particular set of conditions (8) and (9). From the wave functions obtained from the time-dependent Schrödinger equation we will derive a master equation for the field-density matrix and an equation for the steady-state photon distribution in Sec. IV.

The Schrödinger equation in the second interaction picture (10) can be written as

$$i\hbar\dot{\psi} = V_{II}\psi \quad , \tag{12}$$

where ψ is a column vector with components ψ_a, ψ_b, ψ_c. Equation (12) written in components reads

$$i\dot{\psi}_a = -ig\exp\left(i\frac{\phi}{2}\right)\sin\frac{\phi}{2}a\psi_b + g\exp\left(-i\frac{\phi}{2}\right)\cos\frac{\phi}{2}a\psi_c - i\frac{\gamma}{2}\psi_a \quad ,$$

$$i\dot{\psi}_b = ig\exp\left(-i\frac{\phi}{2}\right)\sin\frac{\phi}{2}a^{\dagger}\psi_a - i\frac{\gamma}{2}\psi_b$$

$$i\dot{\psi}_b = -ig\exp\left(i\frac{\phi}{2}\right)\sin\frac{\phi}{2}a^{\dagger}\psi_a - i\frac{\gamma}{2}\psi_b \quad ,$$

$$i\dot{\psi}_c = g\exp\left(i\frac{\phi}{2}\right)\cos\frac{\phi}{2}a^{\dagger}\psi_a - i\frac{\gamma}{2}\psi_c \quad . \tag{13}$$

Here γ is a decay constant for the levels *a, b, c* (for simplicity, the same for all levels). With the substitutions

$$\psi_a = \exp\left[-\frac{\gamma}{2}(t-t_0)\right]\psi_a' \quad ,$$

$$\psi_b = \exp\left(-i\frac{\phi}{2}\right)\exp\left[-\frac{\gamma}{2}(t-t_0)\right]\psi_b' \quad ,$$

$$\psi_c = \exp\left(i\frac{\phi}{2}\right)\exp\left[-\frac{\gamma}{2}(t-t_0)\right]\psi_c' \quad , \tag{14}$$

the components of the new wave function ψ' satisfy the following equations:

$$i\dot{\psi}_a' = -ig\sin\frac{\phi}{2}a\psi_b' + g\cos\frac{\phi}{2}a\psi_c' \quad ,$$

$$i\dot{\psi}_b' = ig\sin\frac{\phi}{2}a^\dagger\psi_a' \quad ,$$

$$i\dot{\psi}_c' = g\cos\frac{\phi}{2}a^\dagger\psi_a' \quad . \tag{15}$$

Introducing

$$\psi_1' = \cos\frac{\phi}{2}\psi_b' - i\sin\frac{\phi}{2}\psi_c' \quad ,$$

$$\psi_2' = \cos\frac{\phi}{2}\psi_c' - i\sin\frac{\phi}{2}\psi_b' \quad , \tag{16}$$

Eq. (15) can be written as

$$i\dot{\psi}_1' = 0 \quad ,$$

$$i\dot{\psi}_2' = ga^\dagger\psi_a' \quad ,$$

$$i\dot{\psi}_a' = ga\psi_2' \quad . \tag{17}$$

Since the relation between ψ and ψ' is written in Eq. (14) from the solution of Eq. (17) for ψ', the solution of Eqs. (12) and (13) is the following:

$$\psi_a(t)=\exp\left[-\frac{\gamma}{2}(t-t_0)\right]\left\{C\psi_a(t_0)-\exp\left(i\frac{\phi}{2}\right)\sin\frac{\phi}{2}Sa\psi_b(t_0)-i\exp\left(-i\frac{\phi}{2}\right)\cos\frac{\phi}{2}Sa\psi_c(t_0)\right\},$$

$$\psi_b(t)=\exp\left[-\frac{\gamma}{2}(t-t_0)\right]\left\{\exp\left(-i\frac{\phi}{2}\right)\sin\frac{\phi}{2}a^{\dagger}S\psi_a(t_0)+\left(\sin^2\frac{\phi}{2}\overline{C}+\cos^2\frac{\phi}{2}\right)\psi_b(t_0)+\right.$$

$$\left.+i\exp(-i\phi)\sin\frac{\phi}{2}\cos\frac{\phi}{2}(\overline{C}-1)\psi_c(t_0)\right\}\quad,$$

$$\psi_c(t)=\exp\left[-\frac{\gamma}{2}(t-t_0)\right]\left\{-i\exp\left(i\frac{\phi}{2}\right)\cos\frac{\phi}{2}a^{\dagger}S\psi_a(t_0)+\left(\cos^2\frac{\phi}{2}\overline{C}+\sin^2\frac{\phi}{2}\right)\psi_c(t_0)-\right.$$

$$\left.-i\exp(i\phi)\sin\frac{\phi}{2}\cos\frac{\phi}{2}(\overline{C}-1)\psi_b(t_0)\right\}\quad, \tag{18}$$

where $C=\cos\left[g\sqrt{aa^{\dagger}}(t-t_0)\right]$, $S=\dfrac{\sin\left[g\sqrt{aa^{\dagger}}(t-t_0)\right]}{\sqrt{aa^{\dagger}}}$ and $\overline{C}=\cos\left[g\sqrt{a^{\dagger}a}(t-t_0)\right]$.

We shall use these solutions in Sec. IV to obtain a master equation for the field-density operator and the steady state photon distribution.

IV. THE MASTER EQUATION AND THE PHOTON STATISTICS

The density matrix of the three-level Λ atom and the one-mode field described by the Hamiltonian (1) - (3) satisfies the following equation of motion in the second interaction picture determined by Eq. (10):

$$\dot{\rho}=-\frac{i}{\hbar}[V_{II},\rho]\quad. \tag{19}$$

Although, formally, this equation is identical to the one neglecting atomic decay, the spirit in which we employ it is very different, as will be clear from the considerations below. When we take the trace of this equation over the atomic variables (in order to obtain an equation for the reduced density operator of the field only [see Eq. (20) below], then in the right-hand side in the matrix elements appearing in Eq. (22) we effectively replace the atomic variables by their steady-state values (adiabatic elimination of atomic variables), which is justified by the much faster relaxation rate of the atomic variables than that of the field ($\gamma >> \gamma_c$). In doing so, we make use of Eqs. (13). That is, in the resulting master equation for the density operator of the field only, Eq. (28), the atomic relaxation process is fully accounted for.

We introduce the reduced density operator ρ_F for the field only as

$$\rho_F = Tr_{atom}\rho \quad , \tag{20}$$

where Tr_{atom} stands for tracing of ρ over the atom. Consequently, the equation of motion of the field-density operator ρ_F can be obtained from Eq. (19) in the form

$$\dot{\rho}_F = Tr_{atom}\dot{\rho} = -\frac{i}{\hbar}Tr_{atom}[V_{II},\rho] \quad . \tag{21}$$

Using the expression (11) for V_{II}

$$\dot{\rho}_F = -g\sin\frac{\phi}{2}\left\{\exp\left(i\frac{\phi}{2}\right)[a,\rho_{ba}] - \exp\left(-i\frac{\phi}{2}\right)[a^\dagger,\rho_{ab}]\right\} -$$

$$-ig\cos\frac{\phi}{2}\left\{\exp\left(-i\frac{\phi}{2}\right)[a,\rho_{ca}] - \exp\left(i\frac{\phi}{2}\right)[a^\dagger,\rho_{ac}]\right\} + \mathcal{L}_c\rho_F \quad , \tag{22}$$

where $\mathcal{L}_c\rho_F$ describes the effect of field loss due to cavity damping. Its explicit form is given in Eq. (27).

To obtain an expression for ρ_{ab}, ρ_{ac}, and their Hermitian conjugates we first calculate the contribution of one atom injected at time t_0 with arbitrary initial condition into the cavity and then sum the contribution of all atoms injected at random times between $t\text{-}1/\gamma$ and t (i.e., $t\text{-}1/\gamma < t_0 < t$) at rate r. This means that the atom-field interaction is considered on a time scale shorter than the atomic lifetime $1/\gamma$. In this way,

$$\rho_{ab} = r \int_{t-1/\gamma}^{t} dt_0 \psi_a(t,t_0)\psi_b^{\dagger}(t,t_0) \tag{23}$$

and

$$\rho_{ac} = r \int_{t-1/\gamma}^{t} dt_0 \psi_a(t,t_0)\psi_c^{\dagger}(t,t_0) \quad . \tag{24}$$

Substituting the expressions for ψ_a, ψ_b, ψ_c from Eq. (19) into Eqs. (23) and (24),

$$\rho_{ab} = r \int_{t-1/\gamma}^{t} dt_0 \exp[-\gamma(t-t_0)] \times$$

$$\times\Big[\exp\Big(i\frac{\phi}{2}\Big)\sin\frac{\phi}{2} C\rho_{aa}(t_0)\rho_F(t_0)Sa - \exp\Big(i\frac{\phi}{2}\Big)\sin\frac{\phi}{2} Sa\rho_{bb}(t_0)\rho_F(t_0)\Big(\sin^2\frac{\phi}{2}\overline{C} + \cos^2\frac{\phi}{2}\Big) -$$

$$-\exp\Big(i\frac{\phi}{2}\Big)\sin\frac{\phi}{2}\cos^2\frac{\phi}{2} Sa\rho_{cc}(t_0)\rho_F(t_0)(\overline{C}-1) + C\rho_{ab}(t_0)\rho_F(t_0)\Big(\sin^2\frac{\phi}{2}\overline{C} + \cos^2\frac{\phi}{2}\Big) -$$

$$-\exp(i\phi)\sin^2\frac{\phi}{2} Sa\rho_{ba}(t_0)\rho_F(t_0)Sa - i\exp(i\phi)\sin\frac{\phi}{2}\cos\frac{\phi}{2} C\rho_{ac}(t_0)\rho_F(t_0)(\overline{C}-1) -$$

$$-i\sin\frac{\phi}{2}\cos\frac{\phi}{2} Sa\rho_{ca}(t_0)\rho_F(t_0)Sa + i\exp\Big(3i\frac{\phi}{2}\Big)\sin^2\frac{\phi}{2}\cos\frac{\phi}{2} Sa\rho_{bc}(t_0)\rho_F(t_0)(\overline{C}-1) -$$

$$-i\exp\Big(-i\frac{\phi}{2}\Big)\cos\frac{\phi}{2} Sa\rho_{cb}(t_0)\rho_F(t_0)\Big(\sin^2\frac{\phi}{2}\overline{C} + \cos^2\frac{\phi}{2}\Big)\Big] \quad . \tag{25}$$

In the same way,

$$\rho_{ac} = r \int_{t-1/\gamma}^{t} dt_0 \exp[-\gamma(t-t_0)] \times$$

$$\times \Big[i\exp\Big(-i\frac{\phi}{2}\Big)\cos\frac{\phi}{2} C\rho_{aa}(t_0)\rho_F(t_0)Sa - i\exp\Big(-i\frac{\phi}{2}\Big)\sin^2\frac{\phi}{2}\cos\frac{\phi}{2} Sa\rho_{bb}(t_0)\rho_F(t_0)(\overline{C}-1) -$$

$$-i\exp\Big(-i\frac{\phi}{2}\Big)\cos\frac{\phi}{2} Sa\rho_{cc}(t_0)\rho_F(t_0)\Big(\cos^2\frac{\phi}{2}\overline{C}+\sin^2\frac{\phi}{2}\Big) +$$

$$+i\exp(-i\phi)\sin\frac{\phi}{2}\cos\frac{\phi}{2} C\rho_{ab}(t_0)\rho_F(t_0)(\overline{C}-1) - i\sin\frac{\phi}{2}\cos\frac{\phi}{2} Sa\rho_{ba}(t_0)\rho_F(t_0)Sa +$$

$$+C\rho_{ac}(t_0)\rho_F(t_0)\Big(\cos^2\frac{\phi}{2}\overline{C}+\sin^2\frac{\phi}{2}\Big) + \exp(-i\phi)\cos^2\frac{\phi}{2} Sa\rho_{ca}(t_0)\rho_F(t_0)Sa -$$

$$-\exp\Big(i\frac{\phi}{2}\Big)\sin\frac{\phi}{2} Sa\rho_{bc}(t_0)\rho_F(t_0)\Big(\cos^2\frac{\phi}{2}\overline{C}+\sin^2\frac{\phi}{2}\Big) +$$

$$+\exp\Big(-3i\frac{\phi}{2}\Big)\sin\frac{\phi}{2}\cos^2\frac{\phi}{2} Sa\rho_{cb}(t_0)\rho_F(t_0)(\overline{C}-1)\Big] \quad . \tag{26}$$

Since the dynamics of the field is governed by the cavity lifetime $1/\gamma_c$, which is much longer then the atomic lifetime $1/\gamma$, ρ_F does not change appreciably during the integration time interval, and thus $\rho_F(t_0)$ in Eqs. (25) and (26) can be approximated by $\rho_F(t)$.

When $t - t_0 > 1/\gamma$ (i.e., $t - 1/\gamma > t_0$) the contribution to the integral is negligible due to the exponential damping factor. This means that the lower limit of the integration can be extended to $-\infty$.

After performing these steps we can substitute ρ_{ab}, ρ_{ac} and their Hermitian conjugates into the equation of motion (22). We still need the loss term for Eq. (22),

which can be specified in the usual manner [1,17,19],

$$\mathcal{L}_c\rho_F = -\frac{\gamma_c}{2}\left(a^\dagger a\rho_F + \rho_F a^\dagger a - 2a\rho_F a^\dagger\right) \quad . \tag{27}$$

Now taking the n, n' matrix element of the equation of motion of ρ_F it is easy to carry out the time integration, and we obtain the following master equation for the matrix elements of the field-density operator:

$$\begin{aligned}
(\dot{\rho}_F)_{n,n'} = &\left\{-\frac{\overline{\alpha}}{2}\rho_{n,n'}\rho_{aa}\left[n+1+n'+\frac{\beta}{4\overline{\alpha}}(n-n')^2\right]+\overline{\alpha}\rho_{n+1,n'+1}M\sqrt{(n+1)(n'+1)}-\right.\\
&-\eta\rho_{n,n'+1}R\sqrt{n'+1}\left[1-\frac{\beta}{4\overline{\alpha}}(n-n')\right]-\eta\rho_{n+1,n'}R^\dagger\sqrt{n+1}\left[1+\frac{\beta}{4\overline{\alpha}}(n-n')\right]\Big\}N^{-1}_{n,n'}+\\
&+\left\{\overline{\alpha}\rho_{n-1,n'-1}\rho_{aa}\sqrt{nn'}-\frac{\overline{\alpha}}{2}\rho_{n,n'}M\left[n+n'+\frac{\beta}{4\overline{\alpha}}(n-n')^2\right]+\right.\\
&\left.+\eta\rho_{n-1,n'}R\sqrt{n}\left[1+\frac{\beta}{4\overline{\alpha}}(n-n')\right]+\eta\rho_{n,n'-1}R^\dagger\sqrt{n'}\left[1-\frac{\beta}{4\overline{\alpha}}(n-n')\right]\right\}N^{-1}_{n-1,n'-1}-\\
&-\frac{\gamma_c}{2}\left[\rho_{n,n'}(n+n')-\rho_{n+1,n'+1}2\sqrt{(n+1)(n'+1)}\right] \quad ,
\end{aligned} \tag{28}$$

$$\overline{\alpha} = 2r\frac{g^2}{\gamma^2} \quad , \qquad \beta = 8r\frac{g^4}{\gamma^4} \quad , \qquad \eta = r\frac{g}{\gamma} \quad ,$$

$\overline{\alpha}$ and β are the linear-gain coefficient and saturation parameter, respectively,

$$M = \frac{1}{2}\left[(1-\cos\phi)\rho_{bb}+(1+\cos\phi)\rho_{cc}-i\sin\phi\left(\rho_{bc}e^{i\phi}-\rho_{cb}e^{-i\phi}\right)\right] \quad , \tag{29}$$

$$R = \rho_{ab}\sin\frac{\phi}{2}\exp\left(-i\frac{\phi}{2}\right)-i\rho_{ac}\cos\frac{\phi}{2}\exp\left(i\frac{\phi}{2}\right) \quad , \tag{30}$$

$$N_{n,n'} = 1 + \frac{\beta}{2\bar{\alpha}}(n+1+n'+1) + \left(\frac{\beta}{4\bar{\alpha}}\right)^2 (n-n')^2 \quad . \tag{31}$$

It can be seen that Eq. (28) reduces to the well-known field master equation [19] of a one-mode two-level laser, if $R = 0$ (i.e., no atomic coherence between the upper and the lower levels), and the "effective population" of the lower two levels M is equal to ρ_{bb}.

Photon statistics

The equation of motion of the diagonal elements of the field-density matrix is obtained from Eq. (28) by setting $n = n' =: n$. We have an equation for the steady-state photon distribution if the time derivative $\dot{\rho}_{n,n}$ is equal to zero,

$$\dot{\rho}_{n,n} = -\left[\bar{\alpha}\left(\rho_{n,n}\rho_{aa} - \rho_{n+1,n+1}M\right)(n+1) + \eta\left(\rho_{n,n+1}R + \rho_{n+1,n}R^{\dagger}\right)\sqrt{n+1}\right]N^{-1}_{n,n} +$$

$$+\left[\bar{\alpha}\left(\rho_{n-1,n-1}\rho_{aa} - \rho_{n,n}M\right)n + \eta\left(\rho_{n-1,n}R + \rho_{n,n-1}R^{\dagger}\right)\sqrt{n}\right]N^{-1}_{n-1,n-1} +$$

$$-\gamma_c\left[\rho_{n,n}n - \rho_{n+1,n+1}(n+1)\right] = 0 \quad . \tag{32}$$

The differences between Eq. (32) and the equation of motion of $\rho_{n,n}$ of a usual two-level laser are in the variable M, and the terms connected with the off-diagonal elements of the field-density matrix and the initial atomic coherences again.

V. THE FOKKER-PLANCK EQUATION

In this section we employ the Glauber-Sudarshan P representation for the field-density matrix and transform its equation of motion (22) into a Fokker-Planck equation. Calculating the steady-state drift and diffusion coefficients of the Fokker-Planck equation

the characteristics of the lasing system considered in this paper can be studied. Substituting the Glauber representation form of the field-density matrix

$$\rho_F(t) = \int d^2\alpha P(\alpha,\alpha^*,t)|\alpha\rangle\langle\alpha| \tag{33}$$

into Eqs. (25) and (26) for ρ_{ab} and ρ_{ac} calculating the equation of motion (22) (assuming that the mean photon number is large and *1* can be neglected compared to $\alpha\alpha^*$), we obtain the following equation of motion for $P(\alpha, \alpha^*, t)$:

$$\frac{\partial P}{\partial t} = \left[-\frac{\overline{\alpha}}{2}(\rho_{aa} - M)\left(\frac{\partial}{\partial\alpha}\alpha + \frac{\partial}{\partial\alpha^*}\alpha^*\right) + \right.$$

$$\left. + \overline{\alpha}\rho_{aa}\frac{\partial^2}{\partial\alpha\partial\alpha^*} - \frac{\beta}{8}(\rho_{aa} + M)\left(\frac{\partial}{\partial\alpha}\alpha - \frac{\partial}{\partial\alpha^*}\alpha^*\right)^2\right] N^{-1}P -$$

$$-\left(\eta R\left\{\frac{\partial}{\partial\alpha} + \frac{\beta}{4\overline{\alpha}}\left[2\left(\frac{\partial}{\partial\alpha}\alpha - \frac{\partial}{\partial\alpha^*}\alpha^*\right)\alpha^* - \frac{\partial}{\partial\alpha}\left(\frac{\partial}{\partial\alpha}\alpha - \frac{\partial}{\partial\alpha^*}\alpha^*\right)\right]\right\} N^{-1}P + c.c.\right) +$$

$$+\frac{\gamma_c}{2}\left(\frac{\partial}{\partial\alpha}\alpha + \frac{\partial}{\partial\alpha^*}\alpha^*\right)P \tag{34}$$

where

$$P = P(\alpha, \alpha^*, t)$$

and

$$N = 1 + \frac{\beta}{2\overline{\alpha}}\left(2\alpha\alpha^* - \frac{\partial}{\partial\alpha}\alpha - \frac{\partial}{\partial\alpha^*}\alpha\right) + \left(\frac{\beta}{4\overline{\alpha}}\right)^2\left(\frac{\partial}{\partial\alpha}\alpha - \frac{\partial}{\partial\alpha^*}\alpha^*\right)^2 . \tag{35}$$

Introducing I and θ, the intensity and the phase of the field instead of α, where $\alpha = \sqrt{I}e^{i\theta}$, and expanding the equation of motion of (34) $P(I, \theta, t)$ up to second order in the derivatives, we arrive at a Fokker-Planck equation expressed in terms of I and θ,

$$\frac{\partial P}{\partial t} = \left[-\frac{\partial}{\partial I} d_I - \frac{\partial}{\partial \theta} d_\theta + \frac{\partial^2}{\partial I^2} D_{II} + \frac{\partial^2}{\partial \theta^2} D_{\theta\theta} + 2\frac{\partial^2}{\partial I \partial \theta} D_{I\theta} \right] P \quad , \tag{36}$$

where

$$P = P(I, \theta, t) \quad .$$

d_θ and d_I, $D_{\theta\theta}$ and D_{II}, and $D_{I\theta}$ are the phase and intensity drift, the phase and intensity diffusion, and the crossdiffusion coefficients, respectively.

The coefficients of the Fokker-Planck equation written in terms of intensity I and phase θ are the following (from now we use simply α and γ instead of $\overline{\alpha}$ and γ_c):

$$d_\theta = \frac{\alpha}{2i} Z\left(\frac{\beta}{\alpha} I\right)^{-1/2} \quad , \tag{37}$$

$$d_I = \frac{\alpha I}{1 + \frac{\beta}{\alpha} I}\left[\rho_{aa} - M + S\left(\frac{\beta}{\alpha} I\right)^{-1/2} - \frac{\gamma}{\alpha}\left(1 + \frac{\beta}{\alpha} I\right) \right] \quad , \tag{38}$$

$$D_{\theta\theta} = \frac{\beta}{4\left(1 + \frac{\beta}{\alpha} I\right)\frac{\beta}{\alpha} I}\left[\rho_{aa} + \frac{1}{2}(\rho_{aa} + M)\frac{\beta}{\alpha} I - \frac{1}{2} S\left(\frac{\beta}{\alpha} I\right)^{1/2} \right] \quad , \tag{39}$$

$$D_{II} = \frac{\alpha I}{\left(1 + \frac{\beta}{\alpha} I\right)^2}\left[\rho_{aa} + M\frac{\beta}{\alpha} I - S\left(\frac{\beta}{\alpha} I\right)^{1/2} \right] \quad , \tag{40}$$

$$D_{I\theta} = \frac{i\alpha}{8\left(1+\frac{\beta}{\alpha}I\right)} Z\left(\frac{\beta}{\alpha}I\right)^{1/2} \quad , \tag{41}$$

where

$$\rho_{ij} = |\rho_{ij}| \exp(i\varphi_{ij}) = \rho_{ji}^{*} \quad ,$$

that is,

$$|\rho_{ij}| = |\rho_{ji}|$$

and

$$\varphi_{ab} + \varphi_{bc} = \varphi_{ac} \quad ,$$

$$M = \frac{1}{2}\left[(1-\cos\phi)\rho_{bb} + (1+\cos\phi)\rho_{cc} + 2|\rho_{bc}|\sin\phi\sin(\phi+\varphi_{bc})\right] \quad ,$$

$$S = 2\mathrm{Re}\left(Re^{-i\theta}\right) = |\rho_{ab}|\left[-(1-\cos\phi)\sin(\theta-\varphi_{ab}) + \sin\phi\cos(\theta-\varphi_{ab})\right] +$$

$$+|\rho_{ac}|\left[-(1+\cos\phi)\sin(\theta-\varphi_{ac}) + \sin\phi\cos(\theta-\varphi_{ac})\right] \quad ,$$

$$Z = 2i\,\mathrm{Im}\left(Re^{-i\theta}\right) = -i\left\{|\rho_{ab}|\left[(1-\cos\phi)\cos(\theta-\varphi_{ab}) + \sin\phi\sin(\theta-\varphi_{ab})\right] +\right.$$

$$\left.+|\rho_{ac}|\left[(1+\cos\phi)\cos(\theta-\varphi_{ac}) + \sin\phi\sin(\theta-\varphi_{ac})\right]\right\} \quad .$$

Note that all the Fokker-Planck coefficients are phase (θ)-sensitive via S or Z.

It can be seen from Eq. (36),

$$\frac{d}{dt}\langle I\rangle = \langle d_I\rangle \quad , \tag{42}$$

$$\frac{d}{dt}\langle \theta\rangle = \langle d_\theta\rangle \quad , \tag{43}$$

which means, that in steady state $d_I = 0$ and $d_\theta = 0$. We obtain the steady-state intensity $\langle I\rangle$ from the solution of the equation $d_I = 0$ and the steady-state phase $\langle\theta\rangle$ from $d_\theta = 0$; that is, there is phase-locking in the system. The actual values of the diffusion coefficients in steady state are determined by the steady-state intensity $\langle I\rangle$ and phase $\langle\theta\rangle$.

In the P representation the photon number variance [21]

$$\left\langle (\Delta\hat{n})^2\right\rangle = \left\langle :(\Delta\hat{n})^2:\right\rangle + \langle\hat{n}\rangle = \left\langle (\delta I)^2\right\rangle + \langle I\rangle \quad , \tag{44}$$

and the phase variance is

$$\left\langle (\Delta\theta)^2\right\rangle = \left\langle :(\Delta\theta)^2:\right\rangle + \frac{1}{4\langle\hat{n}\rangle} = \left\langle (\delta\theta)^2\right\rangle + \frac{1}{4\langle I\rangle} \quad , \tag{45}$$

where $\hat{n} = a^\dagger a$ and $\delta I = I - \langle I\rangle$, $\delta\theta = \theta - \langle\theta\rangle$. From Eq. (36) we find the equation of motion for the normally ordered photon-number variance and phase variance [21]

$$\frac{d}{dt}\left\langle (\delta I)^2\right\rangle = 2\langle d_I\delta I\rangle + 2\langle D_{II}\rangle \quad , \tag{46}$$

$$\frac{d}{dt}\left\langle (\delta\theta)^2\right\rangle = 2\langle d_\theta\delta\theta\rangle + 2\langle D_{\theta\theta}\rangle \quad . \tag{47}$$

Expanding d_I and D_{II} in terms of δI around the steady state $\langle I\rangle = n_0$, we find that the total steady-state photon-number variance is given by

$$\left\langle (\Delta\hat{n})^2 \right\rangle = n_0 + \left(\frac{D_{II}}{|\partial d_I / \partial I|} \right)_{I=\langle I \rangle, \theta=\langle \theta \rangle} . \tag{48}$$

In the same way, after expanding d_θ and $D_{\theta\theta}$, in terms of $\delta\theta$ around $\langle\theta\rangle = \theta_0$, we find the phase variance to be

$$\left\langle (\Delta\theta)^2 \right\rangle = \frac{1}{4n_0} + \left(\frac{D_{\theta\theta}}{|\partial d_\theta / \partial \theta|} \right)_{I=\langle I \rangle, \theta=\langle \theta \rangle} . \tag{49}$$

In the following we study the cases of incoherent and coherent pumping to see the effect of the injected coherence.

A. Incoherent pumping

There is no injected atomic coherence in this case; that is, $S = 0$ and $Z = 0$. It can be seen from Eqs. (37)-(41) that none of the Fokker-Planck coefficients depends on the phase θ, i.e., there is no phase locking in this system. We obtain the mean photon number $\langle I \rangle = n_0$ from $d_I(n_0) = 0$,

$$n_0 = \frac{\alpha}{\gamma} \frac{\alpha(\rho_{aa} - M) - \gamma}{\beta} , \tag{50}$$

which is not zero (there is laser operation) if ρ_{aa} - $M > \gamma/\alpha$, i.e., the population is inverted. The steady-state diffusion coefficients from Eqs. (39) and (40) are

$$D_{\theta\theta}(n_0) = \frac{\alpha(\rho_{aa} + M) + \gamma}{8n_0} , \tag{51}$$

$$D_{II}(n_0)=\frac{\gamma}{\alpha}\frac{(\gamma+\alpha M)n_0}{\rho_{aa}-M} \quad . \tag{52}$$

Calculating the photon-number variance from Eq. (48),

$$\left\langle(\Delta\hat{n})^2\right\rangle=\frac{\alpha\rho_{aa}}{\alpha(\rho_{aa}-M)-\gamma}n_0 \quad . \tag{53}$$

It can be seen that depending on the effective population M of the lower levels we can find different kinds of laser operations of the system under consideration. If the phase of the microwave field $\phi=\pi$ or $\phi=0$, we have the operation of an ordinary two-level laser because $M = \rho_{bb}$ or $M = \rho_{cc}$, respectively. Choosing the initial population of one of the lower levels zero at an appropriate phase ϕ, we can obtain the noninversion laser operation: if $\phi=\pi$ and $\rho_{bb} = 0$ or $\phi=0$ and $\rho_{cc} = 0$, then $M = 0$. In this case

$$n_0=\frac{\alpha}{\gamma}\frac{\alpha\rho_{aa}-\gamma}{\beta} \quad , \tag{54}$$

$$D_{\theta\theta}(n_0)=\frac{\alpha\rho_{aa}+\gamma}{8n_0} \quad , \tag{55}$$

$$D_{II}(n_0)=\frac{\gamma}{\alpha}\frac{\gamma n_0}{\rho_{aa}} \quad , \tag{56}$$

$$\left\langle(\Delta\hat{n})^2\right\rangle=\frac{\alpha\rho_{aa}}{\alpha\rho_{aa}-\gamma}n_0 \quad , \tag{57}$$

That is, there is no need for population inversion between the upper and lower levels [like in Eq. (50)], because at an appropriate phase ϕ of the microwave field the effective population M can be zero even if the population of one of the lower levels is not zero; the only requirement to obtain laser operation is $\rho_{aa} > \gamma/\alpha$ [from Eq. (54)]. At the same time

comparing Eqs. (55) and (56) to Eqs. (51) and (52) we find that the diffusion coefficients of intensity and phase have decreased (i.e., there is noise quieting) in the noninversion laser case.

This was the case of an ordinary noninversion laser without injected atomic coherence, but with an external microwave field. Now we proceed to a system, where injected coherence is present to reduce the noise further.

B. Coherent pumping

There is injected atomic coherence, thus $S \neq 0$ and $Z \neq 0$. It can be shown, that

$$S^2 - Z^2 = 4\rho_{aa}M \quad .$$

At a steady-state phase θ_0, when $d_\theta = 0$, that is $Z = 0$,

$$S^2 = 4\rho_{aa}M \quad .$$

In this case the Fokker-Planck coefficients have the following forms:

$$d_\theta(\theta_0) = 0 \quad , \tag{58}$$

$$d_I(\theta_0) = \frac{\alpha I}{1+\frac{\beta}{\alpha}I}\left[\rho_{aa} - M + \left(\frac{2\rho_{aa}M}{\frac{\beta}{\alpha}I}\right)^{1/2} - \frac{\gamma}{\alpha}\left(1+\frac{\beta}{\alpha}I\right)\right] \quad , \tag{59}$$

$$D_{\theta\theta}(\theta_0) = \frac{\beta}{4\left(1+\frac{\beta}{\alpha}I\right)\frac{\beta}{\alpha}I}\left[\rho_{aa} + \frac{1}{2}(\rho_{aa}+M)\frac{\beta}{\alpha}I - \left(\rho_{aa}M\frac{\beta}{\alpha}I\right)^{1/2}\right] \quad , \tag{60}$$

$$D_{II}(\theta_0) = \frac{\alpha I}{\left(1+\frac{\beta}{\alpha}I\right)^2}\left[\rho_{aa}^{1/2} - \left(M\frac{\beta}{\alpha}I\right)^{1/2}\right]^2 \quad , \tag{61}$$

$$D_{I\theta}(\theta_0) = 0 \quad .$$

It can be seen from Eq. (61), that

$$D_{II}(\theta_0) \geq 0 \quad ,$$

and since

$$D_{\theta\theta} = \frac{1}{8I^2}\left[D_{II}\left(1+\frac{\beta}{\alpha}I\right) + \alpha\rho_{aa}I\right]$$

[see Eqs. (39) and (40)], thus

$$D_{\theta\theta}(\theta_0) > 0 \quad .$$

In steady state (where the phase is locked to $\langle\theta\rangle = \theta_0$ due to the injected atomic coherence) the photon number $\langle\hat{n}\rangle = n_0$ satisfies the following equation derived from $d_I(\theta_0, n_0) = 0$ using Eq. (59):

$$\left(\frac{\beta}{\alpha}n_0\right)^{3/2} + \left[1 - \frac{\alpha}{\gamma}(\rho_{aa} - M)\right]\left(\frac{\beta}{\alpha}n_0\right)^{1/2} - 2\frac{\alpha}{\gamma}(\rho_{aa}M)^{1/2} = 0 \quad . \tag{62}$$

We note that the third term of Eq. (62), which stems from the nonzero atomic coherence $S = 2(\rho_{aa}M)^{1/2} \neq 0$, acts as a driving force, and there is no need for population inversion

ρ_{aa} - $M > \gamma/\alpha$ for laser operation. At the same time since this term is determined by the effective population M, manipulating the value of M, we inevitably change the value of the third term (i.e., the injected coherence) in Eq. (62), too. Setting M equal to zero (i.e., $\phi = \pi$ or 0 and $\rho_{bb} = 0$ or $\rho_{cc} = 0$, respectively), we reobtain the incoherently pumped noninversion laser case of Sec. V.A because, at the steady-state value of the phase, the disappearance of the injected atomic coherence (i.e., $S = 0$) is a direct consequence of the zero effective population. This means that we cannot use the method of setting M equal to zero to obtain coherently pumped noninversion laser operation, but retaining $M \neq 0$ (i.e., the nonzero "driving force" term), due to the coherent pumping we still have noninversion lasing. Next we investigate the conditions for the minimal noise and maximal laser intensity.

Let us see the case when

$$D_{II}(\theta_0) = 0 \tag{63}$$

minimal, and consequently

$$D_{\theta\theta}(\theta_0) = \frac{\alpha\rho_{aa}}{8I} \quad . \tag{64}$$

In this case

$$\rho_{aa} = M\frac{\beta}{\alpha}I \quad . \tag{65}$$

Substituting this into Eq. (62) we obtain the intensity and phase in steady state,

$$M = \frac{\gamma}{\alpha} \quad , \tag{66}$$

and consequently

$$\rho_{aa} = \frac{\beta\gamma}{\alpha^2} n_0 \quad . \tag{67}$$

Introducing the following relation between the population of the lower levels,

$$\rho_{bb} = m\rho_{cc} \quad , \qquad m \in [0,\infty] \tag{68}$$

and using Eq. (66),

$$M = \frac{1}{2}\left[(1-\cos\phi)\rho_{bb} + (1+\cos\phi)\rho_{cc} + 2|\rho_{bc}|\sin\phi\sin(\phi+\varphi_{bc})\right] = \frac{\gamma}{\alpha} \quad , \tag{69}$$

and the fact that

$$\rho_{aa} + \rho_{bb} + \rho_{cc} = 1 \quad , \tag{70}$$

where ρ_{aa} satisfies Eq. (67), we obtain for n_0 the following general formula:

$$n_0 = \frac{\alpha}{\gamma}\frac{\alpha\left[m(1-\cos\phi)+1+\cos\phi+2\sqrt{m}\sin\phi\sin(\phi+\varphi_{bc})\right]-2\gamma(m+1)}{\beta\left[m(1-\cos\phi)+1+\cos\phi+2\sqrt{m}\sin\phi\sin(\phi+\varphi_{bc})\right]} \quad . \tag{71}$$

We disregard the $\phi = \pi$, $m = 0$ and the $\phi = 0$, $1/m = 0$ pairs because M could not be γ/α in these two cases. It can be seen that for $\phi = \pi$ and $m = 0$ ($\rho_{bb} = 0$) or $\phi = 0$ and $1/m = 0$ ($\rho_{cc} = 0$) we get back the noninversion laser system of Sec. V.A. Taking $\sin\phi = 0$, for $\phi = 0$

$$n_0 = \frac{\alpha}{\gamma}\frac{\alpha-\gamma(m+1)}{\beta} \qquad (1/m \neq 0) \quad , \tag{72}$$

and for $\phi = \pi$

$$n_0 = \frac{\alpha}{\gamma}\frac{\alpha m - \gamma(m+1)}{\beta m} \qquad (m \neq 0) \quad . \tag{73}$$

It can be seen that just in the opposite case of the incoherent noninversion laser, if we set $\phi = 0$ and $m = 0 (1/m \neq 0)$, or $\phi = \pi$ and $1/m = 0$ $(m \neq 0)$ [$M = \rho_{cc}$ (or ρ_{bb}) = $\gamma/\alpha \neq 0$, ρ_{bb} (or ρ_{cc}) = 0, $\rho_{aa} = 1 - \gamma/\alpha$], that is, we put our laser system into a "two-level operation regime," then we obtain the following steady-state photon number:

$$n_0 = \frac{\alpha}{\gamma}\frac{\alpha - \gamma}{\beta} \quad , \tag{74}$$

and we find from Eqs. (63) and (64)

$$D_{II}(\theta_0, n_0) = 0 \quad , \tag{75}$$

$$D_{\theta\theta}(\theta_0, n_0) = \frac{\alpha - \gamma}{8n_0} = \frac{\beta\gamma}{8\alpha} \quad , \tag{76}$$

which are exactly the same as in the two-level laser with injected atomic coherence [19]. Note that there is still no need for population inversion, because if $\rho_{aa} = 1 - \gamma/\alpha < M = \gamma/\alpha$, the photon number is positive (i.e., the laser operates) in the $1 < \alpha/\gamma < 2$ interval. This means that at complete quenching of the intensity noise and large reduction of the phase noise we have noninversion lasing as well. The photon-number variance in steady state is

$$\left\langle (\Delta\hat{n})^2 \right\rangle = n_0 \quad , \tag{77}$$

that is, the photon-number distribution is *exactly* Poissonian. Since

$$\left|\frac{\partial}{\partial\theta}d_\theta\right|_{\theta_0,n_0}=\gamma \quad , \tag{78}$$

thus we find the phase variance to be

$$\left\langle(\Delta\theta)^2\right\rangle=\frac{1+\alpha/\gamma}{8n_0} \quad . \tag{79}$$

When $\alpha/\gamma \cong 1$, the phase variance is approximately the same as that of the coherent state,

$$\frac{1}{4n_0} \quad .$$

Finally we find

$$\left\langle(\Delta\hat{n})^2\right\rangle\left\langle(\Delta\theta)^2\right\rangle=\frac{1}{8}\left(1+\frac{\alpha}{\gamma}\right) \quad , \tag{80}$$

which (at $\alpha/\gamma \cong 1$) is approximately equal to $1/4$, the quantum limit of the minimum uncertainty product. That is, the laser field is in a near-coherent state.

If we take a typical "three-level operation" case, when $m = 1$ [that is, for $\phi = 0$ (or π) $M = \rho_{cc} = \rho_{bb} = \gamma/\alpha \neq 0$, $\rho_{aa} = 1 - 2(\gamma/\alpha)$] in Eqs. (72) and (73), then the steady-state photon number is

$$n_0=\frac{\alpha}{\gamma}\frac{\alpha-2\gamma}{\beta} \quad , \tag{81}$$

when we still have noninversion lasing, if $2 < \alpha/\gamma < 3$. The photon-number distribution is still exactly Poisson: $\left\langle(\Delta\hat{n})^2\right\rangle = n_0$ and the phase variance is $\left\langle(\Delta\theta)^2\right\rangle = (\alpha/\gamma)/8n_0$. This means that the laser field is in the same near-coherent state as in the previous "two-level" case. Overall, even if all three levels are populated, we still have noninversion laser

operation in the range of $2 < \alpha/\gamma < 3$, at the noise characteristics of a near coherent state.

Thus, it is shown that even if we do not set M equal to zero (because in that case we would get back to the incoherent noninversion laser operation: see Sec. V.A), we can reach the noninversion laser operation, where the laser field can be found very near to an ideal coherent state, due to the coherent pumping, if $M = \gamma/\alpha$. Different values of the parameters of the phase of the microwave field ϕ and the ratio of the population of the lower levels $m = \rho_{bb}/\rho_{cc}$ for the same $M = \gamma/\alpha$ result in different operation thresholds.

VI. DISCUSSION AND SUMMARY

We studied the interaction of a three-level atom in the Λ configuration interacting with one mode of the quantized radiation field, where a strong classical coupling is applied between the lower two (closely spaced) levels via an external microwave field, and these lower levels are coupled to the upper one via interacting with the field mode. Starting from the Hamiltonian model of the system transformed into a second interaction picture, and under special detuning conditions and the rotating-wave approximation, we derived the interaction Hamiltonian of the system.

Substituting the Hamiltonian into the time-dependent Schrödinger equation, we solved the model so that the obtained solution contained all the possible initial conditions. Consequently, we could retain all the elements of the following density matrix of the system. Thus we had the possibility to derive a master equation for the reduced field-density operator and the laser photon statistics. Besides the atomic coherence resulting from the applied external microwave field, this equation contained all the atomic coherences between the different atomic levels. The master equation is the same as that of the two-level laser with injected atomic coherence [19], if we substitute ρ_{bb} (or ρ_{cc}) into M, that is, we reobtain the usual master equation of an ordinary two-level laser if the injected coherence is set equal to zero ($R = 0$) and $M = \rho_{bb}$ (ρ_{cc}).

We presented a Fokker-Planck treatment of the system and obtained drift and diffusion

coefficients. The laser operation is studied without and with injected atomic coherence. In the first case an incoherent noninversion laser operation is found depending on the phase of the external microwave field ϕ and the initial populations of the lower two levels. Diffusion coefficients are calculated and small noise reduction is shown compared to the ordinary laser case.

In the second case, when we apply injected atomic coherence the system is shown to be phase sensitive and the laser phase is locked to a particular value θ_0 in the steady state. θ_0 is determined by the phase of the injected atomic coherence φ_{ij} and the external signal ϕ. The diffusion coefficients are calculated at the steady state; they take the value of the locked phase angle θ_0. Both the intensity and the phase-diffusion coefficients are reduced compared to the case of no initial atomic coherence.

The system is studied in the special case, when the diffusion coefficients are minimal: the intensity diffusion vanishes, the phase diffusion has a small, positive value. A general formula for the steady-state photon number is derived, which is investigated for different arbitrary parameter choices of the microwave phase ϕ and the initial population of the lower levels. It is shown that with the appropriate choice of parameters the system can behave as (1) an incoherent noninversion laser [9]: setting $M = 0$ ($\phi = \pi$, $\phi = 0$ and $\rho_{bb} = 0$, or $\rho_{cc} = 0$, respectively), we obtained the steady-state photon number, diffusion and variance of Eqs. (54) - (57), or (2) a coherent noninversion laser if $M \neq 0$. In this case we have the minimum diffusion coefficients if $M = \gamma/\alpha$,

$$D_{II}(\theta_0, n_0) = 0 \quad ,$$

$$D_{\theta\theta}(\theta_0, n_0) = \frac{\beta\gamma}{8\alpha} \quad ,$$

and the steady-state photon number (71) depends on the values of the parameters of the phase of the microwave field ϕ and the ratio of the population of the lower levels $m = \rho_{bb}/\rho_{cc}$, (72) and (73), at the same $M = \gamma/\alpha$.

(a) At the "two-level"-like [19] parameter choice: when $M = \gamma/\alpha$ [$= \rho_{cc}$ (or ρ_{bb}), ρ_{bb} (or ρ_{cc}) $= 0$, $\phi = 0$ (or π)],

$$n_0 = \frac{\alpha}{\gamma}\frac{\alpha-\gamma}{\beta} \quad ,$$

$$D_{\theta\theta}(\theta_0, n_0) = \frac{\alpha-\gamma}{8n_0} \quad ,$$

operating if $1 < \alpha/\gamma < 2$.

(b) At the three-level case: when $M = \gamma/\alpha$ ($= \rho_{bb} = \rho_{cc}$, $\phi = 0$, or π),

$$n_0 = \frac{\alpha}{\gamma}\frac{\alpha-2\gamma}{\beta} \quad ,$$

$$D_{\theta\theta}(\theta_0, n_0) = \frac{\alpha-2\gamma}{8n_0} \quad ,$$

if $2 < \alpha/\gamma < 3$.

The photon number and phase variances are also discussed and it is found that the photon-number distribution is exactly Poissonian, while the phase distribution is (at the threshold) near Poissonian, which means that the laser field approaches a coherent state. This noninversion laser system becomes a quantum-noise-limited active device if, besides the external microwave-field-induced coherence, an injected atomic coherence is also applied.

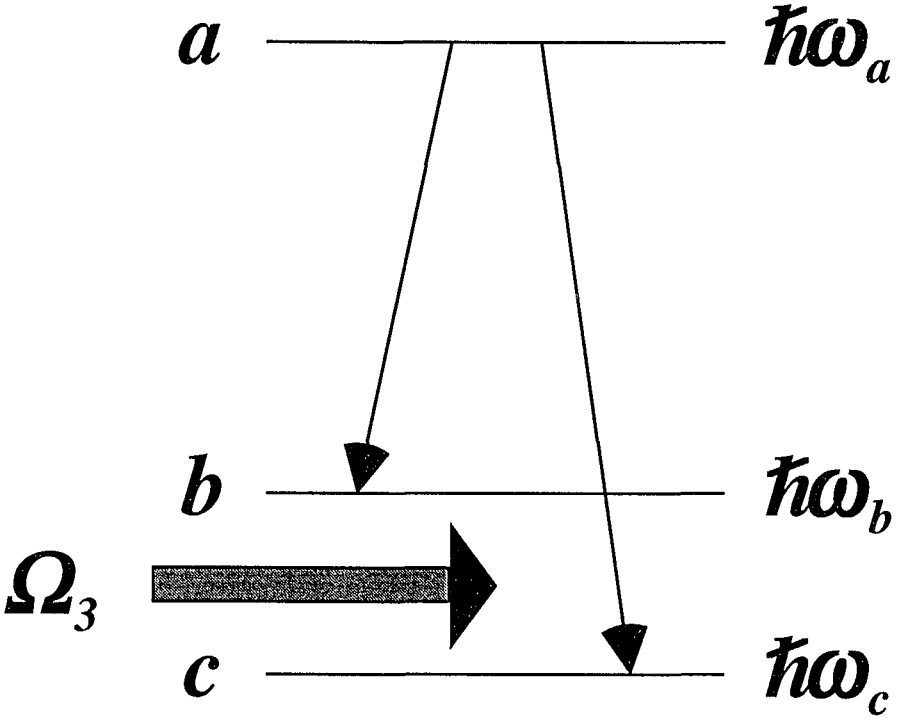

FIG. 1. Scheme of a Λ-type three-level quantum-beat laser having one upper level a and two closely spaced lower levels b and c, with energies $\hbar\omega_a$, $\hbar\omega_b$ and $\hbar\omega_c$, respectively. The allowed atomic transitions and the external microwave field coupling the lower two levels are denoted by arrows.

2.1.2 Two-mode Lasing Without Inversion with Injected Atomic Coherence†

ABSTRACT

Noninversion lasing is investigated in Λ - type three level atomic systems that are coupled to two modes of the electromagnetic field. As a result of the external classical field driving the transition between the lower two closely spaced levels, laser action can be achieved in both modes simultaneously at arbitrarily small initial upper level population (Lasing Without Inversion) provided the pumping exceeds a certain threshold. The relative phase of the two modes is locked to a particular value controlled by the phase of the external field. In addition, new regimes of the laser operation arise when initial coherences between various atomic levels are also injected into the resonator. First of all, laser action can be achieved in both of the two modes at arbitrarily small pumping (no threshold). Injected atomic coherence can control the competition between the modes, and result in a wide variety of multistable steady-state behavior illustrating the very sensitive dynamics.

PACS number(s): 42.50.Gy, 42.60.Lh, 42.60.Mi, 42.65.Pc

I. INTRODUCTION

In the recent years, a considerable amount of theoretical and experimental research has been devoted to atomic coherence effects in laser systems. The motivation behind this work is both fundamental and applied physics. It targets the microscopic mechanism of the emission of light employing active atoms in coherent superpositions of their quantum states involved in the laser action and, on the other hand, searches for practical applications of these mechanisms in constructing new type of lasers and other quantum optical devices. The signature of driving atomic coherence can be traced in the performance of the laser,

viz., in the dynamical and noise characteristics of the radiation. It has been demonstrated, to consider a prominent example, that atomic coherence established between two closely spaced lower levels of three-level (Λ - type) atoms using an external field [1] may lead to laser action even though the active medium is not in an inverted state (Lasing Without Inversion, LWI [1-3]). One interpretation of this effect is that atomic coherence results in nonabsorbing resonances in the system [4]. In addition, injecting initial atomic coherence between all the three levels of the driving atoms can lead to an elimination of the pumping threshold for laser operation, another long-thought key concept of the conventional laser theories, and the system enters its nonlinear regime at arbitrarily small pumping [5]. This is the consequence of the injected atomic coherence, i. e., a driving atomic dipole, that radiates independently of the actual incoherent gain/loss ratio in the system. On the other hand, injected atomic coherence can also result in a reduction of photon-number noise and phase noise in the laser simultaneously [5]. The possibility to significantly reduce the noise in laser systems and produce, for example, squeezed light using injected atomic coherence has attracted much attention in the past few years [6-7]. The practical applications of these quantum coherence phenomena in active optical systems are obvious. Noninversion lasing could be very useful in, for example, laser systems where inversion is difficult to establish (i. e., in the high-frequency domain of the spectrum, VUV or x-ray etc., due to high rate of spontaneous emission), while reduced-noise radiation could be advantageous in, for example, optical communication networks. Let us also mention here two other prominent quantum optical concepts related to effects of atomic coherence. These are the enhanced index of refraction with minimal absorption as suggested by Scully and collaborators [8], and the electromagnetically induced transparency demonstrated by Harris and coworkers [9]. We also note the recently proposed method of generating atomic coherence utilizing a Stark-shifted sublevel crossing a neighboring atomic state by Kocharovskaya et al. [10].

Motivated by the above examples illustrating the significance of atomic coherence in quantum optical systems we, in the present paper, consider the two-mode version of the above mentioned Λ - type three-level LWI systems [5]. The lower two closely spaced levels are driven by an external field and, in addition, atomic coherences between various

states of the three level atoms are injected. The competition between the modes is investigated, together with the onset of noninversion lasing and zero-threshold operation in both of the two modes. We find that atomic coherences play a decisive role in the competition between the two modes; they can be applied, in some cases, to redistribute the energy between the two modes while, in others, they result in instabilities and multistable steady state behavior of the laser modes. These instabilities and the very sensitive dynamics exhibiting critical behavior in the two-mode system suggest that selection of a single mode in the experimental realization of LWI can be an essential criteria to achieve stable operation.

In the next section we present the model of the system by introducing its Hamiltonian and transforming it into an interaction picture. The resulting Scrödinger equation is solved in Sec. III for the time dependent wavefunction that, in Sec. IV, is used to derive the master equation for the field-density matrix. In Sec. V we transform the master equation into a Fokker-Planck equation for the P - function. The drift coefficients of the equation are then analysed in Sec. VI to describe the dynamical behavior of the average intensities and phases of the two modes considering various schemes for injected atomic coherences. Finally, we conclude in Sec. VII.

II. THE MODEL

We consider a system of Λ - type three-level atoms, as shown in Fig. 1, where the $|a\rangle \rightarrow |b\rangle$ and $|a\rangle \rightarrow |c\rangle$ transitions are coupled to two cavity modes of frequencies, Ω_1, and Ω_2, respectively. The two closely spaced lower levels, $|b\rangle$ and $|c\rangle$, are strongly driven by an external (classical) field characterized by the Rabi frequency, $\mathcal{V}$, frequency, Ω_3, and phase ϕ. We also assume injected coherence between the atomic states as a consequence of which the corresponding off-diagonal elements of the initial atomic density matrix are different than zero. This is exactly the same system as the one studied in Ref. [5] in detail except that in the present paper we allow for two separate modes contributing to (competing for) the laser action. Since the formulation and solution of the physical

problem follows the same lines here as in Ref. [5] we confine ourselves to a brief outline of the model and its solution.

The Hamiltonian for the field and one active atom in the Schrödinger picture is given by

$$H = H_0 + V \quad , \tag{2.1}$$

where

$$H_0 = \sum_{i=a,b,c} \hbar\omega_i |i\rangle\langle i| + \hbar\Omega_1\left(a_1^\dagger a_1 + 1/2\right) + \hbar\Omega_2\left(a_2^\dagger a_2 + 1/2\right) \tag{2.2}$$

and

$$V = \hbar g_1 a_1 |a\rangle\langle b| + \hbar g_2 a_2 |a\rangle\langle c| - \frac{1}{2}\hbar\mathcal{V}e^{i(\Omega_3 t+\phi)}|b\rangle\langle c| + H.c. \quad . \tag{2.3}$$

Here, a_1 ($a_1^\dagger$) and a_2 ($a_2^\dagger$), are the annihilation (creation) operators in the two cavity modes, g_1 and g_2, are the coupling constants for the $|a\rangle \rightarrow |b\rangle$ and $|a\rangle \rightarrow |c\rangle$ transitions, respectively. Apparently, the external microwave field is treated semiclassically. Let us define the first interaction picture given by

$$V_I = e^{\frac{i}{\hbar}H_0 t} V e^{-\frac{i}{\hbar}H_0 t} \quad . \tag{2.4}$$

After breaking V_I up into two terms as $V_I = V_1 + V_2$, where

$$V_1 = -\frac{1}{2}\hbar\mathcal{V}\begin{bmatrix} 0 & 0 & 0 \\ 0 & 0 & \exp(i\Delta_3 t - i\phi) \\ 0 & \exp(-i\Delta_3 t + i\phi) & 0 \end{bmatrix} \tag{2.5}$$

and

$$V_2 = \hbar \begin{bmatrix} 0 & g_1 a_1 \exp(i\Delta_1 t) & g_2 a_2 \exp(i\Delta_2 t) \\ g_1 a_1^\dagger \exp(-i\Delta_1 t) & 0 & 0 \\ g_2 a_2^\dagger \exp(-i\Delta_2 t) & 0 & 0 \end{bmatrix} , \tag{2.6}$$

we use V_1 and V_2 to define the second interaction picture given by

$$V_{II} = e^{\frac{i}{\hbar} V_1 t} V_2 e^{-\frac{i}{\hbar} V_1 t} \quad . \tag{2.7}$$

The detunings above are defined as $\Delta_1 = \omega_{ab} - \Omega_1$, $\Delta_2 = \omega_{ac} - \Omega_2$, and $\Delta_3 = \omega_{bc} - \Omega_3$, where $\omega_{ij} = \omega_i - \omega_j$, $i, j = a, b, c$. We assume that the classical driving field is resonant, $\Delta_3 = 0$, and that the second and third fields are detuned as $\Delta_1 = -\Delta_2 \equiv \mathcal{V}/2$. Then, applying the Rotating-Wave-Approximation by neglecting the rapidly varying exponentials (and retaining the slowly varying ones), upper signs (lower signs) in $\exp[i(\Delta_1 \pm \mathcal{V}/2)t]$ and $\exp[i(\Delta_2 \mp \mathcal{V}/2)t]$, we arrive at the interaction matrix given by

$$V_{II} = \frac{1}{2}\hbar g \begin{bmatrix} 0 & a_1 - e^{i\phi} a_2 & a_2 + e^{-i\phi} a_1 \\ a_1^\dagger - e^{-i\phi} a_2^\dagger & 0 & 0 \\ a_2^\dagger + e^{i\phi} a_1^\dagger & 0 & 0 \end{bmatrix} , \tag{2.8}$$

provided $g \equiv g_1 = g_2$. Apparently, the corresponding result for the single-mode system in Ref. [5] is reobtained when $a_1 = a_2$ is assumed.

III. SOLUTION OF THE MODEL

Using the interaction Hamiltonian given by Eq. (2.8) we find the time evolution of the wavefunction of the Λ-system by solving the time-dependent Schrödinger equation in the second interaction picture given by

$$i\hbar\dot{\psi} = V_{II}\psi \quad . \tag{3.1}$$

Here, ψ is a column vector of the three components, ψ_a, ψ_b, ψ_c, and Eq. (3.1) is a system of three coupled differential equations for the three components that read as

$$i\dot{\psi}_a = \frac{1}{2}g\left(a_1 - e^{i\phi}a_2\right)\psi_b + \frac{1}{2}g\left(a_2 + e^{-i\phi}a_1\right)\psi_c - i\frac{\gamma}{2}\psi_a \quad , \tag{3.2}$$

$$i\dot{\psi}_b = \frac{1}{2}g\left(a_1^{\dagger} - e^{-i\phi}a_2^{\dagger}\right)\psi_a - i\frac{\gamma}{2}\psi_b \quad , \tag{3.3}$$

$$i\dot{\psi}_c = \frac{1}{2}g\left(a_2^{\dagger} + e^{i\phi}a_1^{\dagger}\right)\psi_a - i\frac{\gamma}{2}\psi_c \quad . \tag{3.4}$$

The atomic relaxation is introduced via the last terms on the right-hand sides, where γ is the decay constant for the three atomic levels *a, b, c,* for simplicity, assumed to be the same for all levels. Similarly to Ref. [5], this system can be solved simultaneously by introducing the new functions, $\tilde{\psi}_a$, $\tilde{\psi}_+$ and $\tilde{\psi}_-$, defined by the following equations.

$$\psi_a = e^{-\gamma/2(t-t_0)}\tilde{\psi}_a \quad , \tag{3.5}$$

$$\psi_b = e^{-\gamma/2(t-t_0)}e^{-i\phi/2}\left(B_-^{\dagger}\tilde{\psi}_+ + B_+\tilde{\psi}_-\right) \quad , \tag{3.6}$$

$$\psi_c = e^{-\gamma/2(t-t_0)}e^{i\phi/2}\left(B_+^{\dagger}\tilde{\psi}_+ - B_-\tilde{\psi}_-\right) \quad , \tag{3.7}$$

where

$$B_+ = \frac{1}{2}\left(a_1 e^{-i\phi/2} + a_2 e^{i\phi/2}\right) \quad , \tag{3.8}$$

$$B_{-} = \frac{1}{2}\left(a_1 e^{-i\phi/2} - a_2 e^{i\phi/2}\right) \quad . \tag{3.9}$$

In this way, the three differential equations given by Eqs. (3.2) - (3.4) become

$$\dot{\tilde{\psi}}_a = -igA\tilde{\psi}_{+} \quad , \tag{3.10}$$

$$\dot{\tilde{\psi}}_{+} = -ig\tilde{\psi}_a \quad , \tag{3.11}$$

$$\dot{\tilde{\psi}}_{-} = 0 \quad , \tag{3.12}$$

where

$$A = \frac{1}{2}\left(a_1 a_1^{\dagger} + a_2 a_2^{\dagger}\right) \quad , \tag{3.13}$$

and their simultaneous solutions are given by

$$\tilde{\psi}_a(t) = C\tilde{\psi}_a(t_0) - iAS\tilde{\psi}_{+}(t_0) \quad , \tag{3.14}$$

$$\tilde{\psi}_{+}(t) = C\tilde{\psi}_{+}(t_0) - iS\tilde{\psi}_a(t_0) \quad , \tag{3.15}$$

$$\tilde{\psi}_{-}(t) = \tilde{\psi}_{-}(t_0) \quad , \tag{3.16}$$

where $C = \cos\left[g(t-t_0)A^{1/2}\right]$ and $S = A^{-1/2}\sin\left[g(t-t_0)A^{1/2}\right]$. The solutions for ψ_a, ψ_b, ψ_c can be obtained from Eqs. (3.14) - (3.16) using the definitions, Eqs. (3.5) - (3.7), in a straightforward way. We shall use these solutions in the next section to find the master equation for the field-density operator.

IV. THE MASTER EQUATION

The density operator of the three-level Λ atom and the two-mode field satisfies the following equation of motion in the second interaction picture,

$$\dot{\rho} = -\frac{i}{\hbar}[V_{II}, \rho] \quad . \tag{4.1}$$

We want to study the behavior of the field only. To obtain the reduced density operator for the field, ρ_F, we trace the atom-field density operator over the atomic variables, $\rho_F = Tr_{atom}\rho$. Thus, the equation of motion for ρ_F is obtained from Eq. (4.1) as

$$\dot{\rho}_F = Tr_{atom}\dot{\rho} = -\frac{i}{\hbar}Tr_{atom}[V_{II}, \rho] \quad . \tag{4.2}$$

Using the interaction matrix, V_{II}, given by Eq. (2.8), Eq. (4.2) reads as

$$\dot{\rho}_F = -ig\left\{e^{-i\phi/2}\left([B_-^\dagger, \rho_{ab}] + [B_+, \rho_{ca}]\right) + e^{i\phi/2}\left([B_-, \rho_{ba}] + [B_+^\dagger, \rho_{ac}]\right)\right\} + \mathcal{L}_1\rho_F + \mathcal{L}_2\rho_F \quad . \tag{4.3}$$

Here, $\mathcal{L}_i\rho_F$, $i = 1, 2$, accounts for the effect of field losses in the two modes due to cavity damping, and it is explicitly given by

$$\mathcal{L}_i\rho_F = -\frac{\gamma_c}{2}\left(a_i^\dagger a_i\rho_F + \rho_F a_i^\dagger a_i - 2a_i\rho_F a_i^\dagger\right) \quad , \tag{4.4}$$

where γ_c is the cavity damping rate, assumed to be the same for both modes. To obtain an expression for ρ_{ab}, ρ_{ac}, and their Hermitian conjugates we first calculate the contribution of one atom injected at time t_0 with arbitrary initial condition into the cavity and then sum the contributions of all atoms injected at random times between $t\text{-}1/\gamma$ and t (i.e., $t\text{-}1/\gamma < t_0 < t$) at rate r. This means that the atom-field interaction is considered on a time scale shorter than the atomic lifetime $1/\gamma$. In this way,

$$\rho_{ab} = r \int_{t-1/\gamma}^{t} dt_0 \psi_a(t,t_0)\psi_b^{\dagger}(t,t_0) \tag{4.5}$$

and

$$\rho_{ac} = r \int_{t-1/\gamma}^{t} dt_0 \psi_a(t,t_0)\psi_c^{\dagger}(t,t_0) \quad . \tag{4.6}$$

Substituting the solutions obtained for ψ_a, ψ_b, ψ_c in the previous section into Eqs. (4.5) and (4.6) we calculate the matrix elements as follows. Since the dynamics of the field is governed by the cavity lifetime, $1/\gamma_c$, which is much longer then the atomic lifetime, $1/\gamma$, ρ_F does not change appreciably during the integration time interval, and thus $\rho_F(t_0)$ in Eqs. (4.5) and (4.6) can be approximated by $\rho_F(t)$. On the other hand, when $t - t_0 > 1/\gamma$ (i.e., $t - 1/\gamma > t_0$) the contribution to the integral is negligible due to the exponential damping factor. This means that the lower limit of the integration can be extended to $-\infty$. After performing these steps and carrying out the integral we can substitute the results for ρ_{ab}, ρ_{ac} and their Hermitian conjugates into the equation of motion in Eq. (4.3) and obtain the final form of the master equation for the field-density matrix.

We want to remark here that when we took the trace over the atomic variables in Eq. (4.2) then, in the matrix elements appearing on the right-hand side in Eq. (4.3) and calculated according to Eqs. (4.5) and (4.6), we effectively replaced the atomic variables by their steady-state values (adiabatic elimination of atomic variables). This is justified by the much faster atomic relaxation rate than that of the field ($\gamma >> \gamma_c$). In doing so, we made use of our solution for the wavefunction in Eqs. (3.14) - (3.16) and, therefore, in the resulting master equation the atomic relaxation process is fully accounted for.

We do not want to put down the explicit (very complicated) form of the master equation here. In the next section, we transform it into a Fokker-Planck equation instead and, analysing the drift coefficients of the equation, we study the dynamics of the two-mode field.

V. THE FOKKER-PLANCK EQUATION

V.1 Finding the Fokker-Planck equation

In this section we employ the Glauber-Sudarshan P representation for the field-density matrix to transform the operator master equation given implicitly by Eq. (4.3) into a c-number differential equation, the Fokker-Planck equation, for the P - function. An outline of the standard procedure is given in the Appendix, here, we present the final results only. Using the normalized intensities, $\tilde{I}_i = \frac{\beta}{\alpha} I_i$, where $\alpha \equiv \frac{r}{\gamma_c}\frac{g^2}{\gamma^2}$ and $\beta \equiv 4\frac{r}{\gamma_c}\frac{g^4}{\gamma^4}$ are the respective pumping and saturation parameters, and the phases, θ_i, of the two field-modes, $i = 1, 2$, as the variables of the P - function, $P = P\left(\tilde{I}_1, \tilde{I}_2, \theta_1, \theta_2, t\right)$, we arrive at the Fokker-Planck equation given by

$$\frac{1}{\gamma_c}\frac{\partial P}{\partial t} = \Big\{-\partial_{\tilde{I}_1} d_{\tilde{I}_1} - \partial_{\theta_1} d_{\theta_1} + \partial^2_{\tilde{I}_1\tilde{I}_1} D_{\tilde{I}_1\tilde{I}_1} + \partial^2_{\theta_1\theta_1} D_{\theta_1\theta_1} + \partial^2_{\tilde{I}_1\theta_1} D_{\tilde{I}_1\theta_1} -$$

$$-\partial_{\tilde{I}_2} d_{\tilde{I}_2} - \partial_{\theta_2} d_{\theta_2} + \partial^2_{\tilde{I}_2\tilde{I}_2} D_{\tilde{I}_2\tilde{I}_2} + \partial^2_{\theta_2\theta_2} D_{\theta_2\theta_2} + \partial^2_{\tilde{I}_2\theta_2} D_{\tilde{I}_2\theta_2} +$$

$$+\partial^2_{\tilde{I}_1\tilde{I}_2} D_{\tilde{I}_1\tilde{I}_2} + \partial^2_{\theta_1\theta_2} D_{\theta_1\theta_2} + \partial^2_{\tilde{I}_1\theta_2} D_{\tilde{I}_1\theta_2} + \partial^2_{\tilde{I}_2\theta_1} D_{\tilde{I}_2\theta_1}\Big\} P + \ldots \quad . \tag{5.1}$$

Here, we used the notation, $\partial_{x_i} = \frac{\partial}{\partial x_i}$ and $\partial^2_{x_i y_j} = \frac{\partial^2}{\partial x_i \partial y_j}$, for the derivatives, where x_i and y_i are any of the normalized intensity and phase variables of the two modes, $i = 1, 2$, while the higher order terms, $\partial^3_{x_i y_j z_k}$, are omitted. The coefficients under the derivatives, the drift and diffusion terms of the equation denoted by the respective lower and upper case d - s, can be used to analyse the system without solving the equation for the P - function. With the assumption that the mean intensities, $\langle I_1 \rangle$ and $\langle I_2 \rangle$, are much larger than 1, and using $\rho_{ij} = \sqrt{\rho_{ii}\rho_{jj}}\, e^{i\varphi_{ij}}$, $i, j = a, b, c$, for the injected atomic coherences, we now present

the explicit forms of the drift coefficients of the above equation (the diffusion terms are given in the Appendix). They read as

$$d_{\tilde{I}_1} = \frac{\tilde{I}_1}{N_1 N_2}\left[\alpha\left(\rho_{aa} - \frac{1}{2}\overline{M}_1\right)N_1 - \frac{3}{16}\alpha\tilde{I}_2\left(\overline{M}_1 - \overline{M}_2\right) - N_1 N_2\right] \quad , \tag{5.2}$$

$$d_{\theta_1} = \frac{\alpha}{4N_1}\left[M_b - 4\frac{R_3}{\sqrt{\tilde{I}_1}} - \frac{1}{2}\sqrt{\tilde{I}_1\tilde{I}_2}\left(\frac{R_3}{\sqrt{\tilde{I}_2}} - \frac{R_4}{\sqrt{\tilde{I}_1}}\right)\right] \quad , \tag{5.3}$$

and

$$d_{\tilde{I}_2} = d_{\tilde{I}_1}\left(interchange,\ \tilde{I}_1 \Leftrightarrow \tilde{I}_2\ and\ \overline{M}_1 \Leftrightarrow \overline{M}_2\right) \quad , \tag{5.4}$$

$$d_{\theta_2} = -d_{\theta_1}\left(interchange,\ \tilde{I}_1 \Leftrightarrow \tilde{I}_2\ and\ R_3 \Leftrightarrow R_4\right) \quad , \tag{5.5}$$

where

$$N_1 = 1 + \frac{1}{8}\left(\tilde{I}_1 + \tilde{I}_2\right) \quad , \tag{5.6}$$

$$N_2 = 1 + \frac{1}{2}\left(\tilde{I}_1 + \tilde{I}_2\right) \quad , \tag{5.7}$$

$$M_1 = \rho_{bb} + \rho_{cc} + 2|\rho_{bc}|\cos\left(\varphi_{bc} + \phi\right) \quad , \tag{5.8}$$

$$M_2 = \rho_{bb} + \rho_{cc} - 2|\rho_{bc}|\cos\left(\varphi_{bc} + \phi\right) \quad , \tag{5.9}$$

$$M_a = \left(\rho_{bb} - \rho_{cc}\right)\cos\left(\phi - \theta\right) - 2|\rho_{bc}|\sin\left(\varphi_{bc} + \phi\right)\sin\left(\phi - \theta\right) \quad , \tag{5.10}$$

$$M_b = \left(\rho_{bb} - \rho_{cc}\right)\sin\left(\phi - \theta\right) + 2|\rho_{bc}|\sin\left(\varphi_{bc} + \phi\right)\cos\left(\phi - \theta\right) \quad , \tag{5.11}$$

$$R_1 = |\rho_{ab}|\sin(\varphi_{ab} - \theta_1) + |\rho_{ac}|\sin(\varphi_{ac} + \phi - \theta_1) \quad , \tag{5.12}$$

$$R_2 = -|\rho_{ab}|\sin(\varphi_{ab} - \phi - \theta_2) + |\rho_{ac}|\sin(\varphi_{ac} - \theta_2) \quad , \tag{5.13}$$

$$R_3 = |\rho_{ab}|\cos(\varphi_{ab} - \theta_1) + |\rho_{ac}|\cos(\varphi_{ac} + \phi - \theta_1) \quad , \tag{5.14}$$

$$R_4 = |\rho_{ab}|\cos(\varphi_{ab} - \phi - \theta_2) - |\rho_{ac}|\cos(\varphi_{ac} - \theta_2) \quad , \tag{5.15}$$

$$\overline{M}_1 = M_1 - M_a\sqrt{\frac{\tilde{I}_2}{\tilde{I}_1}} - \frac{4R_1}{\sqrt{\tilde{I}_1}} \quad , \tag{5.16}$$

$$\overline{M}_2 = M_2 - M_a\sqrt{\frac{\tilde{I}_1}{\tilde{I}_2}} - \frac{4R_2}{\sqrt{\tilde{I}_2}} \quad . \tag{5.17}$$

Above, we have also introduced the relative phase between the two modes denoted by $\theta \equiv \theta_1 - \theta_2$ the drift coefficient of which can be calculated as $d_\theta = d_{\theta_1} - d_{\theta_2}$. In order to completely determine the Fokker-Planck equation given by Eq. (5.1) we present the diffusion terms in the Appendix.

In the next subsection we outline the procedure employing the drift terms of the equation to investigate the dynamical behavior of the average intensities and phases of the two fields. On the other hand, the diffusion terms prove useful in studying the noise performance of the field. We are not going to deal with these problems in the present paper but, together with investigating the correlations building up between the two modes, they are the subject of a subsequent publication [11].

V.2 Applying the drift terms of the Fokker-Planck equation

Having the Fokker-Planck equation derived, we now employ the drift coefficients to

investigate the time-dependent and steady-state properties of the average intensities and phases of the two field-modes. We should mention at this point that in the P representation the (stochastic) average of the intensity is directly connected to the (quantum mechanical) expectation value of the photon number as $\langle I_i \rangle = \langle n_i \rangle$, $i = 1, 2$. It can be shown in general that

$$\frac{1}{\gamma_c}\frac{d}{dt}\langle x \rangle = \langle d_x \rangle \quad , \tag{5.18}$$

where x is any of the four dynamical variables of the equation, $\tilde{I}_1$, $\tilde{I}_2$, θ_1, and θ_2. After expanding the drift coefficients, d_x, in terms of $\delta x = x - \langle x \rangle$ around the average, $\langle x \rangle$, Eq. (5.18) becomes

$$\frac{1}{\gamma_c}\frac{d}{dt}\langle x \rangle \cong d_x\big|_{\langle all \rangle} \quad , \tag{5.19}$$

where the drift coefficient, d_x, is taken at the average values of all the dynamical variables on the right hand side. Solving the system of differential equations given by Eq. (5.19) we can find the time dependence of the average quantities, while the system of the algebraic equations, $d_x\big|_{\langle all \rangle} = 0$, yields the steady state.

We investigate the stability of the steady states by studying the stability of the phases of the two modes, θ_1 and θ_2 (for the sake of simplicity, we omit the stochastic average signs, $\langle\ \rangle$, from now on). In doing so, we introduce small perturbations, $\Delta\theta_1$ and $\Delta\theta_2$, around the steady state, $\theta_{1,s}$ and $\theta_{2,s}$, and substitute $\theta_1(t) = \theta_{1,s} + \Delta\theta_1$ and $\theta_2(t) = \theta_{2,s} + \Delta\theta_2$ into the corresponding form of Eq. (5.18). Expanding d_{θ_1} and d_{θ_2} around the steady state to the first order in $\Delta\theta_1$ and $\Delta\theta_2$ we arrive at a system of two linear differential equations given by

$$\frac{d\Delta\theta_i}{dt} = \frac{\partial d_{\theta_i}}{\partial \theta_1}\bigg|_{\langle all \rangle} \Delta\theta_1 + \frac{\partial d_{\theta_i}}{\partial \theta_2}\bigg|_{\langle all \rangle} \Delta\theta_2 \quad , \tag{5.20}$$

where $i = 1, 2$, and the derivatives are to be evaluated at steady state. We can assume that, since this is a system of linear equations, a simple exponential solution exists in the form, $\Delta\theta_i(t) = \Delta\theta_i(0)e^{\lambda t}$. The characteristic equation after substituting this ansatz back into the above equations is a quadratic algebraic equation for λ, where the negative definitness of the roots can be analysed applying Hurwitz's criteria. If $Re\lambda < 0$ the initial perturbation decays exponentially back to the steady state while a positive exponent implies increasing deviation off the steady state. Thus, negative definitness is the criterion for stability. We are going to apply this linear stability analyses together with numerical solutions of the coupled differential equations to determine the stability of the steady states.

VI. SOLUTIONS OF THE DRIFT EQUATIONS

VI.1 Incoherent pumping

First, let us consider the simplest case when no atomic coherence is injected initially into the resonator, $|\rho_{ij}| = 0$, $i, j = a, b, c$. It follows that $R_k = 0$, $k = 1, 2, 3, 4$ (see Eqs. (5.12)-(5.15)), and the equations of motion for the two phases reduce into simple forms. In particular, the relative phase satisfies the equation given by

$$\dot{\theta} = \frac{\alpha}{2N_1}(\rho_{bb} - \rho_{cc})\sin(\phi - \theta) \quad , \tag{6.1}$$

the stable steady state solutions of which are

$$\theta = \begin{cases} \phi, & if \quad \rho_{bb} > \rho_{cc} \\ \phi + \pi, & if \quad \rho_{bb} < \rho_{cc} \end{cases} \quad , \tag{6.2}$$

while there is no stable solution for equal lower level populations. Apparently, the phases of the two modes are locked to a relative value that is essentially controlled by the phase of

the external field. However, switching the sign of the initial inversion between the lower two levels will result in a π - jump in the steady state relative phase. Since mode *1* drives the $|a\rangle \rightarrow |b\rangle$ transition and mode 2 the $|a\rangle \rightarrow |c\rangle$, the phase of the mode coupling the upper level to the dominantly populated lower level will be ahead of the other one. The intensities corresponding to the possible stable steady states read as

$$\tilde{I}_1 = \tilde{I}_2 = \begin{cases} \alpha(\rho_{aa} - \rho_{cc}) - 1, & if \quad \rho_{bb} > \rho_{cc} \\ \alpha(\rho_{aa} - \rho_{bb}) - 1, & if \quad \rho_{bb} < \rho_{cc} \end{cases} . \tag{6.3}$$

The intensities in the two modes are equal and determined by the inversion between the upper and the less populated lower level only. The population of the other lower level can be arbitrarily large, larger than that of the upper one (no inversion), without affecting the laser operation. It is "hidden" from the lasing mechanism and results in no extra absorption of the radiation. In particular, if one of the lower levels is empty laser operation can be achieved for arbitrarily small upper level population. This is clearly the effect of the external field coupling the lower two levels. The generated coherence between these two levels destructs the absorptive transition from the dominantly populated lower level to the upper one. The threshold of the laser is given by $\alpha_{th} = (\rho_{aa} - \rho_{xx})^{-1}$, where ρ_{xx} is the population of the less populated lower level.

VI.2 Injected atomic coherence between the lower levels: ρ_{bc}

Since ρ_{ab} and ρ_{ac} are still assumed to be zero, $R_k = 0, k = 1, 2, 3, 4$ (see Eqs. (5.12)-(5.15)) and the equation of motion for the relative phase is given by

$$\dot{\theta} = \frac{\alpha}{2N_1}\left[(\rho_{bb} - \rho_{cc})\sin(\phi - \theta) + 2|\rho_{bc}|\sin(\varphi_{bc} + \phi)\cos(\phi - \theta)\right] . \tag{6.4}$$

Assuming different lower level populations, $\rho_{bb} \neq \rho_{cc}$, the stable solutions for the steady state relative phase read the same as given above in Eq. (6.2), provided the initial phases of

the injected coherence and the external field are set particularly to $\varphi_{bc} + \phi = 0$ or π for $\rho_{bb} > \rho_{cc}$ or $\rho_{bb} < \rho_{cc}$, respectively. However, due to the injected coherence stable solution can also be found for the case of equal lower level populations, $\rho_{bb} = \rho_{cc}$. The criterion for the particular value of the phase locking, in this case, is connected to the initial phase of the injected coherence and the external field, as given by

$$\theta = \begin{cases} \phi + \pi/2, & if \quad \sin(\varphi_{bc} + \phi) < 0 \\ \phi - \pi/2, & if \quad \sin(\varphi_{bc} + \phi) > 0 \end{cases}, \tag{6.5}$$

while the cases of $\phi - \varphi_{bc} = 0$ or π are not stable. The corresponding steady state intensities read as

$$\tilde{I}_{1,2} = (\alpha\rho_{aa} - 1)\left[1 \mp \frac{2|\rho_{bc}|\cos(\varphi_{bc} + \phi)}{\rho_{bb} + \rho_{cc}}\right], \tag{6.6}$$

where the upper (lower) sign corresponds to the first (second) mode. As we have seen above when finding the stable steady state phases, in the case of different lower level populations, $\rho_{bb} \neq \rho_{cc}$, $cos(\varphi_{bc}+\phi)$ must be set to ± 1 provided ρ_{bb} is larger ($+1$) or smaller (-1) than ρ_{cc}. Looking at Eq. (6.6), the intensity of one of the modes can, in this case, be adjusted by controlling the modulus of the injected coherence, $|\rho_{bc}|$, at the expense of the intensity of the other mode. Since $|\rho_{bc}| = \sqrt{\rho_{bb}\rho_{cc}}$ this can be done by adjusting the initial populations in the lower levels. On the other hand, for equal lower level populations, $\rho_{bb} = \rho_{cc}$, the intensities are controlled by the phase of the injected coherence via varying $cos(\varphi_{bc}+\phi)$. Consequently, the intensities in the two modes can be redistributed in both cases, when the lower level populations are different or equal, by controlling the free parameter, modulus or phase, of the injected coherence. In the most extreme cases one of the modes can be switched off completly, e. g. $\tilde{I}_1 \cong 0$, making, at the same time, the intensity of the other mode increase to $\tilde{I}_2 \cong 2(\alpha\rho_{aa} - 1)$. This is twice as large as the balanced intensities in the case of incoherent pumping in subsection VI.1, since

all the energy is being concentrated in one of the modes only.

One should also note when comparing Eq. (6.6) with Eq. (6.3) that, in the present case, neither of the lower levels appear in the prefactor of the formula. Their populations do not affect the total intensity in the two modes, they merely allow for a continuous switching of the intensity from one mode to the other. That is, noninversion lasing appears naturally in the present case corresponding to the highest gain possible in the incoherently pumped system. Apparently, the present scheme reproduces the incoherent one when one of the lower levels is set empty or when $cos(\varphi_{bc}+\phi)$ is zero. (Note, it is not enough to set the coherence, $|\rho_{bc}|$, to zero because we have already made use of the relation, $|\rho_{bc}| = \sqrt{\rho_{bb}\rho_{cc}}$, during the course of the calculation).

VI.3 Injected atomic coherence between the upper and one of the lower levels: ρ_{ab} or ρ_{ac}

Let us consider now injected coherence between the upper and one of the lower two levels, for example ρ_{ab}. In the case when $\rho_{bb} < \rho_{cc}$ we found one solution, called regime *A*, that is stable for any pumping α. The phases of the two modes, in this case, are locked to the phase of the injected coherence as, $\theta_1 = \varphi_{ab} - \pi/2$ and $\theta_2 = \varphi_{ab} + \pi/2 - \phi$, resulting in the relative phase of $\theta = \phi + \pi$. The intensities are equal $\tilde{I} \equiv \tilde{I}_1 = \tilde{I}_2$, determined by the equation given by

$$\tilde{I}^{3/2} - \left[\alpha(\rho_{aa} - \rho_{bb}) - 1\right]\tilde{I}^{1/2} - 2\alpha|\rho_{ab}| = 0 \quad . \tag{6.7}$$

Apparently, injected atomic coherence provides a new driving term in the equation, viz., the third term on the left-hand side. One consequence of this is that, when solving Eq. (6.7), nonzero intensity can be found for any initial population of the three atomic levels including the most extreme cases where the population in the upper level is arbitrarily small. That is, the active atoms do not need to be inverted and Lasing Without Inversion can be realized. On the other hand, laser action can be achieved at arbitrarily small pumping as illustrated by the example depicted in Fig. 2 due to, again, the driving

mechanism of the injected atomic coherence (radiating atomic dipole). Therefore we have, in this case, a laser system operating without inversion and without threshold stable on the whole parameter region of α.

Let us now look at the case when $\rho_{bb} > \rho_{cc}$. The system, in this case, exhibits three different stable regimes at steady state denoted by *A*, *B* and *C* an example for which is depicted in Fig. 2. We have already seen regime *A* above. However, in the present case it is not stable for any pumping parameter but becomes unstable in the region of large α where regimes *B* and *C* take over (starting from $\alpha = 20$ in the Figure). In particular, at the critical value of the pumping where regime *A* becomes unstable the system has three different ways to go, i. e., becomes tristable. In regime *B*, the stable steady state phases do not change as compared to regime *A* but the intensities of the two modes separate according to

$$\tilde{I}_1^{1/2} = R \pm \sqrt{\alpha(\rho_{aa} - \rho_{cc}) - 1 - R^2} \quad , \tag{6.8}$$

$$\tilde{I}_2^{1/2} = R \mp \sqrt{\alpha(\rho_{aa} - \rho_{cc}) - 1 - R^2} \quad , \tag{6.9}$$

where $R \equiv 2|\rho_{ab}|/(\rho_{bb} - \rho_{cc})$. The switch from regime *A* to *B* occurs at the critical value of the pumping given by $\alpha_{crit} = (1 + R^2)/(\rho_{aa} - \rho_{cc})$. This critical point corresponds to the equal intensities, $\tilde{I} = \tilde{I}_1 = \tilde{I}_2 = R^2$. The two alternative signs in Eqs. (6.8) and (6.9) suggest that regime *B* provides a bistable operation where the intensities of the two modes can be interchanged: they can alternatively occupy the upper and lower branches in Fig. 2. We note that this scheme realizes a noninversion laser system where the intensities are determined by the inversion between the upper and the less populated lower level.

The third branch in Fig. 2 corresponds to regime *C* and also starts from α_{crit}. Here, the intensities of the two modes are equal, $\tilde{I} \equiv \tilde{I}_1 = \tilde{I}_2$, and explicitly read as

$$\tilde{I} = \alpha(\rho_{aa} - \rho_{cc}) - 1 \quad . \tag{6.10}$$

This brings us back to the intensities found in the case of incoherent pumping given by Eq. (6.3). However, in the present case the phase locking between the two modes is different. It is a function of the intensity (i. e., the pumping parameter, α) that, using Eq. (6.10), explicitly reads as $sin(\varphi_{ab} - \theta_1) = - sin(\varphi_{ab} - \theta_2 - \phi) = R/\sqrt{\alpha(\rho_{aa} - \rho_{cc}) - 1}$. That is, injected coherence does not affect the intensities in regime *C* but modifies the region of stability and the steady state phases of the two modes.

In summary, the system exhibits critical behavior as a function of the pumping parameter, α. Regime *A*, occupying the region of small pumping, starts from zero threshold and realizes a noninversion laser. An example for the evolution of the intensities in the phase space, $\tilde{I}_1 - \tilde{I}_2$, toward, in this case, a single-valued steady state is depicted in Fig. 3. The time-dependent behavior of the field is obtained by numerically solving the system of differential equations for the intensities and the phases given by the drift equations (see Eq. (5.19)). The results confirm that regime *A* is stable, remains to be stable for any pumping, and it is the only stable operation when $\rho_{bb} < \rho_{cc}$. However, in the opposite case when $\rho_{bb} > \rho_{cc}$, regime *A* becomes unstable and splits up into three new branches at a critical value of the pumping, α_{crit}. These are regimes *B* and *C*, all in noninversion operation, where regime *B* itself is bistable while *C* is single-valued. Typical evolution toward the tristable steady state in the phase space, $\tilde{I}_1 - \tilde{I}_2$, is depicted in Fig. 4. Apparently, the numerical solutions agree with the results obtained from the analytical stability analysis for the stable steady states. They also demonstrate that the time evolution toward steady state depends critically on the initial conditions. It can be seen in the Figure that starting from the same intensities but different phases the system will evolve into a different steady state. Finally, we want to remark that the system exhibits similar behavior for injected coherence, ρ_{ac}, except the roles of ρ_{bb} and ρ_{cc} are interchanged.

VI.4 Injected atomic coherence between all the levels: ρ_{ab}, ρ_{ac} and ρ_{bc}

We now consider the scheme where all the possible atomic coherences, ρ_{ab}, ρ_{ac} and

ρ_{bc}, are injected. It is found that stable steady state operation can be achieved for arbitrary initial population of the atomic levels provided the phase of the external field is locked to the phase of the injected lower level coherence as $\varphi_{bc} + \phi = 0$ or π. Let us set, in particular, the initial population as $\rho_{bb} > \rho_{cc}$ and select the arbitrary phases to be $\varphi_{bc} + \phi = \pi$; the consequences of the other alternative settings will be discussed at the end of the subsection. In this parameter region, an example for the steady-state intensities of the two modes as functions of the pumping parameter, α, is given in Fig. 5 where the solid and dashed lines depict the intensities of the first and second modes, respectively. The curves are labeled with the letters, A, B_1, B_2 and B_3, indicating the various regimes that we are going to consider in detail.

In regime A, the steady state phases of the two modes are locked to the phases of the individual injected atomic coherences as $\theta_1 = \varphi_{ab} - \pi/2$ and $\theta_2 = \varphi_{ac} - \pi/2$. It follows from the relation, $\varphi_{ab} + \varphi_{ac} = \varphi_{bc}$, that the relative phase between the modes locks to $\theta = -\varphi_{bc}$ that is equal to $\phi + \pi$ (see presumption in the previous paragraph). The corresponding intensities of the two modes are calculated from the equation given by

$$\tilde{I}_2^{3/2} - \frac{M_2}{\rho_{bb}+\rho_{cc}}\left\{\alpha\left[\rho_{aa}-(\rho_{bb}+\rho_{cc})\right]-1\right\}\tilde{I}_2^{1/2} - \frac{2\alpha R_2 M_2}{\rho_{bb}+\rho_{cc}} = 0 \qquad (6.11)$$

and

$$\tilde{I}_1^{1/2} = \frac{R_1}{R_2}\tilde{I}_2^{1/2} \quad , \qquad (6.12)$$

where R_1, R_2 and M_2 are defined by Eqs. (5.12), (5.13) and (5.9), respectively. From the stability analyses we find that this particular steady state in regime A is stable for pumping parameters below the critical pumping, α'_{crit}, that reads as

$$\alpha'_{crit} = \frac{1+4\rho_{aa}(\rho_{bb}+\rho_{cc})/(\rho_{bb}-\rho_{cc})^2}{\rho_{aa}-2\rho_{cc}} \quad . \qquad (6.13)$$

We want to note that this critical point corresponds to an upper limit in the intensities given by $\tilde{I}_2^{1/2} < 2\rho_{aa}/(\rho_{ab} - \rho_{ac})$. It follows from Eq. (6.11) that injected coherence results in an extra driving term and, as depicted in Fig. 5, the threshold of the laser is zero. It can also be seen that the intensities are connected to the inversion between the upper and the two lower levels combined. Thus, none of the two lower levels is hidden in this scheme but, since solutions can be found for arbitrarily large lower level populations, noninversion lasing is realized, nevertheless. Eq. (6.11) is a generalization of Eq. (6.7) in which scheme ρ_{ab} is injected only. In fact, in the particular case of $\rho_{cc} = 0$ Eqs. (6.11) and (6.12) reduce into Eq. (6.7) and the critical points of stability coincide exactly, as expected.

Next, let us look at the remaining three regimes, B_1, B_2 and B_3, together. The steady state phases in regimes B_1 and B_2 are the same as in regime A while, in regime B_3, the phase of the first mode switches to $\theta_1 = \varphi_{ab} + \pi/2$ and the relative phase to $\theta = -\varphi_{bc} + \pi$. The intensities are given by the equations reading as

$$\tilde{I}_1^{1/2} = \frac{2}{\rho_{bb} + \rho_{cc}} \left[R_1 \pm R_2 \sqrt{\frac{\rho_{bb} + \rho_{cc}}{4\rho_{aa}} (\alpha\rho_{aa} - 1) - 1} \right] \tag{6.14}$$

$$\tilde{I}_2^{1/2} = \frac{2}{\rho_{bb} + \rho_{cc}} \left[R_2 \mp R_1 \sqrt{\frac{\rho_{bb} + \rho_{cc}}{4\rho_{aa}} (\alpha\rho_{aa} - 1) - 1} \right] , \tag{6.15}$$

where the upper signs correspond to regimes B_1 and B_3, and the lower ones to B_2. The stability analyses suggests that these regimes are all stable above a critical value of the pumping parameter given by

$$\alpha_{crit} = \frac{3\rho_{aa} + 1}{\rho_{aa}(\rho_{bb} + \rho_{cc})} . \tag{6.16}$$

It follows from Eqs. (6.14) and (6.15), and from the steady state phases above (also see Fig. 5) that regimes B_2 and B_3 exhibit phase bistability; the intensities in the two regimes

are the same for any pumping but the phases (actually, θ_1 and θ only) have two different stable steady states. It can also be seen form the factor, $(\alpha\rho_{aa}-1)$, that both of the lower levels are absent from the inversion term and, therefore, these regimes realize an optimum scheme for noninversion lasing where the population of the lower levels can be arbitrarily large. On the other hand, regimes B_1, B_2 and B_3 result in a splitting of the intensities of regime A at the critical pumping, α_{crit}, (see Fig. 5) reminiscent of that in subsection VI.3. The present scheme is more complicated, however, because the intensities of the two modes in regime A are not equal and, therefore, each branch splits up into two separate branches, B_1 and B_2 (B_3), individually. Nevertheless, the two systems correspond to one another both in their regimes A as discussed above and in their regimes B. Apart from regime C missing from the present system, the two schemes exhibit similar dynamical behaviors approaching toward the same structure when ρ_{cc} is decreasing. In the case when $\rho_{cc} = 0$, in particular, the two systems coincide exactly, as expected.

The scheme considered so far in the present subsection was set up in the particular case where $\rho_{bb} > \rho_{cc}$ and $\varphi_{bc} + \phi = \pi$. Let us briefly summarize what happens when selecting the other alternatives. Switching to $\varphi_{bc} + \phi = 0$ results in an exact interchange of the intensities, $\tilde{I}_1 \Leftrightarrow \tilde{I}_2$, (i. e., switch of the solid and dashed lines in Fig. 5) and in a shift of the phase of one of the modes, depending on the regime, by π with respect to its above discussed steady-state value. In particular, for $\rho_{bb} > \rho_{cc}$ θ_1 switches in regimes A, B_1 and B_2 while θ_2 switches in B_3. For $\rho_{bb} < \rho_{cc}$ it is vice versa, θ_1 shifts in B_3, and θ_2 in A, B_1 and B_2. On the other hand, switching from $\rho_{bb} > \rho_{cc}$ to $\rho_{bb} < \rho_{cc}$ keeping the value of $\varphi_{bc} + \phi$ the same results in an interchange of $\rho_{bb} \Leftrightarrow \rho_{cc}$ in the above formulas determining, for example, the magnitudes of the intensities or the locations of the critical points.

As a summary to this subsection, we can say that the system in this scheme operates in several different regimes in a multistable way exhibiting critical behavior. The intensities are single-valued in the small pumping region starting from zero threshold while, at a critical point, they split up into tristable structures, reminiscent of that in subsection VI.3. The phases of the two modes lock to the phases of the injected coherences between the

upper and lower levels as $\theta_1 = \varphi_{ab} \pm \pi/2$ and $\theta_2 = \varphi_{ac} \pm \pi/2$ depending on the initial parameters and the actual regime of operation. Above the critical point the system also exhibits phase bistability. This scheme realizes Lasing Without Inversion in a crucially unstable way due to injected atomic coherences and the interplay between the two coexisting modes.

VII. SUMMARY

We investigated the interaction of Λ - type three level atomic systems with two modes of the radiation field where the lower two closely spaced levels of the atoms are coupled by an external field. In addition, we also assumed injected atomic coherences between various levels of the active atoms. The purpose of the peresent paper was to study multimode effects in Lasing Without Inversion (LWI) together with other quantum coherence phenomena due to injected atomic coherences. After solving the Schrödinger equation of the model in the interaction picture we calculated the master equation for the two-mode field-density matrix. The master equation was converted into a Fokker-Planck equation for the P - representation the drift coefficients of which were then used to obtain the coupled equations of motion for the average intensities and phases in the two modes. We solved these equations for various initial conditions and control parameters of the system such as the initial populations of the atoms, injected coherences, phase of the external field etc.

We found that noninversion lasing in both modes is possible as a result of the external driving field. Similarly to the single-mode case [5], the coherence induced between the two lower levels results in nonabsorbing resonances between the upper and the lower levels of the atoms and, therefore, the population in one (or both) of the lower levels can be excluded from the consideration of the effective population inversion for lasing action. We also found that the relative phase of the two modes is locked to the phase of the external field. In addition, including injected atomic coherences into the system laser action can be realized at any arbitrarily small pumping (zero threshold) in both modes [5]. This is due to

the injected atomic dipoles radiating independently of the actual gain/loss ratio in the system. In conclusion, we have shown that Lasing Without Inversion can be achieved at zero-threshold operation in two phase-locked modes simultaneously.

We also found that injected atomic coherence between the lower two levels of the atoms can be used to redistribute the intensity between the two competing modes. In particular, one of the modes can be shut down making the other mode two times "brighter" as compared to the symmetrical case. It can be also seen in this scheme that non of the lower level populations appear in the inversion factor in the intensity formula but that of the upper level only. This suggests that both of the lower levels correspond to nonabsorbing resonances in this scheme. On the other hand, injecting atomic coherence between the upper and one of the lower levels the system, besides zero-threshold noninversion lasing, exhibits critical multimode behavior. We found multiple branching at critical points of the pumping parameter at steady state where the, thus far, equal intensities can separate into different branches or further remain equal. In particular, the intensities of the two modes can exhibit bistable and tristable behavior at steady state accompanied by single-valued phases in this scheme. These phenomena become more complicated when coherences between all the atomic levels are injected. In this case, the intensities of the two modes are not equal at any pumping and, therefore, the multiple branching takes place on each mode's intensity separately. Besides intensity-multistability, we found phase bistability at other regions of the pumping parameter where single-valued intensities are accompanied with phases having two stable steady states simultaneously.

This critical behavior suggests that the dynamics of the system can become essentially multistable/unstable and highly sensitive to initial conditions when more than one modes are present in the resonator. Therefore, in order to realize Lasing Without Inversion in experiments in a stable way the mode selection should be a crucial criteria. On the other hand, the system can also become a candidate to investigate critical phenomena in physical systems where the goal actually would be to realize and study instabilities.

APPENDIX

The Fokker-Planck equation given by Eq. (5.1) has been obtained from the master equation given implicitly by Eq. (4.3) according to the following standard procedure. Substituting the Glauber-Sudarshan representation form of the field-density matrix,

$$\rho_F(t) = \int d^2\alpha_1\, d^2\alpha_2\; P\left(\alpha_1,\alpha_1^*,\alpha_2,\alpha_2^*,t\right)\left|\alpha_1,\alpha_2\right\rangle\left\langle\alpha_1,\alpha_2\right| \quad , \tag{A.1}$$

into the master equation, we find the equation of motion for $P\left(\alpha_1,\alpha_1^*,\alpha_2,\alpha_2^*,t\right)$ in the form given by

$$\begin{aligned}\frac{1}{\gamma_c}\frac{\partial P}{\partial t} = \Big\{ & -\partial_{\alpha_1} d_{\alpha_1} - \partial_{\alpha_1^*} d_{\alpha_1^*} + \partial^2_{\alpha_1\alpha_1} D_{\alpha_1\alpha_1} + \partial^2_{\alpha_1^*\alpha_1^*} D_{\alpha_1^*\alpha_1^*} + \partial^2_{\alpha_1\alpha_1^*} D_{\alpha_1\alpha_1^*} - \\ & -\partial_{\alpha_2} d_{\alpha_2} - \partial_{\alpha_2^*} d_{\alpha_2^*} + \partial^2_{\alpha_2\alpha_2} D_{\alpha_2\alpha_2} + \partial^2_{\alpha_2^*\alpha_2^*} D_{\alpha_2^*\alpha_2^*} + \partial^2_{\alpha_2\alpha_2^*} D_{\alpha_2\alpha_2^*} + \\ & + \partial^2_{\alpha_1\alpha_2} D_{\alpha_1\alpha_2} + \partial^2_{\alpha_1^*\alpha_2^*} D_{\alpha_1^*\alpha_2^*} + \partial^2_{\alpha_1\alpha_2^*} D_{\alpha_1\alpha_2^*} + \partial^2_{\alpha_1^*\alpha_2} D_{\alpha_1^*\alpha_2} \Big\} P \quad + \quad \ldots \quad , \end{aligned} \tag{A.2}$$

where $P = P\left(\alpha_1,\alpha_1^*,\alpha_2,\alpha_2^*,t\right)$. Here, we used the notation, $\partial_{\alpha_i} = \dfrac{\partial}{\partial\alpha_i}$ and $\partial^2_{\alpha_i\alpha_j} = \dfrac{\partial^2}{\partial\alpha_i\partial\alpha_j}$, for the derivatives while the higher order terms, $\partial^3_{\alpha_i\alpha_j\alpha_k}$, $i, j, k = 1, 2$, are omitted. Instead of dealing with this form of the Fokker-Planck equation we transform it into polar form, where P is now considered as a function of the intensities, I_1, I_2, and phases θ_1, θ_2 of the two modes. These are defined by the equations, $\alpha_1 \equiv \sqrt{I_1}e^{i\theta_1}$ and $\alpha_2 \equiv \sqrt{I_2}e^{i\theta_2}$. After introducing the normalized intensities, $\tilde{I}_1$ and $\tilde{I}_2$, defined in Sec. V, the Fokker-Planck equation given by Eq. (A.2) becomes Eq. (5.3). The drift terms in this equation are given in Sec. V while here, we present the diffusion coefficients provided the same assumption applies, $\langle I_1\rangle$ and $\langle I_2\rangle >> 1$. These terms are given by

$$D_{\tilde{I}_1\tilde{I}_1} = \frac{\beta\tilde{I}_1}{(N_1N_2)^2}\left\{\rho_{aa}\left(1+\frac{1}{2}\tilde{I}_2\right)N_1^2+\frac{1}{16}\overline{M}_1\tilde{I}_1N_2^2+\right.$$

$$\left.+\frac{3}{16}\left(\overline{M}_1\tilde{I}_1+\overline{M}_2\tilde{I}_2\right)\left[N_1N_2-\frac{\tilde{I}_1}{8}(2N_2+3)\right]\right\} \quad , \tag{A.3}$$

$$D_{\tilde{I}_1\tilde{I}_2} = -\frac{\beta\tilde{I}_1\tilde{I}_2}{(N_1N_2)^2}\left\{\rho_{aa}N_1^2+\frac{1}{16}(\overline{M}_1+\overline{M}_2)N_2^2+\frac{3}{64}\left(\overline{M}_1\tilde{I}_1+\overline{M}_2\tilde{I}_2\right)(N_1N_2+3)\right\} \quad , \tag{A.4}$$

$$D_{\theta_1\theta_1} = \frac{\beta}{4\tilde{I}_1N_1^2N_2}\left\{\rho_{aa}\left(1+\frac{1}{4}\tilde{I}_1\right)N_1^2-\frac{1}{16}\overline{M}_1\tilde{I}_1N_2+\right.$$

$$\left.+\frac{3}{16}\left(\overline{M}_1\tilde{I}_1+\overline{M}_2\tilde{I}_2\right)\left[N_1+\frac{\tilde{I}_1}{24}(2N_1+3)\right]\right\} \quad , \tag{A.5}$$

$$D_{\theta_1\theta_2} = \frac{\beta}{8N_1^2N_2}\left\{\rho_{aa}N_1^2-\frac{1}{8}(\overline{M}_1+\overline{M}_2)N_2+\frac{1}{32}\left(\overline{M}_1\tilde{I}_1+\overline{M}_2\tilde{I}_2\right)(2N_1+3)\right\} \quad , \tag{A.6}$$

$$D_{\tilde{I}_1\theta_1} = \frac{\beta\sqrt{\tilde{I}_1/\tilde{I}_2}}{32N_1^2N_2}\left\{\tilde{I}_1\tilde{I}_2\left(\frac{R_3}{\sqrt{\tilde{I}_2}}-\frac{R_4}{\sqrt{\tilde{I}_1}}\right)(N_1-3)-2\tilde{I}_2\left(M_b-4\frac{R_3}{\sqrt{\tilde{I}_2}}\right)N_2\right\} \quad , \tag{A.7}$$

$$D_{\tilde{I}_1\theta_2} = \frac{\beta\sqrt{\tilde{I}_1/\tilde{I}_2}}{32N_1^2N_2}\left\{\tilde{I}_1\tilde{I}_2\left(\frac{R_3}{\sqrt{\tilde{I}_2}}-\frac{R_4}{\sqrt{\tilde{I}_1}}\right)(N_1-3)-\tilde{I}_2\left(M_b-4\frac{R_3}{\sqrt{\tilde{I}_2}}\right)N_2+\tilde{I}_1\left(M_b-4\frac{R_4}{\sqrt{\tilde{I}_1}}\right)N_2\right\} \quad , \tag{A.8}$$

together with

$$D_{\tilde{I}_2\tilde{I}_2} = D_{\tilde{I}_1\tilde{I}_1}\left(interchange,\ \tilde{I}_1 \Leftrightarrow \tilde{I}_2 \ and\ \overline{M}_1 \Leftrightarrow \overline{M}_2\right) \quad , \tag{A.9}$$

$$D_{\theta_2\theta_2} = D_{\theta_1\theta_1}\left(interchange,\ \tilde{I}_1 \Leftrightarrow \tilde{I}_2 \ and\ \overline{M}_1 \Leftrightarrow \overline{M}_2\right) \quad , \tag{A.10}$$

$$D_{\tilde{I}_2\theta_2} = -D_{\tilde{I}_1\theta_1}\left(interchange,\ \tilde{I}_1 \Leftrightarrow \tilde{I}_2 \ and \ R_3 \Leftrightarrow R_4\right) \ , \tag{A.11}$$

$$D_{\tilde{I}_2\theta_1} = -D_{\tilde{I}_1\theta_2}\left(interchange,\ \tilde{I}_1 \Leftrightarrow \tilde{I}_2 \ and \ R_3 \Leftrightarrow R_4\right) \ . \tag{A.12}$$

Finally, we want to remark that the drift terms of the sum and difference phases, $\mu \equiv \theta_1 + \theta_2$ and $\theta \equiv \theta_1 - \theta_2$, and the sum and difference intensities, $\tilde{I}_\pm = \tilde{I}_1 \pm \tilde{I}_2$, can be calculated as the sums and the differences of the individual drift terms themselves, respectively. On the other hand, the corresponding diffusion coefficients read as

$$D_{\mu\mu} = D_{\theta_1\theta_1} + D_{\theta_2\theta_2} + D_{\theta_1\theta_2} \ , \tag{A.13}$$

$$D_{\theta\theta} = D_{\theta_1\theta_1} + D_{\theta_2\theta_2} - D_{\theta_1\theta_2} \ , \tag{A.14}$$

and

$$D_{\tilde{I}_\pm\tilde{I}_\pm} = D_{\tilde{I}_1\tilde{I}_1} + D_{\tilde{I}_2\tilde{I}_2} \pm D_{\tilde{I}_1\tilde{I}_2} \ , \tag{A.15}$$

indicating that the noises in these quantities are connected to the cross-correlations between the two modes. On the other hand, the cross terms of the sum/difference quantities themselves are given by

$$D_{\mu\theta} = 2\left(D_{\theta_1\theta_1} - D_{\theta_2\theta_2}\right) \ , \tag{A.16}$$

$$D_{\tilde{I}_+\tilde{I}_-} = 2\left(D_{\tilde{I}_1\tilde{I}_1} - D_{\tilde{I}_2\tilde{I}_2}\right) \ . \tag{A.17}$$

The noise performance of the system, together with the correlations between the two modes will be the subject of a subsequent publication [11].

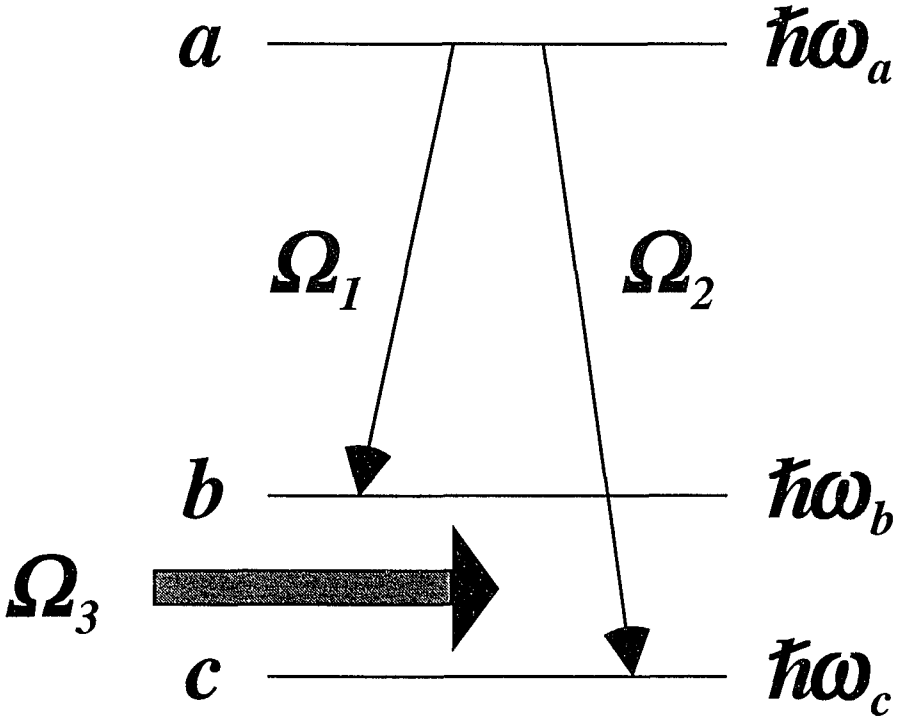

FIG. 1: Scheme of a two-mode laser driven by Λ - type three-level atoms where the two laser modes of frequencies Ω_1 and Ω_2 couple the upper level, a, to the lower two levels, b and c, and the external field, Ω_3, drives the transition between the lower two closely spaced levels, b and c.

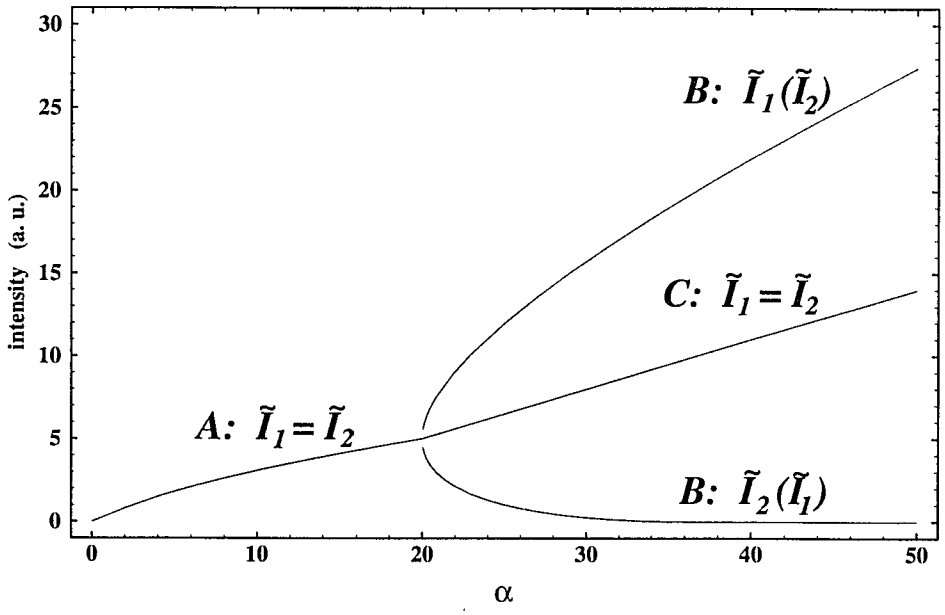

FIG. 2: Steady state normalized intensities of the two modes, $\tilde{I}_1$ and $\tilde{I}_2$, as functions of the pumping parameter, α. Atoms are injected in a coherent superposition of levels a and b the populations of which are $\rho_{aa} = 0.4$ and $\rho_{bb} = 0.5$. At a critical value of the pumping, $\alpha_{crit} = 20$, regime A splits up into three new branches where, in regime B, the intensities of the two modes alternatively occupy the upper and lower branches in the figure (bistability) while in C they stay equal.

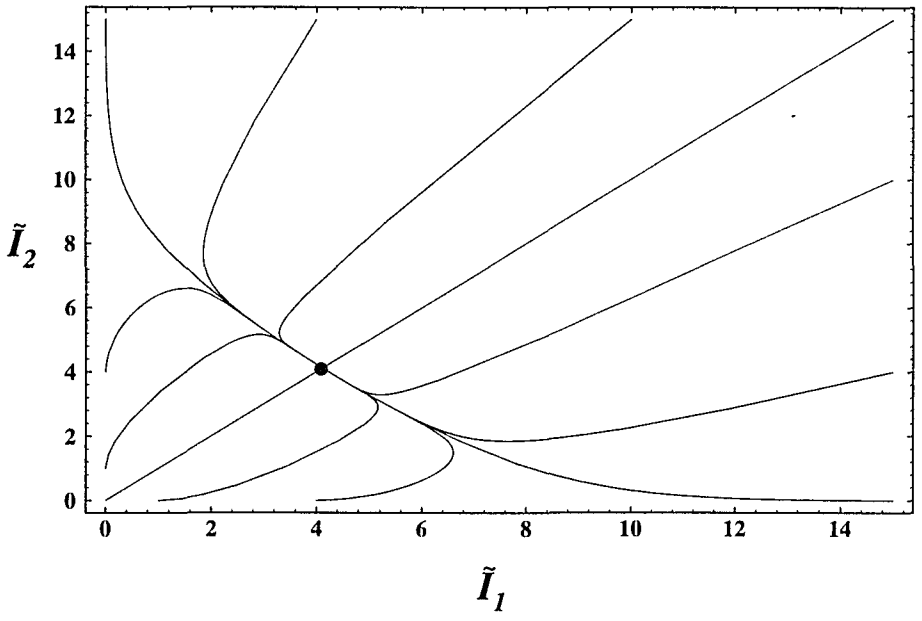

FIG. 3: Evolution toward a single-valued steady state in regime *A* at $\alpha = 15$ of Fig. 2 where $\phi = \varphi_{ab} = 0$ and the initial conditions for the phases are $\theta_{1,0} = -\theta_{2,0} = -\pi/2$ (i. e., starting from the steady-state value of the phases). The steady state intensities are equal ($\tilde{I}_1 = \tilde{I}_2 \cong 4$) as indicated by a spot in the figure.

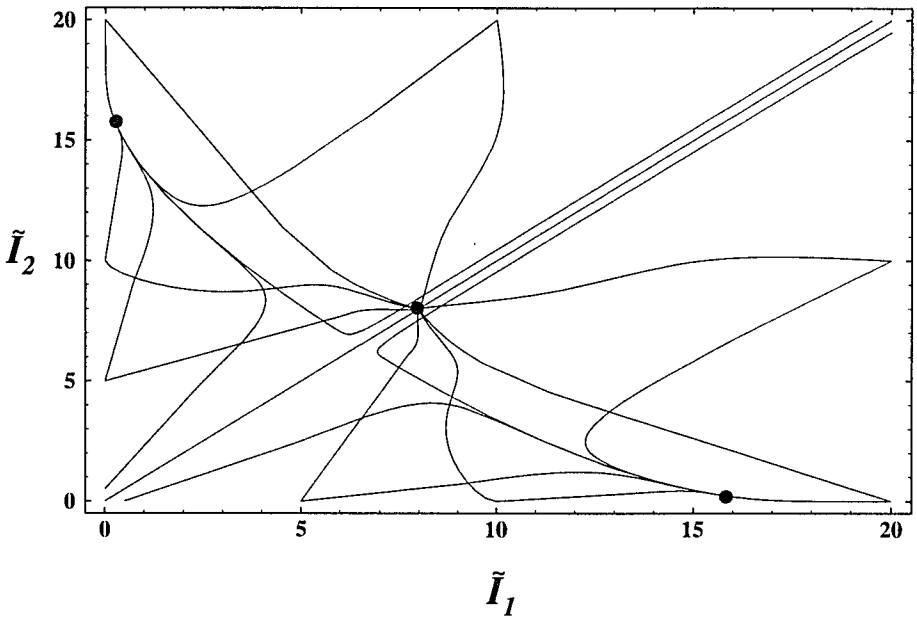

FIG. 4: Evolution toward a tristable steady state of regimes B and C at $\alpha = 30$ of Fig. 2 using $\phi = \varphi_{ab} = 0$. In the case when the initial phases are $\theta_{1,0} = \theta_{2,0} = 0$, the steady state corresponding to regime C is realized (see spot in Figure at $\tilde{I}_1 = \tilde{I}_2 = 8$). For $\theta_{1,0} = -\theta_{2,0} = -\pi/2$ we have two stable pairs of intensities where $\tilde{I}_1$ and $\tilde{I}_2$ are alternatively equal to 0.25 and 15.8. They correspond to the two branches of regime B in Fig. 2, and are realized depending on the initial conditions for the intensities.

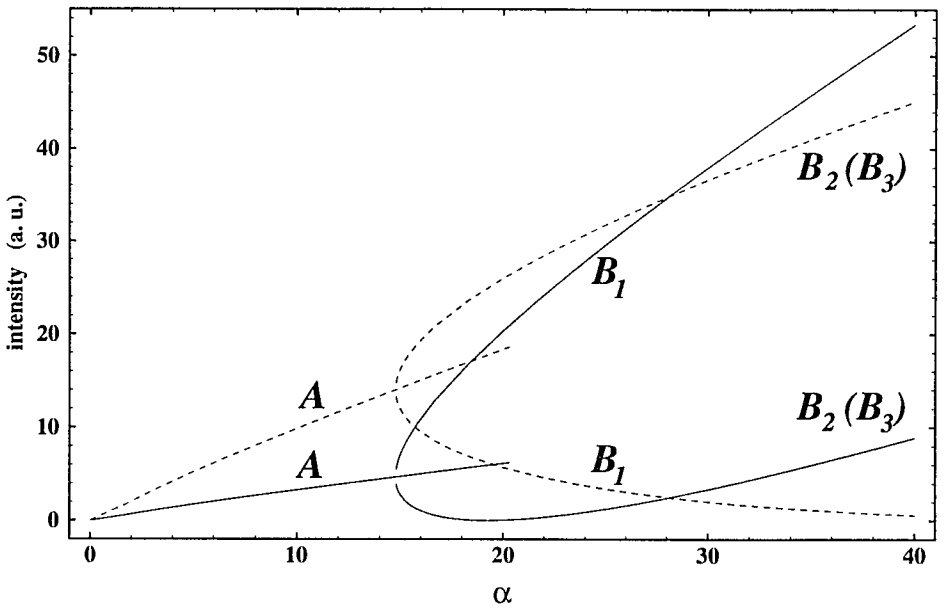

FIG. 5: Steady state normalized intensities of the two modes, $\tilde{I}_1$ and $\tilde{I}_2$, depicted by respective solid and dashed lines as functions of the pumping parameter, α, when all injected atomic coherences, ρ_{ab}, ρ_{ac} and ρ_{bc}, are assumed. The initial population of the states are $\rho_{aa} = 0.7$ and $\rho_{bb} = 0.28$. Structures similar to Fig. 2 are apparent: regimes A of each mode split up into two respective branches, B_1 and B_2 (B_3), at a critical point, $\alpha \cong 14.8$. The two equal-intensity regimes, B_2 and B_3, exhibit phase bistability.

3. QUANTUM COHERENCE IN PUMP-COUPLED MICROMASERS

3.1 The Micromaser

3.1.1 Phase Structures in the Micromaser Photon Statistics†

ABSTRACT

It is shown that the photon statistics of the micromaser consist of phase structures formed by the ridges that connect the peaks of the probability distribution in the θ - k space. A condition is given separating the system into "semiclassical" and "quantum" regimes above and far above threshold, respectively. In the semiclassical regime the phases are monotonous and coincide with the steady state solutions of the semiclassical theory. Their structure reflects typical features of the micromaser dynamics such as transition jumps between the phases become smaller with increasing θ. This signifies the onset of the Jaynes-Cummings collapse. Due to the quantized nature of the field the phases first disintegrate and then restructure into new kinds of phases in the quantum regime. The equations of state of these phases, $\theta = \theta(k)$, are not monotonous implying that large single peaks, the quantum island states (*QIS*), can arise in the neighborhoods of their minima. The oscillations that the system undergoes between the two kinds of quantum island states, QIS^- and QIS^+, as a function of θ are the revivals of the phase transitions. The disintegration and transformation of phases recurs periodically as the pumping is increasing and the group of phases in the semiclassical region is followed by consecutive phase structures in the quantum regime. The corresponding sequences of collapses and revivals are directly related to the Jaynes-Cummings collapse-revival effect. We find the experimental demonstration of these phase structures and the accompanying *QIS* feasible.
PACS Number(s): 42.50.Dv, 42.52+x

I. INTRODUCTION

One of the most extensively studied systems in quantum optics is the so-called micromaser, or one-atom maser [1]. It couples a single quantized mode of a high-Q microwave cavity to a sparse beam of two-level atoms realizing the fundamental Jaynes - Cummings model [2]. Due to its theoretical tractability [3, 4] and experimental accessibility [1] it has proved to be particularly well suited to study quantum effects in the interaction between radiation and matter. Unusual quantum features of this system have been predicted theoretically and demonstrated experimentally, such as the Jaynes-Cummings collapse - revival [5]. Nonclassical photon statistics have been found in its radiation field including number states [6], trapping states [7], the quantum island states [8], and macroscopical superpositions [9]. It has also been suggested that macroscopic correlated systems could be built by coupling such micromasers together to study the quantum correlation effects between their nonlocal fields [10], or to couple them to other quantum devices in, for example, atomic interferometers to test the principle of complementarity [11].

In the present paper we study the photon statistics of a micromaser pumped by a monoenergetic beam of two-level atoms with Poissonian pumping statistics. It will be shown that the probability distribution exhibits ensembles of phases. In order to display their structure we investigate the system in the two-dimensional parameter space of the pump parameter, θ, and the photon number, k. A correspondence between the quantum [3] and semiclassical [4] theories of the problem will be pointed out and used to find the equation of state of the phases. The photon statistics of the system will be shown to separate into "semiclassical" and "quantum" regimes showing characteristically different behaviors due to the crucial effect of the quantized nature of the field in the latter regime. As we shall see later this picture of phase structures of the photon statistics explains several features of the micromaser both qualitatively and quantitatively.

In the second and third sections we investigate the semiclassical and quantum regimes of the system, respectively. Sec. IV is devoted to summary and discussions, while in the

Appendix we derive some of the necessary formulas used in the paper.

II. THE SEMICLASSICAL REGIME

Let us consider a micromaser [1] where a single quantized mode of a high-Q microwave cavity is pumped by a monoenergetic beam of two-level excited atoms. Assuming that there is at most one atom present in the cavity at a time and that the interaction time, τ, is much shorter than the cavity lifetime, $1/\gamma$, the photon statistics can be calculated as [3]

$$p_n(\theta) = p_0(\theta)\prod_{k=1}^{n} E(k,\theta) \quad , \tag{2.1}$$

where

$$E(k,\theta) = \frac{N_{ex}}{k(\bar{n}_b + 1)}\beta(k,\theta) + \frac{\bar{n}_b}{\bar{n}_b + 1} \tag{2.2}$$

and

$$\beta(k,\theta) = \sin^2\left(\theta\sqrt{k/N_{ex}}\right) \quad . \tag{2.3}$$

Here, the average number of atoms inside the cavity during the cavity lifetime is given by $N_{ex} = r/\gamma$ where r is the average rate of injection of the atoms, and the pumping parameter is defined by $\theta = g\tau\sqrt{N_{ex}}$ where g is the atom-field coupling constant. Finite thermal radiation is also assumed specified by the average number of thermal photons, $\bar{n}_b$.

It is apparent from Fig. 1 that this quantum solution for the photon statistics specifies an ensemble of phases in the $\theta - k$ space where small changes in the pumping parameter, θ, result in small changes in the photon number, k. The smooth evolution along the

phases is periodically interrupted by abrupt transitions between them at certain critical values of θ. Their structure is reminiscent of that of the (multi-) stable steady states of the semiclassical theory of the system [4] illustrating the connection between the quantum and the semiclassical approach (compare Figs. 1 and 2). Applying the stable (unstable) solutions for the semiclassical steady states this correspondence can be used to determine the location of the peaks (minima) and the equation of state for the phases of the photon statistics. It is, however, unique in the quantum theory to provide a probability distribution along the possible locations of the stable steady states and to account for the effects originating in the shape of the photon statistics. This is beyond the grasp of the semiclassical approach. Let us now review some of these quantum effects. It can be seen in Figs. 1, 6 and 7 that, apart from some exceptional cases, the photon statistics is confined to a narrow region of the photon number, k, centered around approximately *40%* of N_{ex}. The envelope of the peaks is a bell-like curve (see Fig. 3) that is fairly independent of θ. Multipeaked photon statistics arise when the phases populated in this region of k overlap at a given pump parameter, θ. This overlap forces the system to switch from one phase to the next via first order phase transition accompanied by a sharp peak in the photon number noise [1, 3-4, 8]. Fig. 2 illustrates how the quantum treatment results in a suppression of the multistable behavior. The average photon number becomes single-valued as it selects between the available branches of the semiclassical theory according to the probability distribution of the quantum theory. It can be seen, however, that the phase transitions decay to a θ - independent constant value as the number of overlapping phases increases. This occurs because due to the increasing number of the peaks under the bell - curve the average photon number becomes less sensitive to the appearances of new peaks. This effect is directly related to the Jaynes - Cummings collapse [5] since the atomic inversion, w, is a simple function of the average photon number, $\langle n \rangle$, given by $w = 1 - 2\left(\langle n \rangle - \bar{n}_b\right)/N_{ex}$ (see derivation in the Appendix). In the case of no thermal radiation, $\bar{n}_b = 0$, the so-called "trapping states" show up [7]. They significantly modify the phase structure by trapping the system in a lower order phase in certain narrow regions of the pumping parameter, θ (see Fig. 4).

As we mentioned above, we can make use of the correspondence between the quantum and semiclassical theories to find the equation of the phases. The semiclassical steady states are determined by the equation (see Ref. [4] and an alternate derivation in the Appendix)

$$\theta\sqrt{(k_0+1)/N_{ex}} = \mp Arc\sin\left(\sqrt{(k_0-\bar{n}_b)/N_{ex}}\right) + l\pi \quad , \tag{2.4}$$

where the minus (plus) sign corresponds to the stable (unstable) solutions depicted by solid (dotted) lines in Fig. 2, while $l = 0, 1, 2, \ldots$ specifies one of their branches. It can be seen by comparing Figs. 1 and 2 that the peaks (minima) of the photon statistics coincide with the stable (unstable) solutions. Equation (2.4), can be simplified if we assume small number of thermal photons, $\bar{n}_b \cong 1$, and also $1 << k_0 << N_{ex}$. The latter approximation is justified by the above mentioned general feature of the photon statistics being confined to a narrow region of the photon number around $0.4\, N_{ex}$. This way, the first term on the right hand side of Eq. (2.4) can be reduced to $\mp\sqrt{k_0/N_{ex}}$. On the left hand side we can neglect the $+1$ provided

$$\theta\sqrt{(k_0+1)/N_{ex}} - \theta\sqrt{k_0/N_{ex}} << 1 \tag{2.5}$$

in a vicinity of k_0. This difference can be approximated with $\theta/\sqrt{4k_0N_{ex}}$ for $k_0 >> 1$ that results in the condition for the pumping parameter given by

$$\theta << \sqrt{k_0 N_{ex}} \quad . \tag{2.6}$$

In this region of the parameters the quantized nature of the field does not play a significant role and, therefore, we call it the "semiclassical" regime of the micromaser. Since there cannot be peaks for $k_0 > N_{ex}$ [8] this condition tells us in short that θ cannot be larger than N_{ex} in this regime. Using these approximations Eq. (2.4) reduces to the simple formula,

$$k_{0\pm} = N_{ex}\left(\frac{l\pi}{\theta \pm 1}\right)^2 \quad , \tag{2.7}$$

determining the location of the peaks and minima of the photon statistics, $k_{0\pm}$, for a given θ in the semiclassical regime taking the plus and minus signs, respectively. The system exhibits a structure of apparently continuous and smooth phases here as depicted in Figs. 1, 2 and 6. However, as we will show later on these phases will be disintegrated and reshaped at high pumping parameters beyond the region of Eq. (2.6) where the discreteness of the photon number becomes significant.

The same result can be obtained by using the function, $E(k, \theta)$, of the quantum solution given by Eq. (2.2). One finds a peak (minimum) of the photon statistics at a photon number, k_0, if $E(k_0, \theta) > 1$ (<1) and $E(k_0+1, \theta) < 1$ (>1). In the case when the change in the function, $E(k, \theta)$, produced by one discrete step of the photon number from k_0 to k_0+1 is small the quantum nature of the radiation field is not significant and these two conditions can be approximated in a neighborhood of $k_0 >> 1$ with

$$E(k_0, \theta) = 1 \qquad \text{and} \qquad \pm\left(\frac{\partial E}{\partial k}\right)(k_0, \theta) < 0 \quad , \tag{2.8}$$

where the upper (lower) sign corresponds to a peak (minimum). In order to specify the region where these conditions are valid and to visualize the effect of the quantized photon number let us define the discrete counterpart, $E_k(\theta)$, of the continuous function, $E(k, \theta)$, as the curve connecting the discrete points, $(k, E(k, \theta))$ taken at integer values of k, by straight lines. The continuous function, $E(k, \theta)$, oscillates faster for larger θ (and smaller k) suggesting that its counterpart is going to deviate from it high above threshold (and at small photon numbers). We find that $E_k(\theta)$ follows $E(k, \theta)$ well if $\beta(k, \theta)$, given by Eq. (2.3), varies slowly with k in a neighborhood of k_0, i. e., if the conditions given by Eq. (2.5) and consequently by Eq. (2.6) for $k_0 >> 1$ apply. In this region of the parameters, i. e., in the semiclassical regime, $E_k(\theta)$ can be approximated by the

continuous function, $E(k, \theta)$, and Eq. (2.8) can be used. An example for this case is depicted in Fig. 5, while the deviation between the two functions is apparent in Figs. 9 and 10 that will be discussed later on in detail. One can see in Fig. 5 that $E(k, \theta)$ is an oscillatory function and its minima are given by the curves,

$$\theta_{min}^2 k_{min} = (l\pi)^2 N_{ex} \quad , \tag{2.9}$$

in the $\theta - k$ space where l is an integer. Expanding $E(k, \theta)$ with respect to θ for a given k_0 around one of the minima, θ_{min}, we find that $E \leq 1$ if $\theta_{min} - 1 \leq \theta \leq \theta_{min} + 1$, provided $k_0 << N_{ex}$. The derivative of $E(k, \theta)$ with respect to k in the vicinity of $k_0 >> 1$ at the lower (upper) end of this interval is negative (positive). Thus, considering the above conditions for peaks (minima) of the photon statistics, Eq. (2.8), we find for $1 << k_0 << N_{ex}$ that they are located on curves shifted downward (upward) by 1 with respect to the curves of the minima of the function $E(k, \theta)$. Carrying out this shift in Eq. (2.9) we reobtain the same result as in Eq. (2.7). It determines the location of the peaks and the minima of the photon statistics in the so-called semiclassical regime of the micromaser specified by Eq. (2.6).

III. THE QUANTUM REGIME

It can be seen in Fig. 6 that the photon statistics become diffuse as one increases the pumping parameter, θ, beyond the semiclassical regime. The reason for this is that the granular feature of the phases originating in the discreteness of the photon number becomes significant as a result of their increased slope. In other words the branches of the stable solutions for steady states of the semiclassical theory get closer to each other than one quantum of the photon number resulting in a disintegration of the phases of the photon statistics. Based on the dominant role of the quantized nature of the radiation field we call this region of the parameters where Eq. (2.6) does not apply the "quantum regime" of the

micromaser. However, as it can be seen in Fig. 7 the fragments of the disintegrated phases of the semiclassical regime form new structures at larger pumping parameters. The diffuse region is followed by an ensemble of new kinds of apparently smooth phases accompanied by sharp single peaks, the so-called "quantum islands" [8]. The formation of the new phases can be understood as another way to connect the location of the nonzero probabilities of the disintegrated phases on the discrete lattice of the photon number. New connection rules can be determined by introducing new parameters of the phases. Since there are several ways to connect the probability points, therefore, there are several possible connection rules and phase parameters that can be introduced. Let us define, $L = l - sk_0$, as a new parameter where k_0 is the photon number and $s = 0, 1, 2, \ldots$ parametrizes the different connection rules. The parameter of the semiclassical regime, l, can be reobtained for $s = 0$, while several new ones are given by $s > 0$. Substituting the new parameter, L, into Eq. (2.4) we obtain

$$\theta\sqrt{(k_0+1)/N_{ex}} = \mp Arc\sin\left(\sqrt{(k_0-\bar{n}_b)/N_{ex}}\right)+(L+sk_0)\pi \quad . \tag{3.1}$$

Since the disintegration of the old phases and the formation of the new ones is a direct consequence of the quantized nature of the radiation field, Eq. (3.1) has nothing to do with the semiclassical theory unless $s = 0$. However, it can now be used to find the location of the peaks (minima) of the photon statistics in the quantum regime the same way as we used Eq. (2.4) before for the semiclassical region. The correspondence between Eq. (3.1) and the quantum phases is apparent in the examples depicted in Figs. 7 and 8 for $s = 1$. The solid (dotted) lines in Fig. 8 coincide with the peaks (minima) of the photon statistics in Fig. 7. The curves with a solid branch on their lower (higher) photon number sides correspond to the upper (lower) sign in Eq. (3.1). The average photon number is depicted by a thick solid line in Fig. 8. The disintegration of the phases of the semiclassical regime, $s = 0$, led to the formation of the $s = 1$ quantum phases. This is, however, generally true. A disintegrated phase structure of order s is followed by a set of new phases and quantum islands of order $s + 1$. The single semiclassical regime is followed by several

consecutive quantum regions.

It can be seen in Figs. 7 and 8 that the phases in the quantum regime are not monotonous curves in the θ - k space as those in the semiclassical region. Their minima (i. e. the minima of the equations of state of the phases, $\theta = \theta(k)$) are located at

$$k^{min} \cong L/s \qquad \text{and} \qquad \theta^{min} \cong 2\pi\sqrt{sLN_{ex}} \mp 1 \quad , \tag{3.2}$$

provided $1 << k^{min} << N_{ex}$. These points are important because, as we will see later on, large single peaks, the quantum islands, can arise in their vicinity due to the small slope of the phases. In order to understand this and to find a compact formula for the peaks (minima) of the photon statistics we make use of the function, $E(k, \theta)$, and its discrete counterpart, $E_k(\theta)$, again. These functions are also going to help us to explain why the two branches of each curve in Fig. 8 are alternatively representing peaks (solid lines) and minima (dotted lines) of the photon statistics. The equation of the minima of the function, $E(k, \theta)$, when introducing the new parameter, L, can be obtained from Eq. (2.9) as

$$\theta_{min}^2 k_{min} = \left[(L + sk_{min})\pi\right]^2 N_{ex} \quad . \tag{3.3}$$

As a consequence of the nonzero parameter, s, the curves of the minima of the function $E(k, \theta)$ obtained from Eq. (3.3) as the function, $\theta = \theta(k)$, in the $\theta - k$ space exhibit minima at

$$k_{MIN} \cong L/s \qquad \text{and} \qquad \theta_{MIN} \cong 2\pi\sqrt{sLN_{ex}} \quad , \tag{3.4}$$

provided $1 << k_{MIN}$. The location of the peaks (minima) of the photon statistics can now be calculated similarly to the semiclassical region above by shifting the curves of Eq. (3.3) by 1 provided $k_{MIN} << N_{ex}$. Thus, we reobtain the results for the extreme points of the phases/minima given by Eq. (3.2) above as $k^{min} = k_{MIN}$ and $\theta^{min} = \theta_{MIN} \mp 1$.

However, due to the non-monotonous feature of the curves in this case a shift downward (upward) will give us the peaks (minima) only for photon numbers, $k < k_{MIN}$, while opposite shifts are necessary for $k > k_{MIN}$. This is why the two branches of the curves in Fig. 8 alternatively represent the peaks and minima depicted by solid and dotted lines, respectively. Therefore, the equations of the phases of order s are given by

$$(\theta \pm 1)^2 k_0 = \left[(L + sk_0)\pi\right]^2 N_{ex} \quad , \tag{3.5}$$

where the upper (lower) sign corresponds to the peaks (minima) of the photon statistics for the lower region of the photon numbers, $k < k_{MIN}$, while for the upper part of the photon numbers, $k > k_{MIN}$, the signs, $\pm$, need to be switched to $\mp$. Combining these conditions together we finally obtain for a given θ the location of the peaks along one of the phases of the photon statistics in the quantum regime as

$$k_{0\pm} = \frac{k_{MIN}}{\theta_{MIN}^2}\left[\theta \pm 1 \mp \sqrt{(\theta \pm 1)^2 - \theta_{MIN}^2}\right]^2 \quad , \tag{3.6}$$

where k_{MIN} and θ_{MIN} determine via s (> 0) and L the actual phase that we are considering (see Eq. (3.4) above), and the upper (lower) sign gives us a peak below (above) the minimum, k_{MIN}, of the actual phase. The expression for the minima of the photon statistics can be obtained by switching the two signs, $\pm \rightarrow \mp$.

It can be seen in Fig. 7 that all the phases in the quantum regime exhibit sharp peaks in the vicinity of the minima of their curves. Suppressing everything else at optimum pumping they are the only significant features of the photon statistics (see Figs. 9, 10 and 11). These are the so-called "quantum island states" (*QIS*) discussed in Ref. [8] in detail. It follows from the product form of Eq. (2.1) that high peaks in the photon statistics are generated when the oscillations of $E_k(\theta)$ as a function of k are slow. There are long intervals in this case where $E_k(\theta)$ is steadily smaller (larger) than *1* and, consequently, the probability $p_k(\theta)$ is monotonously decreasing (increasing). This, after normalization, will result in a large peak at the beginning (end) of the interval. One would expect by

looking at Eq. (2.3) that the oscillations are faster for larger pumping parameter, θ, resulting in rapidly oscillating photon statistics. However, this is not so. Although the oscillations of $E(k, \theta)$ are faster its discrete counterpart, $E_k(\theta)$, can deviate from it in the quantum regime as a consequence of the discrete photon number. The oscillations of $E_k(\theta)$ are particularly slow in the neighborhoods of the minima of the phases in the θ - k space due to the small slope of the phase curves. Some examples are depicted in Figs. 9 and 10 exhibiting long intervals where the $E_k(\theta)$ functions are steadily smaller or larger than *1* resulting in the corresponding *QIS* shown underneath. The two kinds of slowly varying intervals can be interpreted as two special cases of the Moire-effect between the oscillations of $E(k,\theta)$ and the discrete periodic lattice of the photon number. Suppressing the most part of the photon statistics this effect plays the role of a trapping mechanism making the *QIS* the "trapping states" of the system. This trapping effect has obviously nothing to do with the one in Ref. [7]. Here, the *QIS* are the consequence of the the quantized nature of the radiation field and the coherent oscillatory nature of the atom-field interaction reflected by the function, $\beta(k,\theta)$, in Eq. (2.3). Together with the whole phase structure of the photon statistics, these states are insensitive to (a moderate amount of) thermal radiation.

The two kinds of slowly varying "Moire-intervals" also suggest that there are two kinds of quantum island states, QIS^- and QIS^+, depending whether $E_k(\theta)$ is smaller or larger than *1* in that particular interval, respectively. Therefore, QIS^- (QIS^+) are sitting on the low (high) photon number sides of the phase curves close to the minima (compare Figs. 7 and 8). Their exact locations can be calculated using Eq. (3.6) provided the necessary pumping is known. However, the optimum pumping, θ_{QIS}, that produces the largest single peaks is difficult, in general, to determine due to the complicated structure of $E_k(\theta)$. Considering Figs. 7 and 8 it can be said that the largest peaks can be produced using a pumping, θ_{QIS}, that is equal or slightly smaller than the minimum of a phase curve, θ^{min}. Using $\theta^{min} = \theta_{MIN} \mp 1$ we obtain the optimum pumping to produce *QIS* given by

$$\theta_{QIS^{\pm}} \lessapprox \theta_{MIN} \mp 1 \quad , \tag{3.7}$$

where the upper (lower) sign corresponds to QIS^{+} (QIS^{-}), and θ_{MIN} is given in Eq. (3.4). However, these are only the possible locations of the *QIS*. Although a long constant interval of $E_k(\theta)$ in the vicinity of the minimum of a phase is necessary for the build-up of a large *QIS* - peak it is not, in general, sufficient. As it can be seen in the examples of Fig. 9 QIS^{-} (QIS^{+}) cannot be generated in the high (low) photon number side of the photon statistics. This is a consequence of the product form of the photon statistics given by Eq. (2.1) and the overall confinement centered around the *40%* of N_{ex}. Apparently, we do not have this problem in Fig. 10. Both QIS^{-} and QIS^{+} can be produced in that region of the pumping where the minimum of the phases (and the corresponding long interval of constant $E_k(\theta)$) are situated in the main stream of the photon statistics, i. e. around $k = 40$ in our example. Apart from the rapid transitions between them the micromaser resides in either QIS^{-}, or QIS^{+} (see Figs. 7 and 8). Therefore, any pumping will result in large single peaks in this region although the optimum cases are still determined by Eq. (3.7).

In other words, due to the isolated large *QIS* - peaks isolated phases become greatly populated in this region of θ at the expense of those of the others. Similarly to the beginning of the semiclassical regime, there is practically no overlap between the populated parts of these dominant phases that makes the phase transitions abrupt between them. This suggests the interpretation for the oscillations between the well-defined phases, i. e. between QIS^{-} and QIS^{+}, as a revival of the phase transitions following the collapse in the semiclassical regime. We should remark here that there are apparent differences in the characteristics of the phase transitions and of their collapses between the semiclassical and quantum regimes due to the different origins of the phase structures themselves. The phase transitions between QIS^{-} and QIS^{+} result in the oscillations in the average photon number, $\langle n \rangle$, as depicted in Fig. 8 and 12. Since $\langle n \rangle$ is a simple function of the atomic population (see in the Appendix) the same kind of oscillations can be found in the atomic inversion.

Therefore, the collapse of the oscillations in the semiclassical region and their revival in the quantum regime are directly connected to the Jaynes-Cummings collapse and revival effect [5]. As we mentioned above there are several consecutive structures in the quantum regime parametrized by $s > 1$ (there is only one in the semiclassical regime, $s = 0$). The disintegration and reshaping of the phase structures, therefore, correspond to a collapse in the semiclassical region and a sequence of consecutive collapses and revivals in the quantum regime as depicted in Fig. 12.

The different regimes of phases can, especially for small N_{ex}, overlap. This usually mixes the phase structures up although, at particular pumping parameters, also allows for a production of (incoherently) superposed *QIS* corresponding to different regimes. In the example depicted in Fig. 13 the QIS^{+} around $k = 62$ belongs to $s = 2$ while QIS^{-} around $k = 22$ belongs to $s = 3$ resulting in two well-separated co-existing sharp peaks. We have chosen $N_{ex} = 100$ in this paper in order to separate the different structures in the quantum regime for better presentation. However, as it can be easily shown the same phase structures and corresponding *QIS* arise for lower N_{ex} as well at, as it can be seen in Eq. (3.4), smaller pumping parameters. We, therefore, find that the experimental realization of these features of the photon statistics including, in particular, the quantum island states is accessible especially for lower values of N_{ex}.

IV. SUMMARY

In the present paper the photon statistics [3] of the micromaser [1] have been studied in the two-dimensional space of the pumping parameter, θ, and photon number, k. We have found that the peaks of the probability distribution form various phase structures in this space transforming into one another as the pumping parameter, θ, increases. The first group of phases is situated in the so-called "semiclassical" regime determined by the condition given in Eq. (2.6). The curves of these peaks are monotonous and coincide with the stable solutions for the steady states of the

semiclassical theory [4]. Their structure together with their populations, i. e. the probability distributions along them, result in typical features in the dynamics of the micromaser such as the collapsing phase transitions in the average photon number as a function of θ. However, when the pumping, θ, increases beyond the semiclassical regime the phases disintegrate due to the discreteness of the photon number. The micromaser enters its "quantum regime". New kinds of phases build up from the disintegrated fragments of the old ones that are not monotonous any longer. Single large probability peaks, the so-called "quantum island states" (*QIS*), can arise in the vicinity of their minima that have been absent from the semiclassical regime [8]. In the optimum cases the system makes periodic phase transitions between the two kinds of quantum island states, QIS^- and QIS^+. These oscillations as a function of θ together with the collapse of the phase transitions in the semiclassical regime correspond to the Jaynes-Cummings collapse - revival effect. The disintegration and transformation of phase structures recurs periodically as the pumping, θ, is increasing, and the group of phases in the semiclassical region is followed by a sequence of phase structures in the quantum regime. Therefore, the average photon number, $\langle n \rangle$, exhibits periodic collapses and revivals corresponding to each structure. We find the experimental demonstration of these phase structures accompanied by the quantum island states feasible using the presently available facilities.

APPENDIX

Let us consider the master equation of the micromaser for the interaction-picture field density matrix, ρ, given by [8]

$$\frac{d\rho}{dt} = r\left(C\rho C + S^{\dagger}\rho S\right) + \mathcal{L}\rho \quad , \tag{A.1}$$

where, in the gain term, $C = cos\left(g\tau\sqrt{aa^{\dagger}}\right)$, $S = \frac{sin\left(g\tau\sqrt{aa^{\dagger}}\right)}{\sqrt{aa^{\dagger}}}a$, and the loss term reads as

$$\mathcal{L}\rho = \left(\frac{\gamma}{2}\right)\left[(\bar{n}_b + 1)\left(2a\rho a^\dagger - a^\dagger a\rho - \rho a^\dagger a\right) + \bar{n}_b\left(2a^\dagger \rho a - aa^\dagger \rho - \rho aa^\dagger\right)\right] \quad . \quad \text{(A.2)}$$

We find the equation of motion for the average photon number as [3]

$$\frac{d}{dt}\langle n\rangle = r\left\langle sin^2\left(g\tau\sqrt{aa^\dagger}\right)\right\rangle - \gamma\left(\langle n\rangle - \bar{n}_b\right) \quad . \quad \text{(A.3)}$$

The same result can be obtained when, assuming separable gain and loss cycles in the case of $\tau << 1/\gamma$, we use the return map given by

$$\rho^{(k+1)} = e^{\mathcal{L}/r}\left(C\rho^{(k)}C + S^\dagger \rho^{(k)} S\right) \quad , \quad \text{(A.4)}$$

where k is the number of atoms traversed the cavity and $1/r$ is the mean time interval between the atoms for Poissonian pumping statistics. Approximating the time derivative of $\langle n\rangle$ with $r\left(\langle n\rangle^{(k+1)} - \langle n\rangle^{(k)}\right)$ and assuming $1/r << 1/\gamma$, i. e. the cavity lifetime much longer than the time spacing between the atom, we reobtain Eq. (A.3). We find the semiclassical rate equation from Eq. (A.3) by approximating the quantum expectation values by their semiclassical counterparts as

$$\frac{dn}{dt} = r\,sin^2\left(g\tau\sqrt{n+1}\right) - \gamma\left(n - \bar{n}_b\right) \quad , \quad \text{(A.5)}$$

that results in Eq. (2.4) at steady state.

Calculating the atomic density matrix as

$$\rho_{(atom)}(\tau) = Tr_{(field)}\left[U(\tau)\rho_{(atom)}(0)\otimes\rho(0)U^\dagger(\tau)\right] \quad , \quad \text{(A.6)}$$

where U is the time evolution operator of the Jaynes-Cummings model, $\rho_{(atom)}(0)$ and $\rho(0)$ are the initial density matrices for the atom and the field, respectively, the matrix element for the lower atomic state is found to be $\rho_{bb} = \left\langle sin^2\left(g\tau\sqrt{aa^\dagger}\right)\right\rangle$, provided we started with initially excited atoms, $\rho_{aa} = 1$. This can be substituted into Eq. (A.3) and we obtain

$$\frac{d}{dt}\langle n\rangle = r\rho_{bb} - \gamma\left(\langle n\rangle - \bar{n}_b\right) \quad . \tag{A.7}$$

Therefore, the steady state average photon number, $\langle n\rangle_{ss}$, is directly connected to the final atomic population as $\rho_{bb}\, N_{ex} = \langle n\rangle_{ss}$ - $\bar{n}_b$, resulting in the inversion, $w = \rho_{aa}$ - ρ_{bb}, given by

$$w = 1 - 2\frac{\langle n\rangle_{ss} - \bar{n}_b}{N_{ex}} \quad . \tag{A.8}$$

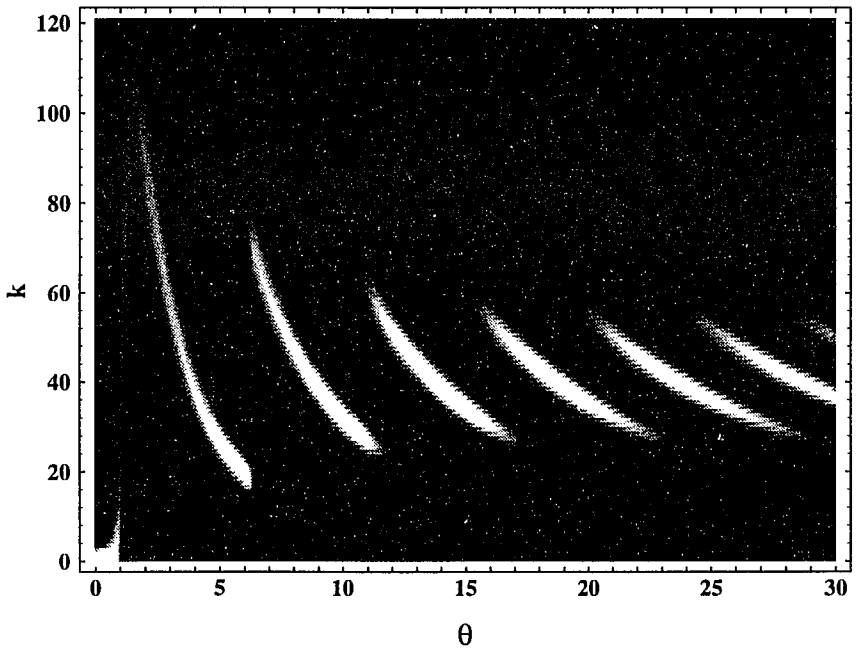

FIG. 1: Density plot of the photon statistics in the semiclassical regime for $N_{ex} = 100$ and $\bar{n}_b = 0.5$. Lighter points in the figure show higher probabilities. Bright ridges are apparent showing the phase structure of the system.

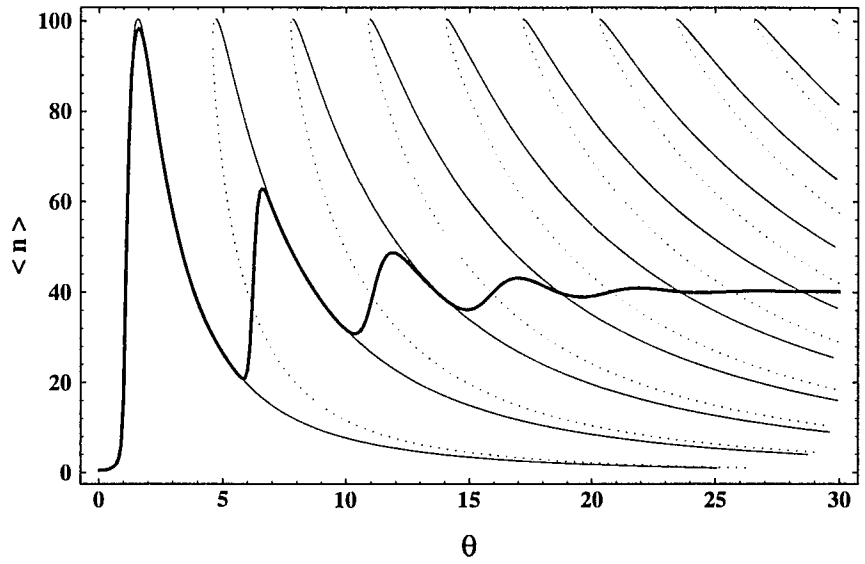

FIG.2: Stable and unstable solutions of the semiclassical theory depicted by light solid and dotted lines, respectively. The stable solutions correspond to the bright ridges in Fig. 1. The average photon number, $\langle n \rangle$, calculated from the photon statistics of Fig. 1 is represented by a heavy solid line showing the transitions that the system makes between the phases as a function of the pumping parameter, θ.

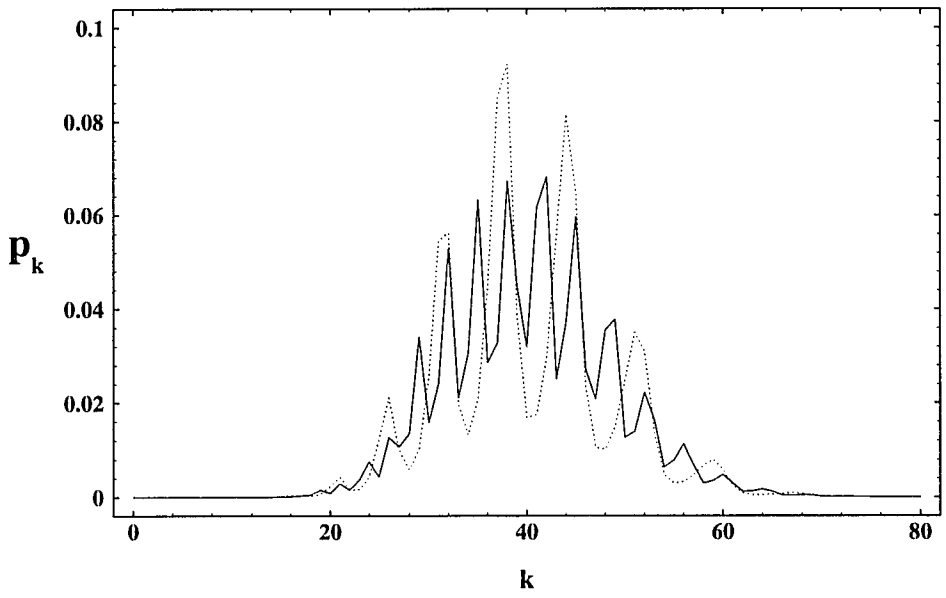

FIG. 3: Photon statistics at $\theta = 60$ and 120 depicted by dotted and solid lines, respectively. The envelope of the peaks is a bell-like curve that is apparently fairly independent of θ.

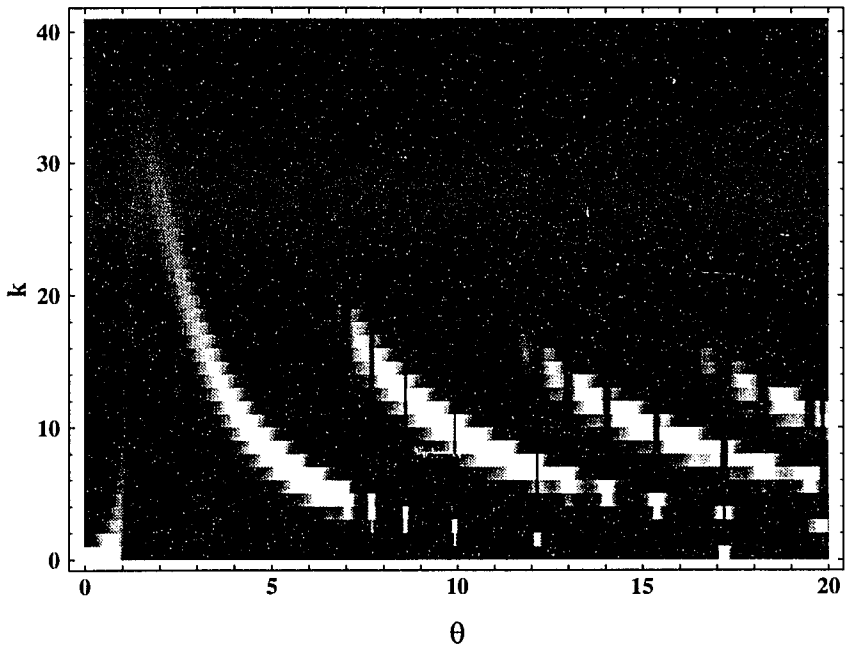

FIG. 4: Density plot of the photon statistics for $N_{ex} = 30$ and $\bar{n}_b = 0$. The distinct bright spots are the probability peaks of the trapping states. The dark lines parallel to the k-axis above the peaks indicate how the probability distribution is blocked and the system is forced back to a lower order phase in this case.

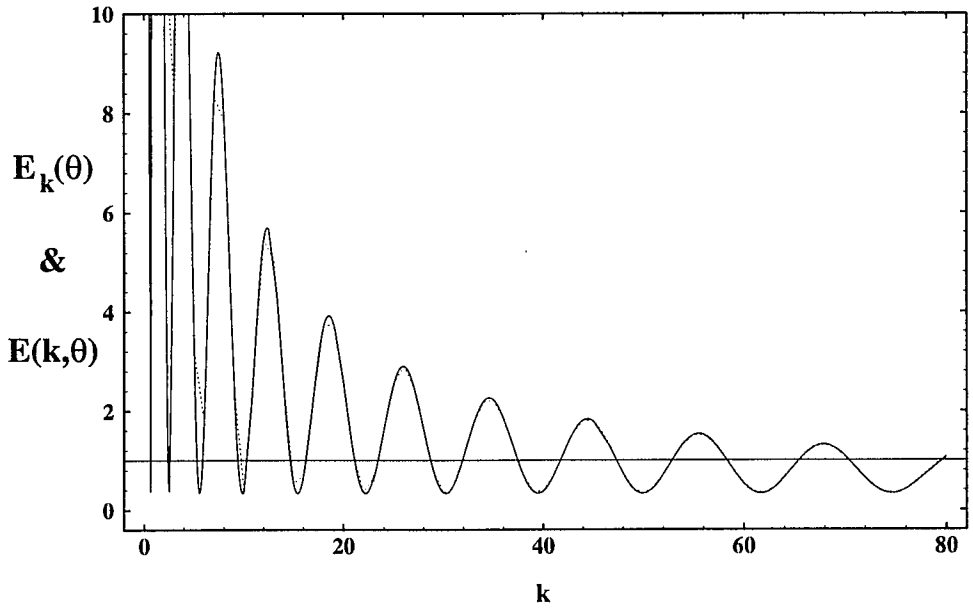

FIG. 5: The function, $E(k,\theta)$, and its discrete counterpart, $E_k(\theta)$, depicted by solid and dashed lines, respectively, for $\theta = 40$, $N_{ex} = 100$ and $\bar{n}_b = 0.5$. For these parameters the two functions agree rather well. The agreement will disappear for larger θ.

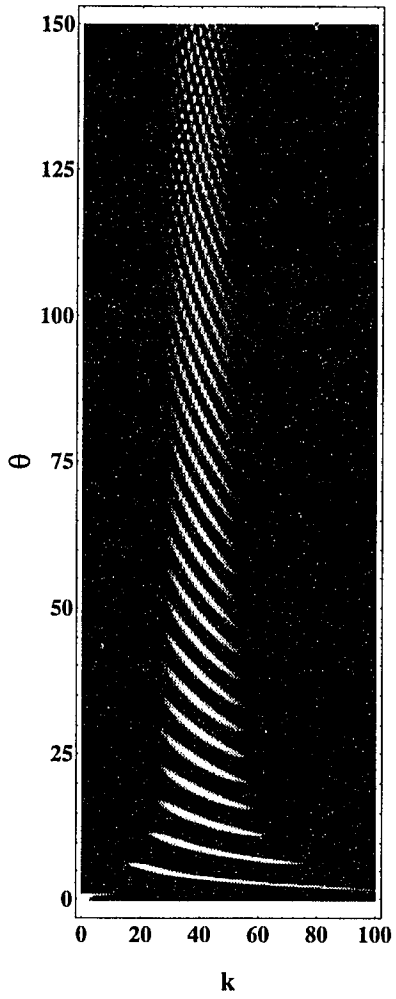

FIG. 6: Density plot of the photon statistics for $N_{ex} = 100$ and $\bar{n}_b = 0.5$. The bright ridges of the semiclassical regime become diffuse for large θ as the system approaches the quantum regime. They disintegrate because due to the increased slope of the phases the discreteness of the photon number becomes more significant.

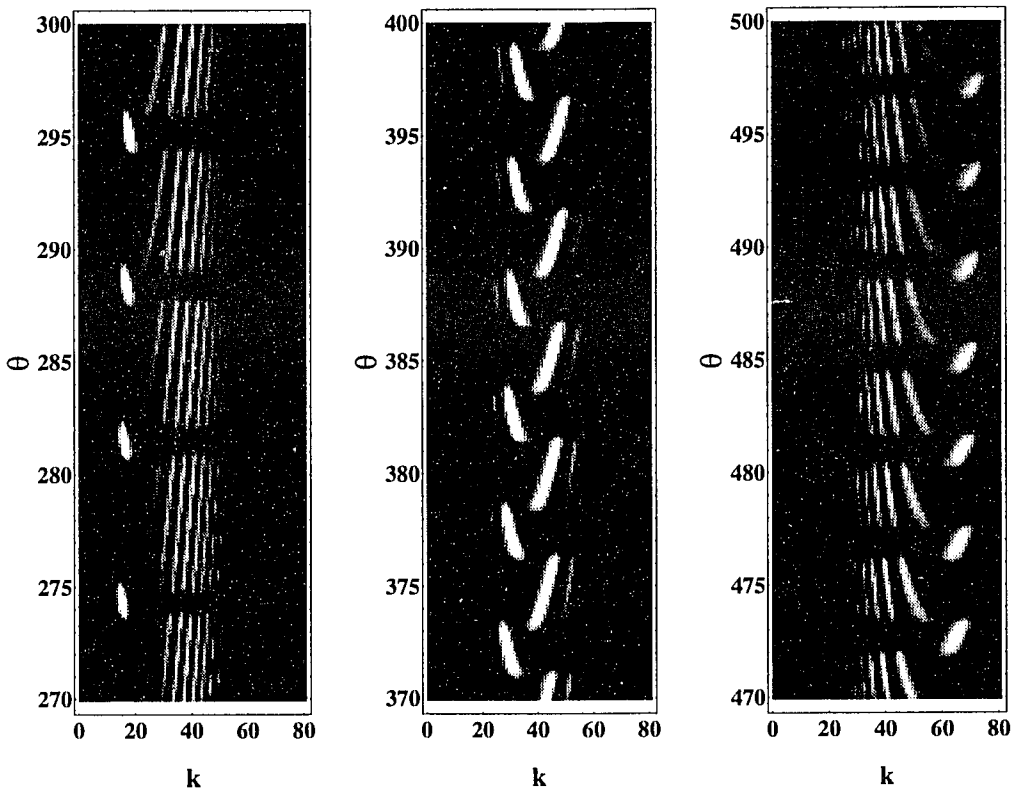

FIG. 7: Density plots of three regions of the photon statistics in the quantum regime of $s = 1$ for $N_{ex} = 100$ and $\bar{n}_b = 0.5$. Bright ridges and well localized spots are apparent showing the phase structure and the accompanying quantum island states of the system, respectively.

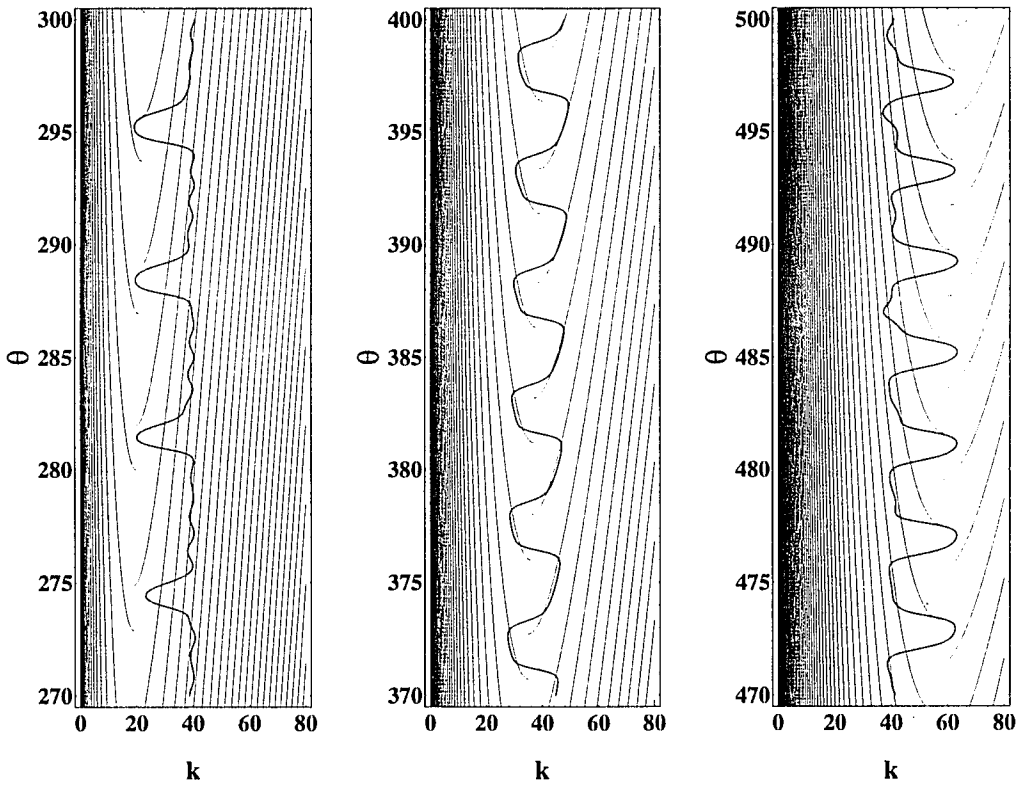

FIG.8: Phase structure given by Eq. (3.1) where the phases and the minima are depicted by light solid and dotted lines, respectively. The light solid lines correspond to the bright ridges in Fig. 7. The average photon number, $\langle n \rangle$, calculated from the photon statistics of Fig. 7 is represented by a heavy solid line. The phase transitions that the system makes between the quantum islands as a function of θ are apparent in the middle figure.

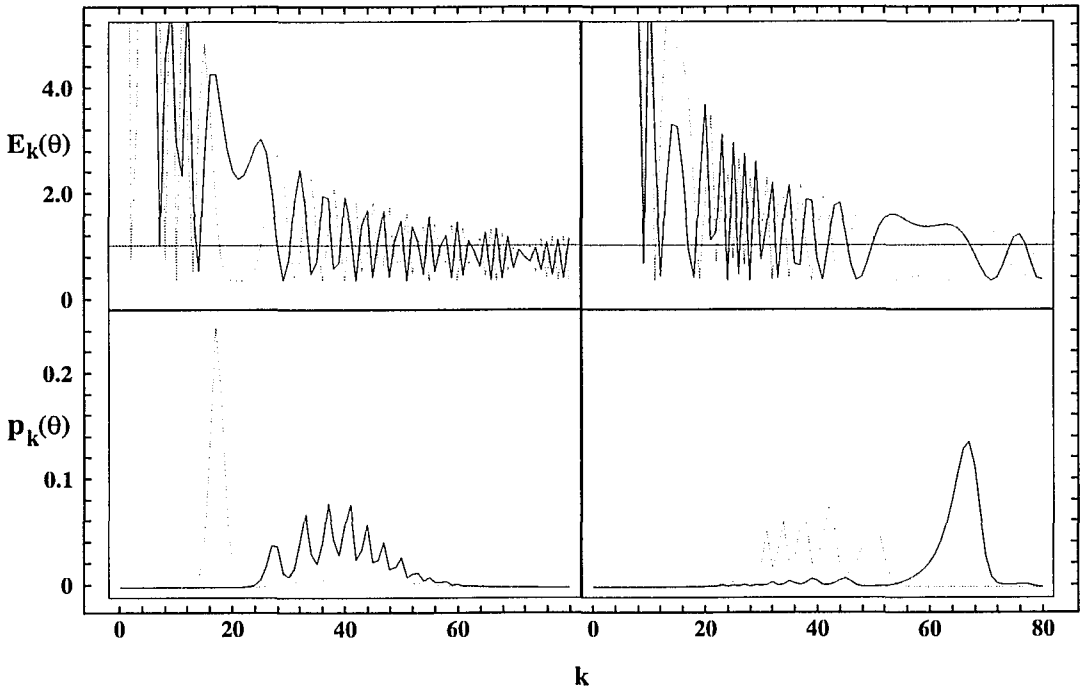

FIG. 9: The functions, $E_k(\theta)$, in the upper and the corresponding photon statistics in the lower part of the figure for four different pumping parameters: $\theta = 286$ and 288 depicted by solid and dotted lines in the left and $\theta = 481$ and 483 depicted by solid and dotted lines in the right part of the figure, respectively.

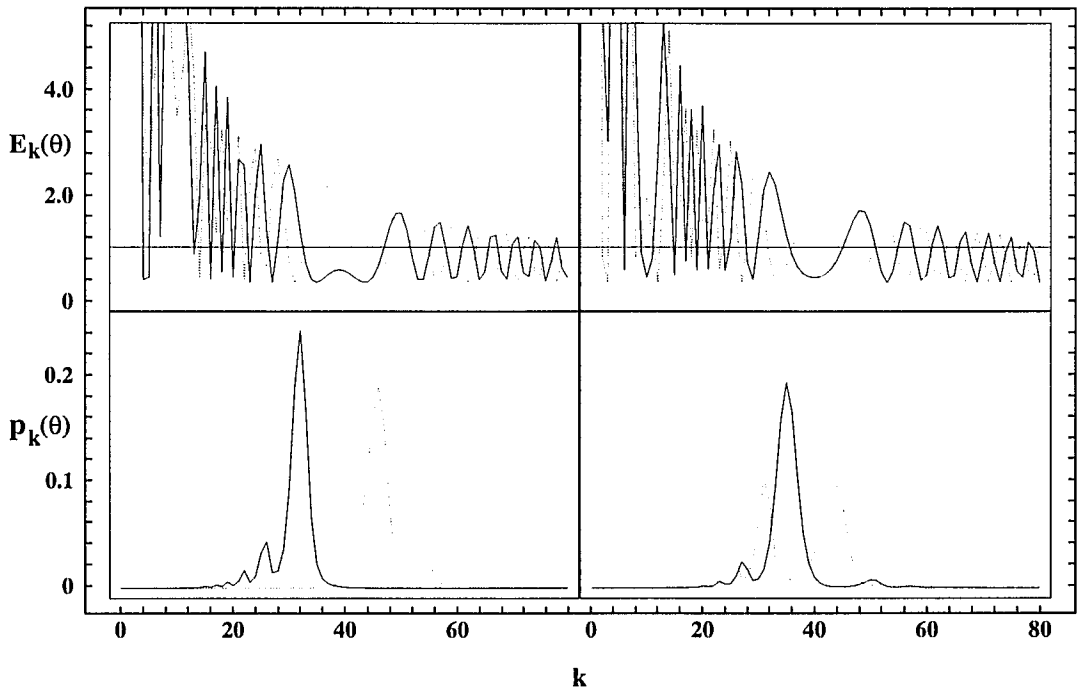

FIG. 10: The functions, $E_k(\theta)$, in the upper and the corresponding photon statistics in the lower part of the figure for four different pumping parameters: $\theta = 393$ and 395 depicted by solid and dotted lines in the left and $\theta = 397$ and 399 depicted by solid and dotted lines in the right part of the figure, respectively.

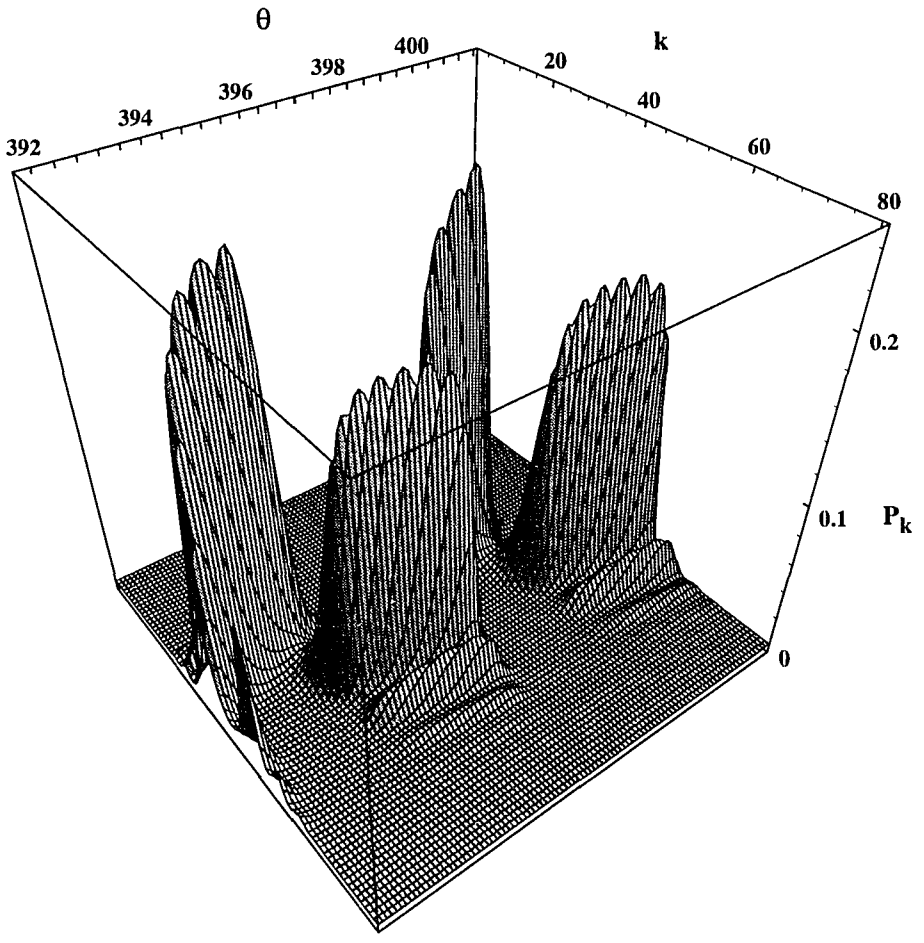

FIG.11: Three dimensional plot of the photon statistics exhibiting consecutive quantum island states, QIS^- and QIS^+.

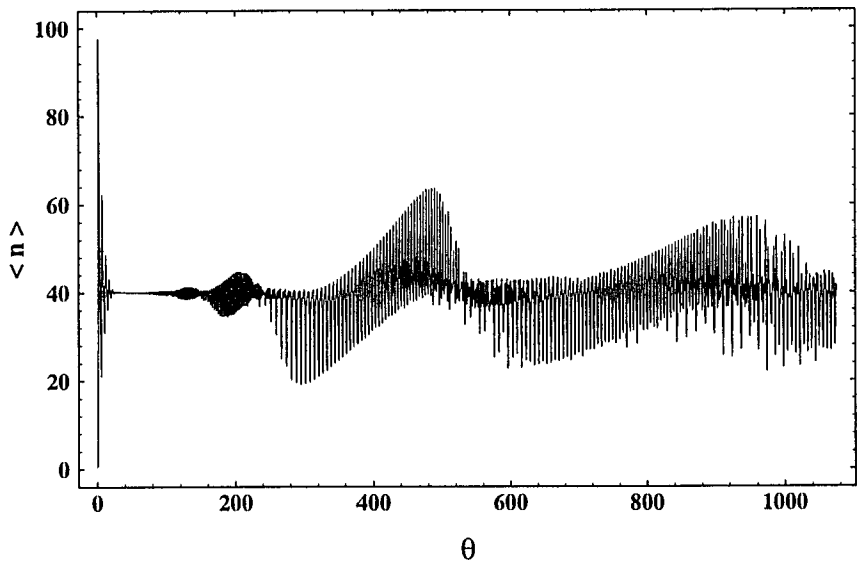

FIG. 12: Average photon number, $\langle n \rangle$, for $N_{ex} = 100$ and $\bar{n}_b = 0.5$ showing consecutive collapses and revivals belonging to the $s = 0$ semiclassical and $s = 1$, 2 quantum regimes.

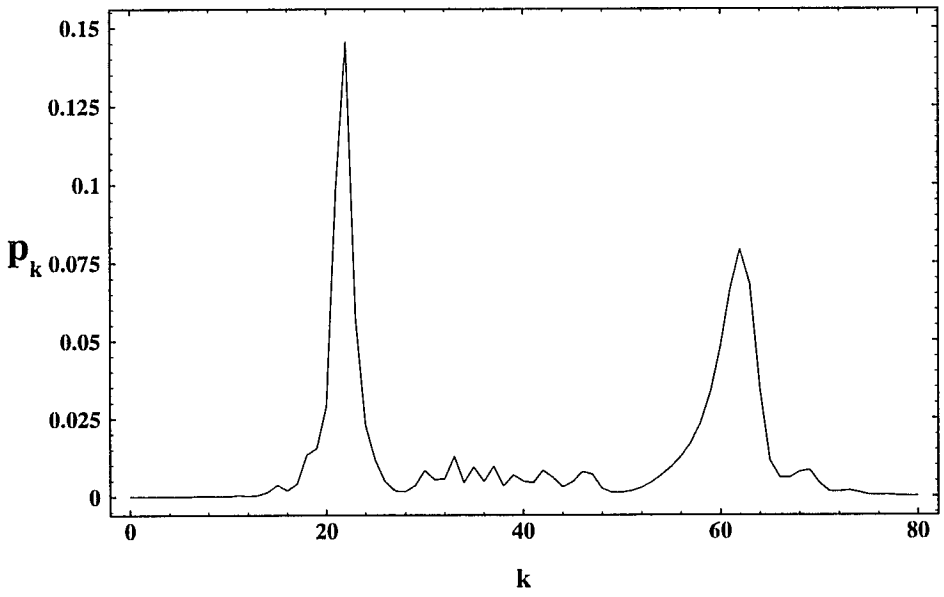

FIG. 13: The photon statistics at $\theta = 943$ exhibit a superposition of two well-separated quantum island states, QIS^{+} (high) and QIS^{-} (low photon number), belonging to the $s = 2$ and 3 quantum regimes, respectively.

3.1.2 Quantum Island States in the Micromaser†

ABSTRACT

We study the photon statistics of a micromaser with nonzero thermal background for a large range of the pumping parameter θ. The photon statistics are examined in a two dimensional space, parametrized by θ and k, where k is the photon number. For values of θ which are not too large there are prominent peaks in the photon-number distribution. The locations of these peaks are determined by well-defined structures in θ-k space. These structures lie along curves in this space. As θ is increased these structures disappear and the number distribution becomes diffuse. When θ becomes sufficiently large, however, new structures which are well localized in θ and k appear. We call these states "island states". These states exhibit strong squeezing of the photon number and are fairly insensitive to the thermal background. Their noise increases slowly due to fluctuations of the atomic beam as long as the spread in values of the pump parameter θ is smaller then the distance between the islands. Bistable behavior can be induced by fluctuations overlapping adjacent island states. We also present the photon statistics of a micromaser pumped by atoms in a mixture (incoherent superposition) of their upper and lower levels. It is shown that the noise in island states can be drastically reduced by an optimum amount of injected absorption. These features render these states experimentally feasible, so that they could be used for generating squeezed quantum states of the radiation field well-localized in θ and k.

PACS Numbers: 42.50.Dv, 42.52+x

I. INTRODUCTION

Perhaps the simplest problem in the study of the interaction between radiation and matter is that of a two-level atom coupled to a single mode of the electromagnetic field. This system, despite its apparent simplicity, has many interesting and unusual features. The advent of the micromaser has permitted the direct study of this problem in the laboratory [1-8]. A micromaser consists of a microwave cavity and a stream of excited atoms which drive the field inside the cavity. The beam is sufficiently sparse so that no more than one atom is in the cavity at any time. This device has been used to investigate nonclassical aspects of the interaction between radiation and matter [9-14], the production of number states [15,16], trapping states [17-21], and subtleties of the quantum measurement process [22].

In this paper we study certain aspects of the photon statistics of the micromaser with Poissonian pumping. We find that at strong pumping the photon statistics have some unusual features which could prove useful in the generation of sub-Poissonian states even in the presence of thermal noise and a small velocity spread in the atomic beam. In order to display these features we examine the photon statistics in a two-dimensional parameter space. One parameter is just the photon number, k, and the other is the pump parameter of the micromaser, θ. The pump parameter is directly proportional to the amount of time each atom spends interacting with the field, and the larger θ is the stronger the pumping.

In Fig. 1 we plot $p(k,\theta)$, the probability that there are k photons in the field if the pump parameter is θ. The brightness of a point, (k,θ), on the plot indicates the value of $p(k,\theta)$ at that point. Bright spots correspond to large values of $p(k,\theta)$, and dark spots correspond to small values of $p(k,\theta)$. Note that we have assumed that there is thermal noise present. In the region $\theta < 100$ there are bright ridges which correspond to large peaks in the number distribution. These features have been extensively studied [8]. In the region $100 < \theta < 250$ the bright features which correspond to large peaks in the photon number distribution disappear and the distribution becomes rather diffuse.

Around $\theta = 250$ a new type of peak appears, one that is well localized in both k and θ. Note that when these peaks appear they are the only feature in the photon number distribution, i. e. all the $p(k,\theta)$ with k outside of the peak are very small (see Fig. 2). It is the presence of these structures, which we refer to as island states, which we would like to explain.

In order to do so we first need to discuss some general properties of the photon statistics. This is done in Section II. In Section III the island states themselves are considered. Some of their unusual noise characteristics are studied in Section IV. Section V is devoted to summary and discussions. In the Appendix we derive the photon statistics for the case when the atoms enter the cavity in an incoherent superposition of the upper and lower levels of the masing transition.

II. PHOTON STATISTICS OF THE MICROMASER

Let us now consider a micromaser consisting of a high Q microwave cavity and a beam of excited atoms. Denote the cavity lifetime by $1/\gamma_c$, the atom-field coupling constant by g, and the atomic injection rate by r. The time, τ, which an atom spends in the cavity interacting with the field depends on the velocity of the atom and can vary from atom to atom. We shall consider the case of a monoenergetic beam in which each atom has the same velocity and hence the same τ. The micromaser is usually operated in the regime in which there is at most only one atom in the cavity at any time and also in which the cavity damping time is much longer than the atom-field interaction time. This implies that

$$\tau << 1/r \quad , \qquad \text{and} \qquad \tau << 1/\gamma_c \quad . \tag{2.1}$$

Introducing $N_{ex} = r/\gamma_c$, the average number of atoms traversing the cavity during a cavity lifetime, and $\theta = g\tau(N_{ex})^{1/2}$, the pumping parameter, these conditions become [8]

$$\theta << \frac{g}{\gamma_c \sqrt{N_{ex}}} \quad , \qquad \text{and} \qquad \theta << \frac{g\sqrt{N_{ex}}}{\gamma_c} \quad . \tag{2.2}$$

We shall be interested in the large N_{ex} regime in which case the first of these conditions imposes the greater restriction. Typical values of the parameters in actual experiments are $g = 44\ kHz$, $\tau = 1.5 \times 10^{-4} s$, $N_{ex} = 100$, and $\gamma_c = 3\ Hz$ [1]. These values give $\theta = 66$ and $g/[\gamma_c (N_{ex})^{1/2}] = 1500$ and, thus, the first and stronger of the inequalities in Eq. (2.2) is well satisfied. With the construction of new superconducting cavities underway it is feasible that pump parameters of the order of a few hundred, which is the range we investigate here, can be reached in the near future (note that both sides of the first inequality in Eq. (2.2) are proportional to $\gamma_c^{-1/2}$).

The photon statistics of the micromaser are given by [8]

$$p(k,\theta) = p(0,\theta) \prod_{m=1}^{k} E(m,\theta) \quad , \tag{2.3}$$

where $p(0,\theta)$ is obtained by normalizing the distribution, and the function $E(m,\theta)$ is given by

$$E(m,\theta) = \frac{N_{ex}}{m(n_b+1)} \beta(m,\theta) + \frac{n_b}{n_b+1} \quad , \tag{2.4}$$

with

$$\beta(m,\theta) = \sin^2\left(\theta \sqrt{\frac{m}{N_{ex}}}\right) \quad . \tag{2.5}$$

In the above equations n_b is the number of thermal photons present. It is possible to gain a considerable amount of information about the general features of $p(k,\theta)$ by examining the behavior of the function $E(m,\theta)$. Note that it is only values of this

function when m is an integer which enter into the photon statistics.

For a fixed value of θ the function $E(m,\theta)$ oscillates as a function of m (Fig. 3). The oscillations are bounded by the functions

$$E_{\min}(m)=\frac{n_b}{n_b+1} \quad , \qquad \text{and} \qquad E_{\max}(m)=\frac{N_{ex}}{m(n_b+1)}+\frac{n_b}{n_b+1} \quad . \quad (2.6)$$

That is, $E_{min}(m) \le E(m,\theta) \le E_{max}(m)$ where $E_{min}(m)$ and $E_{max}(m)$ are obtained from Eq. (2.4) by setting $\beta(m,\theta)$ to zero and one, respectively. The rapidity of the oscillations depends upon the values of θ and N_{ex}. If θ increases or N_{ex} decreases the oscillations become more rapid. If the oscillations are slow then a plot of $E(m,\theta)$ versus m, where m takes only integer values, will closely resemble a plot of $E(m,\theta)$ versus m where m is regarded as a continuous variable (see Fig. 3). This resemblance will disappear when the oscillations become rapid. In order to make this distinction a bit more precise let us denote by $E_m(\theta)$ the curve formed by connecting the points $(m,\ E(m,\theta))$, where m takes only integer values, by straight lines. That is, the points $(1,\ E(1,\theta))$ and $(2,\ E(2,\theta))$ are connected by a straight line, the points $(2,\ E(2,\theta))$ and $(3,\ E(3,\theta))$ are connected by another straight line, etc. Therefore, if θ is not too large, then $E(m,\theta)$ and $E_m(\theta)$ will be similar , but this similarity will disappear as θ becomes larger. We shall find that there are situations where $E(m,\theta)$ oscillates wildly, but $E_m(\theta)$ varies relatively slowly.

We can use $E(m,\theta)$ to find the peaks in the photon-number distribution. For fixed θ the function $p(k,\theta)$ is an increasing function of k, i. e. $p(k,\theta) > p(k\text{-}1,\theta)$, if $E(k,\theta) > 1$. Similarly it is a decreasing function of k if $E(k,\theta) < 1$. There is a peak in the number distribution at k_0 if $p(k,\theta)$ changes from an increasing to a decreasing function at k_0. This requires that $E(k_0,\theta) > 1$, but $E(k_0+1,\theta) < 1$. There is a minimum in the distribution at k_1 if $E(k_1,\theta) < 1$ and $E(k_1+1,\theta) > 1$. A peak will be large if $E_m(\theta)$ is slowly varying in the vicinity of the peak. If this condition is satisfied there will be a substantial range of k values below the peak for which $E_k(\theta)$

> 1. When this large number of values of $E_k(\theta)$, all of which are greater than one, are multiplied together they will produce a large peak. On the other hand if $E_m(\theta)$ varies rapidly near the peak there will in general be only a small range of k values below the peak for which $E_k(\theta) > 1$. This means that only a small number of values of $E_k(\theta)$ which are greater than one will be multiplied together to give the peak. This will produce a small peak.

An immediate consequence of the argument in the previous paragraph is that there can be no peaks in the distribution for $k > N_{ex}$. This follows from the fact that $E_{max}(k) < 1$ for $k > N_{ex}$ (see Eq. (2.6)). Because $E(k,\theta) \leq E_{max}(k)$ this implies that $E(k,\theta) < 1$ for $k > N_{ex}$.which in turn implies that for k in this range $p(k,\theta)$ is a monotonically decreasing function of k. Therefore, any interesting structure in the photon-number distribution occurs in the range $0 \leq k \leq N_{ex}$.

The task of describing the photon-number distribution in a given range of k values is greatly simplified if θ and N_{ex} are such that $E_k(\theta)$ and $E(k,\theta)$ are similar in this range. This will be true if $\beta(k,\theta)$ varies slowly there. In particular, $E_k(\theta)$ and $E(k,\theta)$ will be close for k in a neighborhood of k_0 if a change of one in k produces a small change in $\beta(k,\theta)$. For $k_0 >> 1$, if

$$\theta\sqrt{\frac{k_0+1}{N_{ex}}} - \theta\sqrt{\frac{k_0}{N_{ex}}} \cong \frac{\theta}{2\sqrt{k_0 N_{ex}}} << 1 \quad , \tag{2.7}$$

then this condition will be satisfied. Therefore, our condition for being able to approximate $E_k(\theta)$ by $E(k,\theta)$ near $k = k_0$, where $k_0 >> 1$, is

$$\theta << \sqrt{k_0 N_{ex}} \quad . \tag{2.8}$$

We shall say that a region of photon statistics which satisfies this condition is in the semiclassical regime. If it does not we shall say that it is in the quantum regime. In the semiclassical regime we can describe the photon statistics in terms of a continuous

function, but in the quantu n regime the discrete nature of the variable k becomes important.

Let us briefly consider the semiclassical regime before moving into the quantum one. Our conditions for a peak at k_0 now become

$$E(k_0,\theta)=1 \quad , \qquad \text{and} \qquad \left(\frac{\partial E}{\partial k}\right)(k_0,\theta)<0 \quad . \tag{2.9}$$

The second condition guarantees that we have a peak instead of a minimum. An examination of Eq. (2.4) shows that the first condition will be satisfied if

$$\left|\sin\left(\theta\sqrt{\frac{k_0}{N_{ex}}}\right)\right|=\sqrt{\frac{k_0}{N_{ex}}} \quad , \tag{2.10}$$

and the second will be true if

$$(n-\tfrac{1}{2})\pi<\theta\sqrt{\frac{k_0}{N_{ex}}}<n\pi \quad , \tag{2.11}$$

where n is a positive integer. Eqs. (2.10) and (2.11) give us a simple prescription for finding peaks in the photon-number distribution in the semiclassical regime.

It is possible to solve these equations if $(k_0/N_{ex}) << 1$. If k_0 satisfies the equation

$$(\theta+1)\sqrt{\frac{k_0}{N_{ex}}}=n\pi \quad , \tag{2.12}$$

where n is a positive integer, then k_0 satisfies Eq. (2.11), and

$$\left|\sin\left(\theta\sqrt{\frac{k_0}{N_{ex}}}\right)\right|=\left|\sin\left(n\pi-\sqrt{\frac{k_0}{N_{ex}}}\right)\right|\cong\sqrt{\frac{k_0}{N_{ex}}} \quad . \tag{2.13}$$

This implies that Eq. (2.10) is satisfied as well. Therefore, the maxima in the photon-number distribution are given by

$$k_{0n} = N_{ex}\left(\frac{n\pi}{\theta+1}\right)^2 \quad . \tag{2.14}$$

These are the curves along which the bright ridges lie in the $\theta < 100$ region of Fig. 1.

Finally let us note that in the semiclassical regime the location of the peaks is independent of the number of noise photons, n_b. On the other hand, as n_b increases the bounds for $E(m,\theta)$, $E_{max}(\theta)$ and $E_{min}(\theta)$, both approach one. This means that the numbers which are multiplied together to produce the maxima and minima of the number distribution become closer to one. Therefore, as n_b increases the positions of maxima and minima do not change, but the minima become shallower and the maxima become lower.

III. QUANTUM REGIME AND ISLAND STATES

As θ is increased beyond the semiclassical region the sharp peaks in the photon number distribution disappear and the distribution becomes diffuse. This can be seen clearly in Fig. 1 where the bright structures which were the dominant features in the distribution for $\theta < 100$ disappear when θ is in the range $100 < \theta < 250$. Around $\theta = 250$ new structures begin to appear. Unlike those at lower values of θ these are localized in both θ and k (see Fig. 2). Because they resemble "islands" in θ-k space we refer to them as "island states". These structures have consequences for both the average and the variance of the photon number (see Figs. 4 and 5). Note that the normalized variance can fall below one for $300 < \theta < 500$ indicating that the photon statistics are sub-Poissonian. We now want to examine the reasons for the re-emergence of structure in the distribution at these values of θ. We shall present a simple theory for the location of the island states. This theory has limitations which

will be discussed after the theory itself has been presented.

Let us begin by considering $\beta(k,\theta)$ in the neighborhood of a point k_0. If we write $k = k_0 + \delta k$, where $\delta k << k_0$, we have

$$\beta(k,\theta) \cong \sin^2\left(\theta\sqrt{\frac{k_0}{N_{ex}}} + \frac{\theta}{2}\sqrt{\frac{1}{k_0 N_{ex}}}\,\delta k\right) \quad . \tag{3.1}$$

As we saw in the preceding section we can have a large peak at k_0 if $\beta(k,\theta)$ is a slowly varying function of k for a range of k near k_0. In the semiclassical region this happens because the coefficient multiplying δk is small. Another possibility is that this coefficient is close to $s\pi$, where s is a positive integer. Then a change of δk by one will produce a change in the argument of sin^2 of approximately $s\pi$ and β itself will change only slightly. This implies that while the function $E(k,\theta)$ is very rapidly varying near k_0, the function $E_k(\theta)$ is slowly varying.

Our equations for a maximum are now Eq. (2.14) and

$$\frac{\theta}{2}\sqrt{\frac{1}{k_0 N_{ex}}} = s\pi \quad . \tag{3.2}$$

These equations must be solved for θ and k_0 in terms of s and n. Doing so we find for $N_{ex} >> 1$

$$\theta \cong \pi\sqrt{2snN_{ex}} \qquad\qquad k_0 \cong \frac{n}{2s} \quad . \tag{3.3}$$

Note that instead of curves in θ-k space, which gave us the peaks in the semiclassical region, we now have a set of points (islands).

Let us now go back to Fig. 1. The series of islands starting around $\theta = 250$ corresponds to $s = 1$; those starting around $\theta = 530$ correspond to s = 2. This conclusion is reached by comparing Eq. (3.2) with Fig. 1. Eqs. (3.3) and (3.4) work

better with increasing k_0. For example, one of the first islands occurs at about $k_0 = 13$ and $\theta = 252$. According to Eqs. (3.3) and (3.4), however, a k_0 of *13* should give $\theta = 226$, an error of *11%*. For the island at about $k_0 = 20$ and $\theta = 302$ the agreement is better. In this case our equations give for $k_0 = 20$ a value of $\theta = 281$, an error of *7%*. This dependence on k_0 is not surprising in that our analysis was based upon expanding the argument of sin^2 in terms of $1/k_0$. The larger k_0 is the better our expansion will be.

This also suggests why there are no islands in Fig. 1 for k_0 less than about *10*. In order to see this let us carry out the expansion of the argument of $\sin^2$ to one more term

$$\beta(k,\theta) \cong \sin^2\left(\theta\sqrt{\frac{k_0}{N_{ex}}} + \frac{\theta}{2}\sqrt{\frac{1}{k_0 N_{ex}}}\,\delta k - \frac{\theta}{8}\sqrt{\frac{1}{k_0^3 N_{ex}}}\,(\delta k)^2\right) . \tag{3.4}$$

In order for $E_k(\theta)$ to be slowly varying near k_0 it is necessary that the first derivative term in the argument of sin^2 (the term proportional to δk) satisfy Eq. (3.2), and that it give the dominant behavior in δk. That is, the second derivative term, which is proportional to $(\delta k)^2$, must be small. If it is not then as δk changes by one the argument of sin^2 will not change by $s\pi$ and $E_k(\theta)$ will vary rapidly. The ratio between the second and first derivative terms is proportional to $1/k_0$. This implies that as k_0 increases the importance of the second derivative term becomes small. For k_0 less than about *10*, however, the second derivative term is too large and the dephasing it produces destroys the maximum.

Another limitation of this theory is the following. Suppose that θ and k_0 satisfy Eq. (2.12) and that k_0 is an integer. In general, because of the requirement that k_0 is an integer, k_0 and θ will not satisfy Eq. (3.2) exactly, but will instead be a solution of

$$\frac{\theta}{2}\sqrt{\frac{1}{k_0 N_{ex}}} = s\pi + \varepsilon \tag{3.5}$$

where $\varepsilon << 1$. This means that in the neighborhood of k_0, $\beta(k,\theta)$ will be given by

$$\beta(k,\theta) \cong \sin^2\left(n\pi - \sqrt{\frac{k_0}{N_{ex}}} + (s\pi + \varepsilon)\,\delta k \right) \quad . \tag{3.6}$$

Now if $\varepsilon > 0$, then $\beta(k,\theta)$ is a decreasing function of k near k_0 and we have a maximum of $E_k(\theta)$ at k_0. On the other hand, if $\varepsilon < 0$, $\beta(k,\theta)$ is an increasing function of k near k_0 and no maximum will occur near k_0.

Therefore, what Eqs. (3.3) give us are approximate locations of possible island states. Whether an island state actually occurs at one of these locations probably requires a numerical evaluation of $E_k(\theta)$, but Eqs. (3.3) do explain some of the global features of the island states.

IV. PHOTON NUMBER FLUCTUATIONS IN A QUANTUM ISLAND STATE (QIS): NUMERICAL RESULTS

We now want to study how the photon number noise produced by quantum island states can be modified. First we consider the effect of a finite velocity spread in the atomic beam. This produces a spread in the pump parameter θ and increases the noise in an island state if the spread is large enough. It can lead to bistable behavior. We also consider the effect of injecting the atoms in a mixture (incoherent superposition) of their upper and lower states. This can, rather surprisingly, lead to a considerable reduction in the number fluctuations of an island state.

As we just noted, fluctuations in the velocities of the atomic beam lead to fluctuations in the pump parameter θ. A numerical averaging of the photon statistics has been carried out over a normal distribution of θ around θ_0 with various radii $\Delta\theta$. We considered the case when $N_{ex} = 40$ (n_b was chosen to be 0.1) and examined the effect of this averaging on the island state which occurs at $\theta_0 = 135$. (It should be noted at this point that it follows from Eq. (3.3) that a lower value of N_{ex}

leads to the appearance of the *QIS* at a lower range of θ, cf. the current case where $N_{ex} = 40$ and $\theta_0 \cong 135$ as opposed to Fig. 1 where $N_{ex} = 100$ and $\theta_0 \cong 250$.) The standard deviation σ of the averaged distribution as a function of $\Delta\theta$ is shown in Fig. 6 by a solid line. Apparently, the noise σ jumps from a low level to a high plateau at a certain value of $\Delta\theta$, that is nothing else but approximately the half distance between the consecutive *QIS* peaks. A spread in values of θ, if it is smaller than the distance between the islands, will not move the location of the *QIS*-peak much, and the squeezing as well as the well-localized single-peaked structure of the photon statistics are preserved. Larger fluctuations that overlap two consecutive *QIS*'s provide us with a double-peaked photon statistics, that are obviously not squeezed and σ increases to a high value. The reason for the double-peaked structure is that the consecutive peaks will be superimposed by the fluctuations without having their locations changed, resulting in two peaks in the photon statistics at the original locations of the single (squeezed) *QIS*'s. Thus, the system exhibits bistability induced by the fluctuations in the velocity of the atomic beam. We call this effect velocity noise-induced bistability. In the above example Fig. 6 (solid line) tells us that the system at the given parameters is fairly insensitive to atomic velocity fluctuations if the absolute spread in values of θ is $2\,\Delta\theta < 4$, that is if the relative fluctuation is $2\,\Delta\theta/\theta < 3\%$. Squeezing and the well-localized *QIS* peak are preserved. An example for fluctuations exceeding this limit is given in Fig. 7. Two squeezed *QIS*'s (located at $\theta = 132$ and 135, depicted by dashed and dotted lines in the Figure, respectively) are superimposed by the spread in θ, $2\,\Delta\theta = 6$, around $\theta_0 = 134$, resulting in a double-peaked photon statistics given by the solid line in Fig. 7.

Note, that the effect of velocity fluctuations on the peaks at lower values of θ is characteristically different. Since their locations strongly depend on θ, fluctuations will lead to a widening of the peaks. In the case of *QIS*'s it is not the widening mechanism which increases the noise of the system, but the appearance of the next *QIS*-peak. The interplay between the consecutive peaks due to the velocity fluctuations in the atomic beam and the resulting bistable behavior is specific to *QIS*.

Let us now consider what happens if the atoms are injected in a mixture (incoherent superposition) of their upper and lower states. A derivation of the photon statistics of the micromaser pumped by atoms in a mixture (incoherent superposition) of their upper and lower levels [23] and a brief study of the location of the peaks in both the semiclassical and quantum regimes is given in the Appendix. Here, we want only to show how the *QIS*'s and their noise, in particular, are modified by the injected absorption in the quantum region, and then to compare this to the case where the pump consists only of excited atoms (which is the case we have studied so far).

Consider *QIS*'s in the beginning of the quantum region (for $N_{ex} = 100$, from $\theta = 250$, to $\theta = 300$ in Figs. 4 and 5). Their number distributions consist of a large peak at small k's and several small peaks at large k's (see dashed line in Fig. 8). Except for a narrow region around $\rho_{aa} \cong \rho_{bb}$, the locations of the peaks are not affected by $\rho_{aa} - \rho_{bb}$ (see Eq. (A.13)), because they are determined predominantly by the oscillations of the $\beta(m,\theta)$ function (see Section III). However, the heights of the peaks at large k's decrease as ρ_{bb} increases, resulting in an enhancement of the peaks at small k's (see solid and dotted lines in Fig. 8). We can take advantage of this effect to enhance the contribution of the single large peak at small k's to the photon statistics and to decrease the noise in the *QIS*'s. In the example shown in Fig. 8 the noise in the *QIS* can be decreased from a highly super-Poissonian level ($\sigma = 2.57$) at $\rho_{aa} = 1.0$ to a sub-Poissonian value ($\sigma = 0.7$) by injecting an optimum amount of absorption into the cavity ($\rho_{aa} = 0.8$). It is interesting to see, that the noise for $\rho_{aa} = 0.8$ (dotted line) is smaller than the one for $\rho_{aa} = 0.9$ (solid line), even if the dominant peak is sharper in the latter case. It is the peaks at large k's that are responsible for this. For $\rho_{aa} = 0.8$ they are almost completely suppressed giving considerably smaller contribution to the noise than the ones for $\rho_{aa} = 0.9$.

It is also interesting to compare the photon statistics of *QIS* in Fig. 8 to the highly squeezed distribution at $\theta = 9$ (dot-dash line in Fig. 8). Even though the latter one is wider than the dominant peaks in the former ones, it exhibits much stronger squeezing since the structure of the two distributions is different. For the *QIS* it consists of an

extremely sharp large peak and several hardly noticeable ones, but precisely these small ones are responsible for making the noise much larger. This difference in structure is also the reason for the different behavior as a result of the injected absorption. Comparing the σ-θ diagram for a certain not zero injected absorption (ρ_{aa} - ρ_{bb} < *1.0*) to the one with zero absorption (ρ_{aa} = *1.0*) in Fig. 9, it can be seen that the quantum region shifts toward smaller θ's without changing the location of the islands. This is the result of the enhancement of the peaks at lower k's described above. The quantum region undergoes similar shift toward lower θ's when parameter N_{ex} is decreased, but in that case it is due to the shift in the location of the islands themselves (see Eq. (3.3)). A further increase of losses in the system shifts the quantum regions toward even smaller θ's, and large overlaps between adjacent island regions are possible to occur. It is more difficult to identify *QIS*'s in that case, as well as their squeezing is likely to disappear.

Finally, let us apply what we learned in Section IV/a about velocity fluctuations in the atomic beam to the photon statistics modified by injected absorption. It can be seen in Fig. 6 (N_{ex} = 40, n_b = 0.1, θ = 102) that the noise is squeezed by the injected absorption (ρ_{aa} = 1.00 and 0.85 depicted by dashed and dotted lines, respectively) and is fairly insensitive to velocity fluctuations if the spread $\Delta\theta$ of the pump parameter θ is such that 2 $\Delta\theta$ < 4, i.e. relative fluctuation 2 $\Delta\theta/\theta$ < 4%.

V. SUMMARY

We have seen that for large values of the pump parameter θ new features, the quantum island states (*QIS*), arise in the photon statistics. These states are localized in both θ and k unlike the features which occur at lower values of θ which lie along curves in θ - k space. They exhibit strong squeezing of the photon number even in the presence of thermal noise and fluctuations in the velocity of the atomic beam. The *QIS*'s are fairly insensitive to velocity spread in the atomic beam, which is smaller in

θ than the distance between the islands. We have shown in a specific example that it is possible to generate squeezed *QIS*'s that are insensitive to velocity spread if the relative fluctuation $2\,\Delta\theta/\theta$ is under *4%*. For larger velocity fluctuations we have found double-peaked structures in the photon statistics, that we call velocity noise-induced bistability. It has also been shown that the noise of a *QIS* can be drastically reduced by injecting atoms into the cavity in a mixture (incoherent superposition) of their upper and lower levels. These features render the quantum island states experimentally feasible, so that they could be used for generating quantum states of the radiation field well-localized in θ and k.

APPENDIX

We derive the photon statistics of a micromaser operating under the same conditions as the ones described in Section II, except that the pumping beam now consists of excited and ground state atoms as well. We show how the location of the peaks in the photon statistics is modified in the semiclassical regime (defined by Eq. (2.8)) of the micromaser. The quantum regime of this system is studied in Section IV.

We want to find a master equation for the interaction-picture field density matrix ρ. The steady-state solution of the master equation for the diagonal elements of ρ will give us the steady-state photon statistics of the field. In order to find the master equation we must first find the change produced in ρ by the passage of a single atom through the cavity

$$\delta\rho = \rho(\tau) - \rho(0) \quad , \tag{A.1}$$

where

$$\rho(\tau) = Tr_{(atom)}[U(\tau)\rho_{(atom)} \otimes \rho(0)U^{\dagger}(\tau)] \quad , \tag{A.2}$$

where τ is the interaction time, U is the time evolution operator of the Jaynes-Cummings model, $\rho(0)$ and $\rho_{(atom)}$ are the initial density matrices for the field and for the atom, respectively,

$$\rho_{(atom)} = \begin{pmatrix} \rho_{aa} & 0 \\ 0 & \rho_{bb} \end{pmatrix} \quad . \tag{A.3}$$

The coarse-grained time derivative of the field density matrix is obtained by multiplying $\delta\rho$ by the atomic injection rate, r. We can add the term $L\rho$, given by

$$L\rho = (\gamma/2)[(n_b + 1)(2a\rho a^\dagger - a^\dagger a\rho - \rho a^\dagger a) + n_b(2a^\dagger \rho a - aa^\dagger \rho - \rho aa^\dagger)] \quad , \tag{A.4}$$

to take the cavity loss into account. Here γ is the cavity decay rate for the field, n_b is the average number of thermal photons, and a ($a^\dagger$) are the mode annihilation (creation) operators. Thus, we obtain the master equation for the interaction-picture field density matrix as

$$\frac{d\rho}{dt} = r[\rho_{aa}(C\rho C + S^\dagger \rho S) + \rho_{bb}(\overline{C}\rho\overline{C} + S\rho S^\dagger) - \rho] + L\rho \quad , \tag{A.5}$$

where

$$C = \cos(g\tau\sqrt{aa^\dagger}), \qquad \overline{C} = \cos(g\tau\sqrt{a^\dagger a}), \qquad S = \frac{\sin(g\tau\sqrt{aa^\dagger})}{\sqrt{aa^\dagger}} a \quad , \tag{A.6}$$

with g the coupling constant between the atoms and the field.

The master equation for the diagonal elements $\rho_{nn} \equiv p_n$ can be written in the form

$$\frac{dp_n}{dt} = r[\Im_{n-1} - \Im_n] \quad , \qquad n \geq 1 \quad , \tag{A.7}$$

where, applying the new parameters θ and N_{ex} defined in Section II,

$$\Im_{n-1} = (\rho_{aa}\beta_n + n_b \frac{n}{N_{ex}})p_{n-1} - (\rho_{bb}\beta_n + (n_b + 1)\frac{n}{N_{ex}})p_n \quad , \tag{A.8}$$

with

$$\beta_n = \sin^2\left(\theta\sqrt{\frac{n}{N_{ex}}}\right) \quad . \tag{A.9}$$

At steady-state $\Im_{n-1} = \Im_n$, which implies $\Im_{n-1} = 0$ for any n, if p_n is required to be zero as n goes to infinity. We obtain the steady-state solution for the photon statistics

$$p_n = p_0 \prod_{m=1}^{n}\left(\frac{\rho_{aa}N_{ex}\beta_m + n_b m}{\rho_{bb}N_{ex}\beta_m + (n_b + 1)m}\right) \quad . \tag{A.10}$$

The photon statistics given by Eqs. (2.3) and (2.4) are reobtained from Eq. (A.10) by setting $\rho_{aa} = 1$.

The same argument that is given in Section II can be applied here to show that there can be no peaks in the photon statistics if $k > (\rho_{aa} - \rho_{bb})N_{ex}$. Since $(\rho_{aa}-\rho_{bb}) < 1$ if $\rho_{aa} < 1$, this provides us with a stronger condition than the one we had in Section II (which was $k > N_{ex}$). It is easy to see that there are no peaks in the photon statistics if $\rho_{aa} \leq 1/2$.

In the semiclassical region (see condition Eq. (2.8)) the location of peaks in the photon statistics are determined by Eq. (2.9), resulting in the conditions given by

$$\left|\sin\left(\theta\sqrt{\frac{k_0}{N_{ex}}}\right)\right| = \sqrt{\frac{k_0}{(\rho_{aa} - \rho_{bb})N_{ex}}} \quad , \tag{A.11}$$

and

$$(n-\tfrac{1}{2})\pi < \theta\sqrt{\frac{k_0}{N_{ex}}} < n\pi \quad . \tag{A.12}$$

Solving these equations in a similar way as in Section II, we find the maxima of the photon number distribution for the semiclassical regime given by

$$k_{0n} = N_{ex}\left(\frac{n\pi}{\theta + \frac{1}{\sqrt{\rho_{aa}-\rho_{bb}}}}\right)^2 \quad . \tag{A.13}$$

This equation tells us that except for a narrow region around $\rho_{aa} \cong \rho_{bb}$, the locations of the peaks in this regime are not modified by the injected absorption.

To find the location of the island states in the quantum regime we need to solve this equation and Eq. (3.3) simultaneously for θ and k_0 in terms of s and n in a similar way as in Section III. It is easy to see that Eq. (3.3) is reproduced and, except around $\rho_{aa} \cong \rho_{bb}$, the locations of the islands are not affected by the injected absorption (see also Fig. 9).

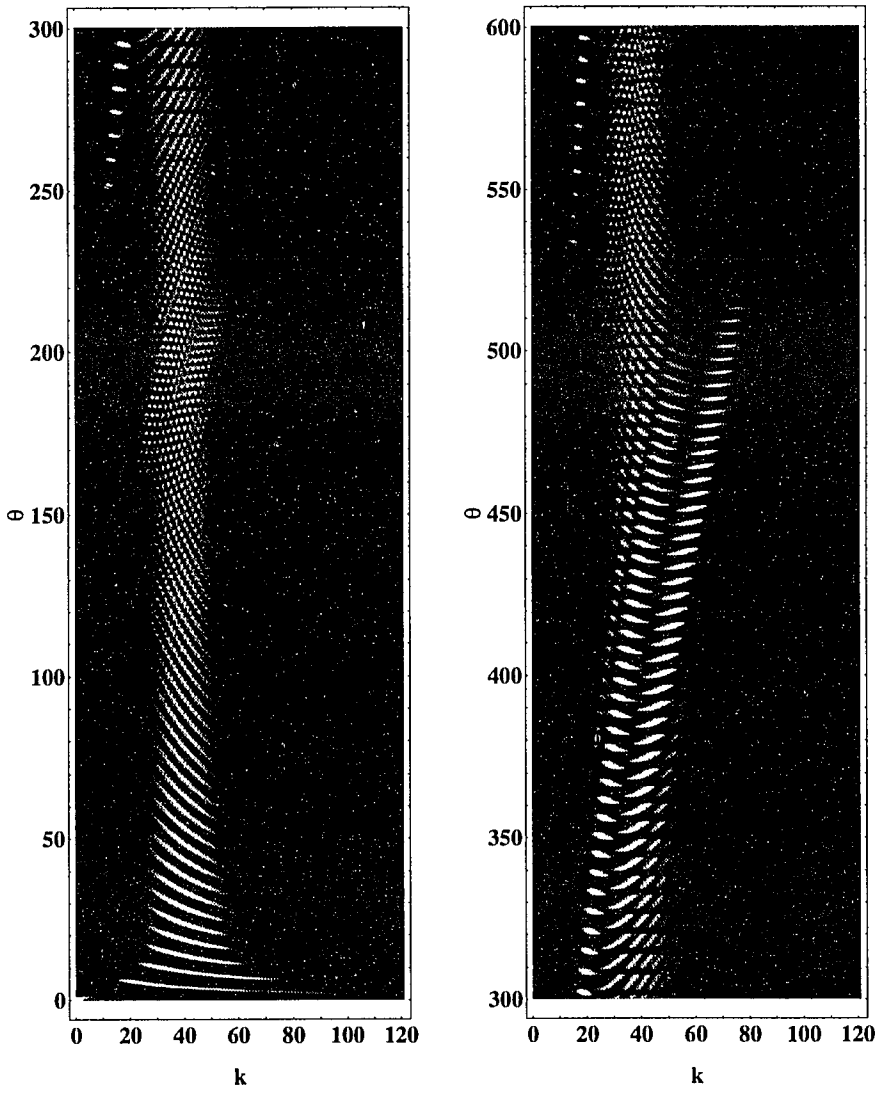

FIG. 1: The density plot of the photon statistics of the micromaser in the θ - k space for $N_{ex} = 100$ and $n_b = 0.5$. Lighter points indicate higher probabilities. Bright ridges are apparent for $\theta < 100$. At higher values of θ island-like features begin to appear.

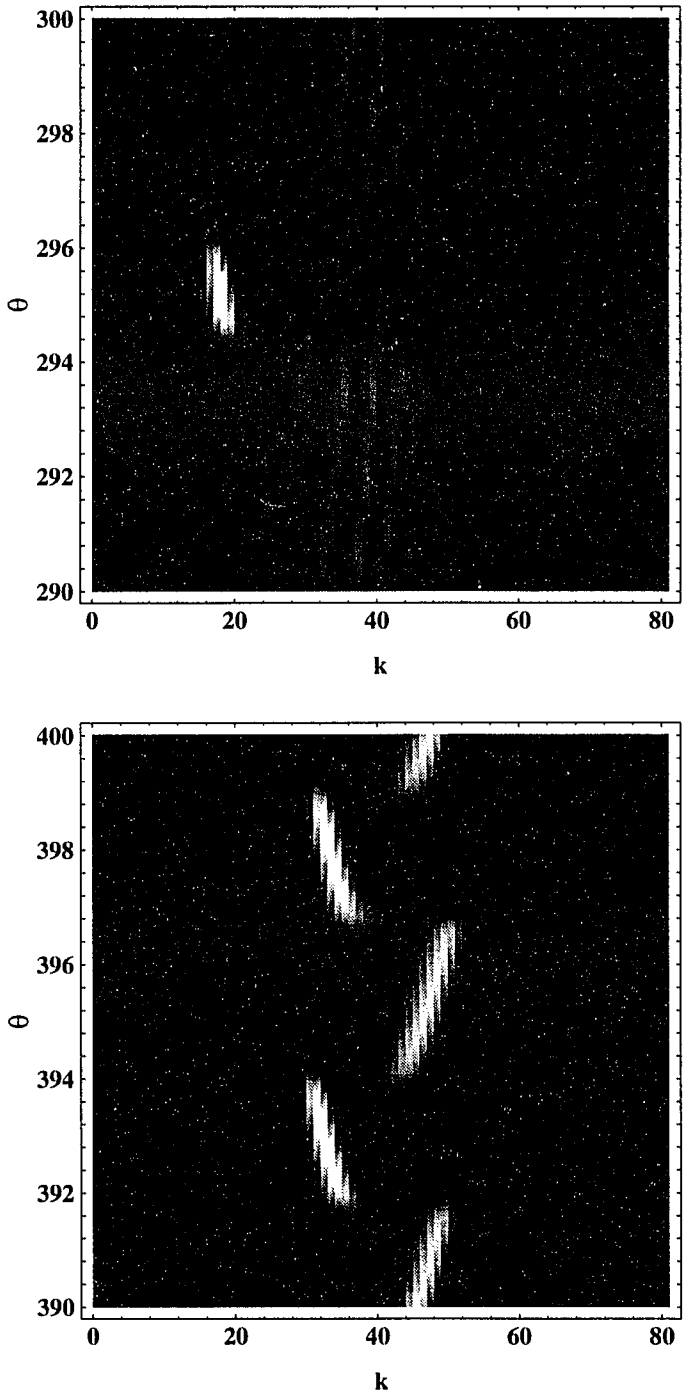

FIG. 2: Two magnified regions of Fig. 1 showing typical Quantum Island States in the quantum regime.

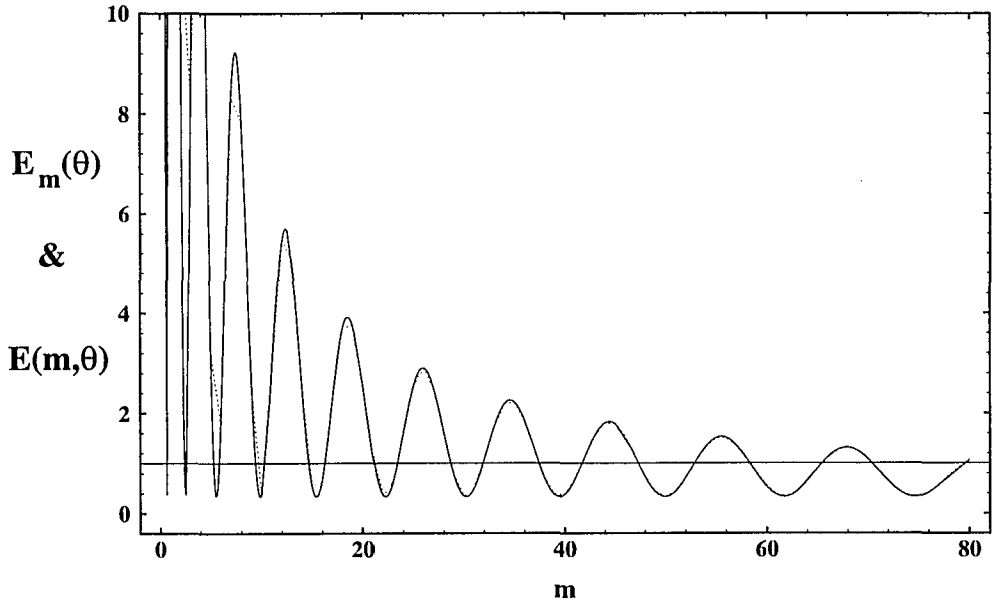

FIG. 3: The function $E(m,\theta)$ for $\theta = 40$, $N_{ex} = 100$ and $n_b = 0.5$ is depicted by a continuous line. The function $E_m(\theta)$ is shown by a dotted line. For these values of θ and N_{ex} they agree rather well. This agreement will disappear as θ increases.

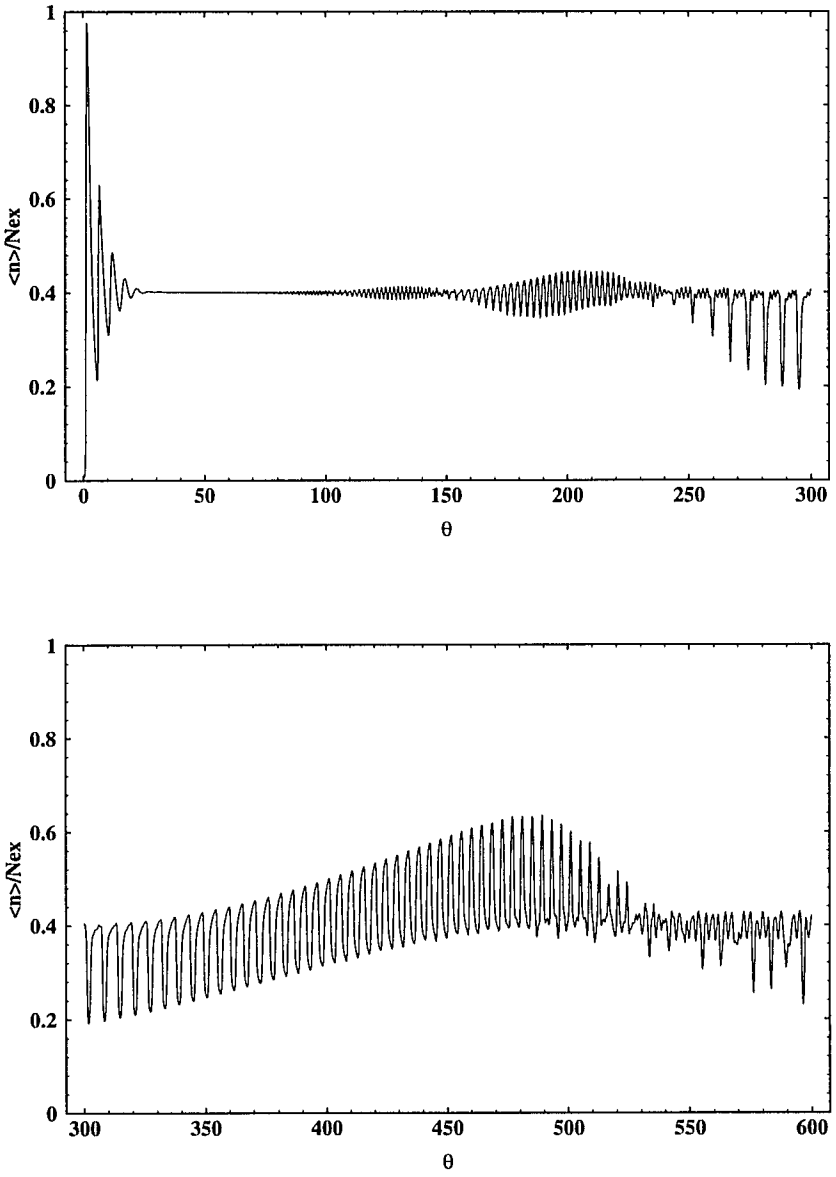

FIG. 4: Normalized average photon number $\langle n \rangle / N_{ex}$ as a function of θ calculated from the photon statistics depicted in Fig. 1.

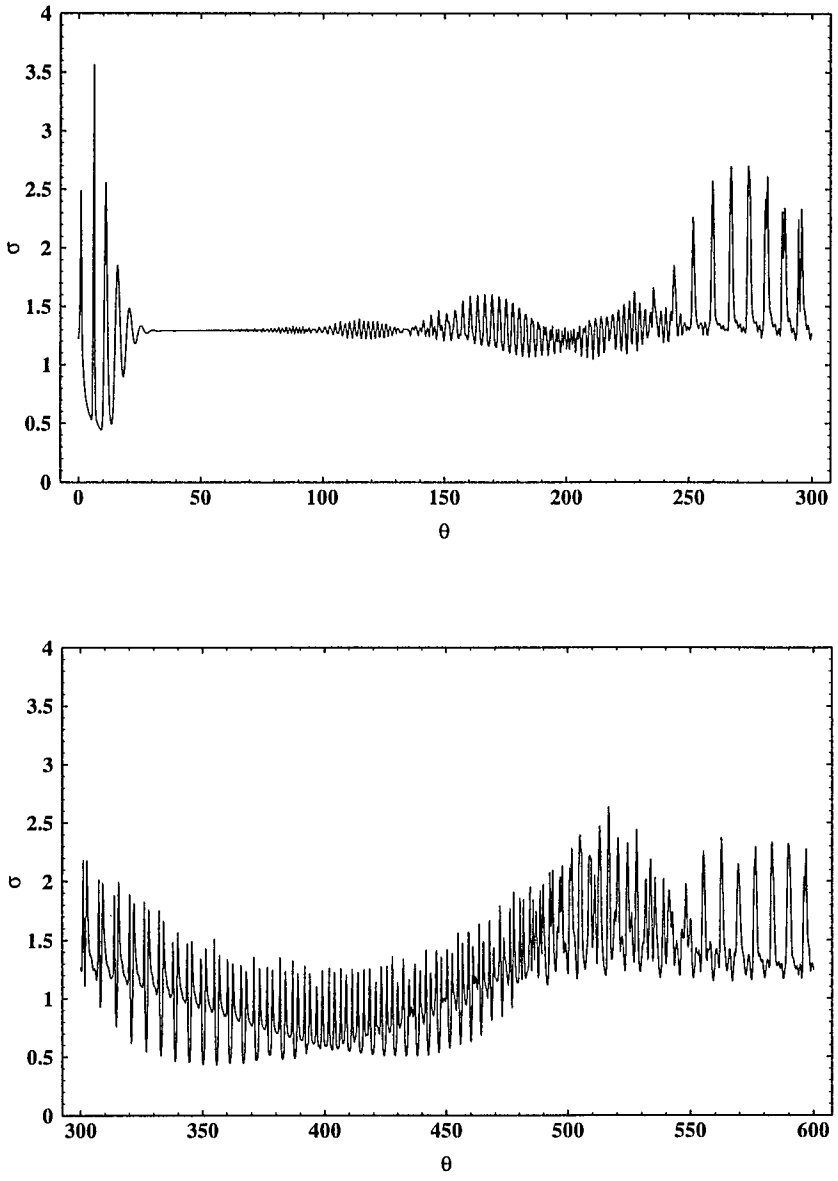

FIG. 5: Normalized standard deviation of the photon number distribution, $\sigma = [\,(\langle n^2\rangle - \langle n\rangle^2)/\langle n\rangle]^{1/2}$ as a function of θ, calculated from the photon statistics depicted in Fig. 1. Note that the photon statistics become sub-Poissonian at the values of the Quantum Island States in the region $300 < \theta < 500$.

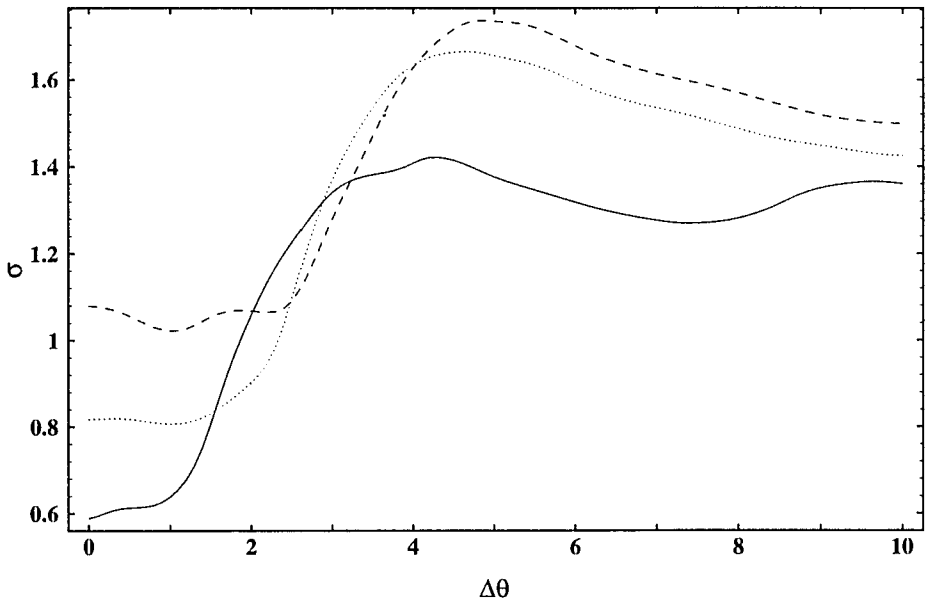

FIG. 6: Normalized standard deviation σ averaged over normal distributions of θ with various radii $\Delta\theta$ around a central value θ_0. At $N_{ex} = 40$, $n_b = 0.1$ continuous line represents the case of $\theta_0 = 135$ (location of a Quantum Island State), $\rho_{aa} = 1.0$. Dashed and dotted lines are at $\theta_0 = 102$ for $\rho_{aa} = 1.0$ and 0.85, respectively. The photon statistics rapidly switch from a sub-Poissonian to a super-Poissonian distribution as soon as fluctuation in θ (the absolute spread $2\ \Delta\theta$) exceeds the distance between the consecutive Quantum Island States.

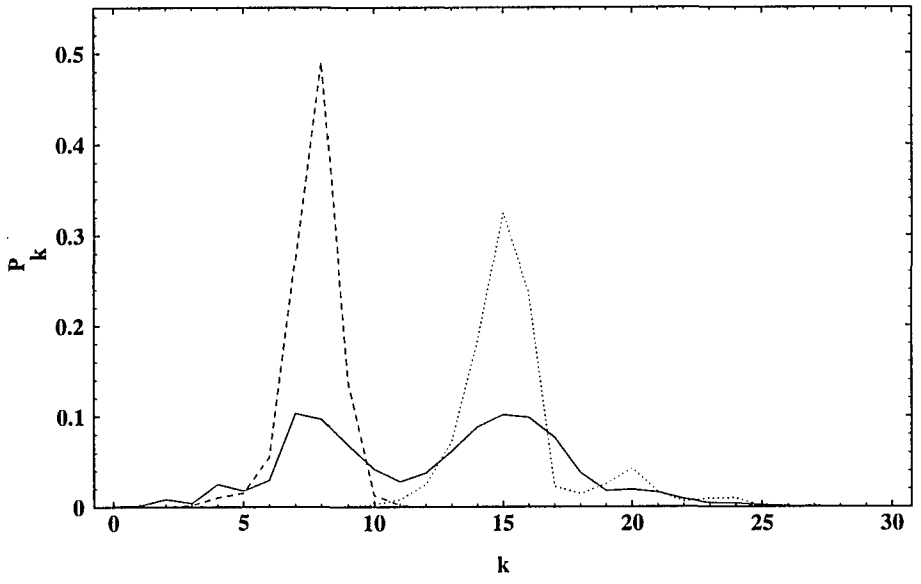

FIG. 7: Photon statistics for $\theta = 134$, $N_{ex} = 40$, $n_b = 0.1$ averaged over the fluctuating θ of radius $\Delta\theta = 3$ is depicted by a continuous line. Fluctuations overlap two (originally squeezed) Quantum Island States at $\theta = 132$ and $\theta = 135$ depicted by dashed and dotted lines, respectively. The resulting double-peaked structure shows bistability in the system induced by the fluctuations in the pump parameter θ.

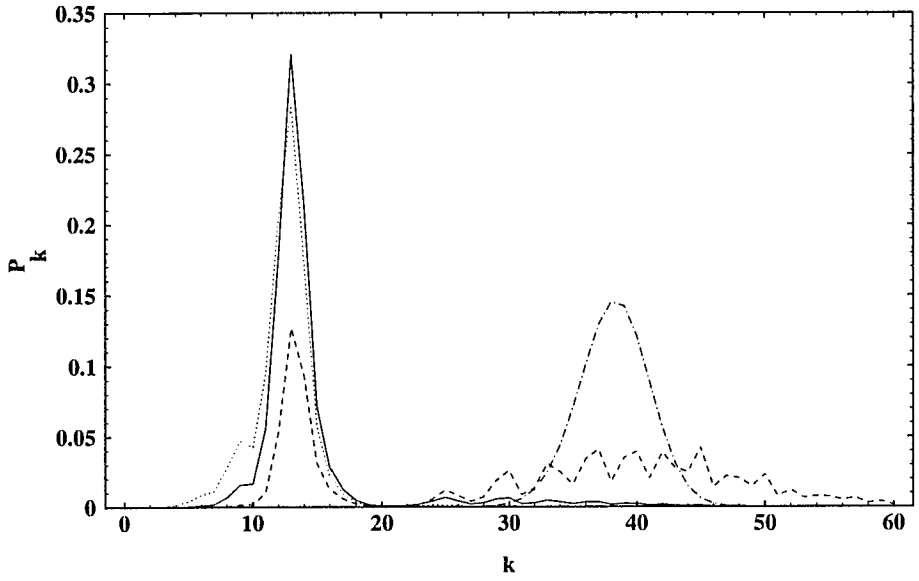

FIG. 8: Photon statistics for $\theta = 259.5$, $N_{ex} = 100$, $n_b = 0.5$. Dashed, continuous and dotted lines are for $\rho_{aa} = 1.0, 0.9$ and 0.8, resulting in standard deviations $\sigma = 2.57, 1.43$ and 0.70, respectively. The peaks are located in the same position, but the large-k regime of the photon statistics is suppressed by the injected absorption. As a comparison the photon statistics at $\theta = 9$ are depicted by a dot-dash line, for which the standard deviation $\sigma = 0.45$.

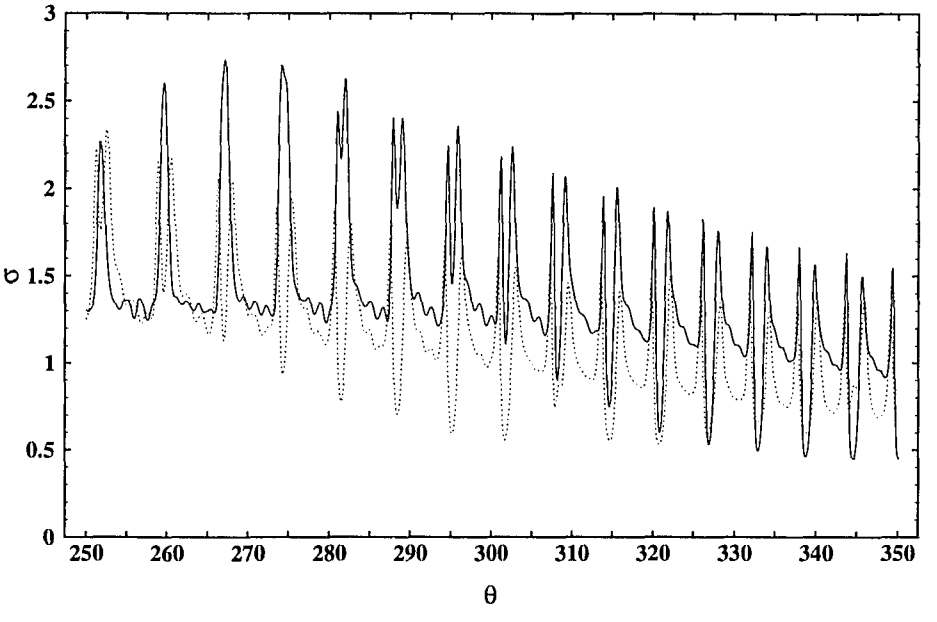

FIG. 9: Normalized standard deviation, σ as a function of θ at $N_{ex} = 100$, $n_b = 0.5$ and for $\rho_{aa} = 1.0$ and 0.9, depicted by continuous and dotted lines, respectively. Note that some of the Quantum Island States become sub-Poissonian due to the injected absorption, as well as the quantum region is shifted toward smaller θ's.

3.2 Pump-coupled Micromasers

3.2.1 Pump-coupled Micromasers: Coherent and Incoherent Coupling†

ABSTRACT

We consider two micromasers coupled via the pumping beam of initially excited two-level atoms traversing the two cavities in a sequence. The atoms pumping the second micromaser are, therefore, prepared by the first one, viz., the population of the two states and coherence between them. In order to see the effects of atomic coherence we contrast the two cases of incoherent and coherent coupling, i. e., when the sates of the atoms are measured between the cavities ("which path") and when not. Using an exact solution of the former setup we find that the second micromaser undergoes abrupt transitions between distinct phases of the photon statistics triggered, via injected absorption, by the first one. In the case of coherent coupling, we consider the exact master equation of the fields first and, after finding its nonlinear expansion, apply the standard technique of Fokker-Planck equation. Complementary to the nonlinear treatment, we also employ numerical simulations to investigate a different regime of the system. In addition to the incoherent effects, we find that atomic coherence significantly modifies the photon number and the number noise of the second field and, at the same time, establishes first order (phase locking) and second order correlations between the two separate fields at steady state. The time development exhibits abrupt jumps in the locked relative phase between zero and π accompanied by shut-offs of the second micromaser. These coherence effects are crucial in the region of small pumping parameters, in particular.

PACS Numbers: 42.50.Dv, 42.52+x

I. INTRODUCTION

Ten years of developments in Rydberg-state spectroscopy and in constructing superconducting microwave cavities of exceedingly high-Q factors made it possible to detect the single-atom single-mode coupling in the so-called micromaser experiments [1]. This system approaches the fundamental Jaynes-Cummings model [2] of the interaction of a two-level atom with a single mode of the quantized radiation field. It exhibits genuine quantum features that are normally masked by macroscopic environmental fluctuations. Some of the prominent examples are the collapse and revival of the Rabi nutation [3], generation of nonclassical photon statistics [1, 4-8], macroscopic quantum superpositions [9], and the quantum-nondemolition measurements of the photon number [10].

Coupling such quantum devices together enables us to to study quantum correlation effects between nonlocal radiation fields [11-14]. Various aspects of the complementarity principle and other fundamentals of quantum mechanics can be investigated in this system [15]. In the present paper, we consider two micromasers that are coupled sequentially by the pumping atomic beam according to Fig. 1. The final state of atoms is measured in a nonselective way by field ionization detectors. The usual micromaser-conditions are assumed: there is at most one atom in the cavities at a time and the cavity lifetime is much longer than the interaction time. The first micromaser affects the behavior of the second one via altering the state of the pumping atoms. It changes the population of the two atomic states and at the same time creates atomic coherence that, entering the second cavity, delivers information about the field in the first one. The latter effect is responsible for the quantum correlation building up between the two nonlocal fields. It has been shown in Ref. [13] that arbitrary entanglement of fields can be produced at steady state in the absence of cavity losses. In the case when dissipation is also present but does not exceed a certain threshold, pure entanglement can be generated in the transient regime [14]. Here we are going to show that correlation between the fields, though not pure entanglement, can survive at steady state even in the presence of large dissipation. As a result of this, the two fields are locked in phase and exhibit interference effects when superposed. We find that

the magnitude of the steady-state first order correlation is particularly large in the small pumping regime, switching its sign from positive to negative at a particular value of the pumping parameter. This corresponds to switching the relative phase of the fields from in-phase to out-of-phase. Similarly, the second order correlation exhibits positive and negative values as a function of the pumping parameter, i. e., the photons coming from the two different sources can be positively correlated and anticorrelated. Investigating the behavior of the second micromaser alone we find that atomic coherence contributes to the field and modifies the photon statistics. This manifests itself in significant changes in the expectation value of the photon number and its noise. These effects disappear as soon as we acquire information about the state of the atoms between the two cavities. This is reminiscent of gaining "which-path" information and consequently losing interference in Young's double-slit experiment.

In the next section we analyze this latter incoherent problem in detail by presenting a simple exact solution. Section III introduces the coherent problem by means of a master equation the nonlinear treatment of which is presented in Section IV. The results of numerical simulations are given in Section V. Section VI is devoted to discussions and summary.

II. INCOHERENT COUPLING: EXACT SOLUTION

The first micromaser modifies the behavior of the second one via altering the state of the atoms in the pumping beam emerging from the first cavity. There are two effects that we need to distinguish between. The incoherent effect, that is due to the change in the population of the two atomic levels and the coherent effect, that is a result of the coherence generated between them in addition. In the present section the former one is studied alone in order to contrast its characteristics with the latter one in the sections to follow.

Therefore, let us assume for now that we do acquire "which-path" information about the state of the atoms between the two cavities and, consequently, destroy the coherence between them. In this case, the second micromaser is driven by a beam of atoms in an

incoherent mixture of their upper and lower states generated by the first micromaser. It is shown in Refs. [8, 16] that the steady state photon statistics of the field for Poissonian pumping is given by

$$p_n'' = p_0'' \prod_{m=1}^{n} \left(\frac{\rho_{aa} \beta_m''^2 + \bar{n}_b'' m / N_{ex}''}{\rho_{bb} \beta_m''^2 + (\bar{n}_b'' + 1) m / N_{ex}''} \right) \quad . \tag{2.1}$$

Here, the double-primes denote quantities pertaining to the second micromaser. It has a cavity decay rate, γ'', average number of thermal photons, $\bar{n}_b''$, atom-field coupling constant, g'', interaction time, τ'' and atom injection rate, r. Thus, the average number of atoms in the second cavity during the photon lifetime is given by $N_{ex}'' \equiv r/\gamma''$, the pumping parameter by $\theta'' \equiv g'' \tau'' \sqrt{N_{ex}''}$ and $\beta_m'' \equiv sin\left(\theta'' \sqrt{m/N_{ex}''} \right)$. The single-primed version of the same parameters will refer to the first micromaser. We want to note here that N_{ex} and θ can be varied in the two micromasers separately via their free parameters of g, τ and γ, although r should be considered the same for both. The steady state population of the upper (lower) state of the incoming atoms, ρ_{aa} (ρ_{bb}), is prepared by the first micromaser which now we want to express as a function of its field.

It is easy to show via tracing over the field states that $\rho_{bb} = \left\langle sin^2\left(g' \tau' \sqrt{a_1 a_1^\dagger} \right) \right\rangle$, where a_1 ($a_1^\dagger$) is the annihilation (creation) operator of the first field. On the other hand, we also know that the equation of motion for the average photon number in the first micromaser in the case of Poissonian pumping is given by

$$\frac{d\langle n_1 \rangle}{dt} = r \left\langle sin^2\left(g' \tau' \sqrt{a_1 a_1^\dagger} \right) \right\rangle - \gamma' \left(\langle n_1 \rangle - \bar{n}_b' \right) \quad , \tag{2.2}$$

where $n_1 \equiv a_1^\dagger a_1$ is the number operator of the first field [1, 4]. Thus, the outgoing incoherent atomic population is very simply coupled to the average number of photons and at steady state it reads as $\rho_{bb} = \left(\langle n_1 \rangle - \bar{n}_b' \right) / N_{ex}'$. Applying this to Eq. (2.1) we readily find the steady state photon statistics of the second micromaser in the case of incoherent

coupling given by

$$p''_n = p''_0 \prod_{m=1}^{n} \left(\frac{\beta''^{\,2}_m \left(N'_{ex} - \left(\langle n_1 \rangle - \bar{n}'_b \right) \right) / N'_{ex} + \bar{n}''_b m / N''_{ex}}{\beta''^{\,2}_m \left(\langle n_1 \rangle - \bar{n}'_b \right) / N'_{ex} + (\bar{n}''_b + 1) m / N''_{ex}} \right) \quad . \tag{2.3}$$

Studying this result the following main characteristics of the incoherent problem have been found. The photon statistics consist of the same structure of distinct "phases" as in the case of an independent micromaser pumped by excited atoms only (see Fig. 2 and Ref. [8]), except that the occupation of these phases is governed by the injected absorption (see Figs. 3 (a) and (b)). In the cases when ρ_{aa} is close to *1* (i. e. $\langle n_1 \rangle$ is small) the photon statistics can approximately occupy the same phases as those of an independent micromaser, while its being significantly less than *1* (i. e. $\langle n_1 \rangle$ is large) forces the system toward lower order phases in the small photon number region (if $\rho_{aa} << 1$, i. e. $\langle n_1 \rangle \cong N'_{ex}$, then close to vacuum). This makes the first micromaser play the role of a *switch* that controls the occupation of and the transitions between the different phases (and vacuum) of the second field via varying the incoherent mixture of the two atomic states, ρ_{aa} and ρ_{bb}, entering the second cavity. In our first example we utilize the regular jumps between the phases in the photon statistics of the first micromaser to switch the second one. The average photon number, $\langle n_1 \rangle$, either abruptly jumps to a higher order phase accompanied by a large peak in the noise or smoothly evolves along a phase with decreasing noise (see dot-dashed lines in Figs. 4 (a) and (b)). After the short first peak at $\theta \cong 1$ corresponding to the threshold established by the cavity losses the average photon number, $\langle n_2 \rangle$, experiences several abrupt jumps (both upward and downward) at those points where $\langle n_1 \rangle$ passes through a value corresponding to a critical absorption (see solid line in Fig. 4 (a)). The smooth evolution of $\langle n_1 \rangle$ through such a point downward turns a new phase on, while the abrupt jump upward turns an actual phase off in the second micromaser. Hence, the occupation of the phases exhibits a typical threshold-like behavior established by the extra loss of injected absorption that is controlled by $\langle n_1 \rangle$ of the first micromaser. Due to the oscillations in $\langle n_1 \rangle$ the second micromaser experiences several

thresholds. In our example depicted in Figs. 3 and 4 there are three "true" thresholds (apart from the one at $\theta \cong 1$) around $\theta = 3.5, 7.8$ and 12.1 where the first phase builds up from vacuum, and several others for example at $\theta = 10.5, 14.2, 18.2$ and 22.2, or at $\theta = 25.2$ and 29 where the second phase builds up from the first one, or the third phase builds up from the second one, respectively. The transitions are also sharp when jumping from a higher order phase to a lower one, for example at $\theta = 6.2, 11.5, 16.9$ from the first phase to vacuum, at $\theta = 11, 16.2, 21.8$ from the second to the first and at $\theta = 25.2$ from the third to the second phase. All these "turn-ons" and "turn-offs" are accompanied by sharp noise-peaks in σ_2 (see Fig. 4 (b)) that proves that the system undergoes phase transitions at these points in both the upward and downward directions. The first two at $\theta = 1$ and 3.5 are continuous while all the others are first-order phase transitions similar to those of an independent micromaser but in this case triggered by the injected absorption modulated by the first micromaser. Thus, every second of them that corresponds to a "turn-off" point coincides with one in the first micromaser field.

Besides utilizing the regular phase-jumps in the average photon number of the first micromaser similar switching effects can be realized using any regimes of $\langle n_1 \rangle$ where the injected absorption experiences significant drops. Two examples for this are the trapping and the quantum island states [8] as depicted in Figs. 5 and 6 showing jumps between the phases similar to the regular case above.

It should be emphasized here that this abrupt switching behavior is a result of the distinct structure of phases in the micromaser photon statistics [8]. Small changes in the injected absorption do not significantly affect the system residing in a certain phase until it exceeds the threshold of the next phase making the field undergo an abrupt phase transition. Another interesting effect to note is that several sub-Poissonian regions of the photon statistics are not significantly sensitive to atomic velocity fluctuations. As it is apparent in Fig. 3 some of the distinct ridges, or islands of the first phase are not smeared out even if we have some fluctuations in θ. For example the structure around $\theta = 20$ withstands a fluctuation as high as 10% and still remains sub-Poissonian. The reason for

this is simple. The photon statistics are forced by the injected absorption to occupy the various phases in their low photon number regions. The phases, following the $\theta \propto 1/\sqrt{k}$ dependence (see Ref. [8]), are much steeper here than in those photon number regions where an independent micromaser normally operates. This implies an unusually strong insensitivity of the photon statistics against θ - fluctuations.

The main features of the system, for example the series of phase transitions, will continue to be a strong effect in the coherent problem discussed in the sections to follow, but as we will see significant modifications will occur as results of the atomic coherence generated by the first micromaser.

III. COHERENT COUPLING: THE EXACT MASTER EQUATION

In Section II we have seen how the first micromaser affected the behavior of the second one via incoherently altering the population of the atomic levels. The rest of the paper considers the coherent problem where we also allow for atomic coherence to be transferred from the first to the second field (i. e., we do not measure the state of the atoms between the cavities) and study its effects as compared to the incoherent case. In this and the next section we deal with the master equation for the two-field interaction-picture density operator, ρ, that can be found by finding the coarse-grained time derivative first. The density operator, $\rho^{(k)}$, after the k^{th} atom passed through the cavities can be calculated as

$$\rho^{(k)} = F\rho^{(k-1)} \equiv Tr_{atom}[U''U'\rho^{(k-1)}\rho_{atom}U'^{\dagger}U''^{\dagger}] \quad , \tag{3.1}$$

where U' and U'' are the time evolution operators for the Jaynes-Cummings model in the first and second cavities, respectively, ρ_{atom} is the atomic density operator (initially excited atom) and we trace over the atomic states to find the reduced operator for the fields. The coarse-grained time derivative can be obtained by multiplying the change of the density matrix due to one atom, $(F\text{-}I)\rho$, where I is the identity operator, by the atomic injection rate, r. Adding the Liouvillian terms, $\mathcal{L}'\rho$ and $\mathcal{L}''\rho$, to account for dissipation in both

cavities we readily obtain the exact master equation given by

$$\frac{d\rho}{dt} = r(F-1)\rho + \mathcal{L}'\rho + \mathcal{L}''\rho \quad . \tag{3.2}$$

Here, the Liouvillian, $\mathcal{L}'\rho$, for the first cavity reads as

$$\mathcal{L}'\rho \equiv \left(\frac{\gamma'}{2}\right)\left[(\bar{n}_b'+1)\left(2a_1\rho a_1^\dagger - a_1^\dagger a_1\rho - \rho a_1^\dagger a_1\right) + \bar{n}_b'\left(2a_1^\dagger\rho a_1 - a_1 a_1^\dagger\rho - \rho a_1 a_1^\dagger\right)\right] \quad , \tag{3.3}$$

and similarly for the second cavity, $\mathcal{L}''\rho$, with γ'', $\bar{n}_b''$, and a_2 ($a_2^\dagger$). In the number representation we can write the master equation in the form given by

$$\begin{aligned}\frac{d}{dt}\rho_{\substack{n_1,m_1\\n_2,m_2}} = &-\frac{1}{2}\mu_{\substack{n_1,m_1\\n_2,m_2}}\rho_{\substack{n_1,m_1\\n_2,m_2}} + A_{\substack{n_1,m_1\\n_2,m_2}}\rho_{\substack{n_1,m_1-1\\n_2-1,m_2}} + A_{\substack{m_1,n_1\\m_2,n_2}}\rho_{\substack{n_1-1,m_1\\n_2,m_2-1}} + \\ &+\Im'_{\substack{n_1,m_1\\n_2,m_2}} - \Im'_{\substack{n_1+1,m_1+1\\n_2,m_2}} + \Im''_{\substack{n_1,m_1\\n_2,m_2}} - \Im''_{\substack{n_1,m_1\\n_2+1,m_2+1}} \quad ,\end{aligned} \tag{3.4}$$

where $n_1, m_1, n_2, m_2 \geq 0$, and

$$\begin{aligned}\mu_{\substack{n_1,m_1\\n_2,m_2}} = &\ 2r\left(1-\alpha'_{n_1+1}\alpha'_{m_1+1}C''_{n_2+1,m_2+1} - \beta'_{n_1+1}\beta'_{m_1+1}C''_{n_2,m_2}\right) + \\ &+\gamma'\left[(\bar{n}_b'+1)\left(n_1+m_1-2\sqrt{n_1m_1}\right) + \bar{n}_b'\left(n_1+m_1+2-2\sqrt{(n_1+1)(m_1+1)}\right)\right] + \\ &+\gamma''\left[(\bar{n}_b''+1)\left(n_2+m_2-2\sqrt{n_2m_2}\right) + \bar{n}_b''\left(n_2+m_2+2-2\sqrt{(n_2+1)(m_2+1)}\right)\right] \quad ,\end{aligned} \tag{3.5}$$

and

$$A_{\substack{n_1,m_1\\n_2,m_2}} = r\alpha'_{n_1+1}\beta'_{m_1}S''_{n_2,m_2} \quad , \tag{3.6}$$

together with

$$\Im'_{\substack{n_1,m_1\\n_2,m_2}} = \left(r\beta'_{n_1}\beta'_{m_1}C''_{n_2,m_2} + \gamma'\bar{n}'_b\sqrt{n_1m_1}\right)\rho_{\substack{n_1-1,m_1-1\\n_2,m_2}} - \gamma'\left(\bar{n}'_b+1\right)\sqrt{n_1m_1}\,\rho_{\substack{n_1,m_1\\n_2,m_2}} \quad , \tag{3.7}$$

and

$$\Im''_{\substack{n_1,m_1\\n_2,m_2}} = \left(r\alpha'_{n_1+1}\alpha'_{m_1+1}\beta''_{n_2}\beta''_{m_2} + \gamma'\bar{n}''_b\sqrt{n_2m_2}\right)\rho_{\substack{n_1,m_1\\n_2-1,m_2-1}} - \gamma''\left(\bar{n}''_b+1\right)\sqrt{n_2m_2}\,\rho_{\substack{n_1,m_1\\n_2,m_2}} -$$

$$-r\beta'_{n_1}\beta'_{m_1}\beta''_{n_2}\beta''_{m_2}\rho_{\substack{n_1-1,m_1-1\\n_2,m_2}} + r\alpha'_{n_1+1}\beta'_{m_1}\alpha''_{n_2}\beta''_{m_2}\rho_{\substack{n_1,m_1-1\\n_2-1,m_2}} + r\beta'_{n_1}\alpha'_{m_1+1}\beta''_{n_2}\alpha''_{m_2}\rho_{\substack{n_1-1,m_1\\n_2,m_2-1}} \quad , \tag{3.8}$$

with $\alpha'_n = cos\left(\theta'\sqrt{n/N'_{ex}}\right)$, $\beta'_n = sin\left(\theta'\sqrt{n/N'_{ex}}\right)$ for the first and α''_n, β''_n for the second micromaser, and $S''_{n,m} = sin\left(\theta''\left(\sqrt{n/N''_{ex}} - \sqrt{m/N''_{ex}}\right)\right)$, $C''_{n,m} = cos\left(\theta''\left(\sqrt{n/N''_{ex}} - \sqrt{m/N''_{ex}}\right)\right)$. This master equation reduces to the detailed balance of the photon statistics given by

$$\frac{d}{dt}\rho_{\substack{n_1,n_1\\n_2,n_2}} = \Im'_{\substack{n_1,n_1\\n_2,n_2}} - \Im'_{\substack{n_1+1,n_1+1\\n_2,n_2}} + \Im''_{\substack{n_1,n_1\\n_2,n_2}} - \Im''_{\substack{n_1,n_1\\n_2+1,n_2+1}} \quad . \tag{3.9}$$

Summing over n_2, that is averaging the second micromaser out, eliminates the third and fourth terms on the right hand side resulting in

$$\dot{p}'_{n_1} = \Im'_{n_1} - \Im'_{n_1+1} \quad , \tag{3.10}$$

where we use $p'_{n_1} \equiv \rho'_{n_1,n_1} = \sum_{n_2} \rho_{\substack{n_1,n_1\\n_2,n_2}}$ and $\Im'_{n_1} \equiv \sum_{n_2} \Im'_{\substack{n_1,n_1\\n_2,n_2}}$. Thus, we reobtain the detailed balance equation of the independent first micromaser that provides us with its well-known steady-state photon statistics after solving $\Im'_{n_1} = 0$ for p'_{n_1} [1, 4, 8].

On the other hand, the sum of Eq. (3.9) over n_1 averages the first micromaser out eliminating the first two terms in the equation and yields

$$\dot{p}''_{n_2} = \Im''_{n_1,n_2} - \Im''_{n_1,n_2+1} \quad , \tag{3.11}$$

where $p''_{n_2} \equiv \rho''_{n_2,n_2} = \sum_{n_1} \rho_{\substack{n_1,n_1 \\ n_2,n_2}}$ and $\Im''_{n_1,n_2} \equiv \sum_{n_1} \Im''_{\substack{n_1,n_1 \\ n_2,n_2}}$. Hence, we need to solve $\Im''_{n_1,n_2} = 0$ for the steady state that explicitly reads as

$$N''_{ex}\beta''^{2}_{n_2} \sum_{n_1} \left(\alpha'^{2}_{n_1+1} \rho_{\substack{n_1,n_1 \\ n_2-1,n_2-1}} - \beta'^{2}_{n_1+1} \rho_{\substack{n_1,n_1 \\ n_2,n_2}} \right) + 2N''_{ex}\alpha''_{n_2}\beta''_{n_2} \sum_{n_1} \alpha'_{n_1+1}\beta'_{n_1} \rho_{\substack{n_1-1,n_1 \\ n_2,n_2-1}} +$$

$$+\bar{n}''_b n_2 \rho''_{n_2-1,n_2-1} - (\bar{n}''_b + 1) n_2 \rho''_{n_2,n_2} = 0 \quad , \tag{3.12}$$

where we used the symmetry of the density matrix, $\rho_{\substack{n_1,m_1 \\ n_2,m_2}} = \rho_{\substack{m_1,n_1 \\ m_2,n_2}}$. It is apparent from Eq. (3.12) that the off-diagonal coherence terms play an essential role in the photon statistics (see the second term). This is generally true: one can find that the field-density matrix consists of non-zero off-diagonal terms that are coupled to the two adjacent (off-) diagonals. This makes it difficult to solve for the photon statistics of the second field even numerically. On the other hand, the off-diagonal coupling causing the trouble here is responsible for the quantum correlation building up between the two fields and the inseparability of the density matrix -- exactly what we are interested in. Averaging (tracing) over either of the two micromasers would result in a diagonal density matrix and the correlation would be lost. It can be shown that we reobtain the result of Section II for the incoherent problem when assuming zero off-diagonals and separable density matrix, $\rho_{\substack{n_1,m_1 \\ n_2,m_2}} = \rho'_{n_1,m_1}\rho''_{n_2,m_2}$, in Eq. (3.12). Here, ρ'_{n_1,m_1} is the first and ρ''_{n_2,m_2} is the second field-density matrix. In this case we obtain

$$\left[N''_{ex}\beta''^{2}_{n_2} \left\langle \alpha'^{2}_{n_1+1} \right\rangle + \bar{n}''_b n_2 \right] p''_{n_2-1} - \left[N''_{ex}\beta''^{2}_{n_2} \left\langle \beta'^{2}_{n_1+1} \right\rangle + (\bar{n}''_b + 1) n_2 \right] p''_{n_2} = 0 \quad . \tag{3.13}$$

After substituting $\left(\langle n_1 \rangle - \bar{n}'_b \right) / N'_{ex}$ for $\left\langle \beta'^{2}_{n_1+1} \right\rangle$ (and similarly $\left\langle \alpha'^{2}_{n_1+1} \right\rangle = 1 - \left\langle \beta'^{2}_{n_1+1} \right\rangle$) the incoherent photon statistics given by Eq. (2.3) in Section II is reconstructed.

In the two sections to follow we are going to attempt to get around this problem in two different ways. First, we are going to consider a nonlinear expansion of the master equation and apply the standard techniques of Fokker-Planck equations. In Section V, we present the results of numerical simulations of this system.

IV. NONLINEAR MASTER EQUATION AND THE FOKKER-PLANCK EQUATION

IV.1 Finding the Fokker-Planck equation

We obtain the nonlinear master equation by expanding Eq. (3.2) to the fourth order of the coupling constant, g [11]. Assuming that the two cavities are identical, i. e., $g \equiv g' = g''$, $\tau \equiv \tau' = \tau''$, $\gamma \equiv \gamma' = \gamma''$, and therefore $N_{ex} \equiv N'_{ex} = N''_{ex}$ and $\theta \equiv \theta' = \theta''$, the equation in the operator form reads as

$$\frac{1}{\gamma}\frac{d\rho}{dt} = -\frac{\theta^2}{2}\left\{\rho\left(a_1a_1^\dagger + a_2a_2^\dagger + 2a_1a_2^\dagger\right)\right\} +$$

$$+\frac{\theta^4}{4!N_{ex}}\left\{\rho\left[\left(a_1a_1^\dagger + a_2a_2^\dagger\right)^2 + 4a_1a_1^\dagger a_2a_2^\dagger + 4\left(a_1a_1^\dagger + a_2^\dagger a_2\right)a_1a_2^\dagger\right] +\right.$$

$$+3\left(a_1a_1^\dagger + a_2a_2^\dagger + 2a_1^\dagger a_2\right)\rho\left(a_1a_1^\dagger + a_2a_2^\dagger + 2a_1a_2^\dagger\right) -$$

$$\left. -4\left(a_1^\dagger + a_2^\dagger\right)\rho\left[a_1a_1^\dagger\left(a_1 + 3a_2\right) + \left(3a_1 + a_2\right)a_2a_2^\dagger\right]\right\} +$$

$$+\frac{1}{2}\left\{\left(\bar{n}_b' + 1\right)\left(a_1\rho a_1^\dagger - a_1^\dagger a_1\rho\right) + \bar{n}_b'\left(a_1^\dagger\rho a_1 - a_1a_1^\dagger\rho\right) +\right.$$

$$\left. +\left(\bar{n}_b'' + 1\right)\left(a_2\rho a_2^\dagger - a_2^\dagger a_2\rho\right) + \bar{n}_b''\left(a_2^\dagger\rho a_2 - a_2a_2^\dagger\rho\right)\right\} \quad + \quad H.c. \quad , \qquad (4.1)$$

where *H. c.* stands for Hermitian conjugate. This equation could be directly used, e. g.,

to calculate the equations of motion of quantities such as the photon number expectation values in the first and second cavities, $\langle n_1 \rangle$ and $\langle n_2 \rangle$, or the first and second order correlations between the fields, $\langle n_{12} \rangle \equiv a_1 a_2^\dagger + a_1^\dagger a_2$ and $\langle n_1 n_2 \rangle$, respectively. Here, we apply another standard technique instead that, besides calculating the above quantities, can also be employed to find the noise characteristics of the system. We transform the above nonlinear master equation into a c-number Fokker-Planck equation for the Glauber-Sudarshan P representation of the field-density matrix. Finding the drift and diffusion coefficients of the Fokker-Planck equation the first and second moments of the P distribution, i. e., the average values of the field amplitudes and their fluctuations, can be calculated. Substituting the Glauber-Sudarshan representation form of the field-density matrix,

$$\rho(t) = \int d^2\alpha_1 \, d^2\alpha_2 \; P\left(\alpha_1, \alpha_1^*, \alpha_2, \alpha_2^*, t\right) \left|\alpha_1, \alpha_2\right\rangle \left\langle \alpha_1, \alpha_2\right| \quad , \tag{4.2}$$

into Eq. (4.1) we arrive at the following equation of motion for $P\left(\alpha_1, \alpha_1^*, \alpha_2, \alpha_2^*, t\right)$

$$\begin{aligned} \frac{1}{\gamma}\frac{\partial P}{\partial t} = \Big\{ & -\partial_{\alpha_1} d_{\alpha_1} - \partial_{\alpha_1^*} d_{\alpha_1^*} + \partial^2_{\alpha_1\alpha_1} D_{\alpha_1\alpha_1} + \partial^2_{\alpha_1^*\alpha_1^*} D_{\alpha_1^*\alpha_1^*} + \partial^2_{\alpha_1\alpha_1^*} D_{\alpha_1\alpha_1^*} - \\ & -\partial_{\alpha_2} d_{\alpha_2} - \partial_{\alpha_2^*} d_{\alpha_2^*} + \partial^2_{\alpha_2\alpha_2} D_{\alpha_2\alpha_2} + \partial^2_{\alpha_2^*\alpha_2^*} D_{\alpha_2^*\alpha_2^*} + \partial^2_{\alpha_2\alpha_2^*} D_{\alpha_2\alpha_2^*} + \\ & + \partial^2_{\alpha_1\alpha_2} D_{\alpha_1\alpha_2} + \partial^2_{\alpha_1^*\alpha_2^*} D_{\alpha_1^*\alpha_2^*} + \partial^2_{\alpha_1\alpha_2^*} D_{\alpha_1\alpha_2^*} + \partial^2_{\alpha_1^*\alpha_2} D_{\alpha_1^*\alpha_2} \Big\} P \quad + \quad \ldots \quad , \end{aligned} \tag{4.3}$$

where $P = P\left(\alpha_1, \alpha_1^*, \alpha_2, \alpha_2^*, t\right)$. We use the notation, $\partial_{\alpha_i} = \dfrac{\partial}{\partial \alpha_i}$ and $\partial^2_{\alpha_i\alpha_j} = \dfrac{\partial^2}{\partial\alpha_i \partial\alpha_j}$, for the derivatives while the higher order terms, $\partial^3_{\alpha_i\alpha_j\alpha_k}$, $i, j, k = 1, 2$, are omitted. The drift coefficients, lower case d, and the diffusion coefficients, upper case D, are given in the Appendix. Introducing the intensities, I_1 and I_2, and phases, φ_1 and φ_2, of the two fields as $\alpha_1 \equiv \sqrt{I_1} e^{i\varphi_1}$ and $\alpha_2 \equiv \sqrt{I_2} e^{i\varphi_2}$ we can transform the Fokker-Planck equation into polar form, where P is now considered as a function of I_1, I_2, and φ_1, φ_2. In this way

the Fokker-Planck equation becomes

$$\frac{1}{\gamma}\frac{\partial P}{\partial t}=\{-\partial_{I_1}d_{I_1}-\partial_{\varphi_1}d_{\varphi_1}+\partial^2_{I_1I_1}D_{I_1I_1}+\partial^2_{\varphi_1\varphi_1}D_{\varphi_1\varphi_1}+\partial^2_{I_1\varphi_1}D_{I_1\varphi_1}-$$

$$-\partial_{I_2}d_{I_2}-\partial_{\varphi_2}d_{\varphi_2}+\partial^2_{I_2I_2}D_{I_2I_2}+\partial^2_{\varphi_2\varphi_2}D_{\varphi_2\varphi_2}+\partial^2_{I_2\varphi_2}D_{I_2\varphi_2}+$$

$$+\partial^2_{I_1I_2}D_{I_1I_2}+\partial^2_{\varphi_1\varphi_2}D_{\varphi_1\varphi_2}+\partial^2_{I_1\varphi_2}D_{I_1\varphi_2}+\partial^2_{I_2\varphi_1}D_{I_2\varphi_1}\}P \quad , \tag{4.4}$$

where $P=P(I_1,\varphi_1,I_2,\varphi_2,t)$. The corresponding drift and diffusion terms are as follows

$$d_{I_1}=\bar{n}_b'+\theta^2+I_1(\theta^2-1)-\frac{\theta^4}{3N_{ex}}(I_1^2+3I_1+1) \quad , \tag{4.5}$$

$$d_{I_2}=\bar{n}_b''+\theta^2+I_2(\theta^2-1)-\frac{\theta^4}{3N_{ex}}[I_2^2+3I_2+1+3(I_1+1)(2I_2+1)]+$$

$$+2\cos(\varphi_1-\varphi_2)\sqrt{I_1I_2}\left[\theta^2-\frac{\theta^4}{3N_{ex}}\left(2I_1+2I_2+\frac{11}{2}\right)\right] \quad , \tag{4.6}$$

$$d_{\varphi_1}=0 \quad , \tag{4.7}$$

$$d_{\varphi_2}=\sin(\varphi_1-\varphi_2)\sqrt{\frac{I_1}{I_2}}\left[\theta^2-\frac{\theta^4}{3N_{ex}}\left(2I_1+\frac{7}{2}\right)\right] \quad , \tag{4.8}$$

$$D_{I_1I_1}=I_1\left[\bar{n}_b'+\theta^2-\frac{\theta^4}{3N_{ex}}(2I_1+1)\right] \quad , \tag{4.9}$$

$$D_{I_2I_2}=I_2\left[\bar{n}_b''+\theta^2-\frac{\theta^4}{3N_{ex}}(2I_2+1+3I_1+3+4\cos(\varphi_1-\varphi_2)\sqrt{I_1I_2})\right] \quad , \tag{4.10}$$

$$D_{\varphi_1\varphi_1} = \frac{1}{4I_1}\left[\bar{n}_b' + \theta^2 - \frac{\theta^4}{3N_{ex}}\left(\frac{I_1}{2} + 1\right)\right] \quad , \tag{4.11}$$

$$D_{\varphi_2\varphi_2} = \frac{1}{4I_2}\left[\bar{n}_b'' + \theta^2 - \frac{\theta^4}{3N_{ex}}\left(\frac{I_2}{2} + 1 + 3I_1 + 3 + 2\cos(\varphi_1 - \varphi_2)\sqrt{I_1 I_2}\right)\right] \quad , \tag{4.12}$$

$$D_{I_1 I_2} = -\frac{3\theta^4}{N_{ex}} I_1 I_2 + 2\cos(\varphi_1 - \varphi_2)\sqrt{I_1 I_2}\left[\theta^2 - \frac{\theta^4}{3N_{ex}}\left(4I_1 + 2I_2 + \frac{5}{2}\right)\right] \quad , \tag{4.13}$$

$$D_{\varphi_1\varphi_2} = \frac{\cos(\varphi_1 - \varphi_2)}{2\sqrt{I_1 I_2}}\left[\theta^2 - \frac{\theta^4}{3N_{ex}}\left(I_1 + \frac{5}{2}\right)\right] \quad , \tag{4.14}$$

$$D_{I_1\varphi_1} = 0 \quad , \tag{4.15}$$

$$D_{I_2\varphi_2} = -\sin(\varphi_1 - \varphi_2)\sqrt{I_1 I_2}\,\frac{\theta^4}{3N_{ex}} \quad , \tag{4.16}$$

$$D_{I_1\varphi_2} = \sin(\varphi_1 - \varphi_2)\sqrt{\frac{I_1}{I_2}}\left[\theta^2 - \frac{\theta^4}{3N_{ex}}\left(4I_1 + \frac{5}{2}\right)\right] \quad , \tag{4.17}$$

$$D_{I_2\varphi_1} = -\sin(\varphi_1 - \varphi_2)\sqrt{\frac{I_2}{I_1}}\left[\theta^2 - \frac{\theta^4}{3N_{ex}}\left(I_1 + 2I_2 + \frac{5}{2}\right)\right] \quad . \tag{4.18}$$

It is advantageous to introduce the new variables, $\varphi \equiv \varphi_1 - \varphi_2$ and $\mu \equiv \varphi_1 + \varphi_2$, since the above coefficients depend only on the relative phase, φ, of the two fields. This should not be surprising since one can intuitively expect that it is the phase difference between the fields that is relevant and not the phases of the fields separately. In this case the drift terms of the newly introduced quantities can be written as $d_\varphi = d_{\varphi_1} - d_{\varphi_2}$ and $d_\mu = d_{\varphi_1} + d_{\varphi_2}$, while their diffusion coefficients are $D_{\varphi\varphi} = D_{\varphi_1\varphi_1} + D_{\varphi_2\varphi_2} - D_{\varphi_1\varphi_2}$, $D_{\mu\mu} = D_{\varphi_1\varphi_1} + D_{\varphi_2\varphi_2} + D_{\varphi_1\varphi_2}$, and $D_{\varphi\mu} = 2\left(D_{\varphi_1\varphi_1} - D_{\varphi_2\varphi_2}\right)$, together with $D_{I_1\varphi} = D_{I_1\varphi_1} - D_{I_1\varphi_2}$, $D_{I_2\varphi} = D_{I_2\varphi_1} - D_{I_2\varphi_2}$, $D_{I_1\mu} = D_{I_1\varphi_1} + D_{I_1\varphi_2}$, and $D_{I_2\mu} = D_{I_2\varphi_1} + D_{I_2\varphi_2}$. This is the Fokker-Planck

equation that we wish to investigate.

IV.2 Applying the Fokker-Planck equation

Having derived the Fokker-Planck equation, we are going to use its coefficients to calculate the time-dependent and steady-state properties of the two fields. It can be shown in general that

$$\frac{1}{\gamma}\frac{d}{dt}\langle x\rangle = \langle d_x\rangle \quad , \tag{4.19}$$

$$\frac{1}{\gamma}\frac{d}{dt}\langle \delta x \delta y\rangle = \langle d_x \delta y\rangle + \langle d_y \delta x\rangle + \langle 1+\delta_{xy}\rangle\langle D_{xy}\rangle \quad , \tag{4.20}$$

where x and y are any of the four dynamical variables of the equation, I_1, I_2, φ, and μ, $\delta x = x - \langle x\rangle$, and δ_{xy} is either *1* or *0* depending whether the two variables x and y are the same or different, respectively. After expanding the drift coefficients, d_x, in terms of δx around the average, $\langle x\rangle$, Eq. (4.19) becomes

$$\frac{1}{\gamma}\frac{d}{dt}\langle x\rangle \cong d_x\big|_{\langle all\rangle} \quad , \tag{4.21}$$

where the drift coefficient, d_x, is taken at the average values of all the dynamical variables on the right hand side. Similarly, Eq. (4.20) reads as

$$\begin{aligned}\frac{1}{\gamma}\frac{d}{dt}\langle \delta x \delta y\rangle \cong\ & \partial_{I_1} d_x\big|_{\langle all\rangle}\langle \delta I_1 \delta y\rangle + \partial_{I_2} d_x\big|_{\langle all\rangle}\langle \delta I_2 \delta y\rangle + \partial_{\varphi} d_x\big|_{\langle all\rangle}\langle \delta\varphi \delta y\rangle + \partial_{\mu} d_x\big|_{\langle all\rangle}\langle \delta\mu \delta y\rangle + \\ & + \partial_{I_1} d_y\big|_{\langle all\rangle}\langle \delta I_1 \delta x\rangle + \partial_{I_2} d_y\big|_{\langle all\rangle}\langle \delta I_2 \delta x\rangle + \partial_{\varphi} d_y\big|_{\langle all\rangle}\langle \delta\varphi \delta x\rangle + \partial_{\mu} d_y\big|_{\langle all\rangle}\langle \delta\mu \delta x\rangle + \\ & + \langle 1+\delta_{xy}\rangle D_{xy}\big|_{\langle all\rangle} \quad .\end{aligned} \tag{4.22}$$

Solving the system of differential equations in Eq. (4.21) we can find the time dependence of the average dynamical variables, while the system of the algebraic equations, $d_x|_{\langle all\rangle} = 0$, yields the steady state. This is how we will make use of the drift terms of the Fokker-Planck equation to find the first moments of the P distribution. We are going to look at the results later on.

Applying these solutions, Eq. (4.22) can be used in a similar fashion for the case of the fluctuations. In particular, taking the time derivative to be zero and solving the system of algebraic equations in Eq. (4.22) for the present problem, the steady-state noise properties of the fields can be calculated as follows

$$\left\langle (\delta I_1)^2 \right\rangle = -\left. \frac{D_{I_1 I_1}}{\partial_{I_1} d_{I_1}} \right|_{\langle all\rangle} , \tag{4.23}$$

$$\langle \delta I_1 \delta I_2 \rangle = \langle I_1 I_2 \rangle - \langle I_1 \rangle \langle I_2 \rangle = -\left. \frac{D_{I_1 I_2} + \partial_{I_1} d_{I_2} \left\langle (\delta I_1)^2 \right\rangle}{\partial_{I_1} d_{I_1} + \partial_{I_2} d_{I_2}} \right|_{\langle all\rangle} , \tag{4.24}$$

$$\left\langle (\delta I_2)^2 \right\rangle = -\left. \frac{D_{I_2 I_2}}{\partial_{I_2} d_{I_2}} \right|_{\langle all\rangle} - \left. \frac{\partial_{I_1} d_{I_2}}{\partial_{I_2} d_{I_2}} \right|_{\langle all\rangle} \langle \delta I_1 \delta I_2 \rangle , \tag{4.25}$$

$$\left\langle (\delta \varphi)^2 \right\rangle = -\left. \frac{D_{\varphi\varphi}}{\partial_\varphi d_\varphi} \right|_{\langle all\rangle} . \tag{4.26}$$

Since in the P representation the (stochastic) average of the intensity is connected to the (quantum mechanical) expectation value of the photon number as $\langle I_i \rangle = \langle n_i \rangle$, $i = 1, 2$, and the intensity fluctuation to the normally ordered photon number variance as $\left\langle (\delta I_i)^2 \right\rangle = \left\langle : (\Delta n_i)^2 : \right\rangle$, the total photon number variance in each cavity field is given by

$$\left\langle (\Delta n_i)^2 \right\rangle = \left\langle : (\Delta n_i)^2 : \right\rangle + \langle n_i \rangle = \left\langle (\delta I_i)^2 \right\rangle + \langle I_i \rangle . \tag{4.27}$$

It is sub-Poissonian if the standard deviation,

$$\sigma_{n_i} = \sqrt{\frac{\langle (\Delta n_i)^2 \rangle - \langle n_i \rangle^2}{\langle n_i \rangle}} = \sqrt{\frac{\langle (\delta I_i)^2 \rangle}{\langle I_i \rangle} + 1} \quad , \tag{4.28}$$

is smaller than *1*, i. e., $\langle (\delta I_i)^2 \rangle$ is negative. This is the procedure that we will follow to treat the photon number fluctuations.

In order to find the total noise in the relative phase of the two fields let us define the operator, $a_{12} \equiv a_1 a_2^\dagger$, and the two quadratures given by

$$a_{12,+} \equiv \frac{1}{2}\left(a_{12} e^{-i\varphi} + a_{12}^\dagger e^{i\varphi}\right) \quad , \tag{4.29}$$

$$a_{12,-} \equiv \frac{i}{2}\left(a_{12} e^{-i\varphi} - a_{12}^\dagger e^{i\varphi}\right) \quad . \tag{4.30}$$

In the semiclassical approximation, where we write the amplitudes of the two fields as $(r_i + \delta r_i) exp(\varphi_i + \delta\varphi_i)$, $i = 1, 2$, the two quadratures can be written as

$$a_{12,+} \rightarrow (r_1 + \delta r_1)(r_2 + \delta r_2)\cos(\delta\varphi_1 - \delta\varphi_2) \quad , \tag{4.31}$$

$$a_{12,-} \rightarrow -(r_1 + \delta r_1)(r_2 + \delta r_2)\sin(\delta\varphi_1 - \delta\varphi_2) \quad . \tag{4.32}$$

Keeping the lowest order terms with respect to the deviations we obtain the variances of the quadratures given semiclassically by

$$(\Delta a_{12,+})^2 \rightarrow (r_1 \delta r_2 + r_2 \delta r_1)^2 = [\delta(r_1 r_2)]^2 \quad , \tag{4.33}$$

$$(\Delta a_{12,-})^2 \rightarrow r_1^2 r_2^2 (\delta\varphi_1 - \delta\varphi_2)^2 = r_1^2 r_2^2 [\delta(\varphi_1 - \varphi_2)]^2 \quad . \tag{4.34}$$

Therefore, the noise in the relative phase can be written using the second quadrature as

$$\left\langle (\Delta\varphi)^2 \right\rangle = \frac{\left\langle \left(\Delta a_{12,-}\right)^2 \right\rangle}{\langle n_1 \rangle \langle n_2 \rangle} \quad . \tag{4.35}$$

Although we do not need it here, the noise in the first quadrature, $a_{12,+}$, corresponds semiclassically to the noise in the product of the amplitudes of the two fields (see Eq. (4.33)). We also want to mention at this point that the "phase-like" and "amplitude-like" characters can be interchanged between the two quadratures by using $\varphi \pm \pi/2$ instead of φ in the definitions in Eqs. (4.29) and (4.30).

It is easy to see that the quadrature variances can be expressed using their normally ordered forms as

$$\left\langle \left(\Delta a_{12,\pm}\right)^2 \right\rangle = \left\langle : \left(\Delta a_{12,\pm}\right)^2 : \right\rangle + \frac{1}{4}\langle n_1 + n_2 \rangle \tag{4.36}$$

and, therefore,

$$\left\langle (\Delta\varphi)^2 \right\rangle = \frac{\left\langle : \left(\Delta a_{12,-}\right)^2 : \right\rangle}{\langle n_1 \rangle \langle n_2 \rangle} + \frac{1}{4}\frac{\langle n_1 + n_2 \rangle}{\langle n_1 \rangle \langle n_2 \rangle} = \left\langle (\delta\varphi)^2 \right\rangle + \frac{1}{4}\frac{\langle I_1 + I_2 \rangle}{\langle I_1 \rangle \langle I_2 \rangle} \quad , \tag{4.37}$$

where $\left\langle (\delta\varphi)^2 \right\rangle$ is the phase noise and $\langle I_1 \rangle$, $\langle I_2 \rangle$ are the average intensities obtained from the P representation. Since the two quadratures satisfy the commutation relation,

$$\left[a_{12,+}, a_{12,-}\right] = -\frac{i}{2}(n_1 - n_2) \quad , \tag{4.38}$$

their uncertainty product is given by

$$\left\langle \left(\Delta a_{12,+}\right)^2 \right\rangle \left\langle \left(\Delta a_{12,-}\right)^2 \right\rangle \geq \frac{1}{16} \left| \langle n_1 - n_2 \rangle \right|^2 \quad . \tag{4.39}$$

Thus, using the minimum uncertainty product we can define a normalized quantity for the phase noise given by

$$\sigma_\varphi = \sqrt{\frac{4\langle n_1 \rangle \langle n_2 \rangle}{\left| \langle n_1 - n_2 \rangle \right|} \left\langle (\Delta\varphi)^2 \right\rangle} = \sqrt{\frac{4\langle I_1 \rangle \langle I_2 \rangle \left\langle (\delta\varphi)^2 \right\rangle + \langle I_1 + I_2 \rangle}{\left| \langle I_1 - I_2 \rangle \right|}} \quad . \tag{4.40}$$

σ_φ is smaller than *1* if the phase noise is less than the square root of the minimum uncertainty product of the quadratures, i. e., the phase noise is squeezed. However, the boundary between squeezed and non-squeezed states does not necessarily coincide with that separating classical and nonclassical behavior. In the case of more than one mode, in particular, the condition for difference squeezing [17] is more stringent than that for a state to be nonclassical. Eq. (4.40) determines the squeezing condition. On the other hand, by examining Eqs. (4.36) or (4.37) we see that the boundary between classical (*P* function positive and regular) and nonclassical (*P* function pathological) behavior is given by

$$\left\langle (\Delta\varphi)^2 \right\rangle < \frac{1}{4} \frac{\langle n_1 + n_2 \rangle}{\langle n_1 \rangle \langle n_2 \rangle} \quad , \tag{4.41}$$

i. e., a state is nonclassical if the value of $\left\langle (\delta\varphi)^2 \right\rangle$ obtained from the *P* - representation is negative. This implies that for nonclassical behavior we have

$$\sigma_\varphi < \sqrt{\frac{\langle n_1 + n_2 \rangle}{\left| \langle n_1 - n_2 \rangle \right|}} \quad , \tag{4.42}$$

which is apparently a weaker condition than that above for squeezing, $\sigma_\varphi < 1$. In the most extreme case when the photon numbers in the two fields are approximately equal the boundary for nonclassicality becomes infinity, i. e., all the states are nonclassical. They

are not, however, all squeezed but that subset only for which $\sigma_\varphi < 1$. In the other extreme, when one of the photon numbers is zero Eq. (4.42) reproduces the condition for squeezing, i. e., the boundaries for squeezing and nonclassical behavior coincide.

A similar procedure can be constructed using the Q - representation of the field-density matrix, $Q(\alpha_1,\alpha_1^*,\alpha_2,\alpha_2^*,t)=\langle\alpha_1,\alpha_2|\rho|\alpha_1,\alpha_2\rangle$, by finding the corresponding Fokker-Planck equation. The essential difference between the P - and Q - representations is that they are respectively connected to normally and antinormally ordered operator expressions. Their results for the photon number expectation values and the corresponding noises, together with the respective quantities for the phases, do not differ significantly. We are going to employ the P - representation throughout this section of the paper. The only place where we will also include the Q - representation is the investigation of the time dependence of the system. Here we need to apply the Q - function because, in most of the cases, the numerical solution of the P - function differential equations is not possible due to singularities.

IV.3 Results of the Fokker-Planck treatment

IV.3.A The steady-state behavior

In order to find the steady state of the fields we need to solve the system of algebraic equations, $d_x|_{\langle all\rangle}=0$, obtained by taking the time derivative in Eq. (4.21) zero. Apparently, d_{I_1} together with d_{φ_1} and $D_{I_1I_1}$ do not depend on I_2 or φ_2 (see Eqs. (4.5), (4.7) and (4.9)) since the first micromaser is independent of the second one. Thus, $d_{I_1}|_{\langle I_1\rangle}=0$, a second order algebraic equation for $\langle I_1\rangle$, can be solved in itself for $\langle I_1\rangle=\langle n_1\rangle$ (one solution is physical only) and then the solution can be used in Eq. (4.28) to find σ_{n_1}. These results are depicted as functions of the pumping parameter, θ, in Fig. 7. The well-known first peaks in $\langle n_1\rangle$ and in σ_{n_1} of the exact solution of the micromaser are recovered qualitatively well illustrating the range of validity of the nonlinear treatment.

Next, let us look at the drift term, $d_\varphi = -d_{\varphi_2}$, given by Eq. (4.8). Apparently, the possible steady states obtained from the equation, $d_\varphi\big|_{\langle all \rangle} = 0$, are $\varphi_{ss} = 0$ and π satisfying $\sin(\varphi_{ss}) = 0$ (for the sake of simplicity we omit the stochastic average brackets, $\langle\ \rangle$, in this paragraph). This means, that there is a steady state phase locking between the two fields as a result of the coupling. We find the stable solutions by applying a small perturbation, $\Delta\varphi << \varphi_{ss}$, to the steady state phase. In this case, the equation of motion for the phase becomes

$$\frac{1}{\gamma}\frac{d(\Delta\varphi)}{dt} = A\sin(\varphi_{ss} + \Delta\varphi) \cong \pm A\,\Delta\varphi \quad , \tag{4.43}$$

where A is the factor multiplying $\sin(\varphi_1 - \varphi_2)$ in Eq. (4.8), the plus and minus signs correspond to $\varphi_{ss} = 0$ and π, respectively, and we used the linear expansion, $\sin(\Delta\varphi) \cong \Delta\varphi$. In order to have a stable solution the overall sign of $\pm A$ on the right-hand side must be negative. In this case the perturbation decays back to the steady state while in the other case diverges. This means that the solutions, $\varphi_{ss} = 0$ or π, are stable if A is respectively negative or positive. Using the above solution for $\langle I_1 \rangle$ in the equation, $A=0$, we finally arrive at a third order equation in θ. The solution of this equation, $\theta_2 \cong \sqrt{2}$, (one solution is physical only) gives the pumping parameter at which the steady-state relative phase between the two fields switches from in-phase to out-of-phase as the pumping is increased. This point, on the other hand, coincides with the "second threshold" of the incoherently coupled system of Section II where the intensity of the second field drops to approximately zero, and the atoms exit the first cavity predominantly in their lower state. Clearly, the present coherently coupled system cannot differ significantly from the incoherent one at this particular value of the pumping parameter, θ_2, because the dominance of the lower atomic state between the cavities does not allow for a considerable amount of atomic coherence to be transferred into the second micromaser. The switch of the relative phase, i. e., the "decoupling" of the fields, and the drop of the intensity of the second field at θ_2 are both the manifestations of the depleted upper atomic state. It will be

shown in the next subsection as well as in the next section that the depletion of the upper state as a function of θ together with the other connected effects can also take place during the time evolution of the system as a function of time in a similar way.

But let us look at the steady state intensity of the second micromaser in detail. Knowing the solutions for $\langle I_1 \rangle$ and $\langle \varphi \rangle$ one can solve $d_{I_2}\big|_{\langle all \rangle} = 0$, a fourth order algebraic equation for $\sqrt{\langle I_2 \rangle}$, and then apply the solution to calculate the normalized variances, σ_{n_2} and σ_{φ}, using Eqs. (4.28) and (4.40), respectively. The steady-state photon number, $\langle n_2 \rangle = \langle I_2 \rangle$, is depicted in Fig. 8 as a function of the pumping parameter, θ. We do find the point, $\theta_2 \cong \sqrt{2}$, where the phase locking switches from zero to π and the photon number drops significantly. This proves the argument in the previous paragraph. The intensity is, actually, so small here that the P - representation fails to provide a physical result. The reason for this is that the Fokker-Planck treatment is, in general, not applicable in the case of small intensities. In this method, the field-density matrix is represented by a distribution function (P, in the present case) of continuous variables such as the intensities of the fields. This does not prove to be a good approximation when the discrete nature of the fields becomes significant at small intensities, and the procedure fails. An illustration of this problem can be seen in Fig. 8 showing that the region where the P - representation breaks down shrinks with increasing N_{ex} due to the increasing photon numbers. Luckily, there is no problem with the small intensities in the vicinity of $\theta = 0$, because the nonlinear terms in the drift coefficients are proportional to θ and their contributions around $\theta \cong 0$ are small. Coming back to Fig. 8 it is apparent that between zero and θ_2 the photon number exhibits a very high peak. Comparing it to Fig. 7 we find that $\langle n_2 \rangle$ grows faster with θ than $\langle n_1 \rangle$ and, on the other hand, its peak exactly coincides with the peak in σ_{n_1}. On the other hand, comparing Fig. 8 to the results of the incoherent problem in Sec. II (see Fig. 4 (a)) it can be seen that the intensity-peak below θ_2 is much higher in the present coherently coupled system.

Significant modifications can be found in σ_{n_2} too (see Fig. 9). The first peak of the incoherent noise in Section II seems to split up into a double-peaked structure exhibiting a remarkable decrease of the noise down to the Poissonian noise level around $\theta \cong 1$. This

dip in σ_{n_2} coincides with the peak of $\langle n_2 \rangle$ and σ_{n_1}. On the other hand, no indications of the second noise-peak of the incoherent problem (see Fig. 4 (b)) around $\theta \cong 3.5$ are found, the noise in this region of θ slowly decreases instead. We should remark here that the discontinuity around $\theta \cong 1.5$ is due to the break-down of the P - representation mentioned above. It is interesting to see how the double-peaked structure depends on the parameters, N_{ex}, $\bar{n}_b'$ and $\bar{n}_b''$. To mention two of the most robust effects only we want to note that increasing N_{ex} results in an increase of the first sub-peak only. On the other hand, an increase in $\bar{n}_b'$, quit surprisingly, results in a decrease of the first and, at the same time, in an increase of the second sub-peak. It can be seen from Eqs. (4.24) and (4.25) that the noise in the first micromaser, $\langle (\delta I_1)^2 \rangle$, contributes to the correlation, $\langle \delta I_1 \delta I_2 \rangle$, and the correlation contributes to the noise of the second micromaser, $\langle (\delta I_2)^2 \rangle$. This suggests that the extra noise introduced by the thermal radiation in the first micromaser modifies the generated atomic coherence in such a way that, after entering the second cavity, it can result both in enlarged and reduced photon number fluctuations in the second micromaser depending on the pumping parameter.

The noise in the relative phase, σ_φ, is also very sensitive to the above control parameters and, in a way, behaves similarly to σ_{n_2} (see Fig. 10). The increase of N_{ex} results in a significant increase in the main peak of the noise while the increase in $\bar{n}_b'$ results in a decrease of the noise in the region of small θ. We find no squeezing in the relative phase (the condition is $\sigma_\varphi < 1$) and, apart from the lower-left panel in Fig. 10, no nonclassical behavior (the condition is given by Eq. (4.42)). However, it is surprising to see that finite temperature in the first micromaser (and there only) makes the system behave nonclassically for pumping, $\theta < 0.5$ (lower-left panel in Fig. 10). We explain this effect on similar grounds as the one above for σ_{n_2} where we found that the introduced first-cavity thermal photons can result in reduced/enlarged photon number noise in the second micromaser. Atomic coherence generated in the first micromaser can be improved by the thermal radiation in the first cavity resulting in reduced noise in the second micromaser individually, σ_{n_2} (see previous paragraph), or in reduced noise in the coupling between the

two fields, σ_φ. This is supported by the figures in the lower-right panels in Figs. 9 and 10 where we find that thermal radiation in the second cavity, however, results in increased σ_{n_2} and, at the same time, moves the system into the classical regime in σ_φ. Clearly, thermal noise in the first cavity can strengthen the coherence between the two fields in some region of the pumping parameter via improving the produced atomic coherence, while thermal noise in the second cavity can only weaken it by scrambling the phase between the injected atomic coherence and the field of the second micromaser.

Finally, we want to study the steady-state correlation between the two fields. The first order correlation, $\langle n_{12}\rangle = \langle a_1 a_2^\dagger + a_1^\dagger a_2\rangle$, is calculated in the present formalism as $\langle n_{12}\rangle = 2\cos(\langle\varphi\rangle)\langle\sqrt{I_1 I_2}\rangle$, while the second order correlation as $\langle n_1 n_2\rangle = \langle I_1 I_2\rangle$. In order to find the steady states of these quantities we transform the Fokker-Planck equation by introducing the new variables, $I_x = \sqrt{I_1 I_2}$ or $I_x = I_1 I_2$, calculate their drift coefficients, and solve the algebraic equations, $d_{I_x}\big|_{\langle all\rangle} = 0$, for $\langle I_x\rangle$. Let us first consider $\langle n_{12}\rangle$ and, besides keeping I_1, introduce the new variable, $I_x = \sqrt{I_1 I_2}$. After transforming the Fokker-Planck equation the new drift term for I_x is given by

$$d_{I_x} = \frac{1}{2}\left(\frac{I_x}{I_1} d_{I_1} + \frac{I_1}{I_x} d_{I_2}\right) - \frac{1}{4I_x}\left[\left(\frac{I_x}{I_1}\right)^2 D_{I_1 I_1} + \left(\frac{I_1}{I_x}\right)^2 D_{I_2 I_2} - D_{I_1 I_2}\right] , \qquad (4.44)$$

while, obviously, d_{I_1} has not changed. Knowing $\langle I_1\rangle$ and $\langle\varphi\rangle$ the equation, $d_{I_x}\big|_{\langle all\rangle} = 0$, becomes a fourth order equation for $\langle I_x\rangle$ that can be solved and, thus, the first order correlation, $\langle n_{12}\rangle = 2\cos(\langle\varphi\rangle)\langle I_x\rangle$, can be calculated at steady state. It can be seen in Fig. 11 that this correlation is zero at θ_2, while its magnitude has two maxima on the two sides of θ_2. The change of its sign from positive to negative is, obviously, due to the switch of the relative phase from zero to π. The essential message of this result is that the two fields will exhibit stationary interference effects when superposed. As a comparison, we also show in Fig. 12 a different version of the first order correlation reading as

$$\Re^{(1)} = \frac{\left|\langle n_{12}\rangle\right|}{2\sqrt{\langle n_1\rangle\langle n_2\rangle}} - 1 \quad . \tag{4.45}$$

We find the most interesting region below the divergence at the θ_2 - point.

In order to find the second order correlation, $\langle n_1 n_2\rangle = \langle I_1 I_2\rangle$, let us introduce the new variable as $I_x = I_1 I_2$ and find its drift term in the transformed Fokker-Planck equation,

$$d_{I_x} = \frac{I_x}{I_1} d_{I_1} + I_1 d_{I_2} + D_{I_1 I_2} \quad . \tag{4.46}$$

Similarly to the above, using the solutions for $\langle I_1\rangle$ and $\langle\varphi\rangle$ the equation, $d_{I_x}\big|_{\langle all\rangle} = 0$, is a fourth order equation for $\sqrt{\langle I_1 I_2\rangle}$. Some selected results for $\langle n_1 n_2\rangle$ as a function of θ are depicted in Fig. 13. We also show in Fig. 14 the normalized second order correlation given by

$$\Re^{(2)} = \frac{\langle n_1 n_2\rangle}{\langle n_1\rangle\langle n_2\rangle} - 1 \quad . \tag{4.47}$$

It can be seen that the photons coming from the two separate sources are positively correlated ($\Re^{(2)} > 0$) below θ_2 and anticorrelated ($\Re^{(2)} < 0$) above it. Apparently, anticorrelation is sensitive to N_{ex} (the higher N_{ex} the lower the magnitude of $\Re^{(2)}$) but insensitive to thermal photons, while positive correlation is vice versa.

IV.3.B The time-dependent behavior

Let us now investigate the time evolution of the system toward steady state. To this end we numerically solve the system of *3* coupled differential equations in Eq. (4.19) for $\langle x\rangle = \langle I_1\rangle$, $\langle I_2\rangle$ and $\langle\varphi\rangle$ simultaneously where a rescaled time variable is introduced as $T = \gamma t$.

Similarly to the steady state behavior, we find that in the P - representation the numerical solution of the differential equations fails when, at a certain point during the time development, the intensity of the second field drops to a very low level. The problem is that even if the steady state intensity was high enough and could be found from the algebraic equations the system may, in general, go through low-intensity points on its way toward steady state. The differential equations, therefore, cannot be integrated numerically all the way to the, in fact existing, steady state due to the singularitis at the critical points. It turns out, on the other hand, that even though this is a basic anomaly of the Fokker-Planck treatment itself the Q - function actually does work, and the equations can be integrated for the whole time evolution up to the steady state. Since the Q - representation is connected to the antinormally ordered operator expressions the solutions for the intensities can be used to find the photon number expectation values as $\langle n_i \rangle = \langle I_i \rangle_Q - 1$, $i = 1, 2$. The intensities, $\langle I_i \rangle_Q$, exist at any time for the Q - representation. The above anomaly, however, manifests itself in the inaccuracy of the results for the photon numbers, $\langle n_i \rangle$, if $\langle I_i \rangle_Q$ becomes too small. With the exception of these low-intensity points the results, as we will see in the next section, are in good qualitative agreement with the exact numerical simulations.

Therefore, let us employ the Q - representation to investigate the time-dependent behavior of the system. The drift coefficients obtained from the Fokker-Planck equation for the Q - function are given by

$$d_{I_1}^Q = \bar{n}_b' + 1 + I_1(\theta^2 - 1) - \frac{\theta^4}{3N_{ex}} I_1(I_1 - 1) \quad , \tag{4.48}$$

$$d_{I_2}^Q = \bar{n}_b'' + 1 + I_2(\theta^2 - 1) - \frac{\theta^4}{3N_{ex}}\left[I_2(I_2 - 1) + 3I_1(2I_2 - 1)\right] +$$

$$+2\cos(\varphi_1 - \varphi_2)\sqrt{I_1 I_2}\left[\theta^2 - \frac{\theta^4}{3N_{ex}}\left(2I_1 + 2I_2 - \frac{5}{2}\right)\right] \quad , \tag{4.49}$$

and

$$d_{\varphi}^{Q} = -d_{\varphi_2}^{Q} = -\sin(\varphi_1 - \varphi_2)\sqrt{\frac{I_1}{I_2}}\left[\theta^2 - \frac{\theta^4}{3N_{ex}}\left(2I_1 - \frac{1}{2}\right)\right] \quad , \tag{4.50}$$

since $d_{\varphi_1}^{Q} = 0$. We solve, by using these terms, the system of *3* coupled differential equations in Eq. (4.19) numerically for $\langle x \rangle = \langle I_1 \rangle_Q$, $\langle I_2 \rangle_Q$ and $\langle \varphi \rangle_Q$ simultaneously. Some of our selected results are as follows.

In Figs. 15 (a) and (b) the evolution of the system is depicted in the phase-sapce of $\langle I_1 \rangle_Q$ - $\langle I_2 \rangle_Q$ - $\langle \varphi \rangle_Q$ for the respective pumping parameters, $\theta = 1.1$ and $\theta = 2$, applying various initial conditions. It is apparent that the steady states are in the $\langle \varphi \rangle_Q = 0$ plane in the first and in the $\langle \varphi \rangle_Q = \pi$ plane in the second figure. The steady-state points are reached via sharp jumps of the relative phase. This is also illustrated in Figs. 16 (a) and (b) where some trajectories are depicted as functions of time. It can be seen that for $\theta = 1.1$ the phase jumps occur if the fields are started out-of-phase, opposite to the final equilibrium. However, it is interesting to note that for $\theta = 2$ phase jumps can take place even if the system has been started in its final equilibrium phase (see the trajectory started from zero intensities at a phase of π in Fig. 15 (b), and also the corresponding time evolution in the lower left-hand panel in Fig. 16 (b)). There are actually two phase jumps in this case, jumping out of equilibrium phase and back, resulting in a flip in the intensity of the second micromaser.

The time evolution of the field in the second micromaser can be understood as a consequence of two coexisting driving mechanisms, the stimulated emission/absorption and the driving atomic coherence. We have seen how the former one governed the incoherently coupled system in Section II while the new features of the coherent coupling are the consequences of the latter mechanism. The stimulated emission/absorption is related to the incoherent population of the atoms entering the second cavity and the intensity of the actual field inside the cavity. The populations of the two atomic states determine the weight of emission as compared to absorption while the intensity of the actual field is

related to the magnitude of the energy flowing in the two directions. The larger the upper state population and the field the stronger/weaker the stimulated emission/absorption. There is no condition on the relative phase between the atoms and the field in this case, the initial field will be coherently amplified/attenuated at its initial phase.

In the case of the coherent driving mechanism, however, the main feature is the condition on the phase of the atomic coherence relative to that of the field. The two coupled oscillators, the atomic dipole and the field, are locked in a relative phase of $\pi/2$ and the direction of the flow of energy between them points toward the one that is behind. On the other hand, the populations of the two atomic states determine the magnitude of the atomic coherence, i. e., the strength of the atomic dipole oscillator, and the magnitude of the transferred energy in either direction. The smaller the difference between the populations the stronger the dipole, i. e., in a definite atomic state the coherence is zero. The first micromaser is independent of the second one and serves as a preliminary system to prepare the atoms for the second field to populate their states and generate coherence between them. Since every atom enters the first cavity in its excited state energy can flow from the atoms to the field only and, therefore, the phase of the first field is constantly late by $\pi/2$ behind that of the atom. The phase of the second field, however, can be both before or behind the atoms by $\pi/2$ depending whether the field gains energy from the dipole or not. This is why we have zero and π as the two possible cases for the locking of the relative phase between the two fields themselves.

Whether the field in the second cavity is amplified or not depends on the net effect of the two mechanisms, the stimulated emission/absorption and the driving atomic coherence. They can act constructively when pumping or damping the field simultaneously, and destructively when one of them is pumping while the other is damping alternatively. Let us illustrate the physics of the coexistence of the two mechanisms through the particular example when the intensity of the first field is initially zero. In this case, the state of the first few atoms reaching the second cavity is dominantly the excited state and, therefore, the inversion is large but the dipole strength is small in the first moments of the time development. (Here, it is assumed that we remain inside the region of the, not too large,

pumping parameters that we have been considering so far in this section. In this case the change of the population of the first few atoms when traversing the first cavity is small as compared to a full Rabi cycle.) The initial phase of the coherence relative to the second field depends on the initial relative phase between the two fields while the strength of the stimulated emission (inversion is large) depends on the initial intensity of the second field. Suppose we start from a relative phase of π and the intensity in the second field is zero. This particular case, using the pumping parameter, $\theta = 2$, is illustrated by one of the trajectories in Fig. 15 (b) the time dependence of which depicted in the lower-left panel of Fig. 16 (b). Due to the initial phase, π, the atomic dipole is absorbing from the second field in the beginning and due to the small initial intensity the stimulated emission is weak. Thus, after a very small increase in the intensity due to the weak stimulated emission and the practically zero dipole strength at $T = 0$ the field remains to be very small for some time. However, the dipole strength is increasing and the weight of the stimulated emission as compared to the absorption is decreasing in time due to the increasing intensity of the first field and the consequent turn of the atomic population toward the lower state. Therefore, the intensity becomes zero, i. e., the second field depletes completely, when the dipole together with the stimulated absorption have used up all the energy provided by the stimulated emission. At this point (around $T = 0.75$) the dipole takes over the lead and, after switching the phase between the atom and the second field to $+\pi/2$ due to the still remaining inversion, starts pumping the field. We should remark here that this phase jump to the relative phase of zero between the fields is not related to the depletion of the upper atomic state as the one that we have seen in the steady state behavior but to the depletion of the field by the dipole instead. This is a coherence effect where the atomic coherence turns the field off in opposition to the pumping (although weak) stimulated emission and then takes the lead over to pump the field at the opposite relative phase. Due to the simultaneous pumping by the dipole driving mechanism and the stimulated emission (still strong, because the inversion is positive) the intensity of the field starts to grow fast. At the same time, as a result of the incerasing field in the first cavity the population of the lower atomic state is constantly increasing. This means that the weight of the stimulated

emission/absorption in the pumping is constantly decreasing/increasing until finally the atoms become pure absorbers when the upper state population disappeares. At the same time, the dipole strength increases to a maximum when the inversion turns to zero and, similarly to the stimulated emission, becomes zero when the upper state is depleted. Since its phase is independent of the inversion, the dipole constantly pumps the field because its phase, $+\pi/2$, relative to the field does not change with the change of the atomic population during this interval of time. It is the stimulated absorption only that lowers the intensity of the field. The result of the two processes is that the intensity after reaching a maximum point falls back to zero when the upper state becomes empty (around $T = 2$). This shut-off of the second field is also connected to a jump in the relative phase between the fields opposite to the one above. The atomic population, as the intensity in the first field is increasing in time, starts turning toward the upper state. As a consequence of this, some stimulated emission appears besides the still dominant absorption together with a very weak atomic coherence. Since the inversion is still negative the phase of the arising atomic coherence relative to the second field becomes $-\pi/2$ indicating that energy flows from the field to the atom. This implies a jump in the relative phase of the two fields by π when comparing the relative phase of the newly arising field after the shut-off to the one before it. Clearly, this shut-off is an incoherent effect since it is the result of the depletion of the incoherent upper state of the atoms. The resulting stimulated absorption shuts the field off in contrary to the pumping, although weak, atomic coherence making it possible for the dipole mechanism to develope a new field at a different phase. Finally, the intensity of the first field settles to a steady state freezing the inversion into a particular value and, as a consequence of this, determining the weight of stimulated emission as compared to absorption. The atomic coherence also reaches its steady state remaining in the same phase after the second phase jump.

It is clear from the above that the two intensity-shut-offs and the corresponding phase jumps are the results of two different mechanisms. The first phase jump is a consequence of the particular initial condition for the relative phase and of the resulting initial behavior of

the dipole driving mechanism. This can be seen by starting the same system from another initial relative phase, e. g. zero, as depicted in the upper two panels of Fig. 16 (b). Apparently, the first phase jump is missing the second one can be found only. On the other hand, the two panels in the right column in this Figure show what happens when the second field is started from a high initial intensity. It can be seen in the lower-right panel that due to the high intensity and high inversion the stimulated emission is so strong in the beginning that it dominates over the absorption effect of the dipole mechanism. It follows, that the first shut-off of the field and the corresponding phase jump are missing in this case. However, the Figure exhibits a significant drop in the intensity that, in fact, realizes the "second" shut-off due to the still effective depletion of the upper atomic state. The corresponding "second" phase jump is obviously missing since the dipole is already in the proper phase. This means, that in contrary to the first intensity-shut-off the second one does not depend on particular initial conditions regarding the intensity or the phase of the second field. Since it is connected to the depletion of the atoms, not the fields, it depends on the first field only. Without going into details we refer to Fig. 15 (b) showing examples for various initial conditions. This Figure suggests that increasing the intensity of the first field makes the first intensity-shut-off region shrink and finally disappear while the second intensity-shut-off survives unchanged. Clearly, the first atoms in the beam are not completely inverted for nonzero initial first field but their population between the cavities is turned toward the lower state as the initial intensity of the first field is increased. This makes the first and second intensity-shut-offs shift toward the first atoms of the pumping beam, i. e., toward earlier times, with decreasing time separation. Finally, when the initial intensity of the first field becomes so high that it depletes the upper state population of the very first atom completely the first intensity-shut-off point disappears. As a summary, we have seen that the realization of the first intensity-shut-off depends strongly on the initial conditions regarding the relative phase and the intensities of the two fields. The second shut-off, however, always exists. The point where it occurs in time depends on the initial conditions regarding the intensity of the first field.

Finally we want to note, that the discussed qualitative characteristics of the time

dependence are general, and do not depend significantly on the pumping parameter provided we remain inside the region considered in the present section. As it is apparent from comparing Figs. 15 (a) and 16 (a), illustrating the case of $\theta = 1.1$, to Figs. 15 (b) and 16 (b), where $\theta = 2$, the system is governed by the same above discussed mechanisms in both cases except that the second intensity-shut-off is missing in the case of $\theta = 1.1$, the first one can be realized only. The second shut-off point is missing for $\theta = 1.1$ because, in this case, the fields reach their steady states earlier than the upper atomic state would have been depleted. In other words, the pumping parameter determines where the system settles down when evolving along a universal trajectory. For smaller pumping, i. e. larger losses, the steady state is located on an earlier part of the trajectory while in the case of larger pumping it gets further ahead. This is why the steady state behavior of the system as a function of the pumping parameter, θ, is reminiscent of the time evolution for a given θ.

In conclusion to this section we want to remark at the end that the particular strength of this nonlinear treatment is that it is analytical. Besides the formal understanding of the system by considering the form of the equations another great advantage of this formalism is that we can consider setups involving high photon numbers (i. e., high N_{ex}) without any difficulties. This cannot be said about the exact numerical approaches because, as we will see in the next section, the size of the density matrix in the photon number representation is greatly limited by the capacities of the computers. The price to pay, however, is that the nonlinear theory is not exact. The good news, on the other hand, is that it works better for higher N_{ex} and, thus, constitutes a good complementary to the exact numerical simulations presented in the following section.

V. NUMERICAL SIMULATIONS

We consider two lossy micromasers pumped by a monoenergetic beam of excited two-level atoms going through cavity *1* first and then through cavity *2* with no time delay

between the cavities (see Fig.1). The density of the atomic beam is low enough in order to have at most one atom at a time inside the cavities. The evolution of the field-density matrix during atom number k is inside the cavities is governed by the Jaynes-Cummings interaction according to Eq. (3.1). We assume that the interaction time an atom spends in the cavities is much shorter than the cavity lifetime. (In a typical experimental setup the difference is three orders of magnitude.) In this case we can ignore the decay of the fields during the time an atom is inside the cavities and separate the evolution of the system into two parts: atom-field interaction (pumping) and decay of the fields (damping). Thus, the field-density matrix at the instant when an atom leaves cavity *2* can be calculated from Eq. (3.1) resulting in the matrix $\rho(0)$, the decay of which is then calculated from this initial condition as a function of time by applying the solution of the standard master equation for a field mode of an empty cavity damped to a reservoir of finite temperature given by

$$\rho_n^{\{k\}}(t) = e^{-\gamma\frac{k}{2}t}\sum_{l=0}^{n}\sum_{m=n-l}^{\infty} C_{n,m,l}^{\{k\}}\frac{A^m}{B^{m+k+1}}\left(\frac{A'}{A}\right)^{n-l}\left(\frac{B'}{B}\right)^{l}\rho_m^{\{k\}}(0) \quad . \qquad (5.1)$$

Here, $\rho_n^{\{k\}} \equiv \rho_{nm}$ with $k = m\text{-}n$, γ is the cavity decay rate and t is time. The coefficients are given by

$$C_{n,m,l}^{\{k\}} \equiv (-1)^l\binom{m+k+l}{l}\binom{m}{n-l}\sqrt{\binom{m+k}{n+k}\Big/\binom{m}{n}} \quad , \qquad (5.2)$$

$A \equiv (\bar{n}_b + 1)\left(1-e^{-\gamma t}\right)$, $B \equiv 1+\bar{n}_b\left(1-e^{-\gamma t}\right)$, $A' \equiv e^{-\gamma t} - \bar{n}_b\left(1-e^{-\gamma t}\right)$ and $B' \equiv A' - e^{-\gamma t}$, where $\bar{n}_b$ is the average number of thermal photons. A derivation of this solution is given in Refs. [13, 18]. It is easy to show that in the special case of zero temperature, i. e. $\bar{n}_b = 0$ Eq. (5.1) reduces to

$$\rho_n^{\{k\}}(t) = e^{-\gamma(n+k/2)t}\sum_{m=0}^{\infty}\sqrt{\binom{m+k}{n+k}\binom{m}{n}}\left(1-e^{-\gamma t}\right)^{m-n}\rho_m^{\{k\}}(0) \quad . \qquad (5.3)$$

The two fields decay according to this time dependent density matrix during the time interval until the next atom arrives. Hence, the time evolution of the fields for a stream of atoms is calculated by numerically iterating the two cycles of pumping and damping by applying Eqs. (3.1) and (5.1), respectively. The pump statistics of the micromasers can be taken into account via the distribution of time intervals of the decay cycles in the procedure. Here, however, we consider regular pumping statistics only.

First, as a reference, we show in Fig. 17 the steady-state behavior of the average photon number, $\langle n_1 \rangle$, and the standard deviation of the photon number, σ_{n_1}, of the first micromaser as a function of the pumping parameter, θ. The sharp dips in each figure correspond to the trapping states. Comparing Fig.17 to Fig. 18 one can see that, similarly to the results of the nonlinear theory, the average photon number of the second field, $\langle n_2 \rangle$, grows faster with θ than that of the first one, $\langle n_1 \rangle$. We also find the dip in the photon number noise, σ_{n_2}, around $\theta = 1$ which coincides with the first peak of σ_{n_1}. On the other hand, since the first micromaser makes a transition back to a lower order "phase" of small photon number at the trapping states [8], the atoms entering the second cavity are predominantly in their upper states at these pumping parameters. It follows that atomic coherence is not significant in these cases and the system is very similar to the incoherently coupled scheme. Therefore, similar switching mechanisms can be found here at the trapping states as those in Sec. II. At the same time, the second micromaser behaves very similar to the first one at these pumping parameters, reproducing approximately the same photon number and noise, because it is pumped by almost fully inverted atoms. The smaller the $\langle n_1 \rangle$ at the trapping state the more similar the two micromasers operate. In the case of finite cavity temperature, the trapping states go away and both micromasers recover their "phase-transition"-like operation (see right panels in Figs. 17 and 18).

Considering the behavior of the steady state first order correlation, $\langle n_{12} \rangle$, in Fig. 19 and the corresponding standard deviation given by

$$\sigma_{n_{12}} = \sqrt{\frac{\langle n_{12}^2 \rangle - \langle n_{12} \rangle^2}{|\langle n_{12} \rangle|}} \tag{5.4}$$

we first find that the results of the nonlinear treatment are confirmed in the region of small pumping parameters. However, we can investigate large pumping parameters now in the present case of exact numerical simulations that are beyond the range of validity of the nonlinear method. It can be seen in Fig. 19 that $\langle n_{12} \rangle$ approaches zero with increasing θ and, on the other hand, it is also approximately zero at the trapping states. This means that the off-diagonal elements of the density matrix adjacent to the diagonal go to zero with increasing θ (and at the trapping states) at steady state and the first order correlation disappears. However, the fields do not become completely uncorrelated. The lower two panels in Fig. 21 show that, apart from the trapping states, significant second order correlation, $\Re^{(2)}$, can be found even for large θ. This means, that even though the matrix becomes diagonal for large pumping parameters at steady state correlation between the fields exists via the diagonal terms. Nevertheless, the first and second order correlations both suggest that the largest correlation between the two fields can be found in the small pumping region. In particular, Fig. 21 shows that in the weak pumping regime the second order correlation of the fields, $\Re^{(2)}$, undergoes an oscillation between positive and negative values. The photons coming from the two separate sources can, therefore, be both positively correlated ($\Re^{(2)} > 0$) and anticorrelated ($\Re^{(2)} < 0$) at steady state depending on the pumping parameter.

Figs. 22 and 23 show the respective sum and difference of the steady state normalized photon numbers in the two cavities, $\langle n_{\pm} \rangle = \langle n_1 \rangle \pm \langle n_2 \rangle$, and the corresponding standard variances, $\sigma_{n_{\pm}}$, given by

$$\sigma_{n_{\pm}} = \sqrt{\frac{\sigma_{n_1}^2 \langle n_1 \rangle + \sigma_{n_2}^2 \langle n_2 \rangle \pm 2\left(\langle n_1 n_2 \rangle - \langle n_1 \rangle \langle n_2 \rangle\right)}{|\langle n_1 \rangle \pm \langle n_2 \rangle|}} \quad . \tag{5.5}$$

$\sigma_{n_\pm}$ can be employed to determine whether the second order correlation between the two fields behaves nonclassically using the condition given by

$$\left\langle (n_1 \pm n_2)^2 \right\rangle - \left\langle n_1 \pm n_2 \right\rangle^2 < \left\langle n_1 \right\rangle + \left\langle n_2 \right\rangle \tag{5.6}$$

obtained, similarly to the idea of Eq. (4.42), by studying the regular and pathological behavior of the P - function. Using, for example, σ_{n_+} Eq. (5.6) implies that the system is nonclassical if $\sigma_{n_+} < 1$. In the case of single-mode fields like, e. g., in the two micromasers separately, such a condition for the standard deviation of the photon numbers in the modes determined the sub-Poissonian (super-Poissonian) statistics of the photons, i. e., the bunching (antibunching) of the photons in the modes. In this case the condition looks formally the same but it is about the photon number of the two-field system. Comparing σ_{n_+} to Figs. 17 and 18 we find, in particular, that in some regions of θ σ_{n_+} can exhibit nonclassical behavior even though σ_{n_1} and σ_{n_2} are both super-Poissonian. This is the result of the nonzero anticorrelation, $\langle n_1 n_2 \rangle < \langle n_1 \rangle \langle n_2 \rangle$, the effect of which can be seen in Eq. (5.5). Similarly, σ_{n_+} is enhanced as compared to σ_{n_1} and σ_{n_2} in those regions where the two fields exhibit positive correlation, i. e., $\langle n_1 n_2 \rangle > \langle n_1 \rangle \langle n_2 \rangle$. Considering the difference photon number, $\langle n_- \rangle$ = $\langle n_1 \rangle$ - $\langle n_2 \rangle$, the most significant effect is that, in some regions of the pumping parameter, the photon number in the second cavity, $\langle n_2 \rangle$, grows faster with θ than that of the first one, $\langle n_1 \rangle$. Thus, $\langle n_- \rangle$ can be negative in these regions as it is depicted in Fig. 23. The effect of second order correlation on σ_{n_-} is exactly vice versa as compared to that on σ_{n_+} as it can be seen in Eq. (5.5). That is, σ_{n_-} is decreased (increased) in the regions of positive (negative) correlations.

The consequences of coherences are more apparent in Fig. 24, when comparing $\langle n_2 \rangle$, σ_{n_2}, $\langle n_1 n_2 \rangle$, and $\sigma_{n_1 n_2}$ obtained in the case of coherent coupling to the corresponding quantities of the incoherent coupling. It can be seen that the most significant effects can be found in the region of small pumping parameters, as we expect from the analysis above. Here, $\langle n_2 \rangle$ and $\langle n_1 n_2 \rangle$ are enhanced while σ_{n_2} and

$\sigma_{n_1 n_2}$ exhibit a dip due to the coherences. One can also see that the coherent and incoherent schemes result in approximately the same behavior at the trapping states. Similarly, the above mentioned effects in $\langle n_- \rangle$ and $\sigma_{n_\pm}$, viz., $\langle n_- \rangle$ can be negative and $\sigma_{n_\pm}$ can be enhanced/reduced depending on positive/negative correlation, are contrasted to the incoherent cases in Fig. 25. In particular, $\langle n_- \rangle$ cannot be negative in the incoherent scheme because $\langle n_1 \rangle > \langle n_2 \rangle$ for any θ. On the other hand, significant discrepancies can be seen in σ_{n_+} and σ_{n_-} between the coherent and incoherent cases especially in the small pumping region arising mainly from those correlation effects analysed above.

Some of our selected results of numerical simulations for the time dependence of the system are summarized as follows. We apply regular pumping statistics and the time separation between the atoms is $1/N_{ex} = 1/20$ in the units of the cavity lifetime. The fields are started from vacuum and the cavity temperature is zero, $\bar{n}_b \equiv \bar{n}_b' = \bar{n}_b'' = 0.0$. As a reference, in Fig. 26 we show the time development of $\langle n_1 \rangle$ as a function of the injected number of atoms for $\theta = 0.5, 1.0, 1.5, 2.0, 2.5$ and 3.0. Comparing this figure to Fig. 27 one can see that $\langle n_2 \rangle$, similarly to the steady-state behavior as a function of θ, grows faster than $\langle n_1 \rangle$ as a function of the atom number. On the other hand, it undergoes a flip similar to the shut-offs found in the nonlinear theory indicating a depletion of the upper atomic state due to the first micromaser. The flips become shorter as θ is increasing because it takes less atoms for larger θ to reach a completely depleted upper atomic state. The corresponding first order correlation, $\langle n_{12} \rangle$, depicted in Fig. 28 exhibits a switch in the sign of its steady-state value from positive to negative. In particular, after the second threshold the steady state value of $\langle n_{12} \rangle$ is negative reached via a flip related to the that in $\langle n_2 \rangle$. This corresponds to the switch of the steady-state relative phase in the semiclassical picture from zero to π and can be explained similarly to the argument in the nonlinear treatment in Sec. IV.3.B.

In conclusion to this section we can say that the exact numerical simulations verified the nonlinear results of the previous section in the region of small pumping parameters

and, at the same time, provided further insight into the behavior of the system both here and in the cases of strong pumping. We found, in particular, that the largest correlations between the fields are typical in the region of weak pumping suggesting that the atomic coherence generated by the first micromaser is the largest here. In this regime, the photon statistics of the first micromaser consists of a single wide bell-like curve while at larger pumping parameters they consist of several distinct sharp peaks. Therefore, it is suggetsed that the former structure of a wide single peak is optimum for the largest atomic coherence to be generated. This is supported by the thermal effect found in the previous section, viz., thermal radiation in the first cavity can improve the produced atomic coherence because it widens the peaks of the photon statistics and, at the same time, establishes a wide background similar to the optimum structure for the largest atomic coherence.

VI. SUMMARY

In the present paper we considered two micromasers coupled by sharing a common pumping beam of two-level atoms. This system is reminiscent of Young's two-slit experiment because the atoms have two indistinguishable paths to reach the same final state, viz., they can be in a superposition state between the two cavities. Acquiring information ("which path") about the state of the atoms between the cavities results in a loss of atomic coherence and the second micromaser is pumped by atoms in an incoherent mixture of the two atomic states. Contrasting this latter problem of incoherent coupling to the coherent one we studied the consequences of atomic coherence in this system. We first found that in the case of incoherent coupling the absorption prepared by the first field and injected into the second one switches the second micromaser between distinct phases of the photon statistics. An exact solution was used to investigate this system.

Allowing for atomic coherence to be transferred into the second cavity the behavior

of the system is significantly modified. We attacked the problem in two different ways. First, we found the exact master equation for the field-density matrix and, after finding its nonlinear expansion, transformed it into a Fokker-Planck equation. We followed a standard technique here using the drift and diffusion terms of the equation to investigate the behavior of the fields. Secondly, we carried out a numerical simulation of the problem where the evolution of the fields is separated into driving cycles applying the exact Jaynes-Cummings interaction between the atoms and the fields, and damping cycles calculating the decay of the fields in the empty cavities. The two approaches are complementary. The nonlinear theory can be used for arbitrarily large photon numbers (the larger the better) but works in the region of small pumping parameters only. The numerical simulation, however, is limited for small photon numbers due to the finite speed and storage capacities of computers but can be used in arbitrary regions of the pumping parameter.

We found that atomic coherence significantly modifies the behavior of the system, and the coherence effects are crucial in the region of small pumping parameters, in particular. The photon number and the number noise of the field in the second cavity depart from the corresponding quantities in the incoherently coupled system because besides the stimulated emission related to the incoherent population of the atoms, the atomic coherence, as a new driving mechanism, also contributes to the field. We have seen the consequences of the interplay between the two mechanisms in the nonlinear treatment particularly clearly. Atomic coherence also establishes a correlation between the two fields both in the transient and in the steady state regimes. The first and second order correlations were studied. The first order correlation corresponding to a phase locking of the fields switches its sign between positive and negative values resulting in jumps of the relative phases between zero and π both as a function of time during the time development and as a function of the pumping parameter in the steady state behavior. On the other hand, the steady state second order correlation between the photons coming from the two separate sources exhibits an oscillation between positive and negative values as a function of the pumping parameter. As we mentioned above,

the effect of atomic coherence is the most significant in the region of small pumping parameters. In particular, the first order correlation approaches zero with increasing θ and the correlations established by the diagonal terms of the field-density matrix (i. e., second order) survive only. We want to remark that atomic coherence injected into the second cavity is the largest when the photon statistics of the first micromaser consist of a single wide peak. In this way, finite temparature of the first cavity widening the photon statistics of the first micromaser can improve the generated atomic coherence and result in a larger correlation between the fields. Finite temperature of the second cavity, on the other hand, can only destruct coherence due to the excessive noise.

In conclusion, we have shown that correlation between the two micromasers is a robust effect both in the transient and the steady state regimes in the presence of significant losses and temperature. We expect that these theoretical results could be tested by the presently available experimental facilities.

APPENDIX

The drift and diffusion coefficients of the Fokker-Planck equation of Eq. (4.3) read as

$$d_{\alpha_1} = \left(d_{\alpha_1^*}\right)^* = \frac{1}{2}\left(\theta^2 - 1\right)\alpha_1 - \frac{\theta^4}{4!N_{ex}}\alpha_1\left(4\alpha_1\alpha_1^* + 7\right) \quad , \tag{A.1}$$

$$d_{\alpha_2} = \left(d_{\alpha_2^*}\right)^* = \frac{1}{2}\left(\theta^2 - 1\right)\alpha_2 - \frac{\theta^4}{4!N_{ex}}\left[\alpha_2\left(4\alpha_2\alpha_2^* + 7\right) + \right.$$

$$\left. + 16\alpha_1\left(\alpha_1\alpha_1^* + 2\right) + 24\alpha_2\left(\alpha_1\alpha_1^* + 1\right) + 8\alpha_2\left(\alpha_1\alpha_2^* + \alpha_1^*\alpha_2\right)\right] \quad , \tag{A.2}$$

$$D_{\alpha_1\alpha_1} = \left(D_{\alpha_1^*\alpha_1^*}\right)^* = -\frac{\theta^4}{4!N_{ex}}3\alpha_1\alpha_1 \quad , \tag{A.3}$$

$$D_{\alpha_2\alpha_2} = \left(D_{\alpha_2^*\alpha_2^*}\right)^* = -\frac{\theta^4}{4!N_{ex}}\left(3\alpha_2\alpha_2 + 4\alpha_1\alpha_2\right) \quad , \tag{A.4}$$

$$D_{\alpha_1\alpha_1^*} = \bar{n}_b' + \theta^2 - \frac{\theta^4}{4!N_{ex}}\left(10\alpha_1\alpha_1^* + 8\right) \quad , \tag{A.5}$$

$$D_{\alpha_2\alpha_2^*} = \bar{n}_b'' + \theta^2 - \frac{\theta^4}{4!N_{ex}}\left[10\alpha_2\alpha_2^* + 8 + 24\left(\alpha_1\alpha_1^* + 1\right) + 12\left(\alpha_1\alpha_2^* + \alpha_1^*\alpha_2\right)\right] \quad , \tag{A.6}$$

$$D_{\alpha_1\alpha_2} = \left(D_{\alpha_1^*\alpha_2^*}\right)^* = -\frac{\theta^4}{4!N_{ex}}\left[12\alpha_1\alpha_1 + 8\alpha_2\alpha_2 + 18\alpha_1\alpha_2\right] \quad , \tag{A.7}$$

$$D_{\alpha_1\alpha_2^*} = \left(D_{\alpha_1^*\alpha_2}\right)^* = \theta^2 - \frac{\theta^4}{4!N_{ex}}\left[20\left(\alpha_1\alpha_1^* + 1\right) + 8\alpha_2\alpha_2^* + 18\alpha_1\alpha_2^*\right] \quad . \tag{A.8}$$

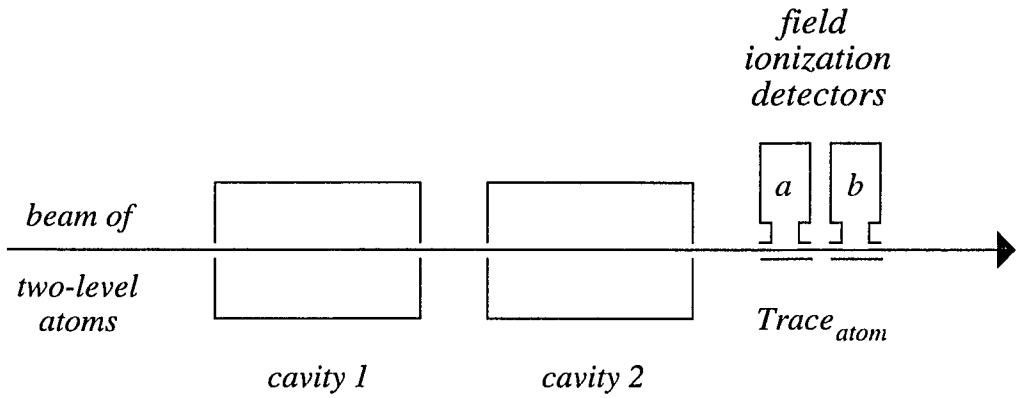

FIG. 1: Schematic arrangement of two micromasers coupled by a beam of two-level atoms the state of which are measured after the interaction by field ionization detectors.

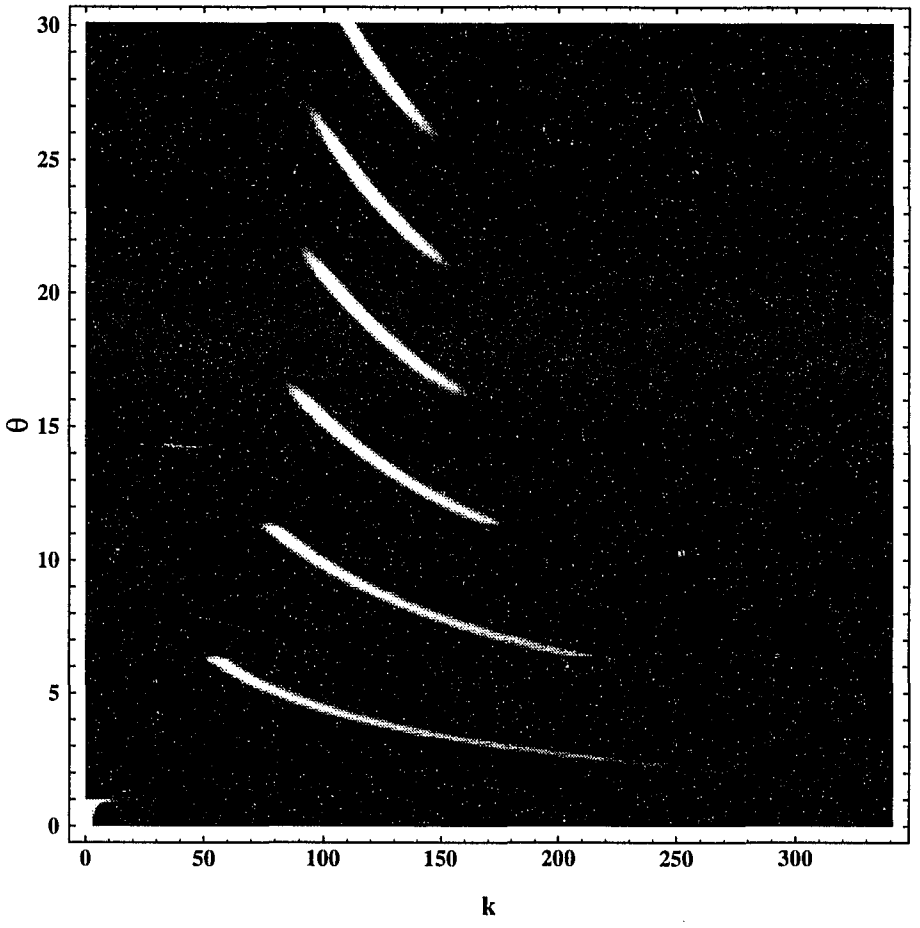

FIG. 2: Density plot of the photon statistics of the first micromaser in the space of pumping parameter, θ, and photon number, k, for $N'_{ex} = 300$ and $\bar{n}'_b = 0.5$. Lighter points indicate higher probabilities. Apparently, the photon statistics consist of distinct phases between which the system makes transitions.

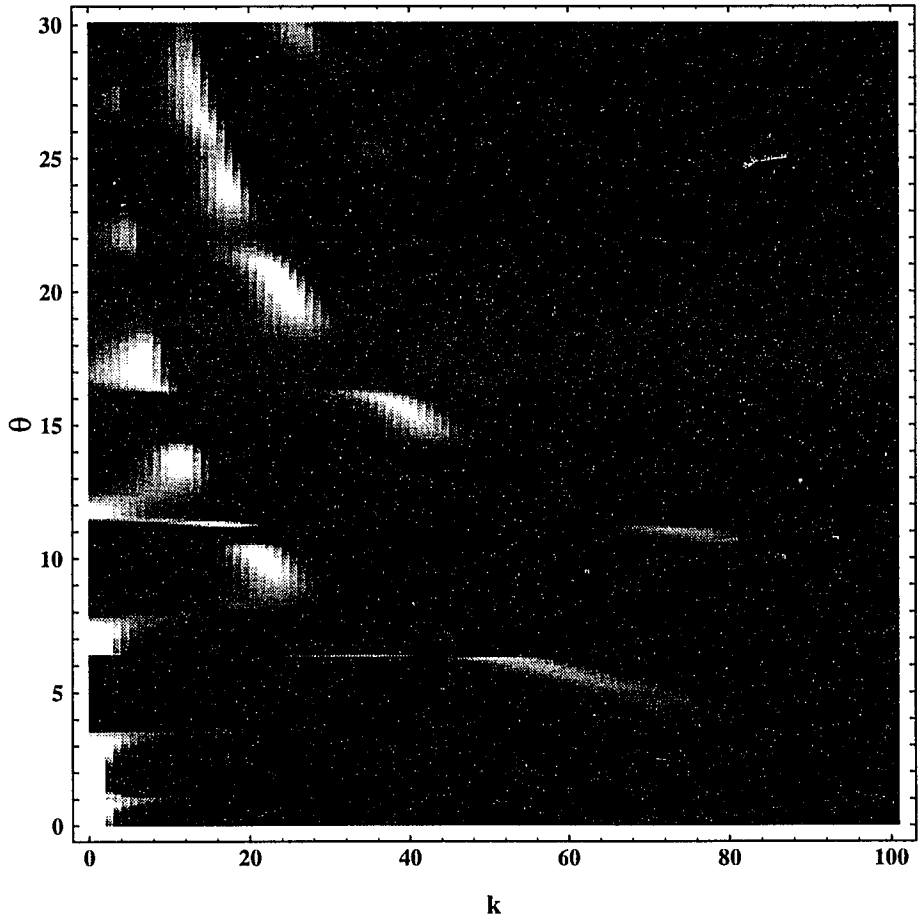

FIG. 3 (a): Density plot of the photon statistics of the second micromaser in the θ - k space for $N'_{ex} = N''_{ex} = 300$ and $\bar{n}'_b = \bar{n}''_b = 0.5$ in the case of incoherent coupling. Transitions between the phases shown in Fig. 2 are apparent triggered, via injected absorption, by the abrupt jumps in the average photon number of the first micromaser.

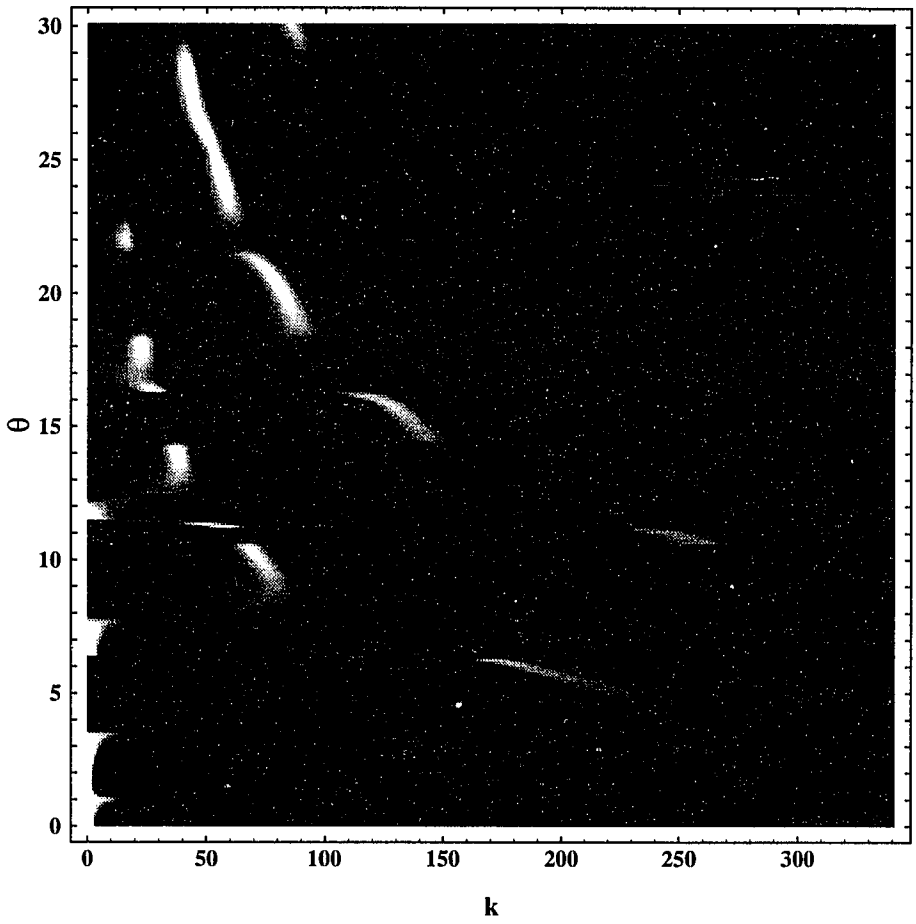

FIG. 3 (b): Same as Fig. 3 (a) for $N''_{ex} = 1000$.

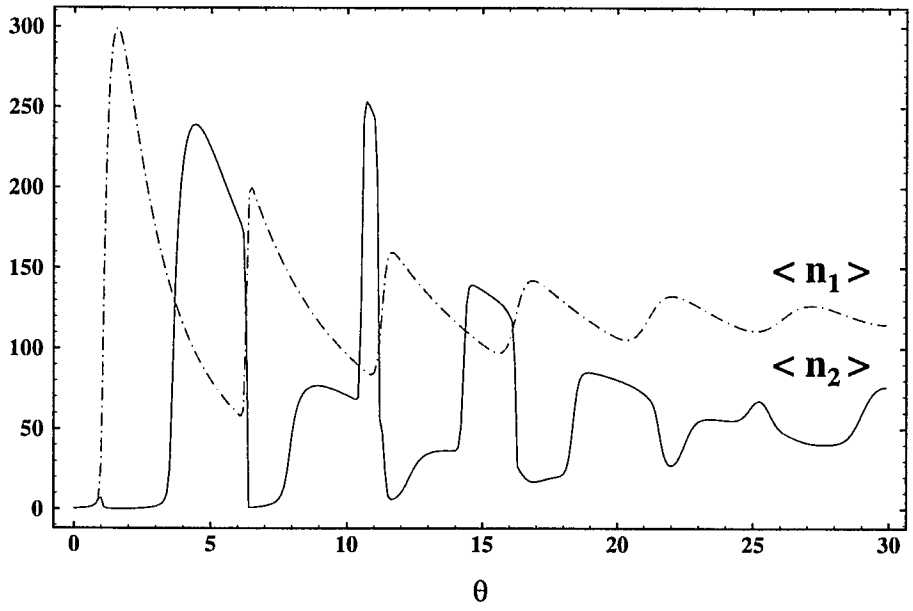

FIG. 4 (a): Average steady state photon numbers, $\langle n_1 \rangle$ and $\langle n_2 \rangle$, of the first and second micromasers as functions of the pump parameter, θ, depicted by dot-dashed and solid lines, respectively. They are calculated from the photon statistics depicted in Figs. 2 and 3 (b), respectively.

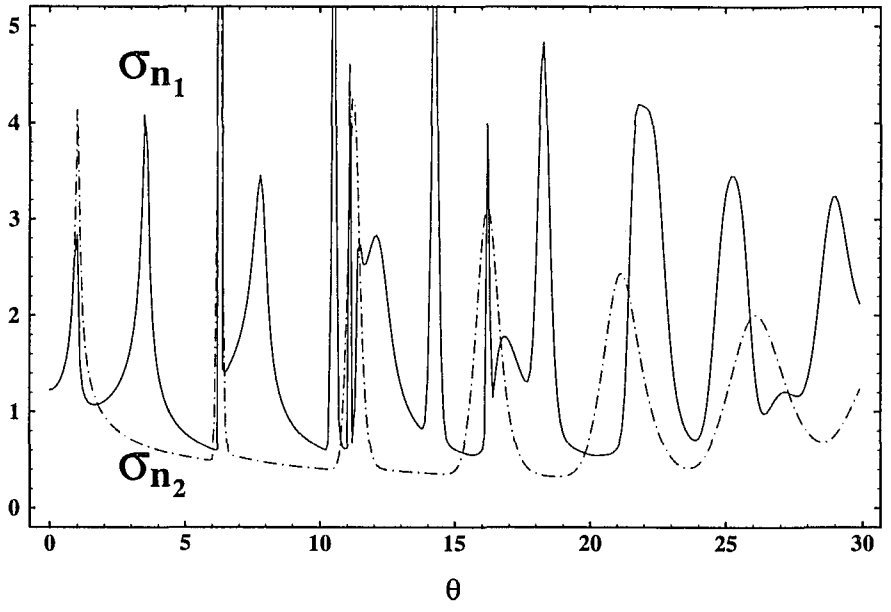

FIG. 4 (b): Normalized standard deviations of the steady state photon number distributions, $\sigma_i = \sqrt{\left(\langle n_i^2\rangle - \langle n_i\rangle^2\right)/\langle n_i\rangle}$, $i = 1, 2$ of the first and second micromasers as functions of the pump parameter, θ, depicted by dot-dashed and solid lines, respectively. They are calculated from the photon statistics depicted in Figs. 2 and 3 (b), respectively.

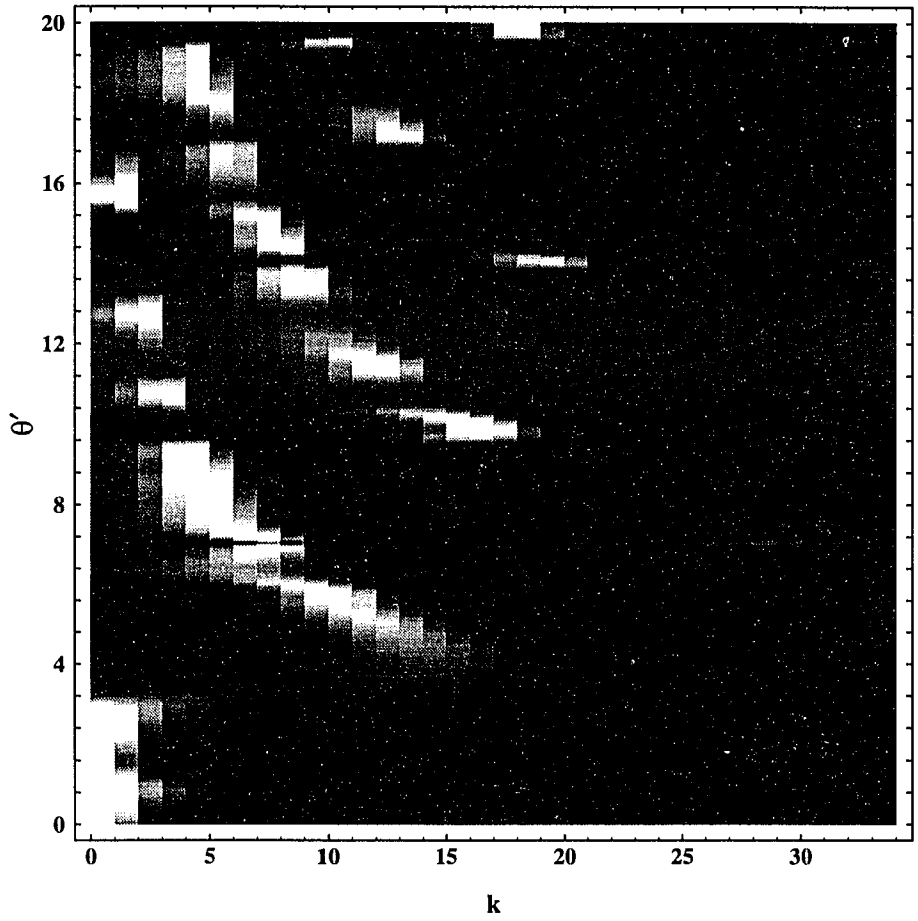

FIG. 5: Density plot of the photon statistics of the second micromaser in the θ - k space for $N'_{ex} = 10$, $N''_{ex} = 50$ and $\bar{n}'_b = 0$, $\bar{n}''_b = 0.2$ in the case of incoherent coupling. Jumps between the phases of an ordinary micromaser of $N_{ex} = 50$ are apparent triggered, via injected absorption, by the trapping states of the first micromaser.

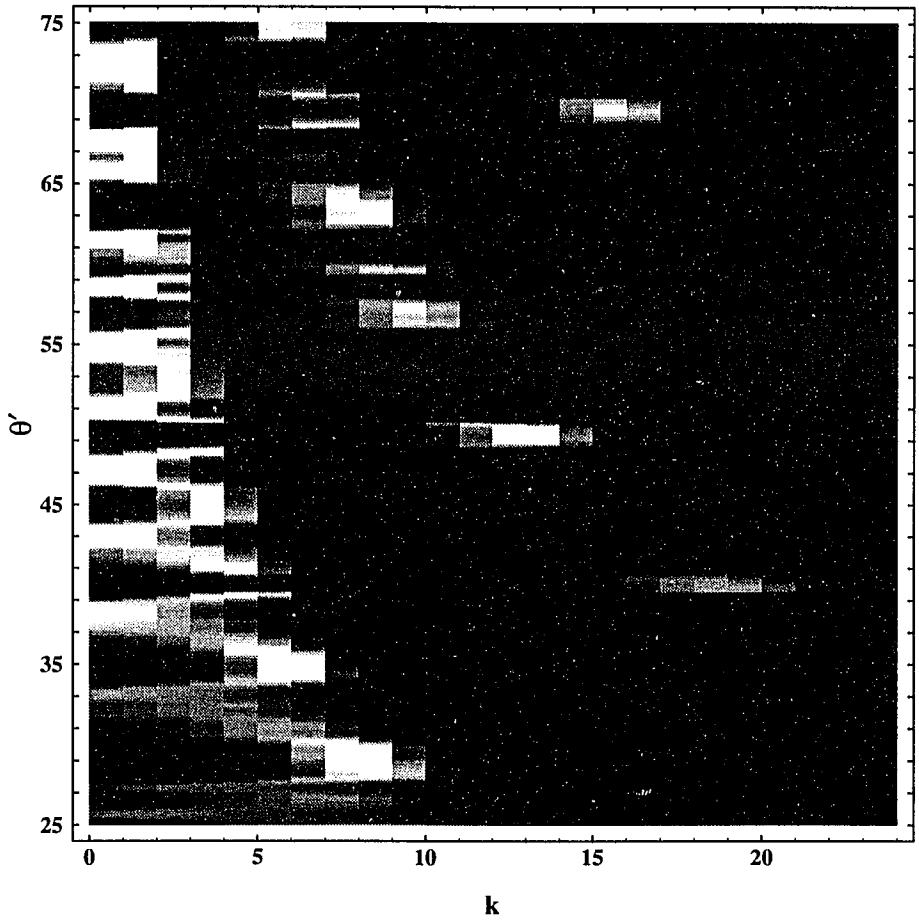

FIG. 6: Density plot of the photon statistics of the second micromaser in the θ - k space for $N'_{ex} = 10$, $N''_{ex} = 40$ and $\bar{n}'_b = \bar{n}''_b = 0.1$ in the case of incoherent coupling. Jumps between the phases of an ordinary micromaser of $N_{ex} = 40$ are apparent triggered, via injected absorption, by the quantum island states of the first micromaser.

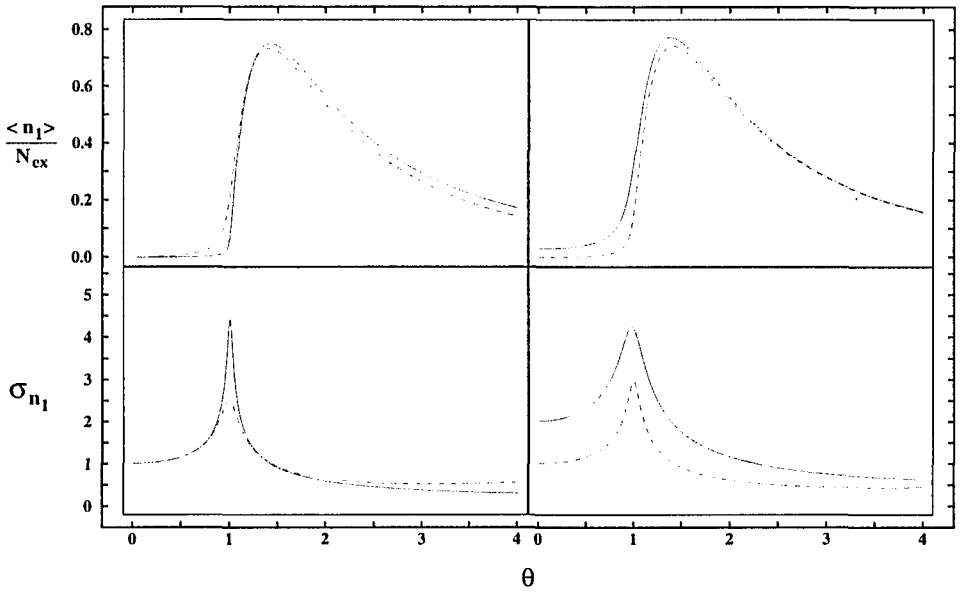

FIG. 7: Steady state normalized photon number in the first cavity, $\langle n_1 \rangle / N_{ex}$, and normalized standard deviation, σ_{n_1}, obtained from the Fokker-Planck equation in the P - representation as functions of the pumping parameter, θ. In the left two panels the N_{ex} - dependence is shown by switching from $N_{ex} = 50$ (dot-dash line) to $N_{ex} = 500$ (solid line) and, at the same time, keeping $\bar{n}_b' = 0.0$. The dependence on the thermal photon number is illustrated in the right two panels using $N_{ex} = 100$ with $\bar{n}_b' = 0$ (dot-dash lines) and $\bar{n}_b' = 3.0$ (solid lines).

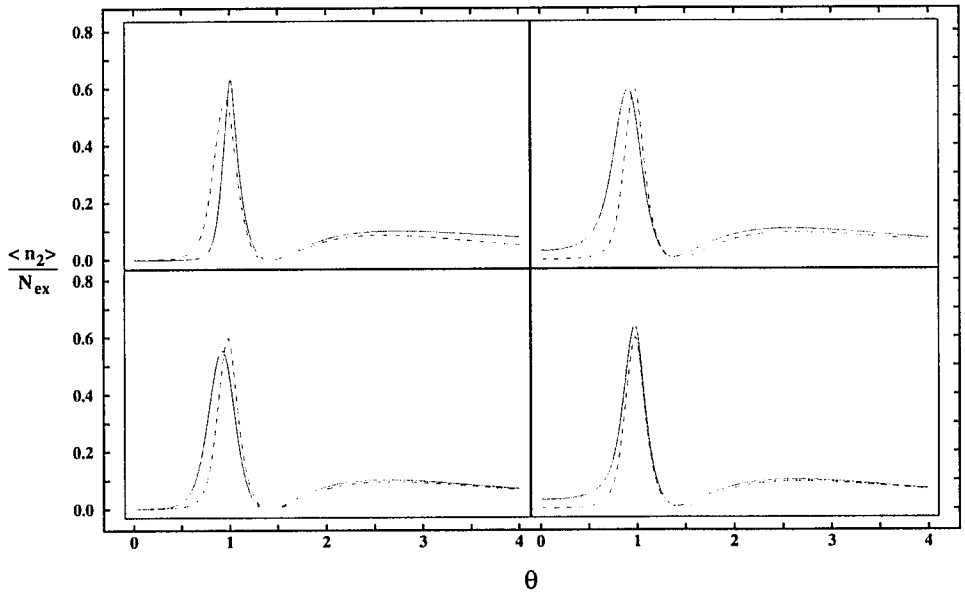

FIG. 8: Steady state normalized photon number in the second cavity, $\langle n_2 \rangle / N_{ex}$, obtained from the Fokker-Planck equation in the P - representation as a function of the pumping parameter, θ. In the upper-left panel the N_{ex} - dependence is shown by switching from $N_{ex} = 50$ (dot-dash line) to $N_{ex} = 500$ (solid line) and, at the same time, keeping $\bar{n}_b' = \bar{n}_b'' = 0.0$ in both cases. The dependence on the thermal photon number is illustrated in the other three panels using $N_{ex} = 100$ and $\bar{n}_b' = \bar{n}_b'' = 0.0$ (dot-dash lines) while choosing $\bar{n}_b' = 3.0$ and $\bar{n}_b'' = 3.0$ in the upper-right, $\bar{n}_b' = 3.0$ and $\bar{n}_b'' = 0.0$ in the lower-left, $\bar{n}_b' = 0.0$ and $\bar{n}_b'' = 3.0$ in the lower-right panels, all depicted by solid lines.

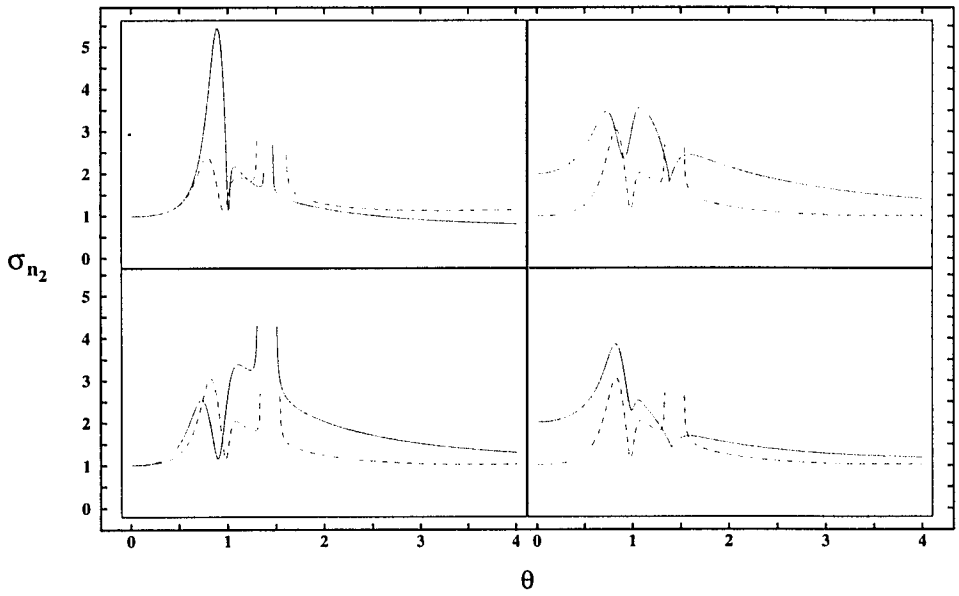

FIG. 9: Steady state normalized standard deviation of the photon number in the second cavity, σ_{n_2}, corresponding to Fig. 8.

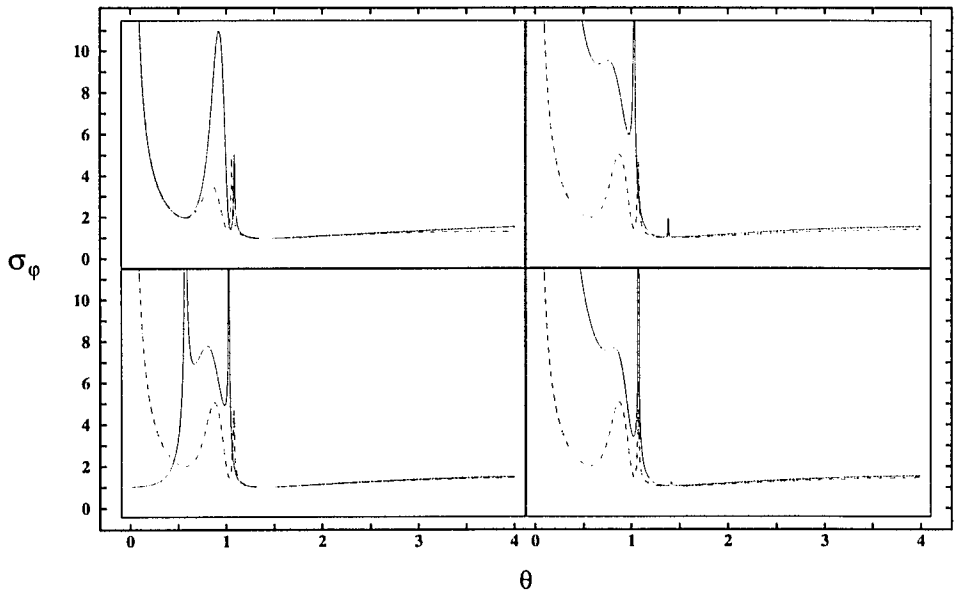

FIG. 10: Steady state noise in the relative phase, σ_φ, corresponding to Fig. 8. The boundary between squeezed and non-squeezed states is represented by the $\sigma_\varphi = 1$ line, while the dotted line separates classical (above line) and nonclassical (under line) behavior using $N_{ex} = 100$ and $\bar{n}_b' = \bar{n}_b'' = 0.0$ (the boundary does not significantly depend on the parameters, see Eq. (4.42)).

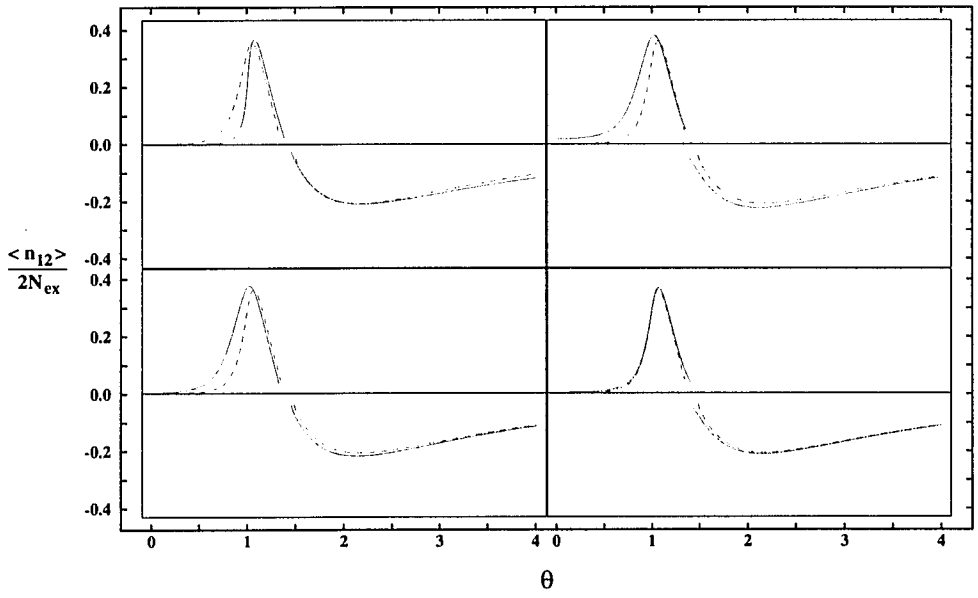

FIG. 11: Steady state normalized first order correlation, $\langle n_{12} \rangle / 2N_{ex}$, corresponding to Fig. 8.

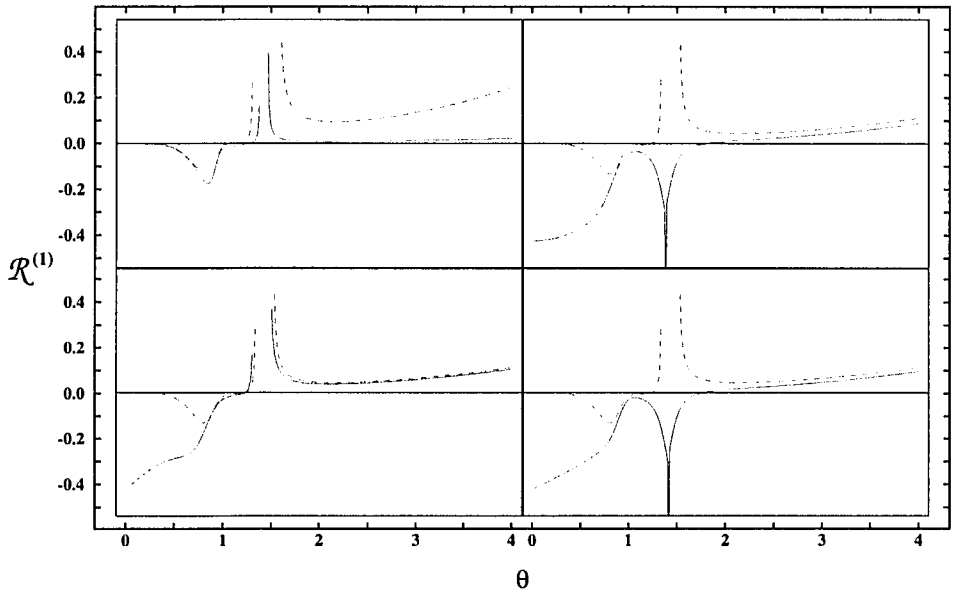

FIG. 12: Steady state first order correlation in the form, $\Re^{(1)}$, corresponding to Fig. 8.

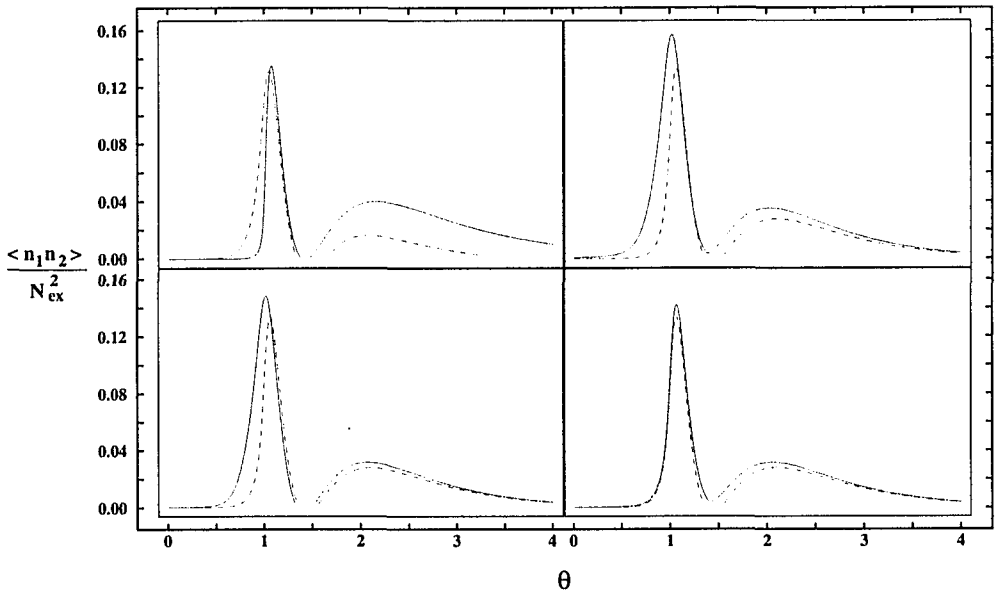

FIG. 13: Steady state normalized second order correlation, $\langle n_1 n_2 \rangle / N_{ex}^2$, corresponding to Fig. 8.

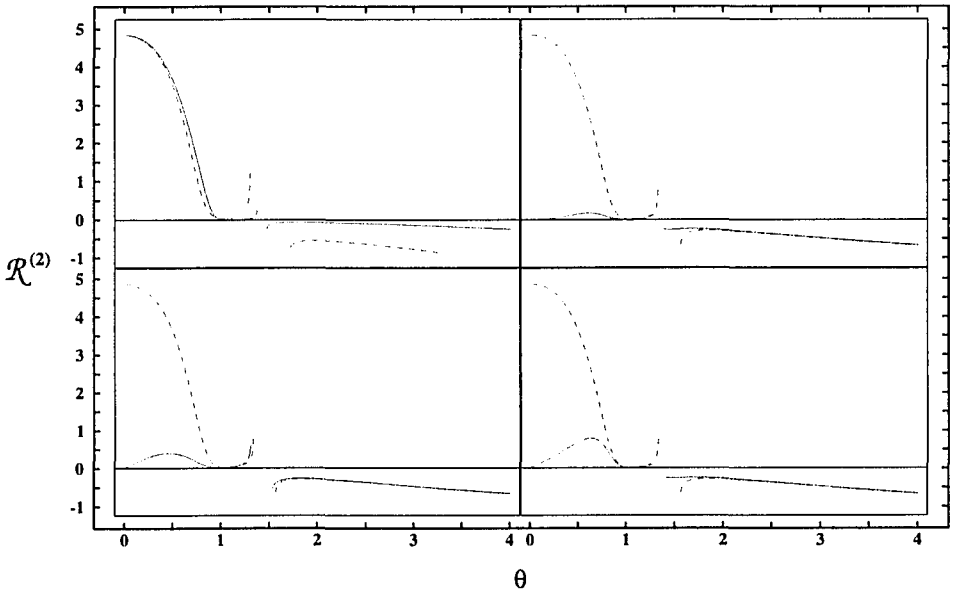

FIG. 14: Steady state second order correlation in the form, $\Re^{(2)}$, corresponding to Fig. 8.

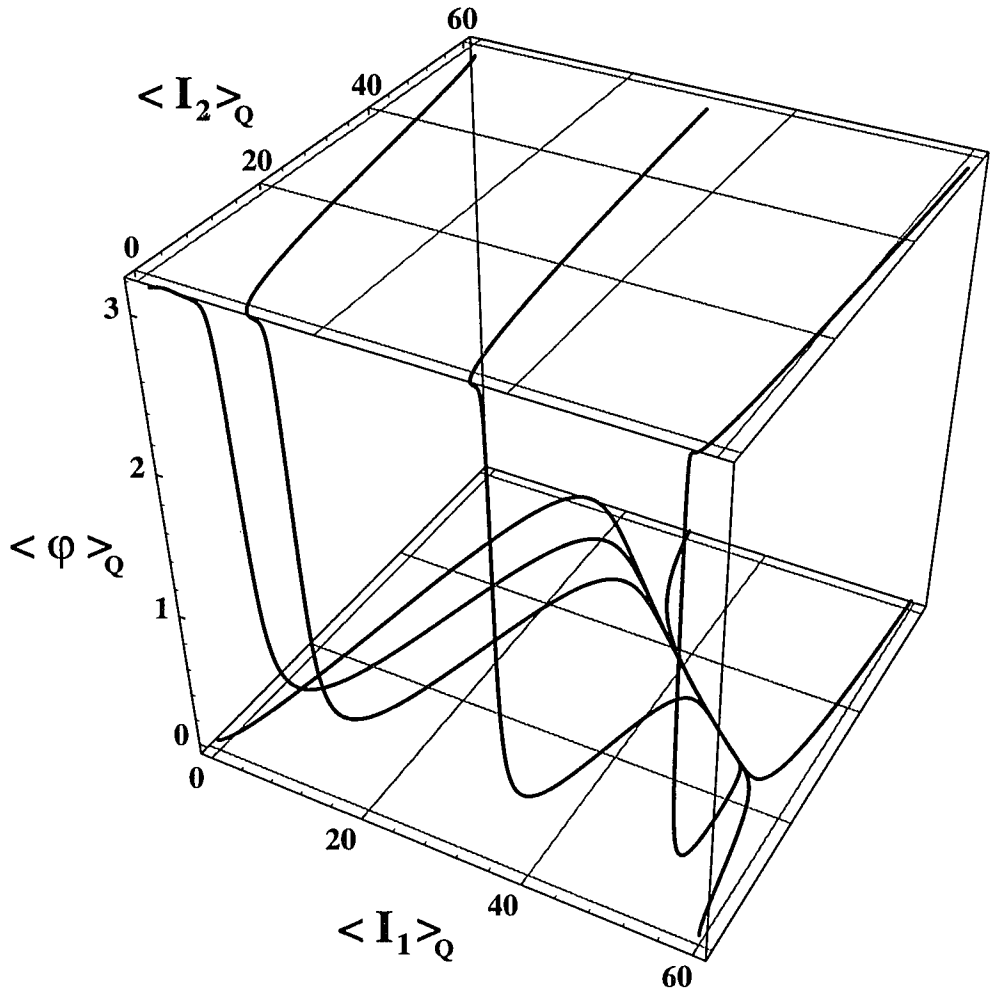

FIG. 15 (a): Evolution of the system in the phase-space of $\langle I_1 \rangle_Q$ - $\langle I_2 \rangle_Q$ - $\langle \varphi \rangle_Q$ obtained from the Fokker-Planck equation in the Q - representation for the pumping parameter, $\theta = 1.1$, using various initial conditions. The parameters are $N_{ex} = 100$ and $\bar{n}_b' = \bar{n}_b'' = 1.0$.

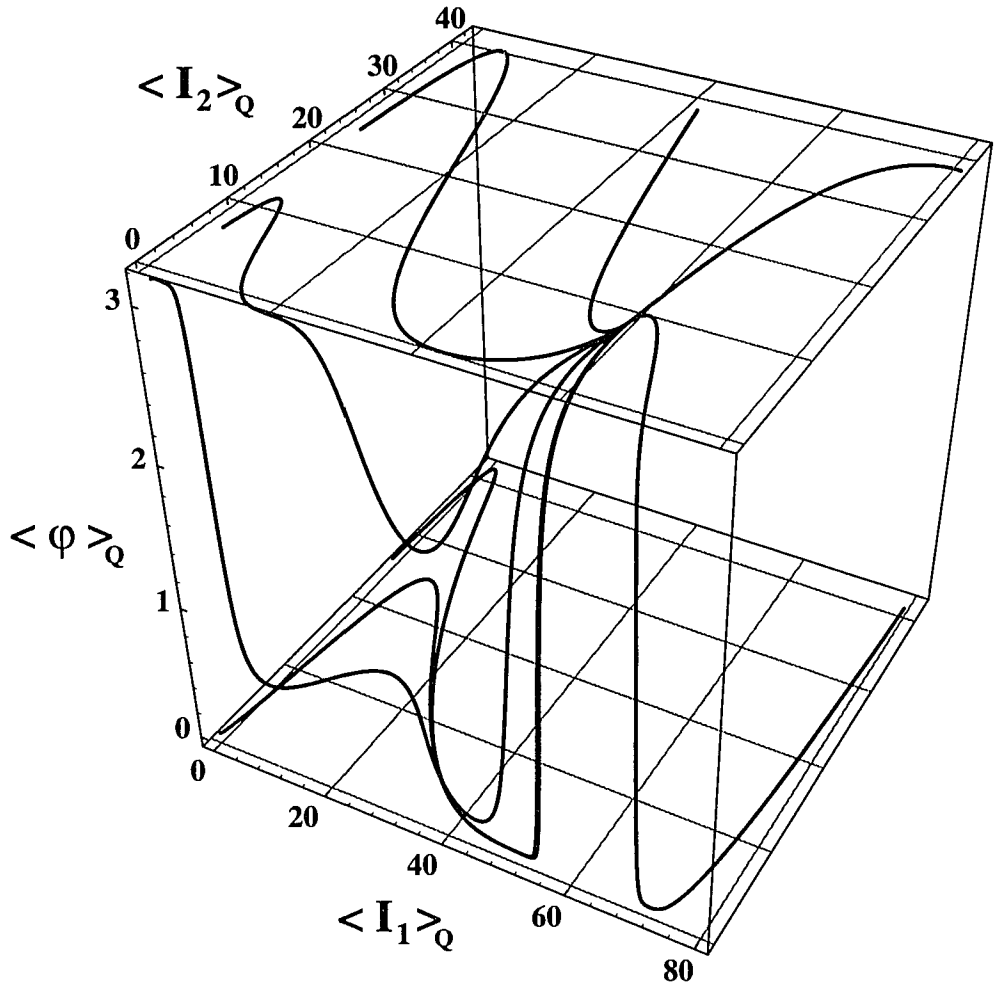

FIG. 15 (b): Evolution of the system in the phase-space of $\langle I_1 \rangle_Q$ - $\langle I_2 \rangle_Q$ - $\langle \varphi \rangle_Q$ obtained from the Fokker-Planck equation in the Q - representation for the pumping parameter, $\theta = 2.0$, using various initial conditions. The parameters are $N_{ex} = 100$ and $\bar{n}_b' = \bar{n}_b'' = 1.0$.

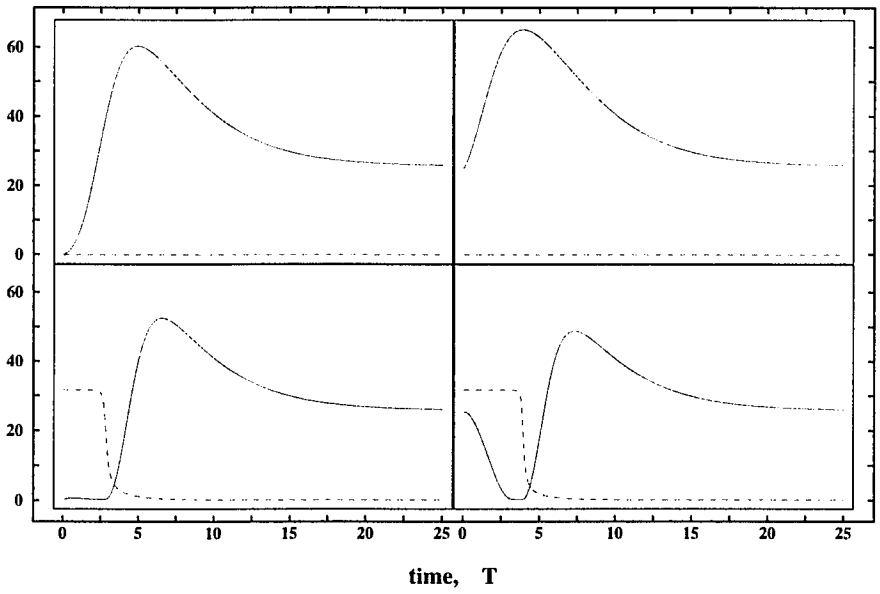

FIG. 16 (a): Time development of the system corresponding to Fig. 15 (a) using various initial conditions. The intensities, $\langle I_1 \rangle_Q$ and $\langle I_2 \rangle_Q$, and the magnified relative phase, $10\langle \varphi \rangle_Q$, are depicted by dotted, solid and dot-dashed lines, respectively.

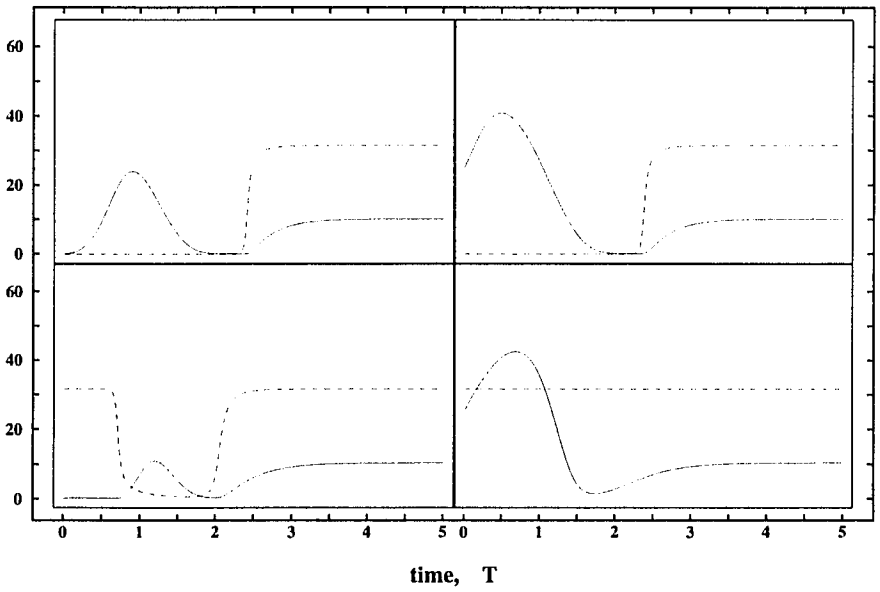

FIG. 16 (b): Time development of the system corresponding to Fig. 15 (b) using various initial conditions. The intensities, $\langle I_1 \rangle_Q$ and $\langle I_2 \rangle_Q$, and the magnified relative phase, $10\langle \varphi \rangle_Q$, are depicted by dotted, solid and dot-dashed lines, respectively.

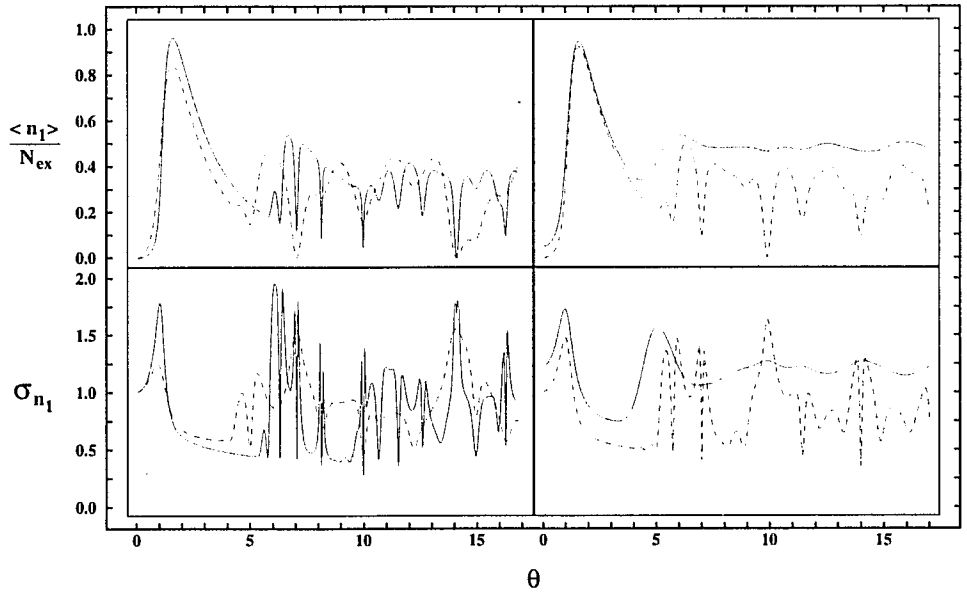

FIG. 17: Steady state normalized photon number in the first cavity, $\langle n_1 \rangle / N_{ex}$, and normalized standard deviation, σ_{n_1}, obtained from numerical simulations as functions of the pumping parameter, θ. In the left two panels the N_{ex} - dependence is shown by switching from $N_{ex} = 5$ (dot-dash line) to $N_{ex} = 20$ (solid line) and at the same time keeping $\bar{n}_b' = 0.0$. The dependence on the thermal photon number is illustrated in the right two panels using $N_{ex} = 10$ with $\bar{n}_b' = 0.0$ (dot-dash lines) and $\bar{n}_b' = 0.5$ (solid lines).

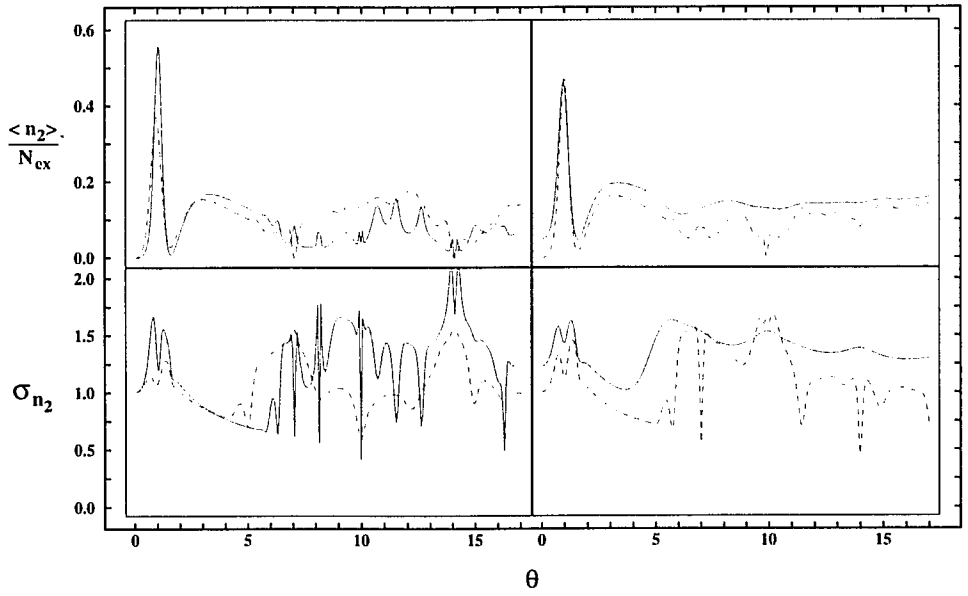

FIG. 18: Steady state normalized photon number in the second cavity, $\langle n_2 \rangle / N_{ex}$, and normalized standard deviation, σ_{n_2}, obtained from numerical simulations as functions of the pumping parameter, θ. In the left two panels the N_{ex} - dependence is shown by switching from $N_{ex} = 5$ (dot-dash line) to $N_{ex} = 20$ (solid line) and, at the same time, keeping $\bar{n}_b = 0.0$ ($\bar{n}_b \equiv \bar{n}_b' = \bar{n}_b''$). The dependence on the thermal photon number is illustrated in the right two panels using $N_{ex} = 10$ with $\bar{n}_b = 0.0$ (dot-dash lines) and $\bar{n}_b = 0.5$ (solid lines).

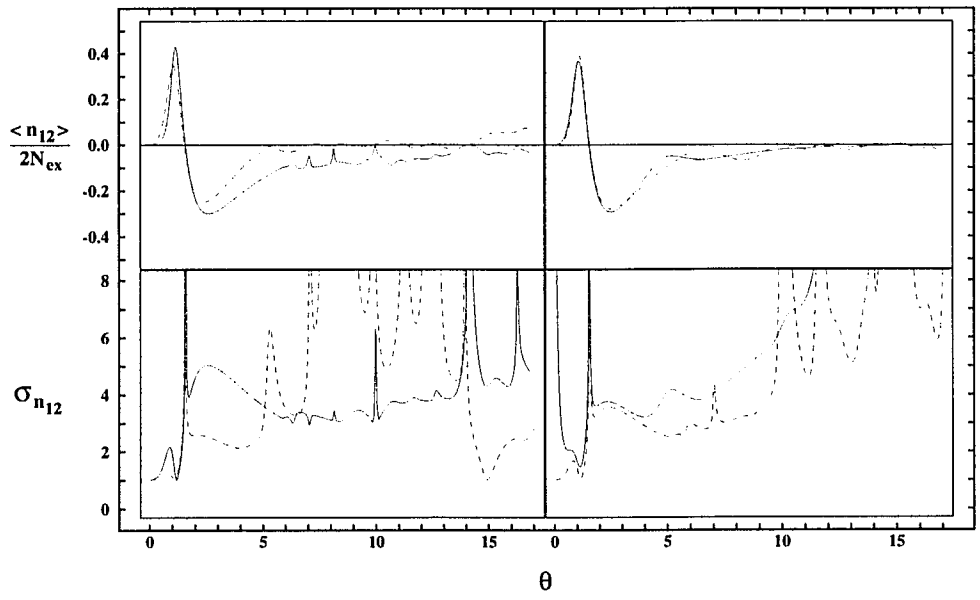

FIG. 19: Steady state normalized first order correlation, $\langle n_{12} \rangle / 2N_{ex}$, and normalized standard deviation, $\sigma_{n_{12}}$, corresponding to Fig. 18.

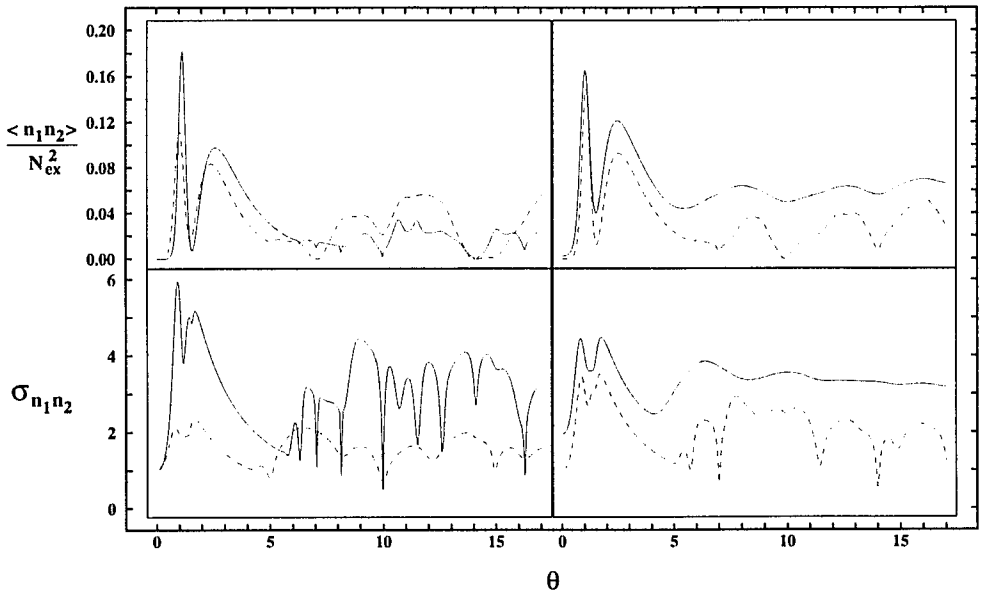

FIG. 20: Steady state normalized second order correlation, $\langle n_1 n_2 \rangle / N_{ex}^2$, and normalized standard deviation, $\sigma_{n_1 n_2}$, corresponding to Fig. 18.

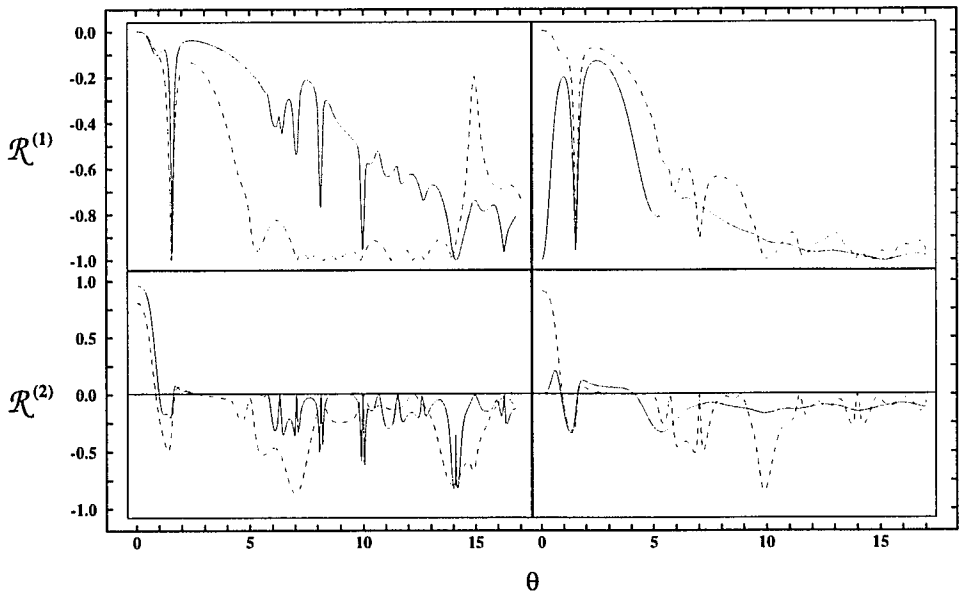

FIG. 21: Steady state first and second order correlations in the forms, $\Re^{(1)}$ and $\Re^{(2)}$, in the upper and lower rows, respectively, corresponding to Fig. 18.

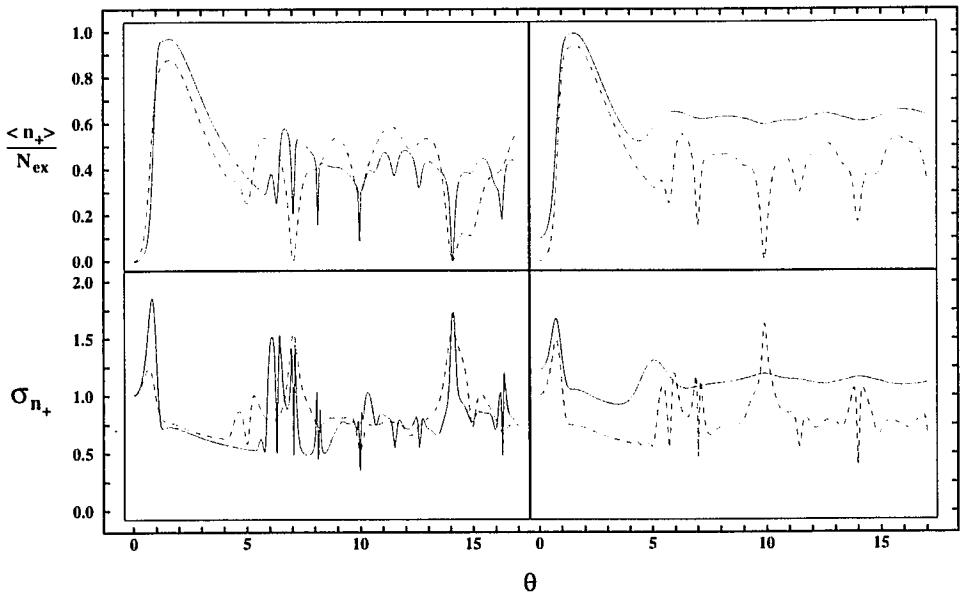

FIG. 22: Sum of the steady state normalized photon numbers in the two cavities, $\langle n_+ \rangle / N_{ex}$, and normalized standard deviation, σ_{n_+}, corresponding to Fig. 18. Comparing to Figs. 17 and 18 one can see that there are some regions in θ where σ_{n_+} is smaller than *1* (sub-Poissonian) even though σ_{n_1} and σ_{n_2} are both larger than *1* (super-Poissonian). This is due to the positive second order correlation between the fields in those regions.

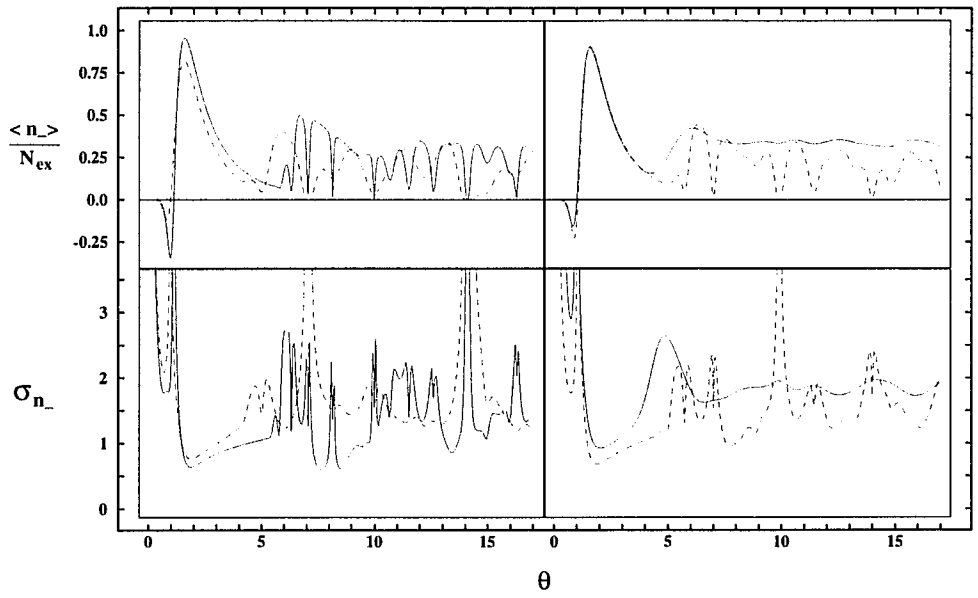

FIG. 23: Difference of the steady state normalized photon numbers in the two cavities, $\langle n_- \rangle / N_{ex}$, and normalized standard deviation, σ_{n_-}, corresponding to Fig. 18. Apparently, $\langle n_2 \rangle$ is larger than $\langle n_1 \rangle$ for $\theta < 1$ due to the correlations.

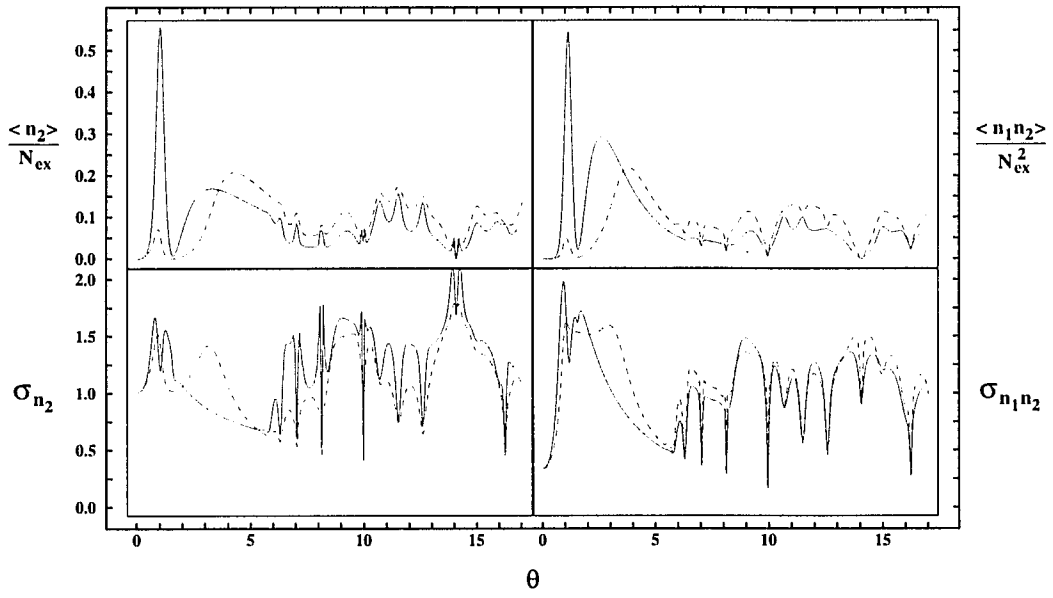

FIG. 24: Left two panels: Steady state normalized photon number in the second cavity, $\langle n_2 \rangle / N_{ex}$, and normalized standard deviation, σ_{n_1}, obtained from numerical simulations as functions of the pumping parameter, θ, for coherent (solid lines) and incoherent coupling (dot-dash lines). The parameters are, $N_{ex} = 20$ and $\bar{n}_b = 0.0$ ($\bar{n}_b \equiv \bar{n}_b' = \bar{n}_b''$). Right two panels: Steady state normalized second order correlation, $\langle n_1 n_2 \rangle / N_{ex}^2$, and normalized standard deviation, $\sigma_{n_1 n_2}$, corresponding to the left two panels.

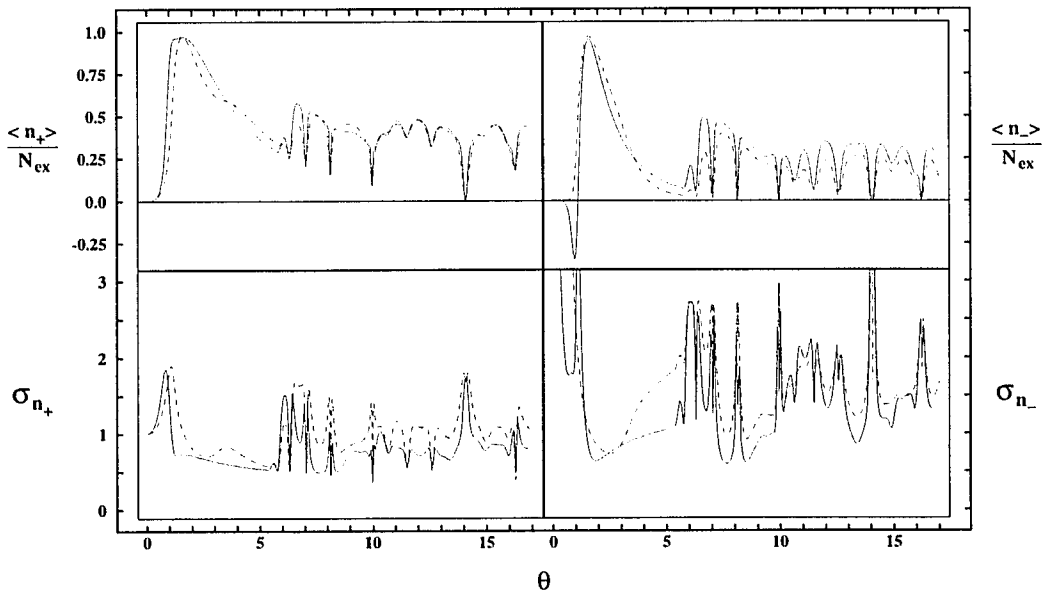

FIG. 25: Left two panels: Sum of the steady state normalized photon numbers in the two cavities, $\langle n_+ \rangle / N_{ex}$, and normalized standard deviation, σ_{n_+}, corresponding to Fig. 24. Right two panels: Difference of the steady state normalized photon numbers in the two cavities, $\langle n_- \rangle / N_{ex}$, and normalized standard deviation, σ_{n_-}, corresponding to Fig. 24. In the case of incoherent coupling, the photon number in the second micromaser is always smaller than that in the first one and, therefore, $\langle n_- \rangle / N_{ex}$ is positive for any θ.

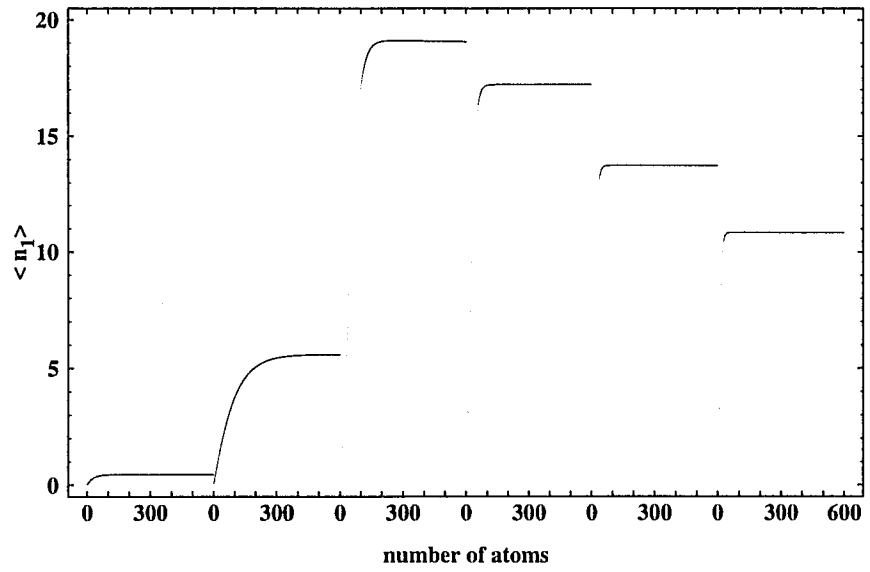

FIG. 26: Time development of the average photon number in the first micromaser, $\langle n_1 \rangle$, as a function of the number of atoms. Here, $N_{ex} = 20$ and $\bar{n}_b' = 0.0$, and the pumping parameter for the curves are $\theta = 0.5, 1.0, 1.5, 2.0, 2.5$ and 3.0 from left to right, respectively.

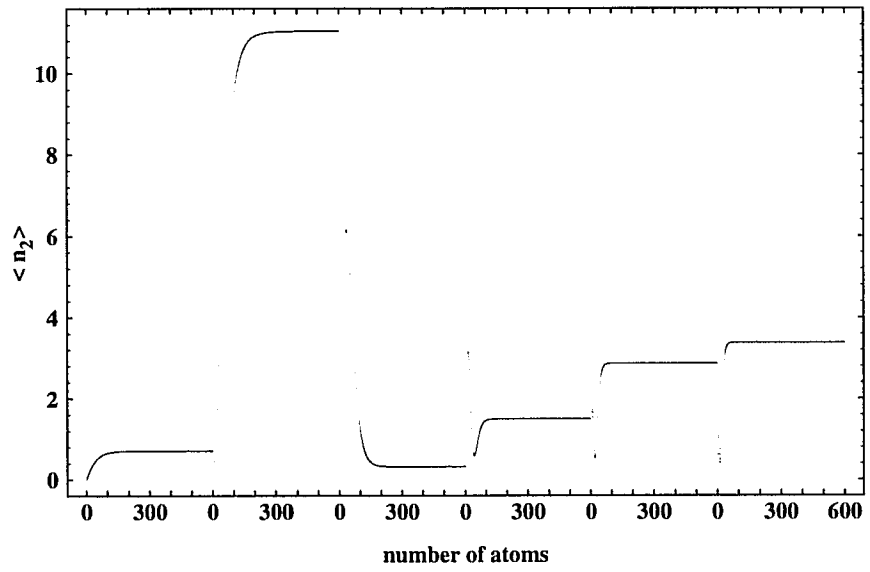

FIG. 27: Time development of the average photon number in the second micromaser, $\langle n_2 \rangle$, as a function of the number of atoms corresponding to Fig. 26 ($\bar{n}_b'' = 0.0$).

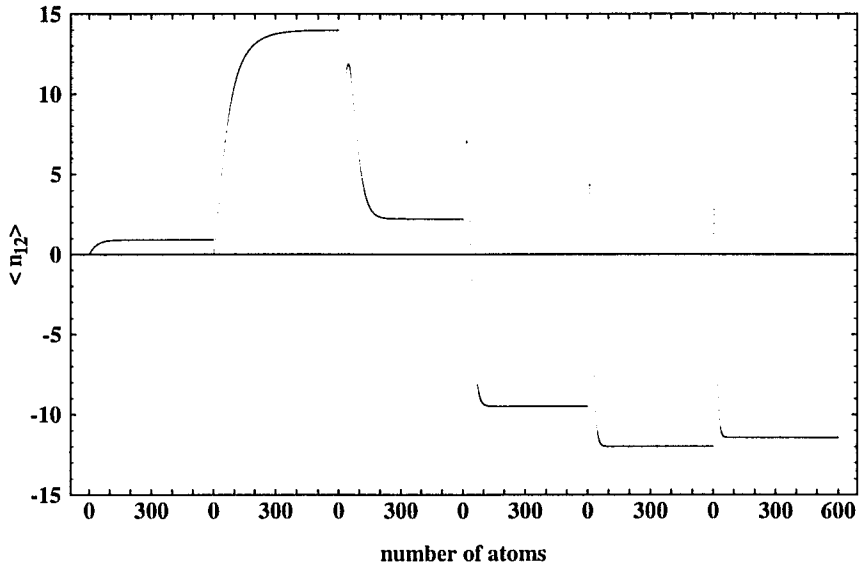

FIG. 28: Time development of the first order correlation, $\langle n_{12} \rangle$, as a function of the number of atoms corresponding to Fig. 27.

3.2.2 Pump-coupled High-Q Micromasers with Conditional Measurements of Atoms: Transient and Steady State Entanglement of Nonlocal Fields†

ABSTRACT

Two lossless micromasers are coupled in series by the common pumping beam of two-level atoms the states of which are measured conditionally after the second cavity. Pure evolutions of the two fields are studied starting from uncorrelated coherent states for the four measurement schemes denoted by *a*-*M′M″*-*a*, *b*-*M′M″*-*b*, *a*-*M′M″*-*b* and *b*-*M′M″*-*a* indicating the state of each atom, $|a\rangle$ or $|b\rangle$, before and after the two maser cavities, M' and M''. It is shown that energy-preserving schemes (first two above) produce a two-dimensional set of distinct Fock states at steady state under the envelope of the initial amplitude distribution of the fields. Since the initial fields were uncorrelated the generated ones will be uncorrelated too. In the case of energy-transferring schemes (second two) the system makes transitions between correlated and uncorrelated regimes. Nonlocal superpositions reminiscent of the form of $|N,N+M\rangle+|N+M,N\rangle$ can be generated at an optimum number of atoms as a result of two co-existing trapping mechanisms. This is a transient entanglement since it is destroyed by the atoms to follow due to the trapping effects themselves. However, we also show that by switching from any of the two energy-transferring schemes to any of the two preserving ones the transient correlation produced by the former scheme can be frozen into a steady state by the latter one. In the absence of dissipations this combination of schemes can generate steady state coherent superpositions of arbitrary number states of two nonlocal fields (nonlocal Schrödinger-cats) at reasonably high detection probabilities of the conditioned atomic states.

PACS Numbers: 42.50.Dv, 42.52+x

I. INTRODUCTION

It has been shown that the one-atom maser [1], or micromaser is a genuine quantum device. The interaction of its single-mode microwave field in a high-Q cavity with the driving two-level Rydberg atoms illustrates the irreconcilable difference between classical and quantum physics particularly clearly [2,3]. Nonclassical states of the radiation field were shown to be created in this system theoretically [4-17] and successfully generated experimentally [18-22]. There has always been a satisfactory agreement between experimental data and theoretical predictions.

One way to prepare such nonclassical fields is to perform measurements [23-25] on the atoms emerging from the interaction cavity making the field part of the entangled atom-field system reduce into the desired quantum state. The outcome of the measurements is not totally predictable, since according to quantum mechanics there is an element of chance attached to it. Nevertheless, a certain sequence of measurements determines the state of the field completely. In other words, we do not know prior to the experiment which state of the field will be produced, but we can redo the experiment until the required sequence of measurements consequently the desired trajectory for the evolution of the state of the field is achieved. This is called conditional measurement.

In this paper we couple two micromasers in series via the common pumping atomic beam [26] and perform conditional measurements on the state of the atoms emerging from the second micromaser (see Fig. 1). We consider four different measurement schemes: when the first micromaser is pumped by atoms in the upper (or lower) state of the maser transition and each of them emerging from the second micromaser is required to be detected in the upper (or lower) state in a row. Let us denote these schemes by a-$M'M''$-a, b-$M'M''$-b, a-$M'M''$-b and b-$M'M''$-a showing the sate of each atom, $|a\rangle$ or $|b\rangle$,before and after the interaction with the two maser cavities, M' and M''. The following assumptions are applied:

Firstly, there is at most one atom present in the cavities at a time in order to avoid

cooperative effects. This is the usual regime in which the one-atom maser experiments operate. As a second condition, we consider extremely high-Q cavities, where the loss of photons during the time of the experiment can be ignored. The quality factor Q of the cavities can reach values of up to 10^{11}, and with a microwave frequency of 20 GHz this results in photon lifetimes of several seconds. Thirdly, thermal photons have to also be suppressed in order to avoid the induced decay of the fields. We can eliminate thermal photons by cooling the cavities down to a temperature of $T = 0.1\ K$ and the corresponding mean photon number at the above microwave frequency is $3 \cdot 10^{-5}$. Finally, we assume 100% detection efficiency for the field ionization detectors measuring the state of the outcoming atoms in order to have each atom detected after the interaction.

By the time the atoms reach the second cavity they have gone through an interaction with the first field. The second micromaser is consequently pumped by atoms in a coherent superposition of their two masing levels depending upon the state of the field in the first one. In other words, there are always two different paths that the atoms can follow to reach the same final state detected the probabilities of which depend upon the state of the field in the first micromaser. Quantum coherence, i.e. quantum correlation between the two fields arises from the interference of the two atomic paths, reminiscent of the one in Young's double slit experiment [26]. As soon as we have "which-path" information, i.e. the state of the atom between the cavities is detected, the coherence disappears. In the absence of losses we can use the wavefunction of the entangled system of the two fields because pure quantum states are achieved. The effect of losses and thermal radiation mixing the quantum states of the fields is investigated in a subsequent publication. It is shown there that coherence survives these decay processes and manifests itself in a typical structure of the density matrix indicating the two different atomic paths.

The present paper studies the evolution of the pure quantum states of the composite system of the two fields for all four schemes described above. The probabilities of the two atomic paths are manipulated via the interaction times in the two cavities. For

initial uncorrelated coherent states of the fields one can produce a two-dimensional set of uncorrelated Fock states using energy-preserving schemes, while in the case of energy-transferring schemes transient entanglement of the fields can be achieved. Combining the two kinds of schemes together we show that steady state production of arbitrary coherent superpositions of macroscopically high photon number states of the two different micromaser fields - often referred to as nonlocal Schrödinger-cats - can be generated [27,28].

The paper is organized as follows: Section II reviews the single lossless micromaser problem with conditional measurements in order to see the effect of measurement and to setup a notation. Section III introduces the corresponding two-cavity problem the results of which are then used to investigate the four above mentioned measurement schemes and their combinations in Section IV. Section V is devoted to discussions and summary.

II. SINGLE MICROMASER WITH CONDITIONAL MEASUREMENTS OF ATOMS

Consider a beam of two-level atoms (upper $|a\rangle$, lower $|b\rangle$) interacting with a resonant microwave field in a lossless cavity of zero temperature. Atoms are consecutively injected in such a way that there is at most one atom in the cavity at a time, and the interaction time is the same for each atom (i. e. no atomic velocity spread). We know the state of the injected atoms before and measure the state of the outcoming atoms after the interaction. Let us consider four different schemes: each atom is injected in its upper (lower) state and detected in its upper (lower) state in a row. Let us denote these cases by: *a-M-a*, *b-M-b*, *a-M-b* and *b-M-a*, showing the state of the atoms before and after the maser cavity *M*.

The state of the field after the k-1^{st} atom left but before the k^{th} atom entered the cavity is given by

$$\left|\Psi^{(k-1)}\right\rangle = \sum_n \Psi_n^{(k-1)} |n\rangle \quad . \tag{2.1}$$

After the interaction the state of the atom-field system reads as

$$\left|\Phi^{(k)}\right\rangle = \sum_n \Psi_n^{(k-1)} \left[C_{n+1}|a,n\rangle - iS_{n+1}|b,n+1\rangle\right] \quad , \tag{2.2a}$$

or

$$\left|\Phi^{(k)}\right\rangle = \sum_n \Psi_n^{(k-1)} \left[C_n|b,n\rangle - iS_n|a,n-1\rangle\right] \quad , \tag{2.2b}$$

if atom number k was injected in its upper, or lower state, respectively. Here $C_n \equiv cos(g\tau\sqrt{n})$ and $S_n \equiv sin(g\tau\sqrt{n})$, where g is the atom-field coupling constant and τ is the interaction time assumed to be the same for each atom.

Now, let us make a state measurement on the k^{th} atom coming out from the cavity and consequently reduce the state of the field to

$$\left|\Psi^{(k)}\right\rangle = N^{(k)} \sum_n \Psi_n^{(k)} |n\rangle \quad , \tag{2.3}$$

where $N^{(k)}$ is the normalization constant and $\Psi_n^{(k)}$ are the new amplitudes. Each measurement step is followed by the renormalization of the state vector by $N^{(k)}$. The new amplitudes, $\Psi_n^{(k)}$, are functions of the old ones, $\Psi_n^{(k-1)}$, and for our four schemes they read as follows.

$$\Psi_n^{(k)} = \Psi_n^{(k-1)} C_{n+1} \quad , \tag{2.4a}$$

$$\Psi_n^{(k)} = \Psi_n^{(k-1)} C_n \quad , \tag{2.4b}$$

$$\Psi_n^{(k)} = \Psi_{n-1}^{(k-1)} S_n \quad , \tag{2.4c}$$

$$\Psi_n^{(k)} = \Psi_{n+1}^{(k-1)} S_{n+1} \tag{2.4d}$$

for the schemes *a-M-a*, *b-M-b*, *a-M-b* and *b-M-a*, respectively, providing us with the iteration rules to determine the evolution of the state of the fields from atom to atom. The probability of finding the k^{th} atom in the desired state is calculated as

$$P^{(k)} = \sum_n \left|\Psi_n^{(k)}\right|^2 = \frac{1}{N^{(k)2}} \quad . \tag{2.5}$$

Starting from an initial field given by the amplitudes, $\Psi_n^{(0)}$, apart from the normalization constant the field amplitudes after the k^{th} atom are given by

$$\Psi_n^{(k)} = \Psi_n^{(0)} C_{n+1}^k \quad , \tag{2.6a}$$

$$\Psi_n^{(k)} = \Psi_n^{(0)} C_n^k \quad , \tag{2.6b}$$

$$\Psi_n^{(k)} = \Psi_{n-k}^{(0)} S_n S_{n-1} \cdots S_{n-(k-1)} \quad , \tag{2.6c}$$

$$\Psi_n^{(k)} = \Psi_{n+k}^{(0)} S_{n+1} S_{n+2} \cdots S_{n+k} \tag{2.6d}$$

for *a-M-a*, *b-M-b*, *a-M-b* and *b-M-a*, respectively.

In the case of the two energy-preserving schemes, *a-M-a* and *b-M-b*, where atoms are injected and detected in the same states it can be seen from Eqs. (2.6a) and (2.6b) that starting from e. g. a coherent state of average photon number $|\alpha|^2$ the state vector evolves toward one or a superposition of several distinct Fock states as atoms go through the cavity. (For the sake of simplicity we are going to use the term "Fock

state" for the states that are actually Fock states only in the limit of k goes to infinity.) These peaks arise under the envelope of the initial amplitude distribution at those n's where the cosine function is equal to plus or minus one, because at any other points the k^{th} power of cosine is equal to zero in the limit of k goes to infinity. This means that the possible location of the peaks is determined by the equation, $g\tau\sqrt{n+1} = l\pi$ for *a-M-a* and $g\tau\sqrt{n} = l\pi$ for *b-M-b*, where $l = 0, 1, 2, \ldots$. Fig. 2 gives two examples for *a-M-a* for an initial coherent state of average photon number, $\alpha^2 = 10$, atom number, $k = 100$ and interaction parameters, $g\tau = 1.0$ and π. A single Fock state, $|9\rangle$, and a superposition of Fock states at integer's squares minus one are generated for $g\tau = 1.0$ and π, respectively. We get very similar results for *b-M-b*, although the peaks are shifted exactly by one toward larger n's due to the $+1$ difference in the argument of the cosine functions in Eqs. (2.6a) and (2.6b). For later purposes we should mention here that due to this reason it is possible to generate the vacuum Fock state, $|0\rangle$, via *b-M-b* which is not possible via *a-M-a*. The physical meaning of the $+1$ is that a two-level atom cannot absorb a photon from, but can emit a photon to the vacuum. Apart from this difference these two schemes apply very similar mechanisms. The measurement process favors those photon numbers for which the Rabi-angle is close to the multiples of π in order to have the same atomic state detected as the one that was injected. The state vector gradually becomes peaked at these photon numbers as atoms pass through.

For the energy-transferring schemes, *a-M-b* and *b-M-a*, where atoms are injected and detected in different states we have a complicated product of different sine functions in Eqs. (2.6c) and (2.6d). The example depicted in Fig. 3 for *a-M-b* shows that the initial distribution of the coherent state separates into two distinct parts as atoms pass through. The iteration rule Eq. (2.4c) tells us that the state vector shifts by one photon and gets multiplied by the same sine function, S_n, every time an atom passes through. Hence, a growing region of the state vector will have zero amplitudes when multiplied by $S_n = 0$, until finally, at a certain atom number, k, the whole wave function becomes zero. For this and all the consecutive atoms the probability of

measuring the desired atomic state, $|b\rangle$, is zero. The atom is trapped in the other state, $|a\rangle$, and the conditional measurement scheme cannot be followed beyond this point. If there is no such an integer number, n, for which $S_n = 0$ exactly, we will end up with a rapidly oscillating amplitude distribution as it can be seen in the figure enlarged due to the disappearance of the regular peaks evolving toward larger photon numbers (in *a-M-b* atoms always leave a photon in the cavity). Although the probability of detecting the lower atomic state is not zero in this case but it is small. The largest separation of the regular peaks that can be achieved before trapping (or before the oscillatory structure would show up) is determined by the location of the trapping states for which $S_{n_t} = 0$, given by $n_t = (l\pi/g\tau)^2$, $l = 1, 2, 3, \ldots$. The distribution is bound to evolve between these boundaries. Apart from the $+1$ difference in the argument of the sine functions in Eqs. (2.4c) and (2.4d) we have exactly the same effect for *b-M-a*, except that the direction of the shift in Eq. (2.4d) is the opposite, consequently the peaks evolve toward lower n's ending up finally in one of the trapping states after a certain number of atoms (in *b-M-a* atoms always absorb a photon from the cavity). Schemes, *a-M-b* and *b-M-a*, apply the same mechanisms. The measurement process suppresses those photon numbers from the distribution for which the Rabi-angle is close to the multiples of π and the emission (absorption) of a photon is prohibited for *a-M-b* (*b-M-a*). After a certain number of atoms the whole state vector becomes practically zero and the atoms are trapped in the upper (lower) state.

We are going to see the implications of these effects in the two-cavity problem in the next sections in "two degrees of freedom". The measurement process will select a pair or more importantly sometimes *two* pairs of photon numbers from the two fields to favor (disfavor). An interference of the two corresponding paths is expected in the latter case indicating that the states of the fields in the two *separate* micromaser cavities are no longer independent but they are *correlated.*

III. COUPLED MICROMASERS WITH CONDITIONAL MEASUREMENTS OF ATOMS

Let us consider now two micromaser fields coupled by the common pumping atomic beam in such a way that atoms first interact with the field in cavity *1* and then proceed to cavity *2* (see Fig. 1). The same assumptions apply as in Section II: no cavity losses, zero temperature, single atom resonant interaction, no atomic velocity spread, 100% detection efficiency. Similarly to Section II we investigate four different schemes: *a*-$M'M''$-*a*, *b*-$M'M''$-*b*, *a*-$M'M''$-*b* and *b*-$M'M''$-*a* indicating the state of each atom, $|a\rangle$ or $|b\rangle$, before and after the two maser cavities, M' and M''.

The state of the field after the k-1^{st} atom left but before the k^{th} atom entered the cavity is given by

$$\left|\Psi^{(k-1)}\right\rangle = \sum_{n_1,n_2} \Psi^{(k-1)}_{n_1,n_2} |n_1, n_2\rangle \quad . \tag{3.1}$$

After the k^{th} atom has interacted with the fields the state of the atom-fields system reads as

$$\begin{aligned} \left|\Phi^{(k)}\right\rangle = \sum_{n_1,n_2} \Psi^{(k-1)}_{n_1,n_2} \Big[& C'_{n_1+1}\left(C''_{n_2+1}|a, n_1, n_2\rangle - iS''_{n_2+1}|b, n_1, n_2+1\rangle\right) - \\ & -iS'_{n_1+1}\left(C''_{n_2}|b, n_1+1, n_2\rangle - iS''_{n_2}|a, n_1+1, n_2-1\rangle\right)\Big] \end{aligned} \quad , \tag{3.2a}$$

or

$$\begin{aligned} \left|\Phi^{(k)}\right\rangle = \sum_{n_1,n_2} \Psi^{(k-1)}_{n_1,n_2} \Big[& C'_{n_1}\left(C''_{n_2}|b, n_1, n_2\rangle - iS''_{n_2}|a, n_1, n_2-1\rangle\right) - \\ & -iS'_{n_1}\left(C''_{n_2+1}|a, n_1-1, n_2\rangle - iS''_{n_2+1}|b, n_1-1, n_2+1\rangle\right)\Big] \end{aligned} \quad , \tag{3.2b}$$

if the atom was injected in its upper, or lower state, respectively. Here,

$S'_{n_1} \equiv sin(g'\tau'\sqrt{n_1})$ and $C'_{n_1} \equiv cos(g'\tau'\sqrt{n_1})$ correspond to the first and the double-primed ones, S''_{n_2} and C''_{n_2}, to the second micromaser. After the interaction with both fields the state of the atom is measured and the state of the fields is reduced to

$$\left|\Psi^{(k)}\right\rangle = N^{(k)} \sum_{n_1,n_2} \Psi^{(k)}_{n_1,n_2} \left|n_1, n_2\right\rangle \quad . \tag{3.3}$$

Each measurement is followed by a renormalization of the state vector by $N^{(k)}$. The new amplitudes, $\Psi^{(k)}_{n_1,n_2}$, are functions of the old ones, $\Psi^{(k-1)}_{n_1,n_2}$, and for our four schemes they read as follows.

$$\Psi^{(k)}_{n_1,n_2} = \Psi^{(k-1)}_{n_1,n_2} C'_{n_1+1} C''_{n_2+1} - \Psi^{(k-1)}_{n_1-1,n_2+1} S'_{n_1} S''_{n_2+1} \quad , \tag{3.4a}$$

$$\Psi^{(k)}_{n_1,n_2} = \Psi^{(k-1)}_{n_1,n_2} C'_{n_1} C''_{n_2} - \Psi^{(k-1)}_{n_1+1,n_2-1} S'_{n_1+1} S''_{n_2} \quad , \tag{3.4b}$$

$$\Psi^{(k)}_{n_1,n_2} = \Psi^{(k-1)}_{n_1,n_2-1} C'_{n_1+1} S''_{n_2} + \Psi^{(k-1)}_{n_1-1,n_2} S'_{n_1} C''_{n_2} \quad , \tag{3.4c}$$

$$\Psi^{(k)}_{n_1,n_2} = \Psi^{(k-1)}_{n_1,n_2+1} C'_{n_1} S''_{n_2+1} + \Psi^{(k-1)}_{n_1+1,n_2} S'_{n_1+1} C''_{n_2+1} \tag{3.4d}$$

for *a*-*M'M''*-*a*, *b*-*M'M''*-*b*, *a*-*M'M''*-*b* and *b*-*M'M''*-*a*, respectively, providing us with the iteration rules determining the evolution of the state of the fields from atom to atom. The probability of finding the k^{th} atom in the desired state is

$$P^{(k)} = \sum_{n_1,n_2} \left|\Psi^{(k)}_{n_1,n_2}\right|^2 = \frac{1}{N^{(k)2}} \quad . \tag{3.5}$$

The evolution of the two fields will be studied in the next section by iterating the amplitudes according to one of the rules above starting from coherent states of the two fields. We are going to investigate the correlations building up between the two micromasers as a result of the interference between the two paths that each atom can

follow when traversing the cavities. In order to do so we define m^{th} order correlation by the nonseparability condition given by

$$\left\langle (\hat{a}_1 \hat{a}_2^{\dagger})^m \right\rangle \neq \left\langle \hat{a}_1^m \right\rangle \left\langle \hat{a}_2^{\dagger m} \right\rangle \quad , \tag{3.6}$$

where $\hat{a}_1$ and $\hat{a}_2$ are the field operators of micromasers *1* and *2*, respectively. We would like to draw attention to the fact that this is a correlation between fields of two different micromasers, i. e. an entanglement of two *nonlocal* subsystems. Thus, carrying out a measurement that reduces the state of one of the fields results in a reduction of the state of the other field located at a different point in space. One example of such state vector of M^{th} order correlation is given by

$$|\Psi\rangle = \frac{1}{\sqrt{2}} \left(|n_1, n_2\rangle \pm |n_1 \pm M, n_2 \mp M\rangle \right) \quad , \tag{3.7}$$

a possible production of which will be shown in the next section (see also in Ref. [28]). .

IV. EVOLUTION OF THE FIELDS FOR VARIOUS CONDITIONAL MEASUREMENT SCHEMES

Let us assume that both fields are initially in coherent states of the same α given by

$$\left|\Psi^{(0)}\right\rangle = e^{-\alpha^2} \sum_{n_1, n_2} \frac{\alpha^{n_1+n_2}}{\sqrt{n_1! n_2!}} |n_1, n_2\rangle \tag{4.1}$$

depicted for $\alpha^2 = 10$ and $k = 0$ in Fig. 5. According to Eq. (3.6) the two fields are uncorrelated because their state vector is separable into a tensor product of two coherent states in the two cavities as $|\alpha\rangle_{cavity1} \otimes |\alpha\rangle_{cavity2}$. We are going to consider typical examples for the evolution of the fields for the four conditional measurement schemes,

a-M'M"-a, *b-M'M"-b*, *a-M'M"-b* and *b-M'M"-a* applying the corresponding iteration rules of Eq. (3.4) and assuming equal interaction parameters, $g\tau \equiv g'\tau' = g''\tau''$, in both cavities.

IV.1. ENERGY-PRESERVING SCHEMES, *a-M'M"-a* AND *b-M'M"-b*

Atoms are injected into the first cavity and detected after the second one in the same state. Let us consider scheme *a-M'M"-a* first. The possible paths the atom can follow are $a_0a_1a_2$ and $a_0b_1a_2$ in Fig. 4. They both preserve the total energy of the two micromasers. Furthermore, $a_0a_1a_2$ preserves the photon number in both cavities separately, while $a_0b_1a_2$ make the photon number increase in the first and decrease in the second cavity. We can manipulate the probabilities of these paths via the interaction times in the cavities. Let us see some typical examples for the evolution and the steady state of the fields at different parameters.

Consider the interaction parameter, $g\tau = 1.0$. Fig. 5 shows that the state of the fields gets localized approximately in the Fock state, $|9,9\rangle$, as atom number k goes to infinity, with some contributions from $|10,8\rangle$, $|11,7\rangle$, ..., $|18,0\rangle$ that are decreasing with k. The solid line in Fig. 7 shows that the probability of finding the atom in the required upper state is increasing with k and is approximately unity for large k's. This effect can be understood in the following way. The initial amplitudes of the coherent fields are the largest around $n_1 = n_2 = 10$. For these photon numbers and for the above interaction times the probability of path $a_0a_1a_2$ is much larger than the one for the alternative path $a_0b_1a_2$, because $C_{10} \cong 1$ and $S_{10} \cong 0$ (see Eqs. (2.2a) and (2.2b)). The fields get localized around $n_1 \cong n_2 \cong 9$ due to path $a_0a_1a_2$ corresponding to a Rabi-angle of π, which localization further increases the enhancement of path $a_0a_1a_2$ itself. Path $a_0b_1a_2$ gives rise to the small contributions from $|10,8\rangle$, $|11,7\rangle$, ..., $|18,0\rangle$. Apart from these small amplitudes this production of a Fock state is very similar to the one discussed in Section II for the case of the single

micromaser. Since path $a_0a_1a_2$ has a very high probability throughout the whole evolution all atoms are practically in their upper state before, between and after the cavities. We practically have two *independent* micromasers both operating in scheme *a-M-a*, where atoms enter and leave both cavities in their upper state. Consequently, the same mechanism applies as the one for the single micromaser in *a-M-a* discussed in Section II, and we get the uncorrelated Fock state, $|9,9\rangle$, as a product of two $|9\rangle$'s depicted in Fig. 2 for each cavities. Small correlation builds up only in the transient regime of co-existing paths.

Let us now look at the interaction parameter, $g\tau = 0.5$. Fig. 6 shows the evolution of the state of the fields, while the probabilities of detecting the emerging atoms in the upper state are given by the dashed line in Fig. 7. For the initial coherent states the probability of path $a_0a_1a_2$ is now much smaller than the one for $a_0b_1a_2$, which implies that the number of photons is initially increasing in cavity *1* and decreasing in cavity 2. This can be seen in Fig. 6 for $k = 10$ and 70. At around $k = 114$ the field in cavity 2 experiences a jump from vacuum to a high photon number, and finally the system settles to a Fock state around $|39,39\rangle$ with some contributions from $|40,38\rangle$, $|41,37\rangle$, $|40,36\rangle$, ..., $|78,0\rangle$. Since $a_0b_1a_2$ has a high probability initially, atoms enter cavity 2 in their lower state. Thus, cavity *1* operates in scheme *a-M-b* and cavity 2 in *b-M-a*. Due to the increasing photon number in cavity *1* this mechanism terminates itself according to the trapping effect in scheme *a-M-b* discussed in Section II. At $n_1 \cong 39$ the probability of dropping a photon in cavity *1* becomes approximately zero, because $S_{n_1+1} \cong 0$, and the system is back to the schemes *a-M-a*, *a-M-a* in both cavities discussed above. The photon number in cavity *1* locks to $n_1 \cong 39$, while the one in cavity 2 becomes peaked according to the mechanism in a single micromaser in scheme *a-M-a*. Thus, the same uncorrelated steady state of the fields is generated as if they were independent, but the time evolution is different. Both fields lock to photon numbers that assure a Rabi angle of π that implies an *a-M-a*, *a-M-a* operation for both micromasers.

At large $g\tau$-s the system does not follow this kind of evolution (see Fig. 8). There

are several photon numbers in this case that drive the atom into both atomic states between the cavities resulting in superimposed *a-M-a*, *a-M-b* operation of the first and *a-M-a* , *b-M-a* operation of the second micromaser. Nevertheless, the state of the fields at steady state settles to a superposition of Fock states in both cavities that assure Rabi angles that are the multiples of π resulting again in an independent *a-M-a*, *a-M-a* operation for both micromasers. In the example in Fig. 8, where the parameter of the initial coherent state is $\alpha^2 = 30$ and $g\tau = \pi$ the fields settle to a steady state superposition of Fock states at integer squares minus one, mainly at *24* and *35*. Thus, the state of the field can be approximated with

$$|\Psi\rangle \cong N(|24,24\rangle + |35,35\rangle + |24,35\rangle + |35,24\rangle) \quad , \tag{4.2}$$

where *N* stands for normalization. It is easy to see that according to Eq. (3.6) the two fields are uncorrelated, because the state vector above is separable as

$$|\Psi\rangle \cong N(|24\rangle + |35\rangle)_{cavity1} \otimes (|24\rangle + |35\rangle)_{cavity2} \quad . \tag{4.3}$$

In these examples for *a- M'M"-a* both micromasers operate at steady state in scheme *a-M-a*, i. e. from the possible paths $a_0a_1a_2$ is realized only. The redistribution of the photons along path $a_0b_1a_2$ changes the probabilities for the two paths in such a way that after a certain time evolution it will ultimately terminate itself. This will put both cavities into independent *a-M-a* schemes and atoms will go along $a_0a_1a_2$ at steady state. Starting from uncorrelated coherent states of both fields there is a *transient entanglement* between them during the photon redistribution process until the steady state is reached. Due to the separability of the initial state the independent production of Fock states under the envelope of the initial amplitude distribution in the two cavities will also be separable providing us with fields that are *uncorrelated* at steady state as well.

Scheme *b- M'M"-b* is very similar to *a- M'M"-a* discussed above with some

minor differences. Firstly, there is a $+1$ difference in the generated Fock states as a result of the $+1$ difference in the arguments of the cosines in Eqs. (2.6a) and (2.6b) similarly to what we have seen in Section II. Secondly, it has also been shown there that due to this $+1$ scheme *b-M-b* can while *a-M-a* cannot generate the vacuum. As a consequence of this the second field jumps to vacuum in the case of scheme *b-M′M″-b* instead of the finite photon number that we have found above for *a-M′M″-a* at $g\tau = 0.5$. Thirdly, the opposite energy transfer between the cavities (the possible paths are $b_0 b_1 b_2$ and $b_0 a_1 b_2$) implies that the set of states contributing to the field additionally to the main Fock states is approximately the mirror image of the one in scheme *a-M′M″-a*. It follows that the degree of (transient) correlation is of the same order in both schemes.

In this subsection we considered the two energy preserving schemes, *a-M′M″-a* and *b-M′M″-b*, where the atoms are injected before and detected after the interaction to be in the same state. There are two possible paths they can follow: one which transports photons from one of the cavities to the other one and another which does not change the photon numbers at all. Only the latter one survives at steady state. The transporting path is transient and serves as a photon redistribution process to set the steady state of the fields in which it then terminates itself. Consequently, both micromasers are independently in the photon-preserving schemes, *a-M-a* or *b-M-b*, at steady state providing us with a set of Fock states assuring Rabi-angles to be the multiples of π located under the envelope of the initial state of the fields. We want to emphasize here that only uncorrelated initial fields have been considered so far. It has been seen from the examples above that if the initial state of the fields were separable, then their steady state would be separable as well, i. e. uncorrelated initial fields provide us with uncorrelated steady state fields. We are going to see in a later subsection that correlated initial fields result in correlated steady state fields. We will show that an entanglement generated via some other schemes can be frozen into a steady state using one of the energy-preserving schemes, *a-M′M″-a,* or *b-M′M″-b*.

IV.2. ENERGY-TRANSFERRING SCHEMES, *a-M′M″-b* AND *b-M′M″-a*, AND TWO-CAVITY TRAPPING

Atoms are injected into the first cavity and detected after the interaction in different states. Let us consider scheme *a-M′M″-b* first. The possible paths are $a_0a_1b_2$ and $a_0b_1b_2$ both increasing the energy of the system by one photon. The former one preserves the energy of the first and the latter one preserves the energy of the second micromaser.

Fig. 9 (a) shows typical evolution of the fields for short interaction times as in our example for $g\tau = 0.3, 0.5,$ and 0.8. It can be seen in the first row of the figure for $g\tau = 0.3$ that since the probabilities of the two atomic paths are approximately equal at these interaction times for the dominant part of the initial field ($C_{10} \cong S_{10}$ in Eqs. (2.2a) and (2.2b)) the amplitude distribution is stretched along a straight line as it is shown for $k = 20$. It is easy to see that the state vector of the system cannot be separated into a product of two, consequently the fields are correlated in this regime. In other words due to the "optimum lack of which-path information" about the state of the atom between the cavities there is a strong interference between the two paths. The distribution, the shape of which becomes thinner as it evolves toward higher photon numbers (in the present scheme, *a-M′M″-b*, atoms are required to leave a photon in one of the two cavities), separates into two regions and finally ends up in a rapidly oscillating structure mainly around the vacuum of cavity *2* and $n_1 \cong 50$ at $k = 40$. The other region at the vacuum of cavity *1* and $n_1 \cong 50$ has already disappeared. This effect cannot be explained by the single cavity trapping mechanism discussed in Section II since the formula $n_t = (l\pi/g\tau)^2$ predicts a trapping for $l = 1$ at the photon number $n_t \cong 100$ that is much higher than where the distribution is located in this example. We will explain later that this is due to a new mechanism that we call *two-cavity trapping* based on the coupling between the two fields to distinguish it from the *single-cavity trapping* discussed in Section II. In the second row for $g\tau = 0.5$ considering the dominant part of the initial field it is highly probable that the atom

leaves a photon in cavity *1* ($C_{10} \cong 0$ and $S_{10} \cong 1$ in Eq. (2.2a)) making the second cavity operate in scheme *b-M-b*. Thus, the photon number increases in both cavities in such a way that the distribution localizes around a point in the n_1 - n_2 space where $n_1 \cong n_2$ showing a balance between the fields. The mechanism is very similar to the one for *b- M'M"-b* except now the distribution as a whole evolves toward higher photon numbers. Due to the localization, or in other words due to the "which-path" information that the atom is in its lower state between the cavities with high probability the two micromasers are uncorrelated in this regime. At $n_1 \cong n_2 \cong 40$ the two fields independently reach their single-cavity trapping points determined by the formula $n_t = (l\pi/g\tau)^2$ for $l = 1$, where the oscillatory structure shows up exactly the same way as it has been discussed in Section II. The uncorrelated evolution ends up in an uncorrelated single-cavity trapping.

These two regimes shown in the first two rows of the figure are the basic mechanisms that the system follows. For larger interaction parameters for example for $g\tau = 0.8$ shown in the third and fourth rows of the figure the system undergoes transitions between them. It can be seen in the third row that it switches from the uncorrelated regime to the correlated one at $k = 15$. However, the stretched distribution evolving toward higher photon numbers experiences a new effect. It becomes double peaked around $k = 30$ showing fields with state vector approximately of the form of

$$|\Psi\rangle \cong N(|15,50\rangle + |50,15\rangle) \quad , \tag{4.4}$$

exhibiting, according to Eq. (3.6), 35^{th} order correlation (N is a normalization constant). This effect is similar to what happened to the distribution at $g\tau = 0.3$ and cannot be explained by the single-cavity trapping effect of Section II. The iteration rule given for the present scheme by Eq. (3.4c) tells us that the distribution separates into two parts as soon as it reaches $n_1 \cong n_2 \cong 35$. At these photon numbers and interaction parameters, $g\tau = 0.8$, the cosines C_{n_1} and C_{n_2} become zero in the formula

resulting in a zero amplitude for the middle of the stretched distribution. This zero amplitude region increases as atoms pass through due to the shift of the amplitudes from atom to atom in a similar way as discussed for the single-cavity trapping effect in Section II, except now it happens in two dimensions. This is a two-cavity trapping effect strongly relying on the coupling between the two fields, because it requires the cosines of both cavities C_{n_1} and C_{n_2} to be zero simultaneously in order to have both terms in the sum zero in Eq. (3.4c). Furthermore, it can be seen that since the amplitudes are shifted in both n_1 and n_2 in the equation the distribution will be suppressed in both directions of the n_1 - n_2 space. In the *single-cavity trapping* the sine function is zero resulting in trapped photon numbers at $n_t = (l\pi/g\tau)^2$, $l = 1, 2, 3, 4, \ldots$, while in the case of the *two-cavity trapping* the cosine function is zero implying $n_{tt} = (l\pi/2g\tau)^2$, $l = 1, 3, 5, \ldots$. Fig. 9 (a) shows that the double-peaked distribution built up by $k = 30$ begins to be destroyed at $k = 35$. The two-cavity trapping suppresses the amplitudes starting from the middle, while the single-cavity trapping bounds the stretched distribution from the ends, showing the presence of the sine functions in the equation. These two mechanisms gradually suppress the state vector and finally result in the oscillatory structures as it can be seen in the figure for $k = 35$. In our example for $g\tau = 0.8$ the $l = 1$ single-cavity trapping lines are located at $n_t \cong 15$ in both directions of n_1 and n_2 binding the stretched distribution from "outside". The two-cavity trapping takes place when the middle of the distribution is at $n_1 \cong n_2 \cong 35$. These two mechanisms determine the location of the two peaks around $n_1 \cong 15$ and 50 as well as $n_2 \cong 50$ and 15 that can be approximated by Eq. (4.4). The photon statistics of the fields that are equal to the square of the amplitude distribution given in the density plots are shown in Fig. 9 (b) for the double-peaked structure depicted in Fig. 9 (a) for $g\tau = 0.8$, and $k = 30$. Similar explanation can be given for what we have seen in the case of $g\tau = 0.3$.

The probabilities that the atoms are detected in their lower state after the interaction according to the scheme a- $M'M''$-b are depicted in Fig. 10 for the three examples of

$g\tau = 0.3, 0.5, 0.8$ given in Fig. 9 (a). It can be seen that the probability drops at the transitions between the uncorrelated and correlated regimes as well as at the trapping. For $g\tau = 0.3$ (solid line) it decreases around $k \cong 20$ due to the two-cavity trapping effect separating the stretched distribution into two regions. For $g\tau = 0.5$ (dashed line) it starts from a low level due to the co-existence of the uncorrelated and correlated regimes and then it drops again when the single-cavity trapping takes place at $k \cong 40$. The dot-dashed line for $g\tau = 0.8$ exhibits drops of the probability around $k \cong 13$ at the transition between the uncorrelated and correlated regimes and around $k \cong 33$ where the effect of the two trapping mechanisms becomes dominant. In order to generate the double-peaked superposition given in Fig. 9 (a) first of all we have to follow the conditional measurement scheme *a*- $M'M''$ -*b* and detect atoms always in their lower state after the interaction. This is made difficult especially by the dips in the probability curve. Furthermore, even if we measured the required sequence of atoms we have to shut the atomic beam down after the 30^{th} atom, because the superposition would be destroyed by the atoms to come due to the trapping effects.

For larger $g\tau$-s the distribution is bound in a dense lattice of single-cavity trapping lines as it can be seen in Fig. 11 for $\alpha^2 = 30$, $g\tau = \pi$. In this case the trapping lines are located around photon numbers of squares of integers mainly at 25, 36 and 49 corresponding to $l = 5, 6$ and 7, respectively, due to the $\alpha^2 = 30$ initial fields in this example. This implies that the system reaches its trapping points after a few atoms very soon. In our example we get a lot of oscillatory structures above atom number $k = 6$ and the field depicted in Fig. 11 disappears.

Scheme *b*- $M'M''$ -*a* is very similar to *a*- $M'M''$ -*b* discussed above. The system experiences similar transitions between correlated and uncorrelated regimes, except the distribution evolves toward lower photon numbers, since in this scheme atoms are required to take a photon away from the fields. This also follows from the opposite shift of the amplitudes in Eq. (3.4d).

In this subsection we considered the two schemes, *a*- $M'M''$ -*b* and *b*- $M'M''$ -*a*, that do not preserve the energy of the system which implies that stationary behavior

cannot be achieved. The regular operation ends when the system runs into trapping points where the amplitude distribution is taken over by complicated rapidly oscillating structures. Nevertheless, in the regular regime before these structures would appear the system can exhibit correlated and uncorrelated regimes as well as transitions between them. In the correlated regime double-peaked photon statistics can be generated due to the effect of the co-existing single- and two-cavity trapping mechanisms. These fields showing high order correlation seem to be difficult to produce in an experiment due to their transient character and the low detection probabilities of the conditioned atomic states. In the next subsection we are going to show that a combination of the energy-transferring and energy-preserving schemes can generate *arbitrary entangled steady states* of the two fields at reasonably high atomic detection probabilities.

IV.3. COMBINATION OF ENERGY-TRANSFERRING AND ENERGY-PRESERVING SCHEMES

It was shown in subsection V.1 that one can generate a set of Fock states located under the envelope of the initial coherent states of the fields by the energy-preserving schemes, although they will be uncorrelated if the initial fields were uncorrelated. In subsection V.2 we learnt, that it is possible to generate correlated fields starting from uncorrelated ones by the energy-transferring schemes although as a result of the trapping effects not at steady state. In the present section we want to combine these two kinds of schemes in such a way that after preparing a correlated state of fields from uncorrelated ones by energy-transferring schemes we use these correlated fields as initial condition and switch to an energy-preserving scheme. This way the generated Fock states will be located under the envelope of the "initial" correlated fields at steady state showing strong correlation between the two micromasers. Let us start the system in the scheme *a- M'M"-b* at interaction times such as $g\tau = 0.142$ from uncorrelated coherent fields of $\alpha^2 = 30$. It can be understood from subsection V.2 that after *100* atoms the generated fields will exhibit a long stretched distribution as depicted in Fig.

12 (a) showing strong correlation between the fields. This correlation would be destroyed by the atoms to come due to the trapping mechanisms if scheme *a- M'M"-b* would be followed any further. We switch our system to another scheme instead. From $k = 101$ we continue in the energy-preserving scheme, *a- M'M"-a*, with altered interaction times, e. g. such as $g\tau = \pi/2$. The interaction time can be changed in an experiment by changing the velocity of the atoms. After the next *200* atoms we get a superposition of three Fock states at squares of even integers minus one depicted in Fig. 12 (b) that could be approximated by

$$|\Psi\rangle \cong N(|99,35\rangle + |63,63\rangle + |35,99\rangle) \quad , \tag{4.5}$$

where N is a normalization factor. This is also the steady state of the fields, since the production of the Fock states is a result of the same mechanism as the one discussed in subsection V.1. In this case, however, the "initial" fields are correlated.

A "two-term" superposition of the fields can be produced if instead of $\pi/2$ we choose $g\tau = 1.0$ to be the new interaction parameter. The generated fields are depicted in Fig. 12 (c) and can be approximated with

$$|\Psi\rangle \cong N(|88,38\rangle + |38,88\rangle) \tag{4.6}$$

showing 50^{th} order correlation at steady state. A three dimensional plot of the photon probability distribution is given in Fig. 13 for this case. In Fig. 12 (d) we show what happens if we switch between the schemes too early. Instead of $k = 100$ we make the same switch as above but now at $k = 50$. Obviously, the distribution at the switch is much broader this time than it was in Fig. 12 (a) allowing for a peak to arise at $|38,38\rangle$.

The probability of finding the atoms in the desired states ($|b\rangle$ before and $|a\rangle$ after the switch) is depicted in Fig. 14. After getting through the risky first scheme, *a-*

M'M"-b, and generating the stretched distribution for scheme *a- M'M"-a* to continue from, the detection of the conditioned atomic states becomes highly probable (unity at large *k*'s) locking the fields into a coherent superposition at steady state. In principle any superposition can be produced by choosing the appropriate initial coherent states and interaction parameters. The initial states set the region in the space, n_1-n_2, where we are going to work. Using scheme *a- M'M"-b* the interaction parameters assure the production of a stretched distribution in this region provided $g\tau\alpha = \pi/4$ is satisfied, and then in scheme *a- M'M"-a* they fix the location of the final Fock states under the envelope of the stretched distribution.

We should mention here, that stretched distributions can be generated by any of the two energy-transferring schemes, and any of the energy-preserving schemes can produce Fock states under the envelope of initial correlated fields. Thus, any pair of the energy-transferring and energy-preserving schemes can be used to produce a steady state entanglement of nonlocal fields with considerably high detection probability.

V. SUMMARY

In the present paper we studied two lossless micromasers coupled by the common pumping beam of two level atoms when the state of the atoms is conditionally measured after the interaction. The atoms can follow two possible paths to reach the same final state the probabilities of which can be manipulated by the interaction times in the two cavities. The interference of two equally probable paths entangles the two fields while a single highly probable path results in two independent micromasers. Hence, the two fields can be correlated or decorrelated as we decide whether to favor two paths simultaneously or only one of them ("which-path" information). This is very similar to Young's double slit experiment.

The pure evolution of the fields starting from uncorrelated coherent states is studied for the four simplest measurement schemes denoted by *a- M'M"-a*, *b- M'M"-b*, *a- M'M"-b* and *b- M'M"-a* showing the state of the atoms, $|a\rangle$ or $|b\rangle$, before and after

the two maser cavities M' and M''. The energy-preserving schemes where all the atoms are injected before and detected after the interaction in the same state can be used to generate an uncorrelated set of Fock states in two dimensions under the envelope of the initial fields at steady state. We have very small transient entanglement of the two micromasers. The probability that the atoms follow the prescribed evolution scheme is high. It increases with atom number, k, and it is approximately unity for large k's and at steady state.

In the case of the energy-transferring schemes the system is shown to operate in correlated or uncorrelated regimes or to make transitions between them depending on the interaction times. An entanglement of the fields resembling to the two-term form of, $|N, N+M\rangle + |N+M, N\rangle$, of M^{th} order correlation can be achieved in the optimum case at a certain number of atoms as a result of the so-called single- and two-cavity trapping mechanisms. This entanglement is a transient effect, because further injection of atoms will destroy the superposition due to the trapping mechanisms themselves. The probability to detect atoms in the required lower state is low in these schemes and exhibit significant drops at the transitions between the correlated and the uncorrelated regimes as well as at the trapping points.

However, it is possible to generate an arbitrary steady state entanglement of the fields with high detection probability by switching the system from an energy-transferring scheme to an energy-preserving one at an optimum atom number. The correlated state of fields generated by the former scheme serves as an initial condition for the latter one. This implies that the Fock states generated by the latter scheme will be located under the envelope of this amplitude distribution and the two nonlocal micromaser fields will be strongly correlated. In principle, arbitrary entanglement of macroscopically large number states of two nonlocal fields (nonlocal Schrödinger-cat) can be achieved via this combination of schemes at steady state with high detection probability.

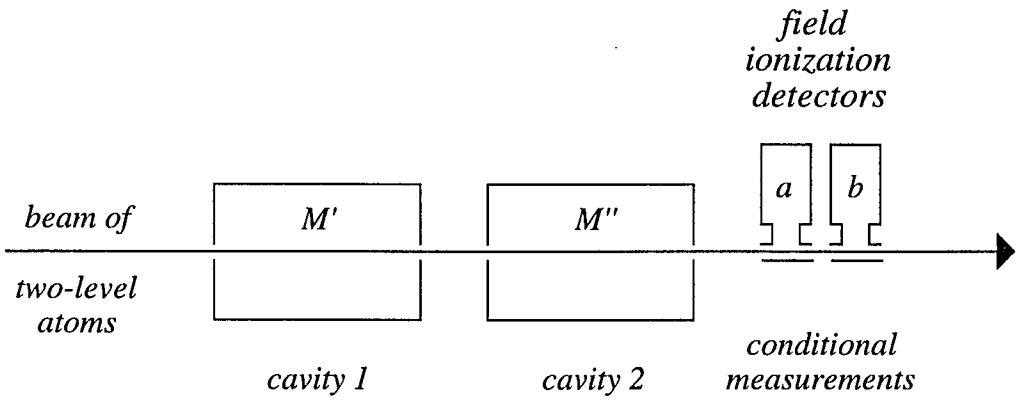

FIG. 1: Schematic arrangement of two micromasers coupled by a beam of two-level atoms the state of which is measured after the interaction.

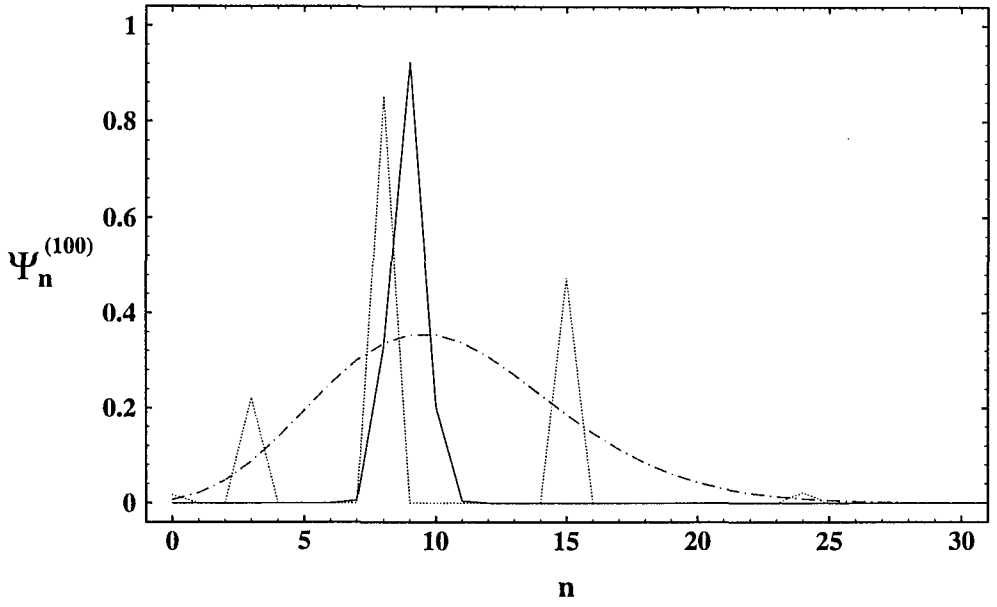

FIG. 2: Amplitude distribution in the number representation of the state vector of the field in a single micromaser in the case of scheme *a-M-a*. The dot-dashed line represents the initial coherent field of parameter $\alpha^2 = 10$. The fields generated at atom number $k = 100$ for $g\tau = 1.0$ and π are depicted by the solid and dotted lines, respectively.

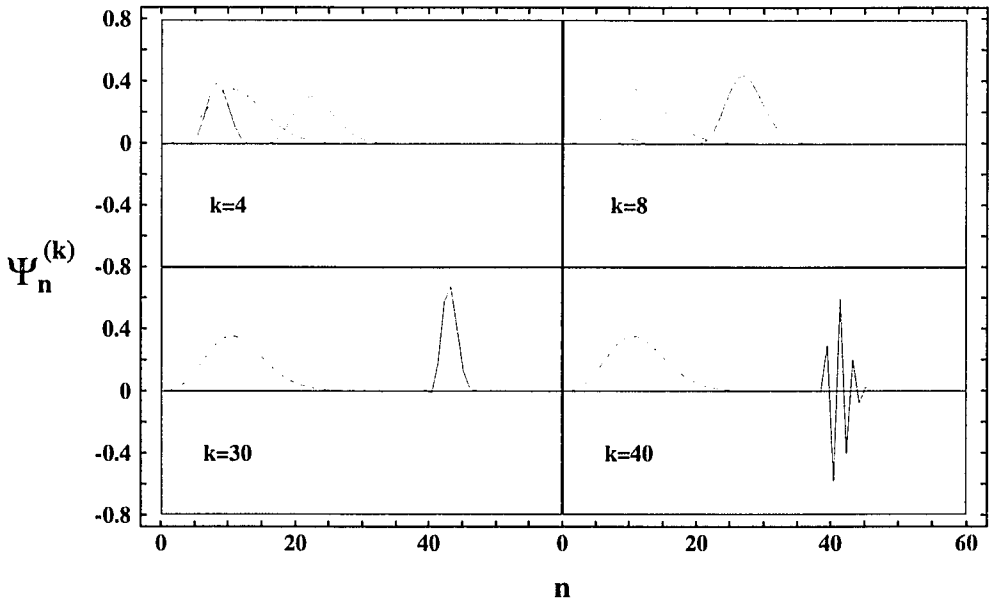

FIG. 3: Amplitude distribution in the number representation of the state vector of the field in a single micromaser in the case of scheme *a-M-b*. The dot-dashed lines represent the initial coherent field of parameter $\alpha^2 = 10$ and the fields generated at different atom numbers $k = 4, 8, 30$ and 40 for $g\tau = 0.9$ are depicted by the solid lines.

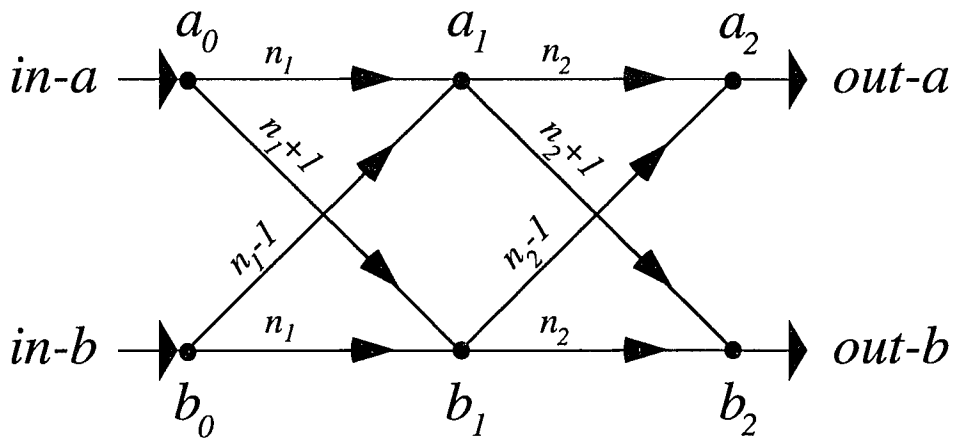

FIG. 4: Possible paths a two-level atom (upper *a*, lower *b*) can follow when passing through the two micromaser fields. The indices *0*, *1* and *2* represent the position of the atom before, between and after the two cavities, respectively. Starting from n_1 and n_2 the final number of photons due to each path is shown above the arrows.

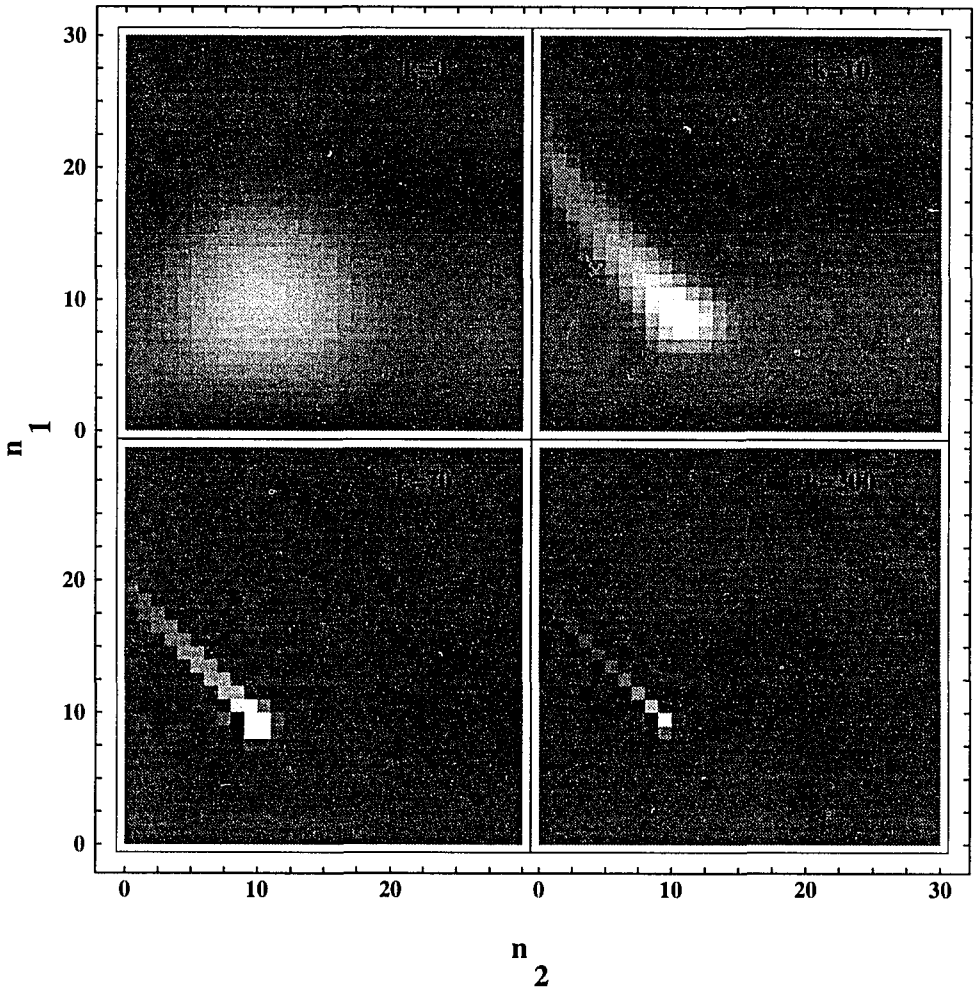

FIG. 5: Density plots showing the evolution of the amplitude distribution of the fields in the number representation in the case of scheme *a- M'M"-a*. Lighter and darker points indicate positive and negative amplitudes, respectively, as compared to the gray base of the zero level. The initial coherent field of parameter $\alpha^2 = 10$ is given by the plot denoted by atom number $k = 0$. The fields generated at $g\tau = 1.0$ for atom numbers $k = 10$, 70 and 300 show a localization around the Fock state, $|9,9\rangle$, with small contributions from $|10,8\rangle$, $|11,7\rangle$, ..., $|18,0\rangle$ that are decreasing with k.

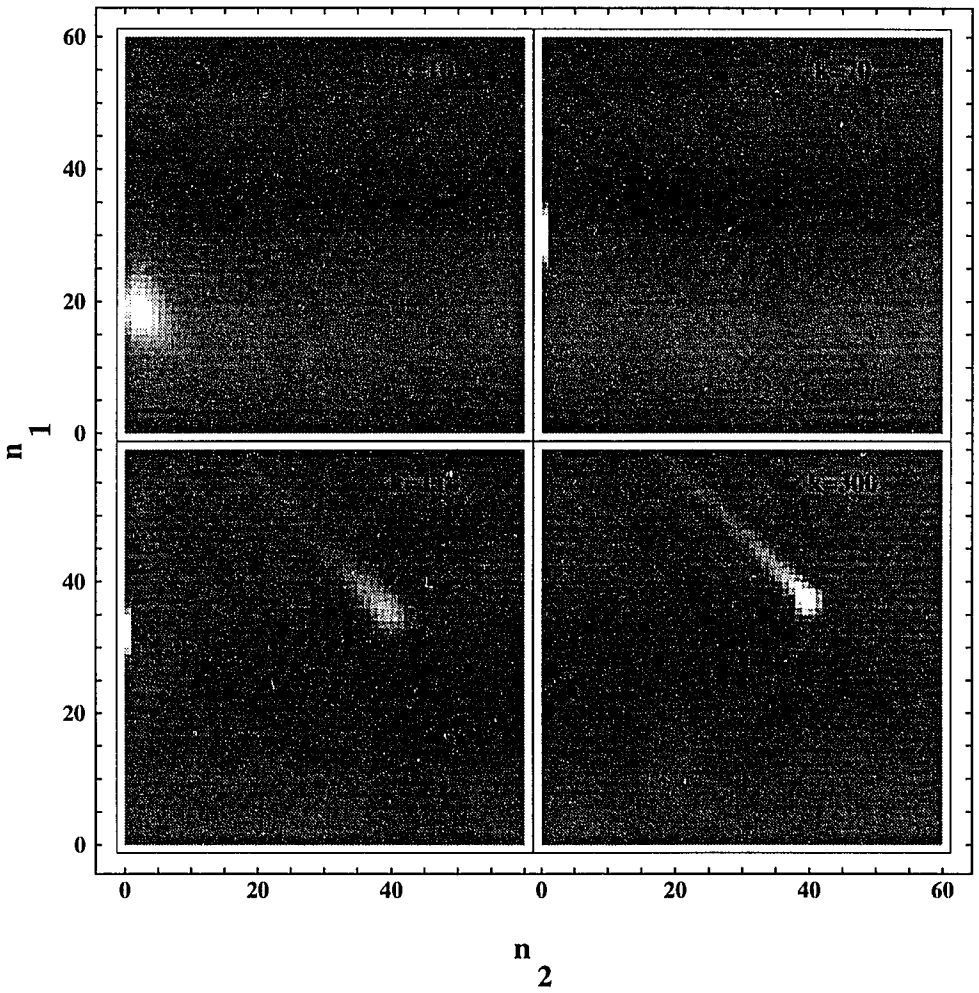

FIG. 6: Density plots showing the evolution of the amplitude distribution of the fields in scheme a-$M'M''$-a starting from the field shown in Fig. 5 for $k = 0$. The generated fields at $g\tau = 0.5$ for atom numbers $k = 10, 70, 114$ and 300 show a jump in the photon number in the second cavity around $k = 114$ and then a localization around the Fock state $|39, 39\rangle$ with small contributions from $|40, 38\rangle$, $|41, 37\rangle$, $|40, 36\rangle$, ..., $|78, 0\rangle$ that are decreasing with k.

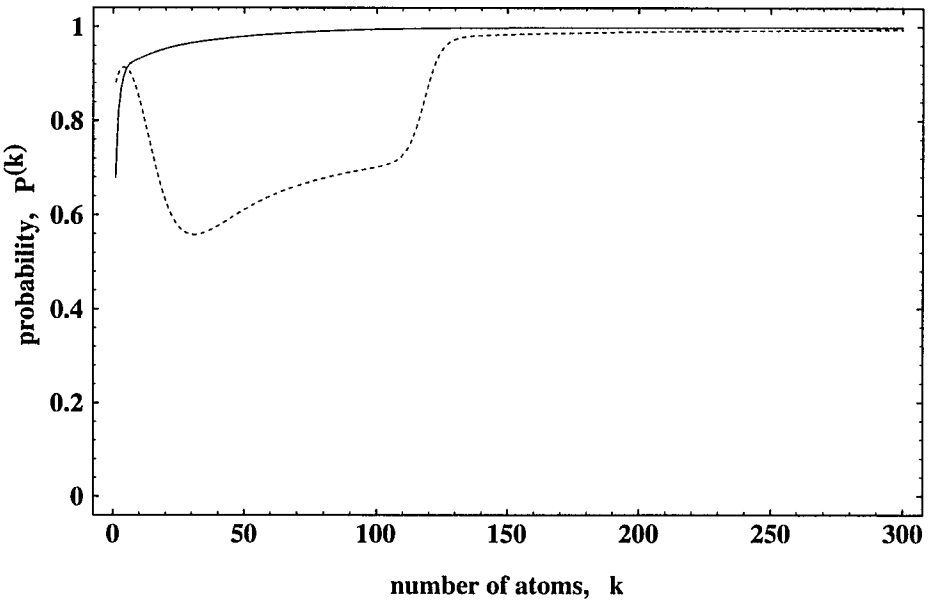

FIG. 7: The probabilities of detecting the upper state, $|a\rangle$, of atom number k in scheme a-$M'M''$-a during the evolution of the fields shown in Figs. 5 and 6 for $g\tau = 1.0$ and 0.5 depicted by the solid and dashed lines, respectively.

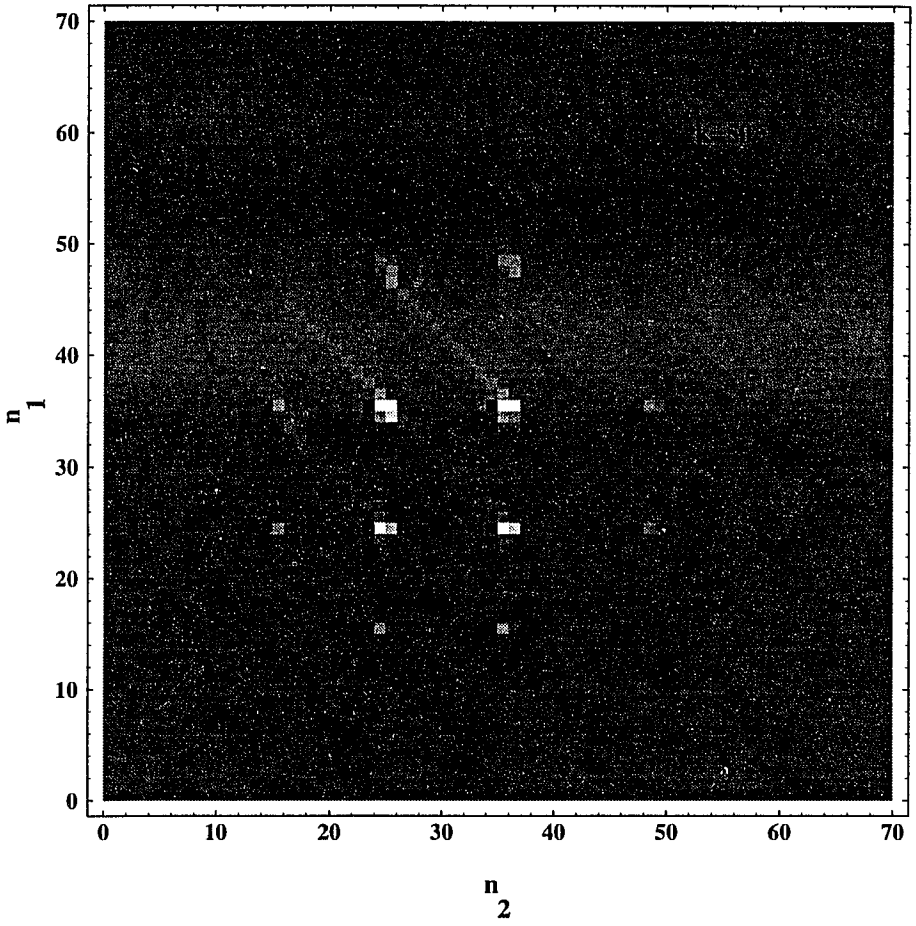

FIG. 8 (a): Density plot of the amplitude distribution of the fields in scheme *a-M'M"-a* at atom number $k = 50$ for $g\tau = \pi$ starting from coherent fields of parameter $\alpha^2 = 30$. The generated Fock states are located at photon numbers that are squares integers minus one under the envelope of the amplitude distribution of the initial fields.

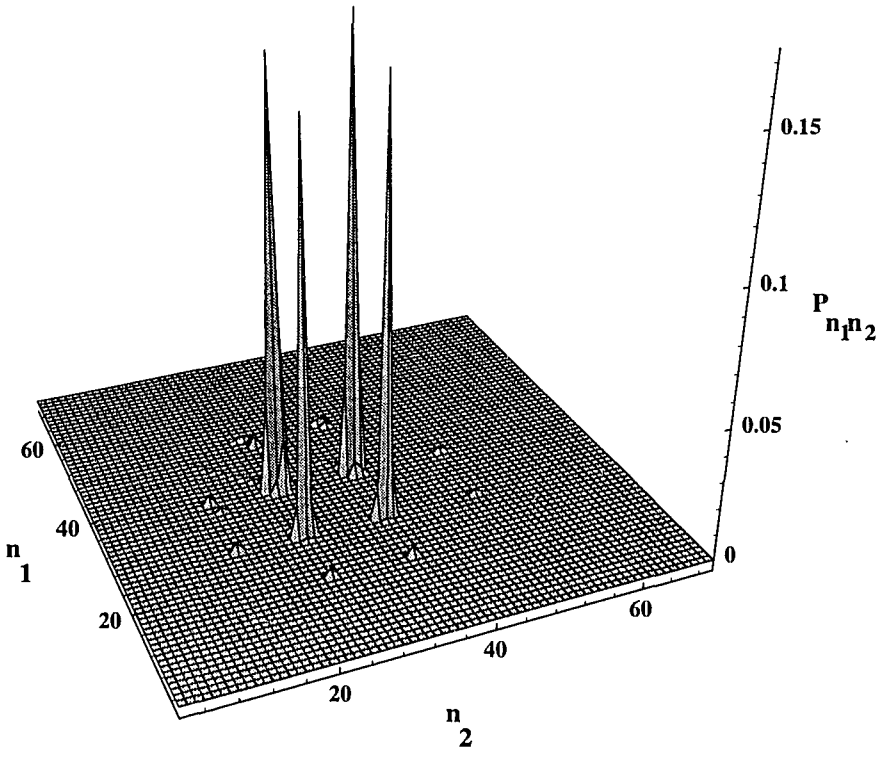

FIG. 8 (b): Three dimensional plot of the photon statistics that are the squares of the amplitudes depicted in Fig. 8 (a).

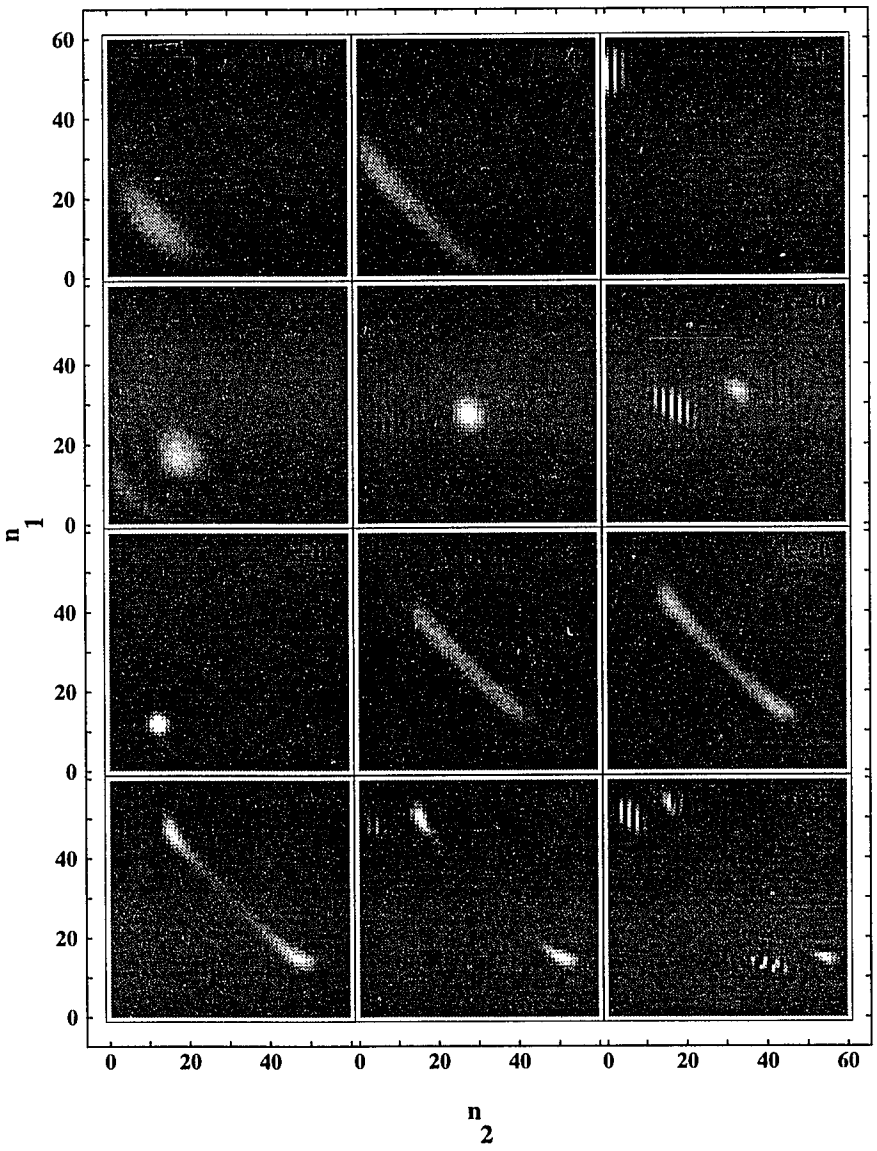

FIG. 9 (a): Density plots showing the evolution of the amplitude distribution of the fields in scheme *a- M'M"-b* starting from coherent fields depicted in Fig. 5 for $k = 0$, where $g\tau = 0.3$ for the first, *0.5* for the second and *0.8* for the third and fourth rows. The first and second rows represent the correlated and uncorrelated regimes, respectively, while a transition between these two regimes as well as a double-peaked distribution at $k = 30$ can be seen in the third and fourth ones.

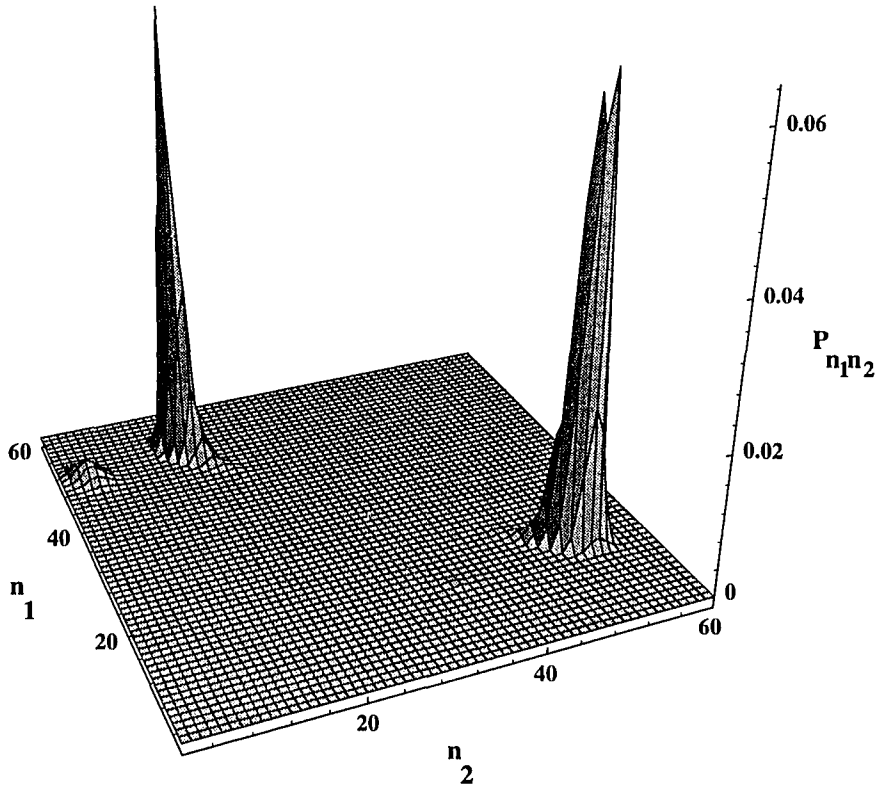

Fig. 9 (b): Three dimensional plot of the photon statistics that are the squares of the amplitudes depicted in Fig. 9 (a) for $g\tau = 0.8$ at atom number $k = 30$ showing a double-peaked probability distribution.

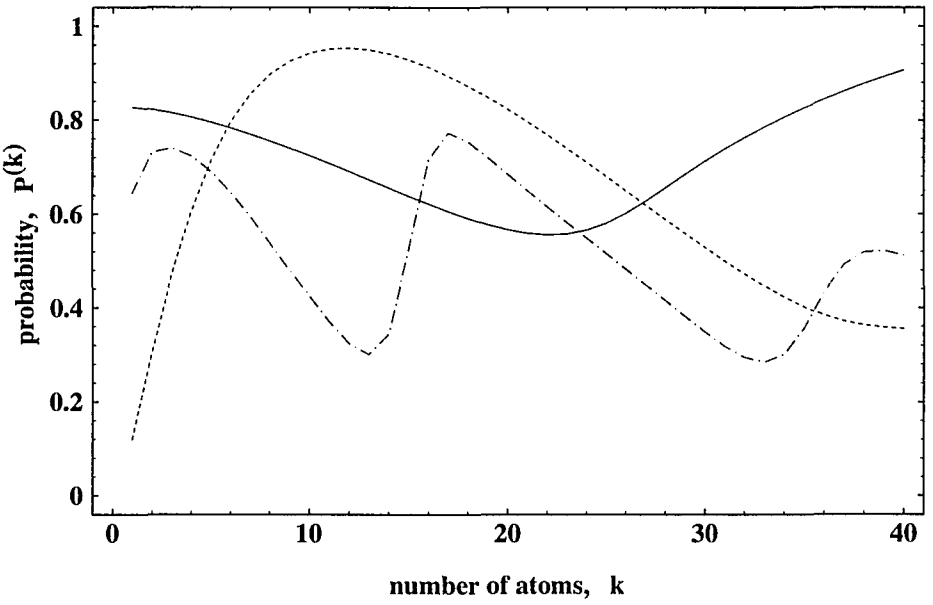

FIG. 10: The probabilities of detecting the lower state, $|b\rangle$, of atom number k in scheme a- $M'M''$ -b during the evolution of the fields shown in Fig. 9 (a) for $g\tau =$ *0.3* , *0.5* and *0.8* depicted by the solid, dashed and dot-dashed lines, respectively.

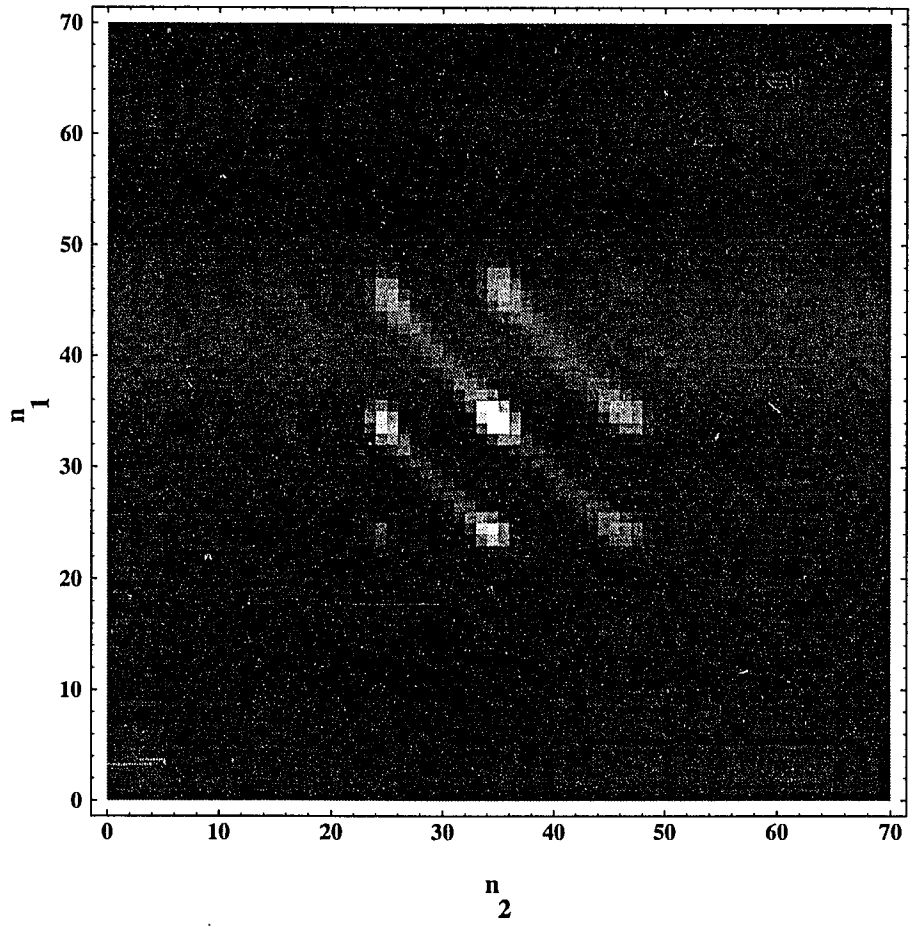

FIG. 11: Density plot of the amplitude distribution of the fields in scheme *a*- $M'M''$ -*b* at atom number $k = 6$ for $g\tau = \pi$ starting from coherent fields of parameter $\alpha^2 = 30$.

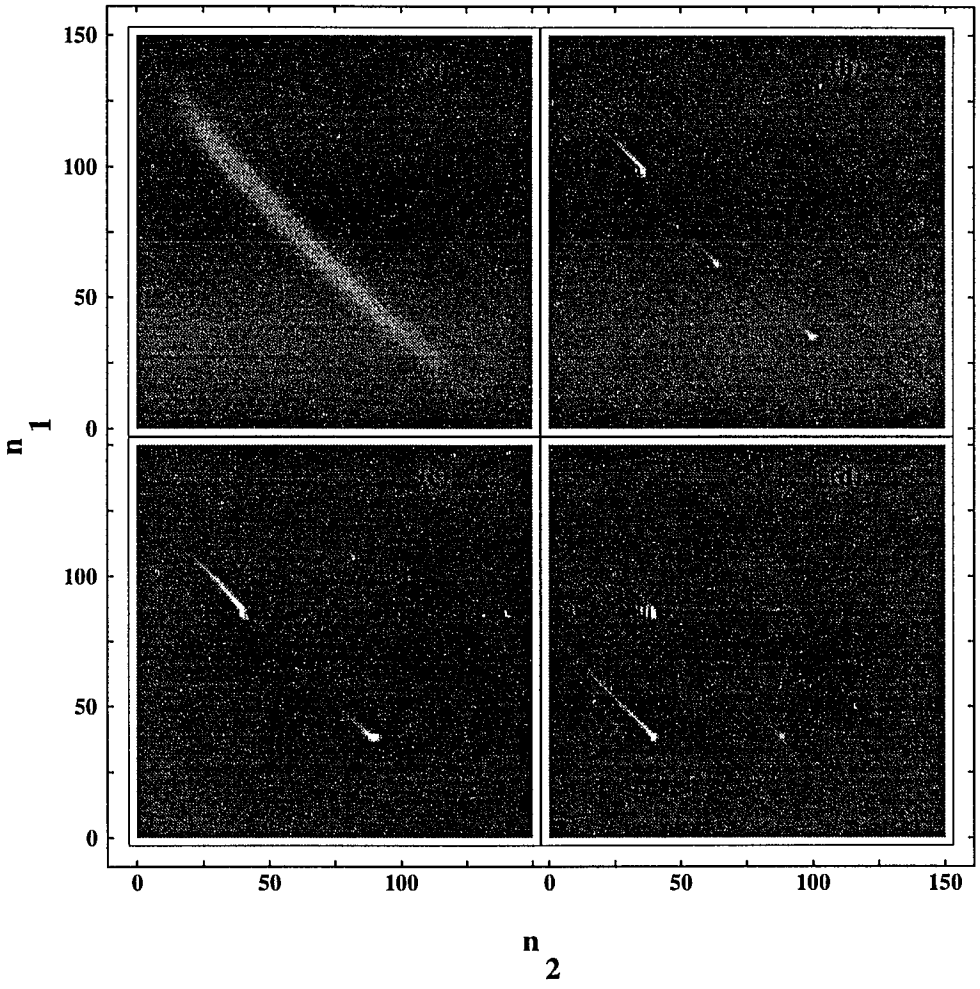

FIG. 12: Density plots of the amplitude distributions of the fields. *(a):* at the 100^{th} atom starting from coherent fields of $\alpha^2 = 30$ in scheme *a-M'M"-b* for $g\tau =$ *0.142* ; *(b):* at the 300^{th} atom after switching from the field generated in *(a)* at the 100^{th} atom to *a- M'M"-a* for $g\tau = \pi/2$; *(c):* same as *(b)* but switching to $g\tau = 1.0$; *(d):* same as *(c)* but switching at the 50^{th} atom.

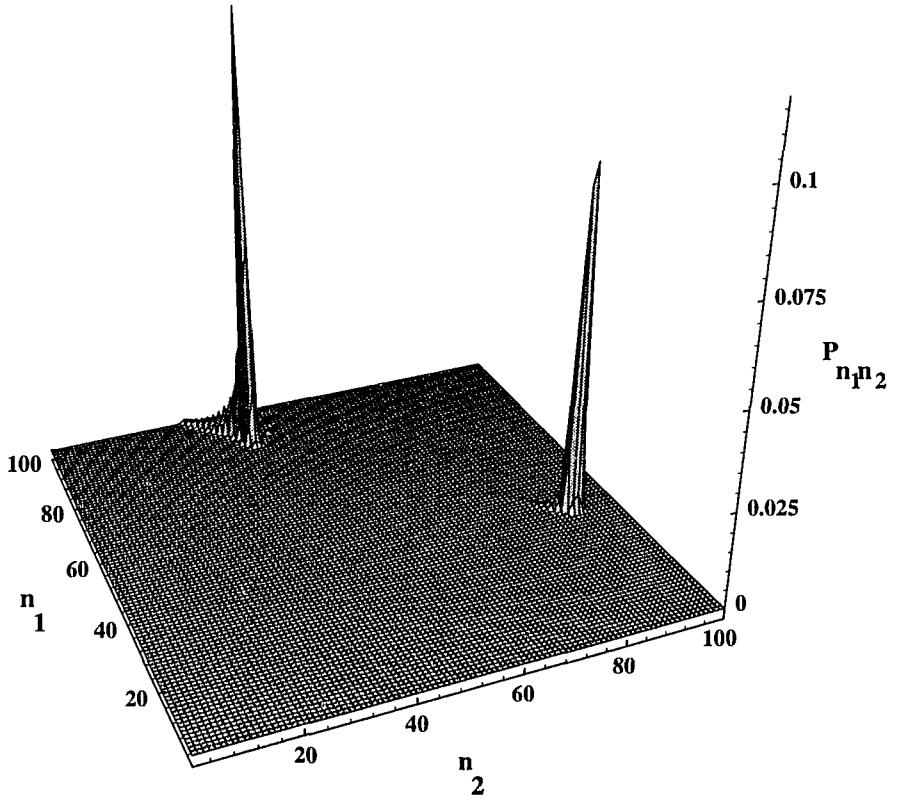

FIG. 13: Three dimensional plot of the photon statistics that are the squares of the amplitudes depicted in Fig. 12 (c) showing a double-peaked distribution at steady state.

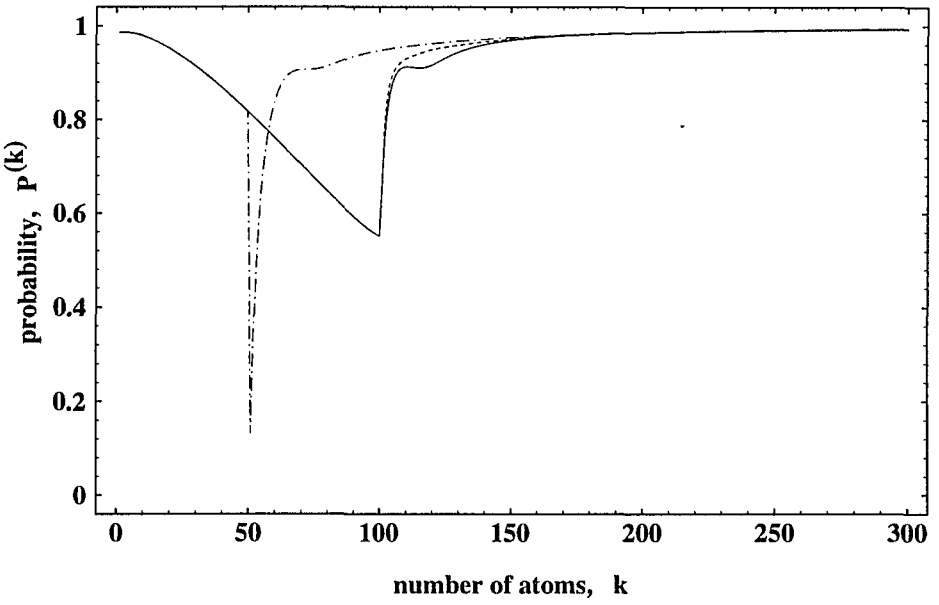

FIG. 14: Probabilities of detecting the required state of atom number k corresponding to the evolution of the fields in the schemes given in Fig. 12 (b), (c) and (d) depicted by solid, dashed and dot-dashed lines, respectively. The probability decreases before the switching, then after a transient at the switching it jumps to a high value and then increases to unity at steady state.

3.2.3 Pump-coupled Micromasers: Entangled Trapping States of Nonlocal Fields†

ABSTRACT

A single beam of excited two-level atoms couples two micromasers in series the fields of which are studied. It is shown that in the absence of dissipation the steady state is an ensemble of two-field trapping number states the realization of which depends upon the initial state of the fields and the interaction parameters, $g'\tau'$ and $g''\tau''$, of the two cavities. A large number of these trapping states are pure quantum states some of them showing entanglement of the two nonlocal micromaser fields of the form $|N,N+M\rangle \pm |N+M,N\rangle$. Here, N and $N+M$ are arbitrary trapping numbers belonging to disconnected blocks of the photon number space, and M specifies the order of correlation between the fields. The time evolution of the system toward steady states is investigated numerically concentrating mainly on the production of pure entangled trapping states of the form above. We describe a special procedure to amplify a number state, $|N,N\rangle$, into such states that is based on conditions regarding the interaction parameters. In principle, N and M can be made arbitrarily large resulting in a steady state nonlocal quantum superposition of distinct macroscopical fields (nonlocal "Schrödinger-cat"). We also present a solution of the standard master equation of a damped harmonic oscillator at finite temperature and apply it to study the effect of dissipation on the production of entangled trapping states at regular and Poissonian pump statistics. It is found that although the entanglement does not survive at steady state it can build up in the short-time transient regime when cavity losses and the number of thermal photons are not too large. In this small-loss (large N_{ex}) regime the quantum correlation between the micromaser fields decays into a steady state classical superposition at a rate depending on the cavity lifetime and the difference (or order of correlation), M, between the superposed photon numbers. In the large-loss (small N_{ex}) regime, however, no transient correlation can be produced and the photon statistics spreads

out toward vacuum for increasing losses. The system undergoes a transition from an uncorrelated to a correlated behavior when the pumping parametrized by N_{ex} exceeds the threshold between the large- and small-loss regimes. Thermal photons enhance the decay of the correlation and by coupling the disconnected blocks of the photon number space they populate the trapping number states of adjacent blocks. However, it is shown that the production of transient entanglement is not significantly affected by thermal radiation and neither by pumping fluctuations. Experimental realization of entanglement of nonlocal micromaser fields employing these two-field trapping states of small photon numbers is shown to be feasible in the short-time transient regime using the presently available high-Q cavities and low temperatures, and could be possible on the macroscopic scale in the near future.

PACS Numbers: 42.50.Dv, 42.52+x

I. INTRODUCTION

The preparation of macroscopic quantum superpositions is of considerable interest in quantum optics. The principle of superposition is one of the most significant contradictions between quantum and classical physics the implications of which are particularly astonishing on the macroscopic level. This problem has been exploited in many different systems for example in the micromaser [1] that is one of the fundamental systems of this field of research [2]. Its importance is based upon its genuine quantum nature exhibiting all the important quantum phenomena of matter-light interaction, and at the same time its theoretical tractability [3, 4] and experimental feasibility [5,6]. Some of the most important examples include collapse and revival of the Rabi nutation [7], generation of nonclassical photon statistics [1-5,8] to the extreme cases of number states [9], trapping states [10] and macroscopic coherent superpositions of its single mode radiation field [1].

The present paper further extends this respectable list of nonclassical effects studying the quantum correlations between two micromasers coupled in series by the common

pumping atomic beam (see Fig. 1) investigating the production of entangled states and nonlocal superpositions of the two micromaser fields [11-13]. One way to prepare such quantum fields is to perform conditional measurements on the atoms emerging from the interaction cavity as discussed in Ref. [12]. However, in this paper we show that the system can be driven into pure entangled trapping states of the two fields without performing conditional measurements. In fact, arbitrary quantum superpositions of the two nonlocal micromaser fields of the form of $|N,N+M\rangle \pm |N+M,N\rangle$ are possible to be generated at steady state in the absence of dissipation, where N and $N+M$ satisfy the trapping conditions in the two micromasers. We describe a two-step procedure to generate these states from the number state, $|N,N\rangle$, that is based on special conditions regarding the interaction parameters, $g'\tau'$ and $g''\tau''$, of the two cavities. Since quantum superpositions and trapping states are known to be very fragile against dissipations [14] and thermal effects [8], the question arises how well our procedure performs in the presence of cavity losses and thermal radiation. Applying our solution of the standard master equation of a damped harmonic oscillator it is shown that these entangled trapping states can be produced in the transient regime when the pumping, N_{ex} exceeds a certain threshold established by the losses. We also find that finite temperature and pumping fluctuations do not significantly modify the transient build-up of the correlation between the fields. According to our estimate, experimental realization of transient entanglement of nonlocal micromaser fields is feasible using the presently available facilities utilizing special configurations of two-field trapping states as for example the one above.

The paper is organized as follows: Section II introduces the steady state solution of the system in the absence of dissipation distinguishing between mixed and pure quantum states. In Section III the time evolution toward steady states is studied especially the pure entangled states of the above form. The effects of dissipation, thermal radiation and pump fluctuations on the build-up of entangled trapping states are investigated in Section IV. The summary and conclusions are presented in Section V.

II. STEADY STATE BEHAVIOR IN THE ABSENCE OF DISSIPATION

We consider two micromasers pumped by a monoenergetic beam of excited two-level atoms going through cavity *1* first and then through cavity *2* with no time delay between the cavities (see Fig.1). The density of the atomic beam is low enough in order to have at most one atom at a time inside the cavities. The effect of dissipation is ignored in the present section, it will be taken into account later on. The state of the atoms is measured after the interaction in cavity *2* , but we do not select a particular result. We assume *100%* detection efficiency for the field ionization detectors measuring the state of the outcoming atoms in order to have each atom measured after the interaction. The state of the fields is described by the reduced density operator obtained by tracing out over the atomic states. This tracing operation is sometimes referred to as a nonselective measurement [15]. The evolution of the system is governed by the Jaynes-Cummings operators U' and U'' during the atom-field interactions in cavities *1* and *2*, respectively. At the instant when the k^{th} atom leaves cavity *2* the field density operator reduces to

$$\rho^{(k)} = Tr_{atom}\left[U''U'\rho^{(k-1)}\rho_{atom}U'^{\dagger}U''^{\dagger}\right] \quad , \tag{2.1}$$

where ρ_{atom} is the atomic and $\rho^{(k-1)}$ is the field-density operator at the instant when the k^{th} atom enters cavity *1*. In the number representation, $\rho^{(k)}_{\substack{n_1,m_1\\n_2,m_2}} = \langle n_1,n_2|\rho^{(k)}|m_1,m_2\rangle$, this reads as

$$\begin{aligned}\rho^{(k)}_{\substack{n_1,m_1\\n_2,m_2}} = {} & \rho^{(k-1)}_{\substack{n_1,m_1\\n_2,m_2}} C'_{n_1+1}C'_{m_1+1}C''_{n_2+1}C''_{m_2+1} + \rho^{(k-1)}_{\substack{n_1-1,m_1-1\\n_2,m_2}} S'_{n_1}S'_{m_1}C''_{n_2}C''_{m_2} + \\ & + \rho^{(k-1)}_{\substack{n_1-1,m_1-1\\n_2+1,m_2+1}} S'_{n_1}S'_{m_1}S''_{n_2+1}S''_{m_2+1} + \rho^{(k-1)}_{\substack{n_1,m_1\\n_2-1,m_2-1}} C'_{n_1+1}C'_{m_1+1}S''_{n_2}S''_{m_2} - \\ & - \rho^{(k-1)}_{\substack{n_1,m_1-1\\n_2,m_2+1}} C'_{n_1+1}S'_{m_1}C''_{n_2+1}S''_{m_2+1} + \rho^{(k-1)}_{\substack{n_1-1,m_1\\n_2,m_2-1}} S'_{n_1}C'_{m_1+1}C''_{n_2}S''_{m_2} -\end{aligned}$$

$$-\rho^{(k-1)}_{\substack{n_1-1,m_1\\ n_2+1,m_2}} S'_{n_1} C'_{m_1+1} S''_{n_2+1} C''_{m_2+1} + \rho^{(k-1)}_{\substack{n_1,m_1-1\\ n_2-1,m_2}} C'_{n_1+1} S'_{m_1} S''_{n_2} C''_{m_2} \quad . \tag{2.2}$$

Here, $S'_{n_1} \equiv sin(g'\tau'\sqrt{n_1})$ and $S''_{n_2} \equiv sin(g''\tau''\sqrt{n_2})$ as well as C'_{n_1} and C''_{n_2} stand for the cosine functions of the corresponding arguments, g' and g'' are the atom-field coupling constants, τ' and τ'' are the interaction times in cavities *1* and *2*, respectively. Representing the four dimensional density matrix as a supermatrix of matrices where one matrix is specified by the photon numbers of the first field, (n_1, m_1), and one element of this matrix is given by those of the second field, (n_2, m_2), Eq. (2.2) tells us that any matrix element, (n_1, m_1, n_2, m_2), is coupled to others located along a "double-square" as depicted in Fig. 2. This shows for example that the photon statistics (diagonal elements, (n_1, n_1, n_2, n_2)) are coupled to the coherence terms (off-diagonals, $(n_1, n_1\pm1, n_2\pm1, n_2)$) indicating the essential role of correlations in this system. The strength of the coupling is determined by the sine and cosine functions in Eq. (2.2). In the interaction picture and in the absence of dissipation the density operator does not evolve during the time interval, t, between the atoms. Thus, successive iterations of Eq. (2.2) yield the stroboscopic time evolution of the fields. This will be studied in the next section by numerically evaluating Eq. (2.2) for a stream of atoms.

It can be seen from Eq. (2.2) that for steady states of the fields one needs

$$C'_{N_1+1} C'_{M_1+1} C''_{N_2+1} C''_{M_2+1} = 1 \quad , \tag{2.3}$$

that is the trapping condition satisfied by any combinations of any four numbers N_1, M_1, N_2 and M_2 for each of which $g\tau\sqrt{N+1} = q\pi$, where q is an integer and N is any of the four numbers. Thus, in the absence of dissipation the only possible steady states of the system are the superpositions of these two-field trapping number states satisfying Eq. (2.3). They include both mixed and pure quantum states of the fields as it can be seen from the supermatrix picture. Populating for example the diagonal trapping number states only will provide us with mixed states of no correlation between the fields, while also

populating the off-diagonal ones will result in correlations between the micromasers and in some cases of pure quantum states. An example is given in Fig. 2 representing the pure quantum state $|0,3\rangle \pm |3,0\rangle$ (apart from a normalization factor) that is an entangled trapping state of the two micromaser fields for the interaction parameters, $g'\tau' = g''\tau'' = \pi$.

We want to select pure states from this broad set of steady states by applying the following factorization argument [1]. Let us assume that the initial state of the fields is given by

$$|\Psi\rangle = \sum_{n_1,n_2} \Psi_{n_1,n_2} |n_1,n_2\rangle \quad . \tag{2.4}$$

We require this state to be a steady state of the fields. Interacting with an atom initially in its upper state, $|a\rangle$, the atom-field system under the Jaynes-Cummings dynamics evolves into the state given by

$$|\Phi\rangle = \sum_{n_1,n_2} \Psi_{n_1,n_2} \Big[\Big(C'_{n_1+1} C''_{n_2+1} |n_1,n_2\rangle - S'_{n_1+1} S''_{n_2} |n_1+1,n_2-1\rangle \Big) |a\rangle -$$

$$-i \Big(C'_{n_1+1} S''_{n_2+1} |n_1,n_2+1\rangle + S'_{n_1+1} C''_{n_2} |n_1+1,n_2\rangle \Big) |b\rangle \Big] \quad . \tag{2.5}$$

The requirement that the fields remain in the same pure state after the interaction implies that $|\Phi\rangle$ must factorize into a tensor product of the initial pure state of the fields given by Eq. (2.4) and a pure state of the atoms as

$$|\Phi\rangle = e^{i\theta} |\Psi\rangle \otimes \big(\alpha |a\rangle + \beta |b\rangle \big) \quad , \tag{2.6}$$

where α, β, θ are independent of n_1, n_2 and $|\alpha|^2 + |\beta|^2 = 1$. Comparing Eqs. (2.5) and (2.6) we readily find

$$e^{i\theta} \alpha \, \Psi_{n_1,n_2} = \Psi_{n_1,n_2} C'_{n_1+1} C''_{n_2+1} - \Psi_{n_1-1,n_2+1} S'_{n_1} S''_{n_2+1} \quad , \tag{2.7}$$

$$e^{i\theta}\beta\,\Psi_{n_1,n_2} = -i\left(\Psi_{n_1,n_2-1}C'_{n_1+1}S''_{n_2} - \Psi_{n_1-1,n_2}S'_{n_1}C''_{n_2}\right) \quad . \tag{2.8}$$

It is apparent from Eq. (2.8) that for a steady state we need $\beta = 0$, and consequently $\alpha = \pm 1$ and $e^{i\theta} = \pm 1$, i. e. atoms to leave cavity *2* in their upper state. This implies that they need to be in their upper state before, between and after the cavities at steady state. Hence, it follows from Eq. (2.7) that the necessary condition for a nonzero field amplitude $\Psi_{N_1,N_2} \neq 0$ is

$$C'_{N_1+1}C''_{N_2+1} = \pm 1 \quad , \tag{2.9}$$

that is satisfied by the two-field trapping conditions

$$g'\tau'\sqrt{N_1^{(p)}+1} = p\pi \quad , \tag{2.10}$$

$$g''\tau''\sqrt{N_2^{(q)}+1} = q\pi \quad . \tag{2.11}$$

Any combination of $N_1^{(p)}$ and $N_2^{(q)}$ determines a point in the photon number space n_1-n_2 where a nonzero amplitude $\Psi_{N_1^{(p)},N_2^{(q)}} \neq 0$ can arise resulting in the most general steady states of the fields given by

$$|\Psi\rangle = \sum_{p,q}\Psi_{N_1^{(p)},N_2^{(q)}}\left|N_1^{(p)},N_2^{(q)}\right\rangle \quad . \tag{2.12}$$

There are no other pure steady states of the system. It is apparent that the solution of Eq. (2.3) provides a broader set of trapping states including the ones given by Eq. (2.12) as well as those for which a pure state vector does not exist. In the case of $g\tau \equiv g'\tau' = g''\tau''$ Eq. (2.12) reduces to the combination of a single set of trapping photon numbers. Choosing for example $g\tau = \pi/\sqrt{5}$ the possible trappings occur at photon numbers $N^{(p)} = 4, 19, 44, \ldots$ for $p = 1, 2, 3, \ldots$ resulting in trapping states such as number states$|4,4\rangle$

or $|19,19\rangle$, and a combination thereof, or such as entangled states exhibiting strong correlation between the two nonlocal micromaser fields [12,13] for example

$$|\Psi\rangle = \frac{1}{\sqrt{2}}(|4,19\rangle + |19,4\rangle) \quad . \tag{2.13}$$

Going back to the supermatrix picture we find that the ensemble of possible trapping number states determined by the interaction parameters, $g'\tau'$ and $g''\tau''$, mark the borders of disconnected blocks inside which the fields are bound to evolve. Unless finite temperature is introduced into the system (as it is going to be studied in Section IV) the fields cannot reach beyond the trapping states and enter the region of another block in the supermatrix, but they must stay in the block where they were started in. Hence, the initial state of the fields and the interaction parameters determine which part of the general trapping state (mixed: Eq. (2.3), pure: Eq. (2.12)) will the system evolve into. The dynamics of the fields will be studied in the next section where, in particular, we are going to describe a procedure that takes advantage of the disconnected structure of blocks in the photon number space and generates various nonlocal superpositions of trapping states (such as Eq. (2.13)) starting from initial fields that overlap several (two) blocks simultaneously.

III. TIME EVOLUTION TOWARD TRAPPING STATES IN THE ABSENCE OF DISSIPATION

We have seen in the previous section that in the absence of dissipation the steady state of the fields consists of various ensembles of two-field trapping number states some of which exhibit pure entanglement of the two nonlocal micromaser fields. In this section we are investigating typical time evolutions of the fields toward steady states considering various initial conditions concentrating mainly on the production of pure entangled states. We compute the density matrix for a stream of atoms by numerically iterating Eq. (2.2).

III.1. Uncorrelated initial states

As a first example let us start the fields from vacuum and set $g\tau = 0.5$. It can be seen from Fig. 3 that the field in the second micromaser experiences an initial flip: after an initial growth it falls back to vacuum around the 20^{th} atom. This "second threshold" corresponds to a complete depletion of the upper atomic level by the first micromaser and it is studied in Ref. [16] in detail. The flip is longer in time and sweeping over larger photon numbers for smaller $g\tau$-s, while it is shorter and will even disappear for larger parameters. After the flip the fields evolve toward $n_1 = n_2 \cong 38$, that is close although not exactly equal to the π-trapping point which is $N_1 = 38.478$. This "pseudo-trapping" point attracts the fields to spend a long time in its vicinity, but then the system moves on. This can be seen from another example depicted in Figs. 4 (a) and (b), where $g\tau = 3\pi/\sqrt{29}$ resulting in the "pseudo-trapping" points attracting the fields to $N_1 = 2.222$, $N_2 = 11.889$, and the "true-trapping" point at $N_3 = 28$. Fig. 4 (a) shows that the system spends long times in the two pseudo-trapping points, but then it finally evolves into its true steady state $|28, 28\rangle$. The evolution of the purity factor defined as $\xi^{(k)} = Tr[\rho^{(k)2}]$ as a function of atom number k is depicted in Fig. 4 (b). We have got very similar effects including the initial flip and the attraction by pseudo-trapping points when starting the fields from a single or from an incoherent mixture of number states, although in the latter case the system may evolve into a classical mixture of several trapping points belonging to different disconnected blocks of the photon number space. (We are using the terms "classical" and "incoherent" as equivalents throughout this paper.) Similarly, starting from initially uncorrelated coherent states the system simultaneously deals with several (both "pseudo-", and "true-") trapping points depending on $g\tau$. After the initial flips it finally settles down to an incoherent mixture of trapping photon numbers located at different disconnected blocks under the envelope of the initial fields showing no correlation between the micromaser fields (this is similar to the problem discussed in Ref. [12] in detail). We could not generate pure entangled states starting from these uncorrelated initial states even if they

overlapped several disconnected blocks of the photon number space.

III.2. Amplification of correlated states, $|\Psi\rangle_n^{(m)}$

We are going to show, however, that a correlated state of the two micromaser fields, $|\Psi\rangle_n^{(m)}$, that exhibits a structure given by

$$|\Psi\rangle_n^{(m)} = \frac{1}{\sqrt{2}}\left(|n, n+m\rangle \pm |n+m, n\rangle\right) \tag{3.1}$$

can be amplified into the pure steady state, $|\Psi\rangle_N^{(M)}$, of the same form as above, provided N and $N+M$ are trapping numbers. It should be mentioned here that defining m^{th} order correlation by the nonseparability condition

$$\left\langle (\hat{a}_1 \hat{a}_2^{\dagger})^m \right\rangle \neq \left\langle \hat{a}_1^m \right\rangle \left\langle \hat{a}_2^{\dagger m} \right\rangle \quad , \tag{3.2}$$

where $\hat{a}_1$ ($\hat{a}_1^{\dagger}$) and $\hat{a}_2$ ($\hat{a}_2^{\dagger}$) are the field operators in micromasers *1* and *2*, respectively, it is easy to show that these states, $|\Psi\rangle_n^{(m)}$, exhibit m^{th} order correlation. We would like to draw attention to the fact that this is a correlation between fields of two spacially separated micromasers, i. e. a *nonlocal* entanglement. The state of one of the fields can be inferred from a measurement made on the state of the other field located at a different point in space.

The amplifying procedure of an initial state, $|\Psi\rangle_n^{(m)}$, the preparation of which will be discussed later on is based on conditions regarding the interaction parameters, $g'\tau'$ and $g''\tau''$, of the two cavities. Choosing the appropriate parameters we want to trap photon number n in its initial value in Eq. (3.1), making $|\Psi\rangle_n^{(m)}$ overlap two different disconnected blocks in the photon number space. Thus, n is going to be a constant throughout the procedure, i. e. $N = n$, while $n + m$ located in the other block disconnected from the one of n can be amplified. Due to the structure of $|\Psi\rangle_n^{(m)}$ the roles of the two fields are interchanged in the two terms: the first and second fields are trapped only in the first and second terms, respectively. Therefore, an increase in m will result in

a symmetrical amplification of the different fields in the different terms until the trapping number $N + M$ is reached, preserving the structure of the entanglement the same as in Eq. (3.1). This also implies an increase in the order of correlation trapped at the value of $m = M$ at steady state. It follows from Eq. (2.5) that since the amplitudes of the initial fields are $\Psi_{n,n+m} = \pm\Psi_{n+m,n} = 1/\sqrt{2}$ this procedure can be carried out by simultaneously satisfying two conditions given by

$$S'_{n+1} = S''_{n+1} = 0 \tag{3.3}$$

and

$$S''_n = 0 \quad . \tag{3.4}$$

The first condition most importantly ensures that a given state, $|\Psi\rangle_n^{(m)}$, gets amplified in the desired way when the atom leaves the interaction in its lower state, while together with the second one they prevent quantum states of structures different than $|\Psi\rangle_n^{(m)}$ from contributing to the state of the fields when the atom leaves in its upper state. In particular, considering the second line of Eq. (2.5) the initial amplitude, $\Psi_{n,n+m}$ ($\Psi_{n+m,n}$), allows only the first (second) term to contribute and the other one is suppressed due to Eq. (3.3). Similarly, in the first line of Eq. (2.5) the first term contributes only and the second one is suppressed for both amplitudes as a result of Eqs. (3.3) and (3.4). These two conditions imply that the interaction parameters must be integer multiples of $\pi/\sqrt{n+1}$ and $\pi/\sqrt{n}$, *simultaneously*. Since this is not, in general, possible we are going to start in the examples to follow with concentrating on the first condition only describing the resulting effect of mixing different structures into the evolution of the fields, and then apply the second condition approximately. It will be shown that this approximate solution for $g\tau$ works very well in the amplifying procedure and the generated states are very close to the pure entangled trapping states, $|\Psi\rangle_N^{(M)}$. We should mention here without going into details that unequal interaction parameters, $g'\tau'$ and $g''\tau''$ (both approximately satisfying Eqs.

(3.3) and (3.4)), result in a reduction and ultimately a loss in the correlation and purity of the fields at steady state due to an asymmetrical amplification of the state vector. Therefore, we require $g\tau \equiv g'\tau' = g''\tau''$, in the amplifying procedure.

As the simplest example let us consider an initial state, $|\Psi\rangle_0^{(m)}$, given by Eq. (3.1) for $n = 0$. It can be seen from Eq. (2.5) that detecting the first atom emerging from the interactions in the upper state, $|a\rangle$, will not change the state of the fields, $|\Psi\rangle_0^{(m)}$, (apart from a phase factor) if $g\tau = q\pi$, where q is an integer. On the other hand detecting the lower state, $|b\rangle$, will increase m by one until the trapping point M is reached, and at the same time preserve $n = 0$ unchanged resulting in the state, $|\Psi\rangle_0^{(m+1)}$. The tracing operation averages the two atomic paths out and the state of the fields is a statistical mixture of the two corresponding quantum states, $|\Psi\rangle_0^{(m)}$ and $|\Psi\rangle_0^{(m+1)}$, both exhibiting the form of Eq. (3.1). Similarly, for all the consecutive atoms the states of the fields during the evolution are always statistical mixtures of quantum states of the form like $|\Psi\rangle_0^{(m)}$ only, no other structures will contibute. This suggests that the system inevitably evolves into the trapping state, $|\Psi\rangle_0^{(M)}$, where M can be any trapping number $M = 3, 8, 15, \ldots$ depending on which disconnected block we are working in. In other words the trajectory of the fields (i. e. the sequence of states they evolve along) consists of states like $|\Psi\rangle_0^{(m)}$ only, where m is increasing with the number of injected pumping atoms while $n = 0$ is kept constant. Fig. 5 (a) depicts the field-density matrix for the first two atoms in the form of a supermatrix (arranged in the same way as in Fig. 2) starting from the initial state, $|\Psi\rangle_0^{(1)}$, at $g\tau = \pi$. Comparing the structure of the pure state, $|\Psi\rangle_0^{(3)}$, depicted in Fig. 2 to Fig. 5 (a) it can be seen that the system evolves along a statistical mixture of pure states, $|\Psi\rangle_0^{(m)}$, of $m = 1, 2, 3$. Numerically iterating Eq. (2.2) for several atoms we find that the fields finally evolve into the trapping state, $|\Psi\rangle_0^{(3)}$. The solid line in Fig. 6 shows that the purity factor $\xi^{(k)}$ experiences an initial drop due to the statistical averaging of the two atomic paths, but then it goes back up to unity at steady state. We should mention at this point that the initial state, $|\Psi\rangle_0^{(1)}$, can be generated from vacuum, $|0,0\rangle$, with probability of one by sending one single excited atom through the cavities at $g'\tau' = \pi/4$ and $g''\tau'' = \pi/2$ (see Eq. (2.5).

For an initial state, $|\Psi\rangle_n^{(m)}$, given by Eq. (3.1) for $n \neq 0$ the time evolution of the system is more complicated. Although the condition given by Eq. (3.3) ensures that m is increased by one and at the same time n is left unchanged when the lower atomic state is detected the state vector is not necessarily preserved as it has been for $n = 0$ above when the upper atomic state is detected. This implies that new quantum states exhibiting structures different than the one given by Eq. (3.1) also contribute to the fields making the trajectory of the system more complicated and as the example given by the dotted line in Fig. 6 shows the purity of the system can be lost at steady state. Here, we start from the initial state, $|\Psi\rangle_1^{(1)}$, and apply $g\tau = \pi/\sqrt{2}$ to satisfy Eq. (3.3). The more complicated trajectory is apparent when comparing the evolution of the field-density matrix depicted in Fig. 5 (b) to Figs. 5 (a) and 2. The steady state of the fields is not the pure state, $|\Psi\rangle_1^{(6)}$, that we aimed at, although it is close to that. The nonzero field-density matrix elements given by the indices as (n_1,m_1,n_2,m_2) are the diagonal terms $(1,1,7,7)$ and $(7,7,1,1)$ equal to 0.500, and the off-diagonal ones $(1,7,7,1)$ and $(7,1,1,7)$ equal to 0.223 (instaed of 0.500) that show a mixed quantum state of purity factor $\xi = 0.600$. Considering another interaction parameter of $g\tau = 2\pi/\sqrt{2}$ for which the condition of Eq. (3.3) is still satisfied the effect is even stronger. Only the diagonal elements $(1,1,7,7)$ and $(7,7,1,1)$ survive at steady state having the same value as above 0.500, the off-diagonal elements are equal to -0.01 resulting in the steady state purity factor $\xi = 0.500$. The evolution of $\xi^{(k)}$ as a function of the atom number k is depicted by the dot-dashed line in Fig. 6. Since new quantum states have been involved in the evolution of the system exhibiting different structures than the one in Eq. (3.1) the state of the fields irreversibly lost all the correlation and purity. The steady state is a classical (nonlocal) mixture of photon numbers 1 and 7 given by the density operator of the form, $|1,7\rangle\langle 1,7| + |7,1\rangle\langle 7,1|$ (apart from a normalization factor).

However, for any initial state of the fields, $|\Psi\rangle_n^{(m)}$, given by Eq. (3.1) one can choose $g\tau$ in such a way that it satisfies the condition given in Eq. (3.3), and at the same time drastically reduces (although does not completely kill) the probabilities of mixing quantum states of different structures into the evolution of the fields by approximately satisfying Eq.

(3.4). In this case, when $g\tau$ is an integer multiple of $\pi/\sqrt{n+1}$ and *at the same time* it is close to an integer multiple of $\pi/\sqrt{n}$ the system does evolve into a steady trapping state that can very well be approximated with the pure entangled trapping state, $|\Psi\rangle_N^{(M)}$. In the example of the initial fields above given by $|\Psi\rangle_1^{(I)}$ we now apply $g\tau = 7\pi/\sqrt{2} = 4.950\ \pi$. The evolution of the purity of the state of the fields is shown in Fig. 7 by the dot-dashed line and an illustration of the evolution of the field-density matrix is depicted in Fig. 5 (c). It is apparent that the system evolves along a trajectory consisting predominantly of state vectors, $|\Psi\rangle_1^{(m)}$, $m = 1, 2, ..., 6$, new states of different forms have no significant contribution. This is similar to the cases of $n = 0$ as it can be seen by comparing Fig. 5 (c) to 5 (a). The steady state diagonal elements are the same as they were in the examples above for $g\tau = \pi/\sqrt{2}$ and $2\pi/\sqrt{2}$, both *(1,1,7,7)* and *(7,7,1,1)* equal to *0.500*, while the off-diagonal terms *(1,7,7,1)* and *(7,1,1,7)* are now equal to *0.496*, resulting in the steady state purity factor $\xi = 0.992$. The steady state of the system is approximately equal to the entangled trapping state, $|\Psi\rangle_1^{(6)}$. We have found very similar steady states for $g\tau = l\pi/\sqrt{2}$, for $l = 7, 10, 17, ...$ (within the $\pm$ sign in Eq. (3.1)), although the time evolution can be very different as depicted in Fig. 7 by the dot-dashed, dotted and solid lines, respectively. The evolution of the system toward its steady state is particularly slow for example for $l = 17$ (solid line) due to its being attracted by the pseudo-trapping state $|1,3\rangle - |3,1\rangle$ along its way around the atom number $k = 9$.

The two micromaser fields can be amplified into arbitrary entangled trapping states, $|\Psi\rangle_N^{(M)}$, starting from an appropriate initial state, $|\Psi\rangle_n^{(m)}$, when the interaction parameters, $g\tau$, (where $g\tau \equiv g'\tau' = g''\tau''$) approximately satisfy Eq. (3.3) and Eq. (3.4) simultaneously. These two conditions ensure that the fields evolve along statistical mixtures of state vectors of the form given by Eq. (3.1) only. In this case the transient drop in the purity due to the statistical average of the mixture goes back up to one as the fields approach the pure trapping state, $|\Psi\rangle_N^{(M)}$. Involving quantum states of different structure into the evolution results in an irreversible loss of purity, and the system evolves into a mixed quantum state of reduced or vanishing correlation. The same occurs in the case of unequal interaction parameters as we mentioned earlier. Although new structures

will not appear when $g'\tau'$ is different than $g''\tau''$ (both approximately satisfying Eqs. (3.3) and (3.4)) the fields will not be amplified symmetrically resulting in a reduction of correlation at steady state. In the example of the initial state, $|\Psi\rangle_l^{(l)}$, above applying $g'\tau'$ and $g''\tau''$ equal to $l\pi/\sqrt{2}$ (l = *7, 10, 17*) now using different l-s for the different cavities the correlation is completely gone and the purity factor is ξ = *0.5* at steady state.

III.3. Preparation of the initial state, $|\Psi\rangle_n^{(l)}$, and switching to its amplification

For $n \neq 0$ the preparation of the fields in the appropriate initial state, $|\Psi\rangle_n^{(l)}$, starting from the number state, $|n,n\rangle$, is not as simple as it has been for $n = 0$ above (on the production of number states see Refs. [9,12,18]). The reason for this is similar to the one in the amplifying step of the procedure above when contrasting the two cases of $n = 0$ and $n \neq 0$, namely, undesirable quantum states show up when the atom leaves the interaction in its upper state. Although the probability of this effect cannot in principle be killed out completely it can be drastically reduced applying the same idea as above. Let us send one single excited atom through the fields started from the number state, $|n,n\rangle$, and set the interaction parameters, $g'\tau'$ and $g''\tau''$, in the two cavities as follows ($g'\tau' = g''\tau''$ is required only in the amplifying procedure, not here). First of all, $g'\tau'$ must satisfy the condition, $|C'_{n+l}| = |S'_{n+l}|$. On the other hand, we need the second interaction parameter, $g''\tau''$, to approximately satisfy conditions, $|S''_{n+l}| \cong 1$ and $S''_n \cong 0$, *simultaneously*. In this case Eq. (2.5) tells us that the probability of detecting the outcoming atom in its upper state is close to zero, while the other atomic path provides us with fields in a state approximately equal to $|\Psi\rangle_n^{(l)}$. We have seen above that this obviously works for vacuum, $n = 0$. In the case of $n = 1$ choosing for example $g'\tau' = \pi/(4\sqrt{2})$ and $g''\tau'' = 17\pi/(2\sqrt{2}) = 6.01\,\pi$ gives us the probability of *0.1 %* to detect the upper atomic state and the generated fields can very well be approximated by the pure state, $|\Psi\rangle_l^{(l)}$. Once the initial state, $|\Psi\rangle_n^{(l)}$, is prepared for amplification by one single atom we can proceed to the second (amplifying) step of the procedure by switching the interaction parameters to the

appropriate values discussed above.

The switching itself sounds simple in principle, but it raises some technical difficulties in a real experiment. It is easy to see that, in general, one cannot match the interaction parameters between the two steps (preparation of the state and its amplification) by simply switching the velocity of the atomic beam. In order to do that the ratio, $g'\tau'/g''\tau''$, would be needed to remain the same throughout the procedure. This, however, is not possible because the equality condition, $g'\tau' = g''\tau''$, of the second step cannot possibly be met in the first one (see conditions above). Since the purpose of this condition is to assure a symmetric amplification it can be ignored only if a trapping state of first order correlation ($m = 1$) is to be produced (since there is no amplification here at all). In this case one can find interaction parameters, $g'\tau' \neq g''\tau''$, that prepare the state, $|\Psi\rangle_n^{(1)}$, starting from the number state, $|n,n\rangle$, in the first step and then trap it by simply switching the atomic velocity in the second one. This obviously imposes a restriction on the set of parameters that have been found above for the two steps separately since now we need only those of them that satisfy the conditions of both steps simultaneously. For example the conditions to generate $|\Psi\rangle_0^{(1)}$ from $|0,0\rangle$ are $g'\tau' = \pi/4 + k\pi/2$ and $g''\tau'' = \pi/2 + l\pi$, while to trap this state are $g'\tau' = p\pi$ and $g''\tau'' = q\pi/\sqrt{2}$. Choosing the integers k, l, p and q to be *2, 8, 5* and *48*, respectively, the ratio $g'\tau'/g''\tau''$ is *5/34* in both steps. Thus, a simple change in the atomic velocity (in this example a decrease by a factor of *4*) after the first atom will trap the fields in the state, $|\Psi\rangle_0^{(1)}$. We should mention at this point that, as it is going to be be shown in the next section (also see Ref. [14]), the smaller the correlation (m) the longer the lifetime of the pure state is at the presence of dissipations (see also in Ref. [14]). Therefore, a simple procedure to generate the long-lived state, $|\Psi\rangle_n^{(1)}$, from the number state, $|n,n\rangle$,is possible. This nonlocal entanglement, as it is discussed in Ref. [19], can prove useful in several interesting applications such as to generate interatomic EPR-correlations between spacially distinct atomic beams that can for example be applied to test quantum complementarity.

The generation of higher order correlations, however, seems to be more complicated. Since the equality condition, $g'\tau' = g''\tau''$, is crucial for pure amplification such

parameters that can be switched by atomic velocities cannot be found. A, rather unrealistic, adjustment of the cavity lengths or of the coupling constants relative between the two cavities seems to be necessary when proceeding from the preparation to the amplification step. There may be some, probably difficult, technical tricks to get around this problem for example shooting the single atom in the first step through the cavities at an angle allowing for a control of the individual interaction times in either of the two cavities separately.

Another possibility to reconcile the two steps of the procedure may be to use conditional measurements in the first step [12]. The two possible outcomes when detecting the final state of the first single atom imply two possible pure states for the fields. We can set the parameters in such a way that one of these would be the desired $|\Psi\rangle_n^{(1)}$ for the fields. Thus, we impose the condition that the atomic state generating $|\Psi\rangle_n^{(1)}$ needs to be detected in order to proceed to the amplifying step of the procedure. Starting for example from the field state, $|1,1\rangle$, and using $g'\tau' = g''\tau'' = 7\pi/4\sqrt{2}$ the detection of the lower atomic state, $|b\rangle$, (the probability of which is about *50%* in this example) ensures that the field state, $|\Psi\rangle_1^{(1)}$, has been generated. (If we detect $|a\rangle$ then we need to reconstruct, $|1,1\rangle$, and start again until $|b\rangle$ is detected.) Now lowering the atomic velocity by a factor of *4* we are back to the same amplifying step as the one discussed in subsection III.2 above in detail to generate the trapping state, $|\Psi\rangle_1^{(6)}$.

We have shown in this section that entangled trapping states, $|\Psi\rangle_N^{(M)}$, given by Eq. (3.1) of arbitrary N and M can be produced using a two-step procedure that is based on conditions regarding the interaction parameters of the two cavities. In principle, N and M can be made arbitrarily large resulting in a nonlocal quantum superposition of distinct macroscopical fields -- sometimes referred to as a nonlocal "Schrödinger-cat". Since quantum superpositions are well-known to be very sensitive to dissipations [14] we are going to study the effect of cavity losses and finite temperature on the method discussed above in the next section.

IV. THE EFFECT OF DISSIPATION ON THE PRODUCTION OF ENTANGLED TRAPPING STATES

Pure steady state entanglement of the nonlocal micromaser fields has been found in the absence of dissipation in the form of trapping states, $|\Psi\rangle_N^{(M)}$, given by Eq. (3.1). In this section we study the effect of finite losses and temperature numerically, concentrating on the production of these states. We assume that the interaction time an atom spends in the cavities is much shorter than the cavity lifetime. (In a typical experimental setup the difference is three orders of magnitude.) In this case we can ignore the decay of the fields during the time an atom is inside the cavities and separate the evolution of the system into two parts: atom-field interaction (pumping) and decay of the fields (damping). Thus, the field-density matrix at the instant when an atom leaves cavity *2* can be calculated from Eq. (2.2) resulting in the matrix $\rho(0)$, the decay of which is then calculated from this initial condition as a function of time by applying the solution of the standard master equation for a field mode of an empty cavity damped to a reservoir of finite temperature given by

$$\rho_n^{\{k\}}(t) = e^{-\gamma\frac{k}{2}t}\sum_{l=0}^{n}\sum_{m=n-l}^{\infty} C_{n,m,l}^{\{k\}}\frac{A^m}{B^{m+k+1}}\left(\frac{A'}{A}\right)^{n-l}\left(\frac{B'}{B}\right)^{l}\rho_m^{\{k\}}(0) \quad . \tag{4.1}$$

Here, $\rho_n^{\{k\}} \equiv \rho_{nm}$ with $k = m\text{-}n$, γ is the cavity decay rate and t is time. The coefficients are given by

$$C_{n,m,l}^{\{k\}} \equiv (-1)^l\binom{m+k+l}{l}\binom{m}{n-l}\sqrt{\binom{m+k}{n+k}\Big/\binom{m}{n}} \quad , \tag{4.2}$$

$A \equiv (n_b+1)\left(1-e^{-\gamma t}\right)$, $B \equiv 1+n_b\left(1-e^{-\gamma t}\right)$, $A' \equiv e^{-\gamma t}-n_b\left(1-e^{-\gamma t}\right)$ and $B' \equiv A'-e^{-\gamma t}$, where n_b is the average number of thermal photons. A derivation of this solution is given in the Appendix (see also Ref. [17]). It is easy to show that in the special case of zero temperature, i. e. $n_b = 0$ Eq. (4.1) reduces to

$$\rho_n^{\{k\}}(t) = e^{-\gamma(n+k/2)t} \sum_{m=0}^{\infty} \sqrt{\binom{m+k}{n+k}\binom{m}{n}} \left(1-e^{-\gamma t}\right)^{m-n} \rho_m^{\{k\}}(0) \quad . \qquad (4.3)$$

The two fields decay according to this time dependent density matrix during the time interval until the next atom arrives. Hence, the time evolution of the fields for a stream of atoms is calculated by numerically iterating the two cycles of pumping and damping by applying Eqs. (2.2) and (4.1), respectively. Apparently, the pump statistics of the micromasers can also be taken into account via the distribution of time intervals of the decay cycles in the procedure. The effect of pump fluctuations will be studied later on by assuming Poissonian statistics for the atomic beam.

In the first examples we consider regular pump statistics and the temperature of the reservoir is assumed to be zero (Eq. (4.3) is applied). We study the effect of cavity losses on the production of entangled trapping states discussed in the earlier sections. Let us start the fields from a pure state, $|\Psi\rangle_0^{(1)}$, and apply $g\tau = \pi$. Fig. 8 shows the evolution of the purity factor $\xi^{(k)}$ for four different values of γt illustrating the evolution of the fields. We find that provided the losses are not too large (in this example if $\gamma t \leq 0.001$) the same entangled trapping state, $|\Psi\rangle_0^{(3)}$, is produced in the short-time transient regime as in the absence of losses followed by a decay of the correlation the rate of which depends on γt (see solid and dot-dashed lines in Fig. 8). For larger losses the complete entanglement has no chance to build up (dashed and dotted lines). Some correlation can be found for $\gamma t = 0.01$ at short times (dashed line), while no correlation at all for $\gamma t = 0.1$ (dotted line). The steady state of the fields in each of these four cases is a mixed quantum state of no off-diagonal elements in the density matrix, i. e. no correlation between the fields. The photon statistics is depicted in Fig. 9 (a), and apparently, the steady state is a (nonlocal) classical superposition of the photon numbers *0* and *3* if $\gamma t \leq 0.001$. The only non-zero matrix elements are the *(0,0,3,3)* and *(3,3,0,0)* equal to *0.5* resulting in a purity factor of $\xi = 0.5$ (see solid and dot-dashed lines Fig. 8). On the other hand, Fig. 9 (a) shows how this classical superposition decays due to losses exceeding this threshold ($\gamma t > 0.001$) until

finally the fields settle down to vacuum (of steady state purity factor $\xi = 1.0$, dotted line in Fig. 8). These two regimes of small and large losses can also be distinguished in the next example where the fields are started from the initial state, $|\Psi\rangle_1^{(1)}$, and $g\tau = 7\pi/\sqrt{2}$ is applied. The evolution of the purity factor $\xi^{(k)}$ is depicted in Fig. 10 for the same four values of γt as in Fig. 8. It can be seen that some correlation builds up in the transient regime if $\gamma t \leq 0.001$ (see solid and dot-dashed lines in Fig. 10) while there is no correlation between the fields at any time if the losses are larger. Comparing Fig. 10 to Fig. 8 it is apparent that the quantum superposition, $|\Psi\rangle_1^{(6)}$, that we want to generate in the present example is more sensitive to cavity losses than the one $|\Psi\rangle_0^{(3)}$ was before, and the threshold for a correlation to build up is higher. This has been discussed by others for example in Ref. [14] that a quantum superposition decays exponentially faster for superposed states of larger separation (or order of correlation, that is M in our case). The steady state photon statistics of the fields for the present example is depicted in Fig. 9 (b) showing a nonlocal classical superposition of photon numbers *1* and *7* for small losses ($\gamma t < 0.001$) that spreads out toward vacuum if the losses were larger.

We also studied the (zero temperature) decay of the entanglement in the two examples of the quantum states above for Poissonian pump statistics. Comparing Fig. 11 to Figs. 8 and 10 it can be seen that apart from the fluctuations there is no significant difference in the decay of the correlation between the regular and Poissonian cases. For small cavity losses where the average of γt is smaller than *0.01* even the fluctuations are negligible. This suggests that the transient production of entanglement is not significantly sensitive to pumping fluctuations.

Now, let us assume that finite thermal radiation is present in the cavities (Eq. (4.1) is applied), and consider regular pump statistics. The most significant effect is that a coupling between the blocks in the photon number space that were disconnected by the trapping states at zero temperature arises. As a result of this new diagonal elements contribute to the density matrix located exactly at the trapping points of the adjacent blocks, although new correlation obviously does not build up. The photon statistics of the fields started from the state, $|\Psi\rangle_0^{(1)}$, applying $g\tau = \pi$ are depicted in Fig. 12 for four different mean number of

thermal photons at a cavity loss of $\gamma t = 0.0001$ showing the new terms rising up at the adjacent trapping points of the system. The larger the temperature the more diagonal trapping points are populated besides the zero temperature ones, *(0,0,3,3)* and *(3,3,0,0)*. Another significant effect of thermal radiation is the enhancement of the decay of correlation between the micromasers. The off-diagonal terms of the field-density matrix decay faster for larger number of thermal photons. As an example, Fig. 13 depicts the evolution of the purity factor $\xi^{(k)}$ toward the state of the fields described in Fig. 12 showing the enhanced decay of correlation for the same four mean number of thermal photons and cavity loss. Comparing Fig. 13 to Fig. 8 it is apparent that for small temperatures ($n_b < 0.01$) the short-time transient entanglement can still be produced. In fact, finite temperature seems to predominantly affect the steady state rather than the transient regime.

Assuming the experimentally available lowest temperature *0.1 K*, and the corresponding mean thermal photon number $n_b = 3 \cdot 10^{-5}$ it is easy to see that in the case of $\gamma t = 0.001$ the effect of thermal radiation can be neglected. If the cavity lifetime were assumed to be $1/\gamma = 1.0$ *second* then according to Fig. 14 the entangled state, $|\Psi\rangle_0^{(3)}$, survives with purity factors of $\xi \cong 90$, *80* and *70 %* for time intervals of about *30*, *80* and *150 milliseconds*, respectively. Introducing the generally used pumping parameters N_{ex} and θ, where $N_{ex} = 1/\gamma t$ and $\theta = g\tau\sqrt{N_{ex}}$ the above pumping corresponds to $N_{ex} = 1000$ and $\theta = \pi\sqrt{N_{ex}} = 99.3$ (since $g\tau = \pi$ is required by the amplifying mechanism to generate the state, $|\Psi\rangle_0^{(3)}$). The above comparison of regular and Poissonian pumping statistics suggests that this estimate is not particularly sensitive to pump fluctuations. It is also in accordance with the two usual "micromaser-conditions". Firstly, assuming the experimentally available coupling $g \cong 40\ kHz$ the separation to pumping and damping cycles is well justified since $\tau << 1/\gamma$. On the other hand it follows from $\gamma t = 0.001$ ($N_{ex} = 1000$) that the time interval between the successive atoms (or the average of it for Poissonian statistics) is about $t \cong 1.0$ *millisecond* that implies that there is at most one atom in the cavities at a time because $\tau << t$. Going for lower values of γt (larger N_{ex}) in order to hold the entanglement for a longer time interval, or to be

able to deal with a superposition of larger separation (or order of correlation) M we need to elongate the cavity lifetime. The time interval t between the atoms could be reduced only if g was enlarged to have the second micromaser-condition satisfied.

As a summary to this section it can be said that although finite dissipation prevents the steady state production of entangled nonlocal fields transient correlation insensitive to thermal radiation and pumping fluctuations can still build up for a pumping, N_{ex}, that exceeds a certain threshold established by the losses. This suggests that the state of the fields undergoes a transition from an uncorrelated to a correlated behavior above threshold. The lifetime of the correlated regime depends on the cavity damping rate γ and the separation (or order of correlation), M, of the two trapped number states in the quantum superposition. Experimental realization of transient entanglement of nonlocal fields employing two-field trapping states of small photon numbers seems to be feasible by the presently available exceedingly high-Q ($Q \cong 10^{10}$) micromaser cavities at low temperatures ($T = 0.1\ K$, $n_b = 3 \cdot 10^{-5}$), and could be extended to macroscopical quantum superpositions by using longer cavity lifetimes and stronger atom-field coupling in the near future.

V. SUMMARY

In the present paper the fields of two coupled micromasers are studied. The state of the atoms establishing the coupling via passing through cavity *1* first and then cavity *2* is nonselectively measured after the interaction (see Fig. 1). In the absence of dissipation the possible steady states are the various superpositions of two-field trapping number states satisfying the trapping condition given by Eq. (2.3), many of which are pure quantum states given by Eq. (2.12). They rely on the fact that the photon number space consists of disconnected blocks in this case of two dimensions due to the two nonlocal fields and each block may contribute to the superposition with its own trapping number state. The realization of one of these steady states, i. e. populating a certain configuration of trapping numbers depends upon the initial state of the fields and the interaction parameters of the

micromasers. The time evolution of the fields toward these steady states is studied numerically concentrating mainly on the production of pure entangled states of the form $|N,N+M\rangle \pm |N+M,N\rangle$. Here, N and $N+M$ are arbitrary trapping numbers belonging to disconnected blocks of the photon number space, and M specifies the order of correlation between the two nonlocal fields. They, in principle, can be made arbitrarily large resulting in a steady state nonlocal quantum superposition of distinct macroscopical fields -- sometimes referred to as a nonlocal "Schrödinger-cat". Starting from a number state, $|N,N\rangle$, these states can be produced using a two-step procedure. First, we introduce some correlation into the system via generating the above state of $M = 1$ by one single atom and then amplify it to a larger M corresponding to the trapping state above. Both steps are based on special conditions regarding the interaction parameters, $g't'$ and $g''t''$, of the two cavities. They are chosen to ensure that the fields evolve along statistical mixtures of state vectors of the form given by Eq. (3.1) only. In this case the purity of the fields after experiencing a transient drop due to the statistical mixture will be regained at steady state showing a pure quantum state of the structure above. An inclusion of different quantum states into the evolution, or an asymmetrical amplification of the state vector (when $g't' \neq g''t''$) would result in an irreversible loss of purity and mixed quantum states of no correlation at steady state. In the absence of losses this procedure provides us with arbitrary (micro- as well as macroscopical) quantum superpositions of nonlocal fields at steady state.

Introducing dissipation into the system by applying our solution of the standard master equation of a damped harmonic oscillator we find that although entanglement in the above form cannot be produced at steady state it can build up in the short-time transient regime if the losses were small enough. The rate of the decay of correlation depends upon the cavity lifetime and the separation (or order of correlation), M, of the photon numbers in the superposition above. On the other hand, for exceedingly large losses correlation has no chance to arise at any time. The system undergoes a transition from an uncorrelated to a correlated behavior when the pumping parametrized by N_{ex} exceeds a certain threshold between the large- and small-loss regimes ($g\tau$ is fixed throughout the procedure). In the

small-loss (large N_{ex}) regime the entanglement finally decays into a classical mixture of the above photon numbers, N and $N+M$, at steady state while in the large-loss (small N_{ex}) regime the photon statistics spreads out toward vacuum. It is also shown that the transient behavior is only slightly modified by finite temperature and pump fluctuations. Finite temperature enhances the decay rate mainly affecting the steady state of the fields, and at the same time establishes a coupling between the disconnected blocks of the photon space allowing for new but only diagonal trapping states to contribute. We conclude that an entanglement of nonlocal micromaser fields can be produced via this nonselective measurement scheme by utilizing the two-field trapping states and the discussed amplification mechanism -- in principle, even on the macroscopic level. Experimental realization of these states seems to be feasible in the transient regime by the presently available facilities for trapping states of microscopically small photon numbers, and could be extended to macroscopical quantum superpositions -- nonlocal "Schrödinger-cats" -- by applying longer cavity lifetimes and stronger atom-field coupling in the near future.

APPENDIX

In Section IV the effect of finite losses and temperature in the two micromaser cavities is studied by applying the time dependent density matrix given by Eq. (4.1). We show here that it is the solution of the standard interaction picture master equation for a field mode of an empty cavity coupled to a reservoir of finite temperature that reads as

$$\dot{\rho} = \frac{\gamma}{2}\left[(n_b + 1)\left(2a\rho a^\dagger - a^\dagger a\rho - \rho a^\dagger a\right) + n_b\left(2a^\dagger \rho a - aa^\dagger \rho - \rho aa^\dagger\right)\right] \quad , \qquad \text{(A.1)}$$

where γ is the coupling constant between the cavity mode and the reservoir, $a^\dagger$ and a are the mode creation and annihilation operators, and n_b is the average number of thermal photons [15]. It can be seen in the number representation that the elements of the density matrix ρ_{nm} are coupled only along the same diagonal. Introducing $\rho_n^{(k)} \equiv \rho_{nm}$, where k

$= m\text{-}n$ the master equation reads as

$$\dot{\rho}_n^{(k)} = \gamma(n_b+1)\left(\sqrt{(n+1)(n+k+1)}\rho_{n+1}^{(k)} - (n+\frac{k}{2})\rho_n^{(k)}\right) + \\ +\gamma n_b\left(\sqrt{n(n+k)}\rho_{n-1}^{(k)} - (n+1+\frac{k}{2})\rho_n^{(k)}\right) \quad . \tag{A.2}$$

Defining the function

$$g^{(k)}(z,t) \equiv \sum_{n=0}^{\infty} \rho_n^{(k)}(t)\sqrt{\frac{(n+k)!}{n!}}z^n \quad , \tag{A.3}$$

the master equation Eq. (A.2) can be transformed into a partial differential equation for $g^{(k)}(z,t)$ given by

$$\frac{\partial g^{(k)}}{\partial t} + (z-1)\left[1-n_b(z-1)\right]\frac{\partial g^{(k)}}{\partial z} = \left[n_b(z-1)(k+1) - \frac{k}{2}\right]g^{(k)} \quad , \tag{A.4}$$

the solution of which reads as

$$g^{(k)}(z,t) = e^{-\gamma\frac{k}{2}t}\sum_{n=0}^{\infty}\rho_n^{(k)}(0)\sqrt{\frac{(n+k)!}{n!}}\frac{A^n}{B^{n+k+1}} \quad , \tag{A.5}$$

where

$$A \equiv 1-(z-1)\left[n_b\left(1-e^{-\gamma t}\right)-e^{-\gamma t}\right] \quad , \tag{A.6}$$

$$B \equiv 1-n_b(z-1)\left(1-e^{-\gamma t}\right) \quad . \tag{A.7}$$

The inverse transformation of Eq. (A.3) is given by

$$\rho_n^{(k)}(t) = \frac{1}{\sqrt{n!(n+k)!}} \left. \frac{\partial^n g^{(k)}}{\partial z^n} \right|_{z=0} \quad , \tag{A.8}$$

resulting in the final solution for the density matrix

$$\rho_n^{(k)}(t) = e^{-\gamma \frac{k}{2} t} \sum_{l=0}^{n} \sum_{m=n-l}^{\infty} C_{n,m,l}^{(k)} \left[\frac{A^m}{B^{m+k+l}} \left(\frac{A'}{A} \right)^{n-l} \left(\frac{B'}{B} \right)^{l} \right]_{z=0} \rho_m^{(k)}(0) \quad , \tag{A.9}$$

where

$$C_{n,m,l}^{(k)} \equiv (-1)^l \binom{m+k+l}{l} \binom{m}{n-l} \sqrt{\binom{m+k}{n+k} \Big/ \binom{m}{n}} \quad , \tag{A.10}$$

and $A' \equiv \partial A / \partial z$, $B' \equiv \partial B / \partial z$. It is easy to show that in the special case of zero temperature this reduces to

$$\rho_n^{(k)}(t) = e^{-\gamma(n+k/2)t} \sum_{m=0}^{\infty} \sqrt{\binom{m+k}{n+k} \binom{m}{n}} \left(1 - e^{-\gamma t}\right)^{m-n} \rho_m^{(k)}(0) \quad . \tag{A.11}$$

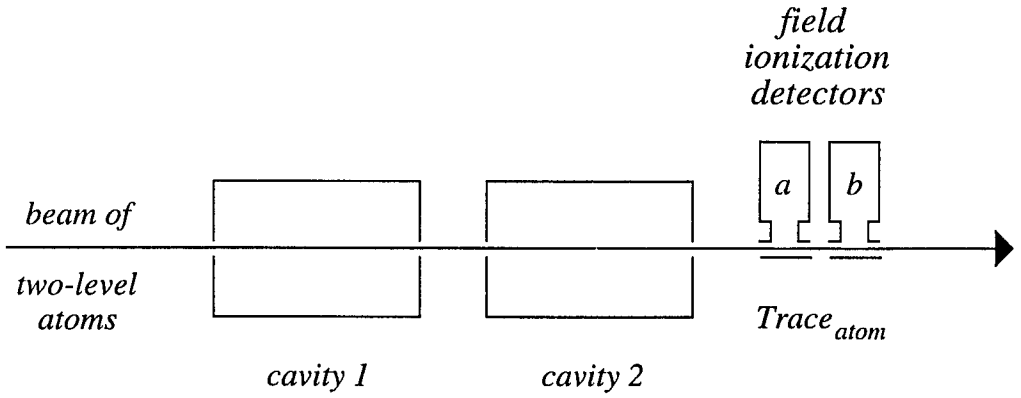

FIG. 1: Schematic arrangement of two micromasers coupled by a beam of two-level atoms the state of which is measured after the interaction by the field ionization detectors without selecting a particular result.

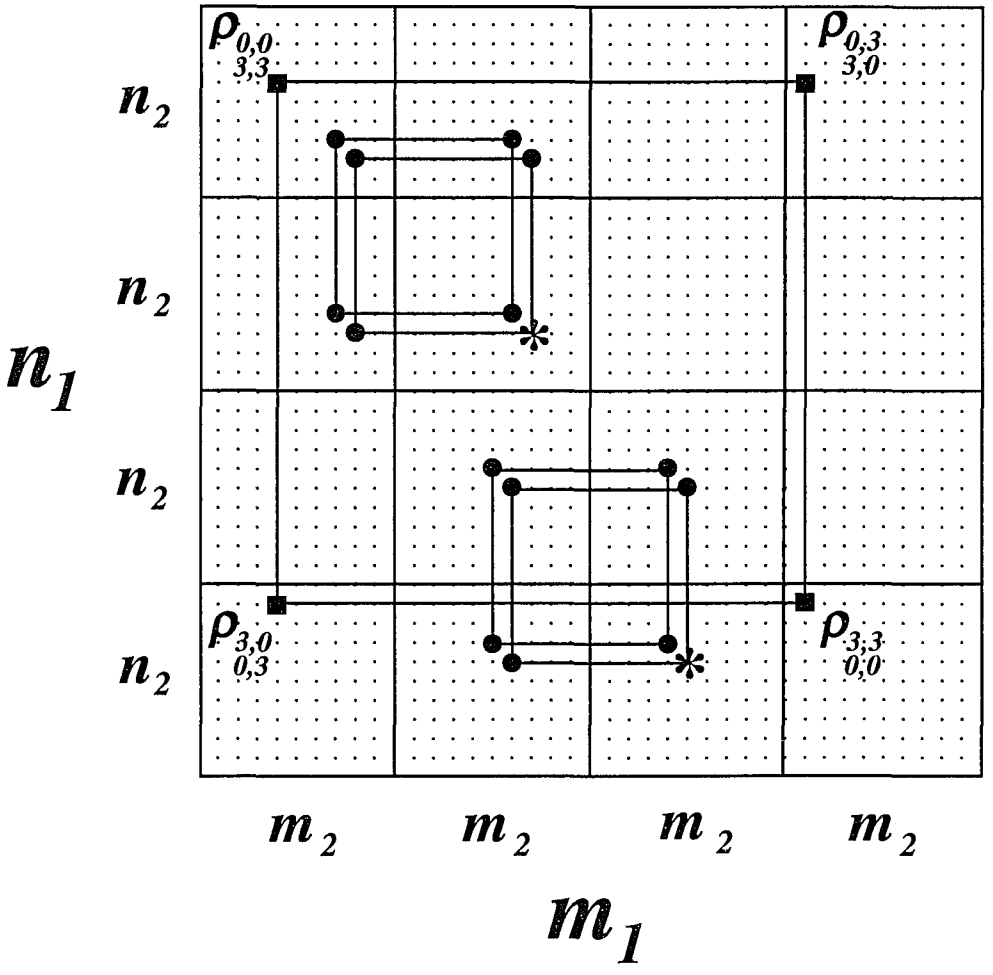

FIG. 2: The structure of the coupling between the elements of the field-density matrix arranged in the form of a supermatrix one matrix of which is given by the photon numbers of the first micromaser n_1 and m_1, while the elements of this matrix are given by n_2 and m_2 of the second micromaser. (The indices, n_1 and n_2, increase downward, m_1 and m_2, to the right.) Two examples show how a matrix element depicted by a star is coupled according to Eq. (2.2) to others located along the "double-square" shown by the solid circles. The four solid rectangles give an example for the structure of a pure state given by $|0,3\rangle \pm |3,0\rangle$ (apart from a normalization factor).

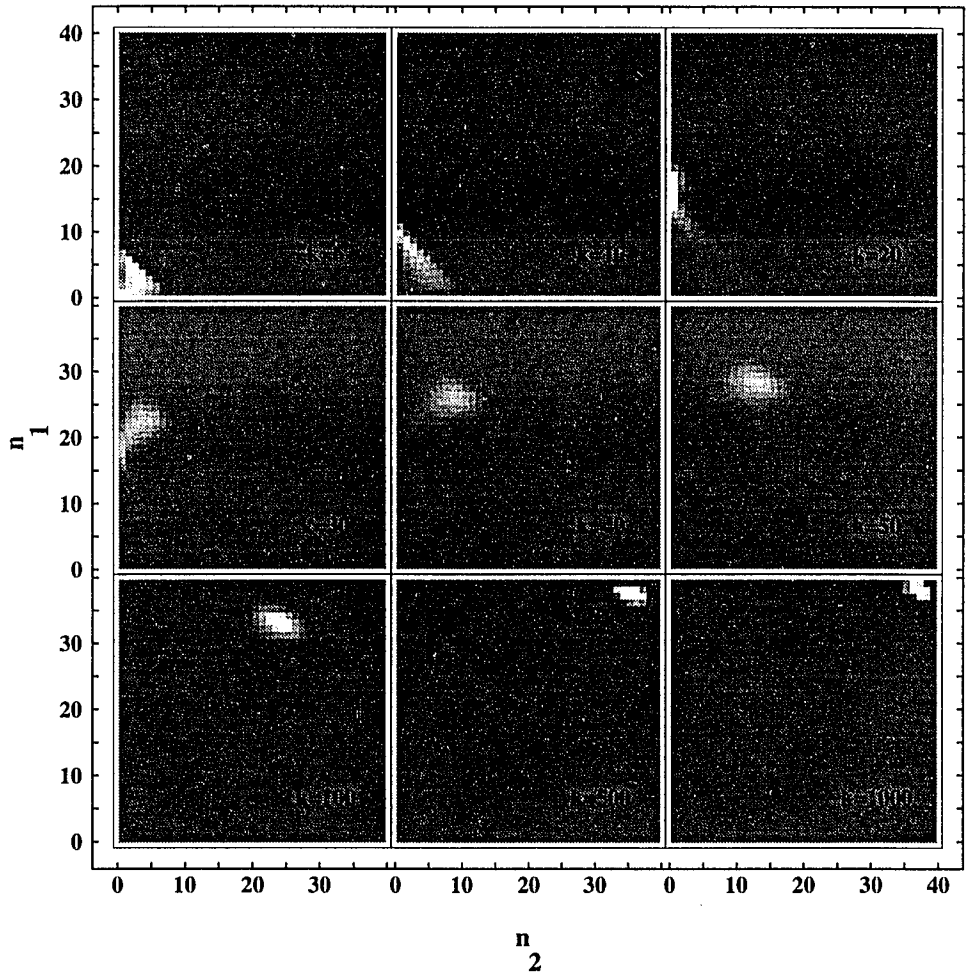

FIG. 3: Density plot of the time evolution of the photon statistics of the fields started from vacuum applying $g\tau = 0.5$. Brighter points correspond to higher probabilities, the gray level to zero and numbers k in the Figure are the atom numbers. After an initial flip lasting until $k \cong 20$ the fields evolve toward $n_1 \cong n_2 \cong 38$ in a well localized structure.

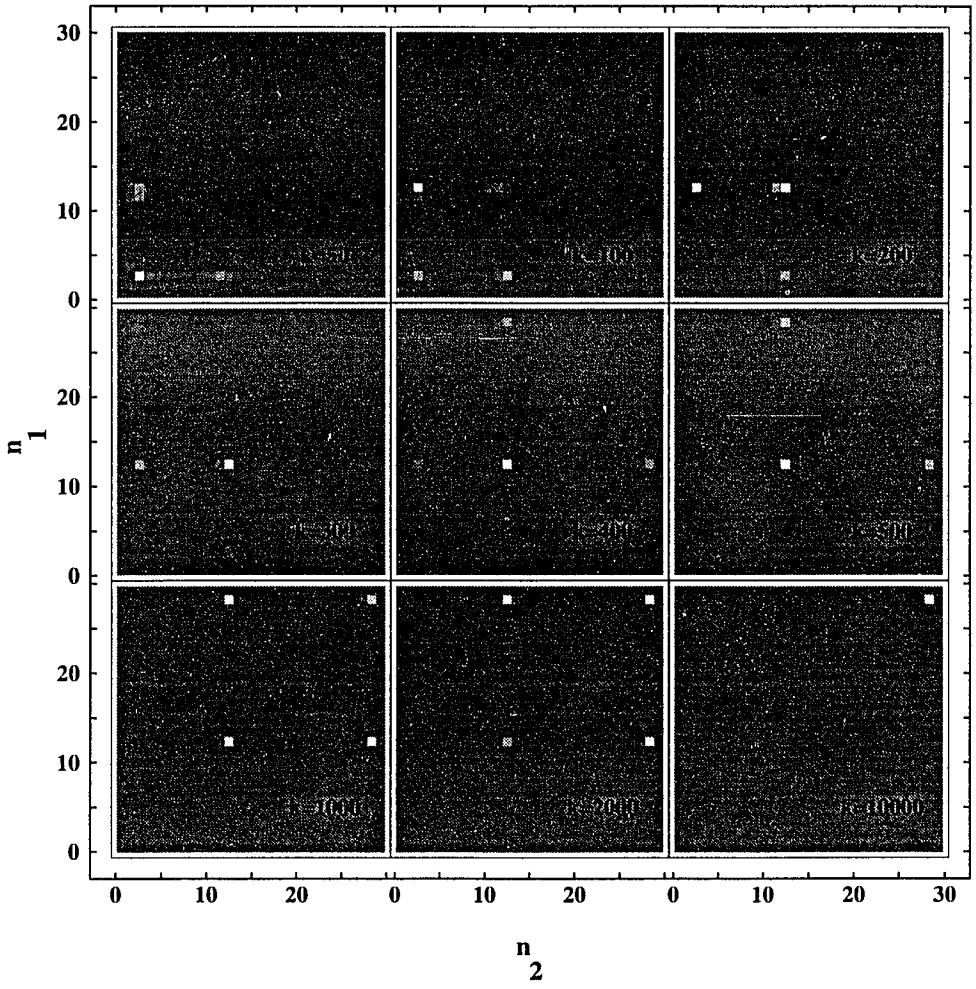

FIG. 4 (a): Density plot of the time evolution of the photon statistics of the fields started from vacuum applying $g\tau = 3\pi/\sqrt{29}$. The system spends long times in the pseudo-trapping points around $N_1 \cong 2$ and $N_2 \cong 12$ and combinations thereof, until finally evolves into the true-trapping point at $N_3 = 28$.

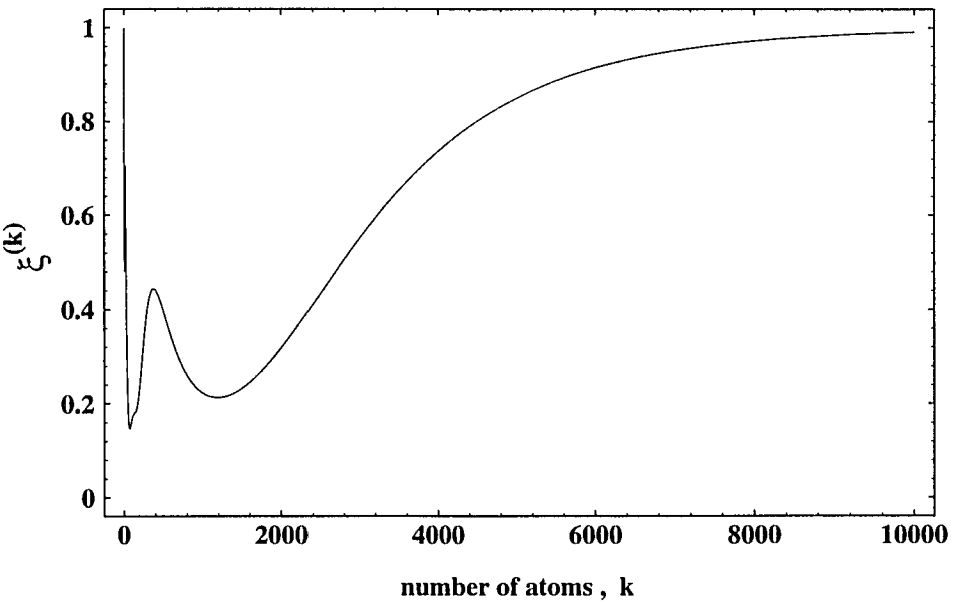

FIG. 4 (b): The evolution of the purity factor, $\xi^{(k)} = Tr[\rho^{(k)2}]$, as a function of the atom number k corresponding to the fields depicted in Fig. 4 (a). The peak around $k \cong 400$ corresponds to a photon statistics that are very similar to that of the number state, $|12, 12\rangle$, at the pseudo-trapping point $N_2 \cong 12$. Finally the steady state is the number state, $|28, 28\rangle$, with purity factor of one.

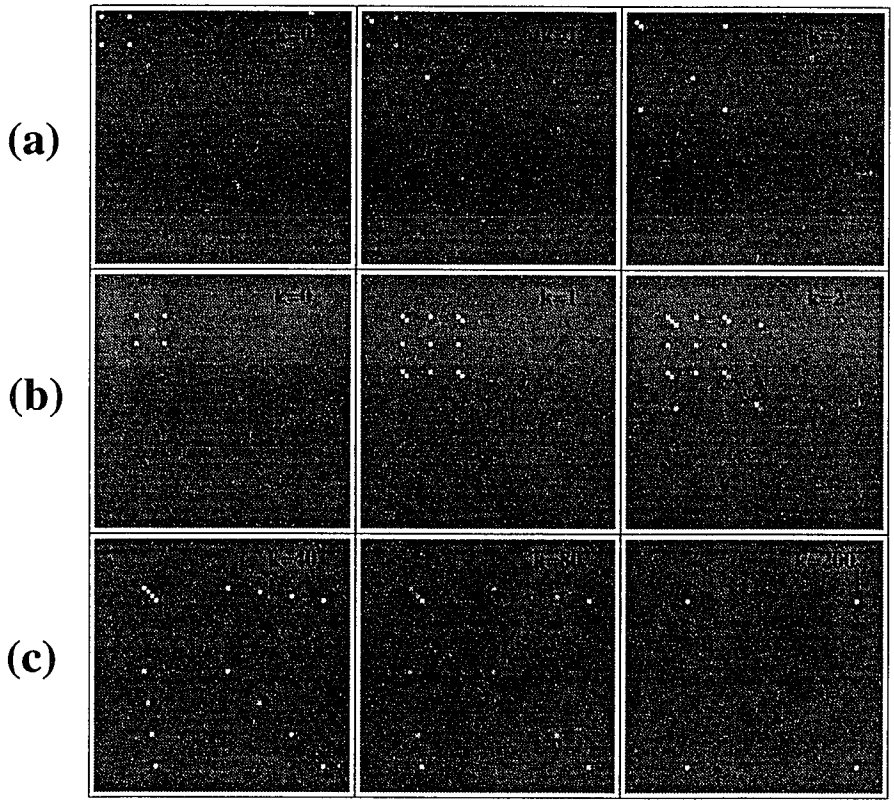

FIG. 5: Density plot of field-density matrices in the form of supermatrices discussed in Fig. 2 at atom numbers k given in the Figure (dark points correspond to negative values). The initial states and applied $g\tau$-s are *row-(a):* $|\Psi\rangle_0^{(1)}$, $g\tau = \pi$, *row-(b):* $|\Psi\rangle_1^{(1)}$, $g\tau = \pi/\sqrt{2}$, and *row-(c)* $|\Psi\rangle_1^{(1)}$, $g\tau = 7\pi/\sqrt{2}$. The evolution of the density matrix shows statistical mixtures of pure states of *row-(a):* $|\Psi\rangle_0^{(m)}$ for m = *1, 2, 3,* and *row-(c):* $|\Psi\rangle_1^{(m)}$ for m = *1, ..., 6* resulting in pure steady states of *row-(a):* $|\Psi\rangle_0^{(3)}$, and *row-(c):* $|\Psi\rangle_1^{(6)}$. In the case of *row-(b)* other states of different structures also contribute resulting in a mixed quantum state of the fields at steady state.

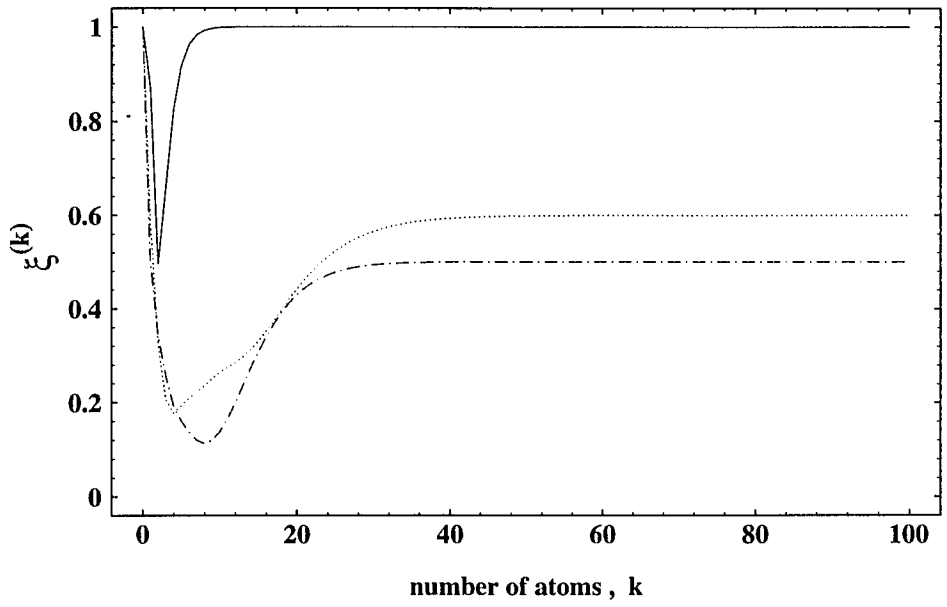

FIG. 6: The evolution of the purity factor $\xi^{(k)}$ as a function of atom number k. The initial states of the fields are the pure states, $|\Psi\rangle_0^{(1)}$, at $g\tau = \pi$ depicted by the solid line, $|\Psi\rangle_1^{(1)}$, at $g\tau = \pi/\sqrt{2}$ depicted by the dotted line, and $|\Psi\rangle_1^{(1)}$, at $g\tau = 2\pi/\sqrt{2}$ depicted by the dot-dashed line. The steady state is a coherent superposition, $|\Psi\rangle_0^{(3)}$, of purity factor $\xi = 1.0$ in the first case, a mixed state showing some correlation indicated by $\xi = 0.6$ in the second case, and a classical mixture of photon numbers 0 and 3 indicated by $\xi = 0.5$ in the third case.

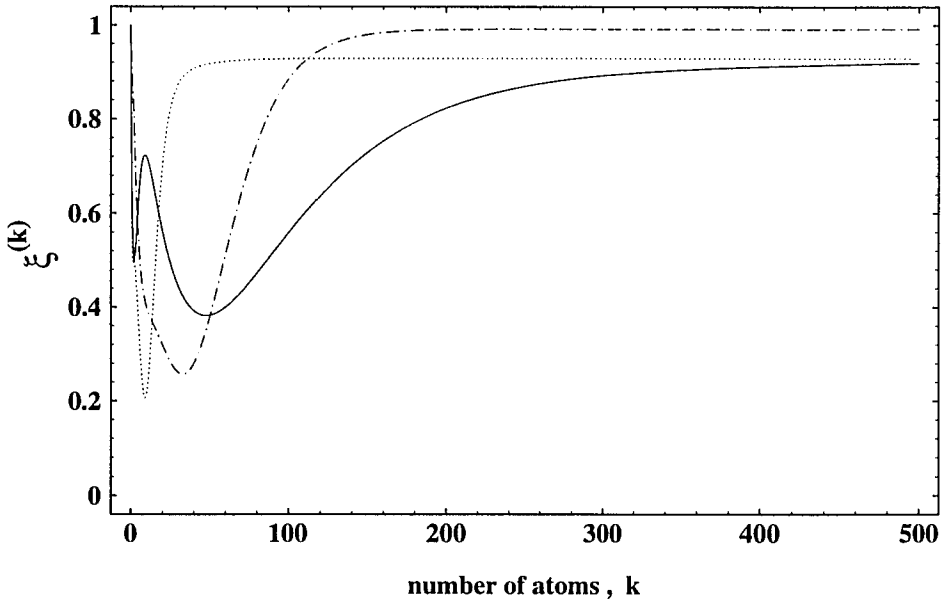

FIG. 7: The evolution of the purity factor $\xi^{(k)}$ as a function of atom number k. The initial state is $|\Psi\rangle_l^{(1)}$ applying $g\tau = l\pi/\sqrt{2}$, where $l = 7, 10, 17$ depicted by the dot-dashed, dotted and solid lines, respectively. The steady state in each case is approximately the same pure quantum state, $|\Psi\rangle_l^{(6)}$, (within the $\pm$ sign in Eq. (3.1)) although the time evolutions are different. The solid line indicates that in the case of $l = 17$ the system is attracted by the pseudo trapping state, $|1,3\rangle - |3,1\rangle$, around $k \cong 9$ that slows its evolution down toward the final state, $|1,7\rangle - |7,1\rangle$, (apart from a normalization factor).

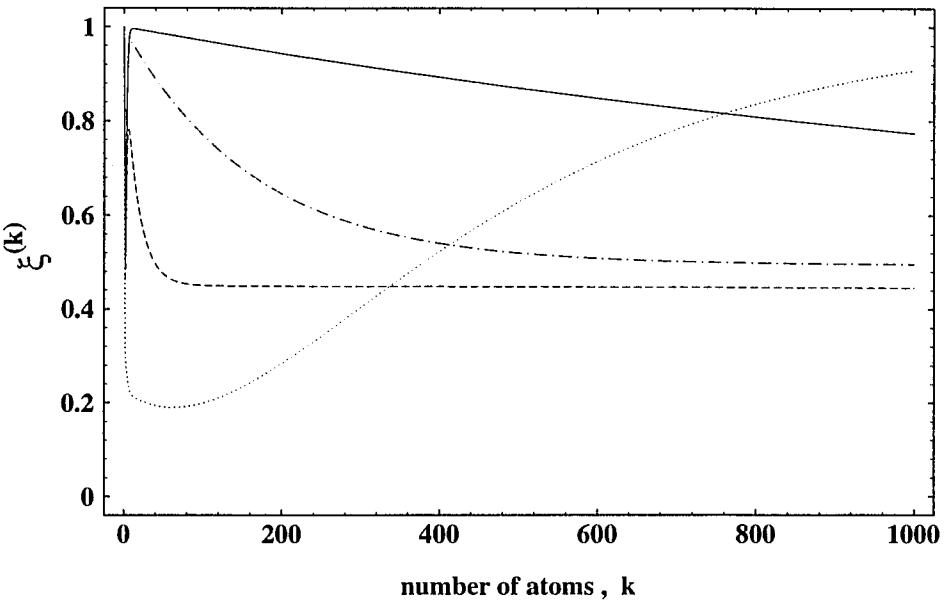

FIG. 8: The evolution of the purity factor $\xi^{(k)}$ as a function of atom number k for four different cavity losses of $\gamma t = 0.0001, 0.001, 0.01,$ and 0.1 depicted by solid, dot-dashed, dashed and dotted lines, respectively. The initial state of the fields is the pure state, $|\Psi\rangle_0^{(1)}$, applying $g\tau = \pi$ that would evolve into the steady state, $|\Psi\rangle_0^{(3)}$, in the absence losses. Apparently, in the cases of small losses (solid and dot-dashed lines) this state can build up in the transient regime where $\xi^{(k)}$ is close to one and then decay into the classical superposition of the above photon numbers *0* and *3*. In the case of large losses (dotted line) there is no transient correlation and the steady state spreads out toward vacuum of $\xi = 1.0$.

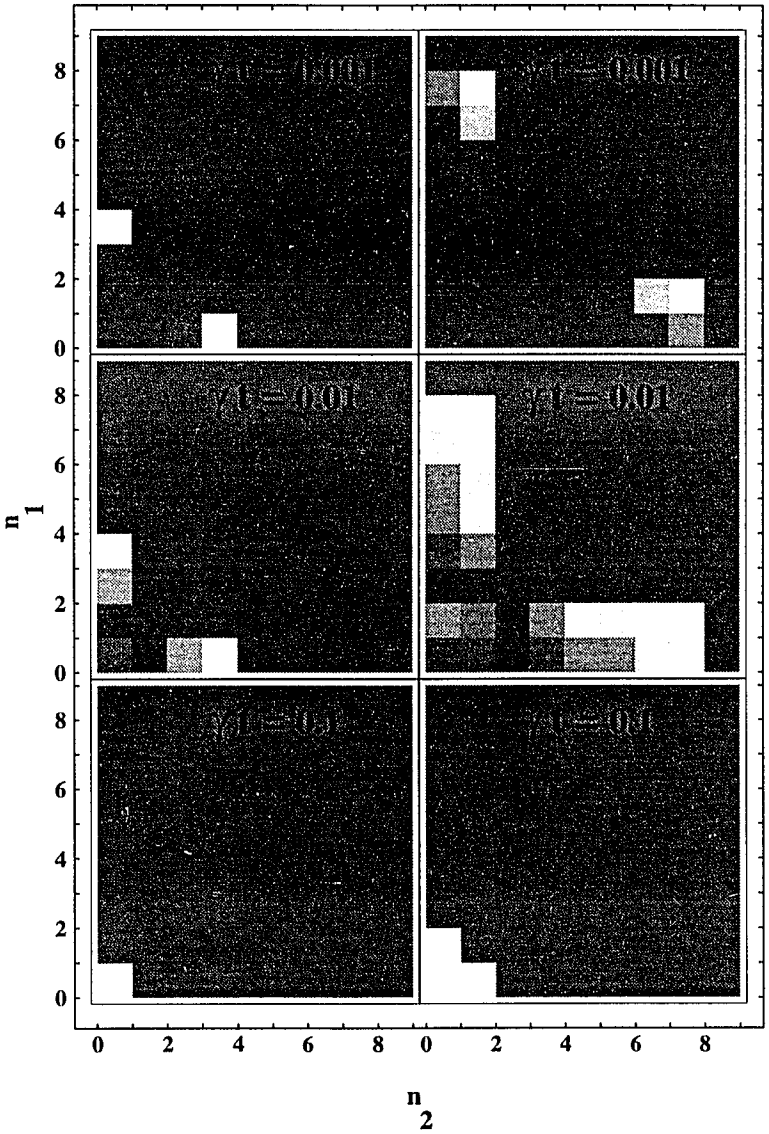

FIG. 9: Steady state photon statistics of the fields started from the initial pure states, *column-(a):* $|\Psi\rangle_0^{(1)}$, at $g\tau = \pi$, and *column-(b):* $|\Psi\rangle_1^{(1)}$, at $g\tau = 7\pi/\sqrt{2}$ for three different losses of γt = *0.001, 0.01* and *0.1* given in the Figure. In the case of small cavity losses the steady states of the fields are classical mixtures of the photon numbers *column-(a): 0* and *3*, and *column-(b): 1* and *7*, that spread out toward vacuum for increasing losses.

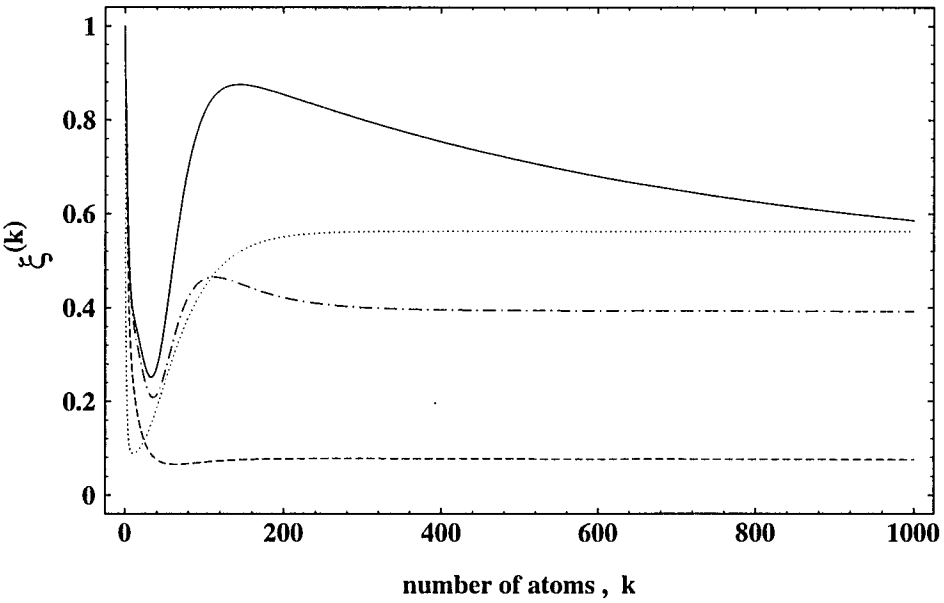

FIG. 10: The evolution of the purity factor $\xi^{(k)}$ as a function of atom number k for four different cavity losses of $\gamma t = 0.0001, 0.001, 0.01,$ and 0.1 depicted by solid, dot-dashed, dashed and dotted lines, respectively. The initial state of the fields is the pure state, $|\Psi\rangle_I^{(1)}$, applying $g\tau = 7\pi/\sqrt{2}$ that would evolve into the steady state, $|\Psi\rangle_I^{(6)}$, in the absence of losses. It can be seen that the losses are large enough to prevent this state to build up at any time although some correlation arises in the case of the smallest amount of loss (solid line).

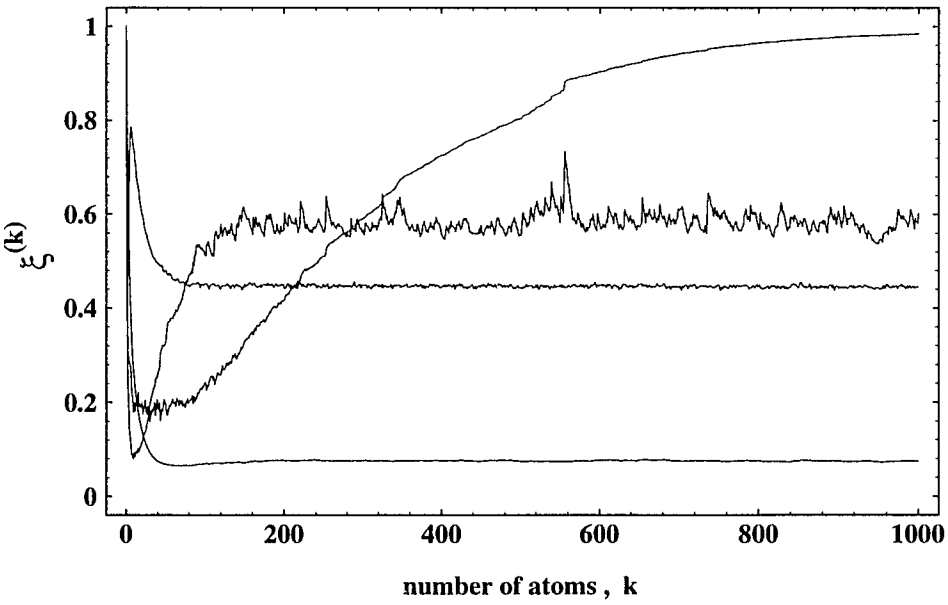

FIG. 11: The evolution of the purity factor $\xi^{(k)}$ as a function of atom number k for Poissonian pump statistics. The initial state of the fields is *(a)* and *(b)*: $|\Psi\rangle_0^{(l)}$, at $g\tau = \pi$, *(c)* and *(d)*:$|\Psi\rangle_1^{(l)}$, at $g\tau = 7\pi/\sqrt{2}$. The average loss is *(a)* and *(c)*: $\gamma t = 0.01$, *(b)* and *(d)*: $\gamma t = 0.1$. Considering Figs. 8 and 10 we find that apart from the fluctuations the short-time transient behavior is not significantly affected as compared to regular pump statistics. For smaller cavity losses, γt, even the fluctuations are negligible.

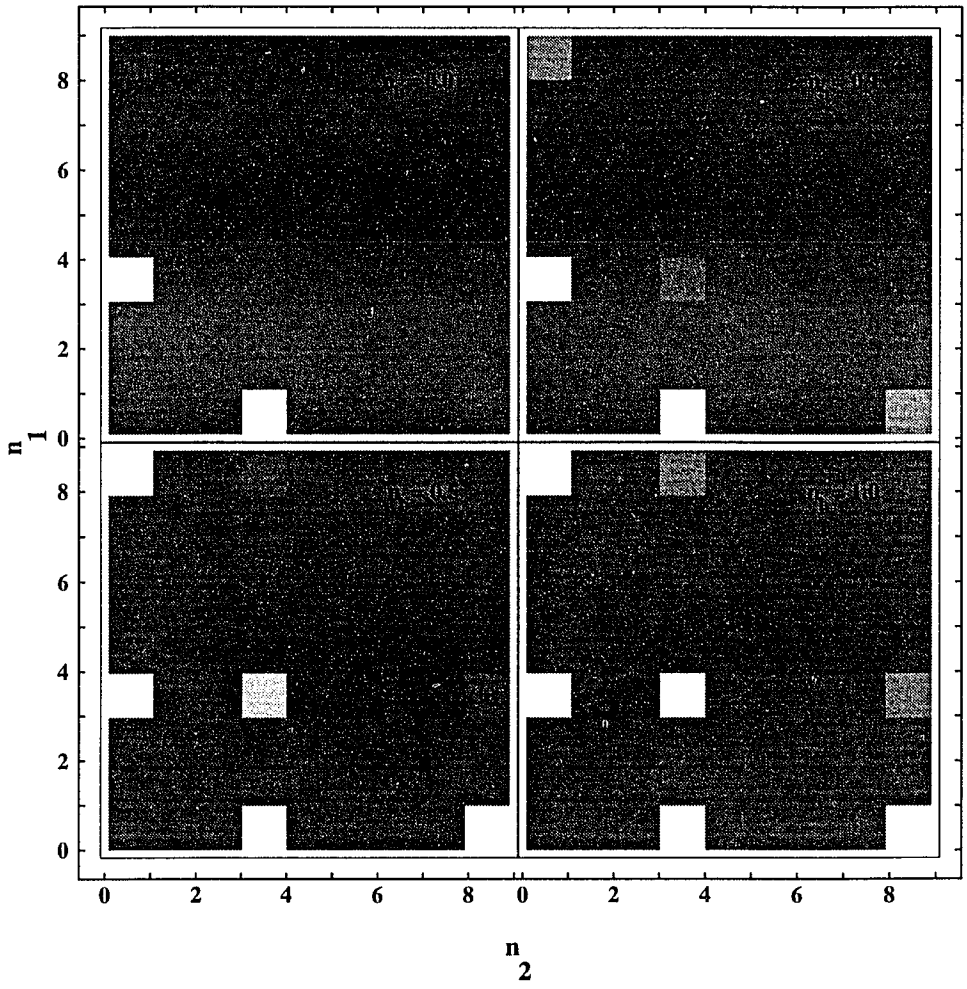

FIG. 12: Density plot of the photon statistics for four different values of the mean thermal photon number n_b that are given in the Figure at cavity loss of $\gamma t = 0.0001$ and at atom number $k = 1000$. The initial state of the fields is the pure state, $|\Psi\rangle_0^{(1)}$, applying $g\tau = \pi$, the steady state of which would be $|\Psi\rangle_0^{(3)}$ in the absence of losses. New trapping states contribute due to the coupling between the blocks that were disconnected at zero temperature.

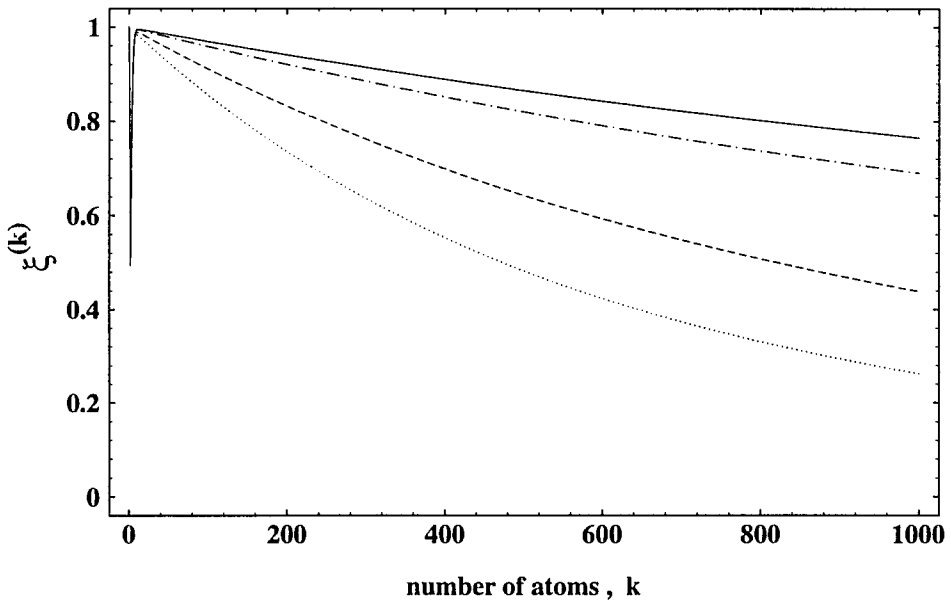

FIG. 13: The evolution of the purity factor $\xi^{(k)}$ as a function of atom number k for four different mean number of thermal photons $n_b = 0.01, 0.1, 0.5$ and 1.0 depicted by solid, dot-dashed, dashed and dotted lines, respectively, at a cavity loss of $\gamma t = 0.0001$. The initial state of the fields is the pure state, $|\Psi\rangle_0^{(1)}$, applying $g\tau = \pi$, the steady state of which would be $|\Psi\rangle_0^{(3)}$ in the absence of losses.

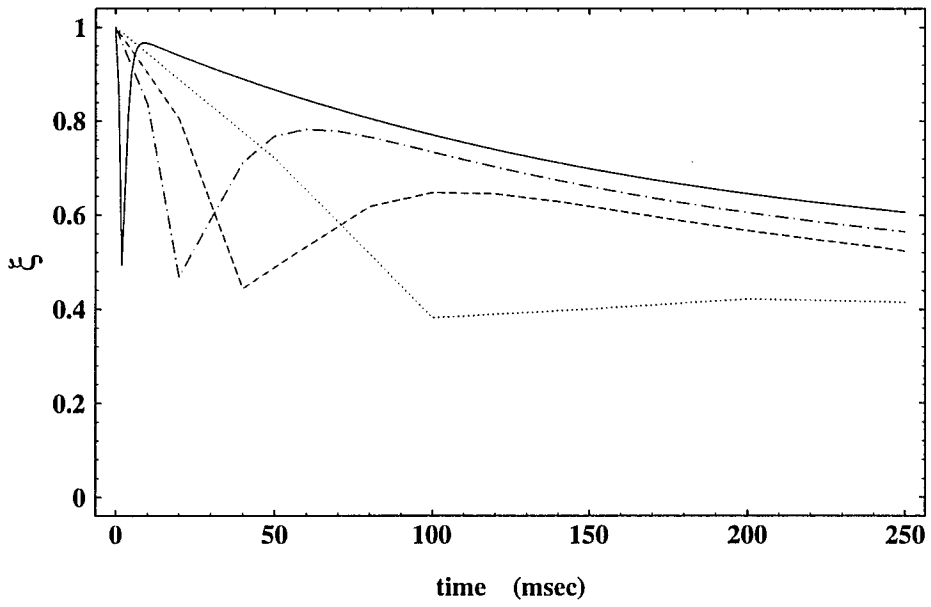

FIG. 14: Time evolution of the purity factor ξ for N_{ex} = *1000, 100, 50* and *20* depicted by solid, dot-dashed, dashed and dotted lines, respectively, when starting from the initial state, $|\Psi\rangle_0^{(1)}$, applying $g\tau = \pi$. Transient correlation starts building up when N_{ex} exceeds *50* that grows up to a complete (transient) entanglement into the state, $|\Psi\rangle_0^{(3)}$, above N_{ex} = *1000*.

3.2.4 Entanglement of Atomic Beams: Tests of Complementarity and Other Applications†

ABSTRACT

It is shown that distinct atomic beams can be (EPR-) entangled when they interact with quantum superpositions of macroscopically separated micromaser fields. Experimentally feasible tests of complementarity are proposed detecting Ramsey interference (or not) in one and "Welcher Weg" information (or not) in the other entangled beam. Available information and fringe contrast can be manipulated using classical and quantum fields. The "quantum eraser" is realized in the former case while it is only a special feature in the latter one. Other applications of entangled atoms are also suggested.

PACS Numbers: 03.65.Bz, 42.50.Wm, 42.50.Dv

The first decade of the micromaser [1] opened a new era in the study of the irreconcilable differences between classical and quantum physics by the experimental realization of the fundamental Jaynes-Cummings coupling [2] between a single two-level atom and a quantized mode of the radiation field. Several nonclassical effects have been predicted theoretically and demonstrated experimentally in this system illustrating the quantized nature of the radiation field. Some of the prominent examples are the collapse and revival of the Rabi nutation [3], generation of nonclassical photon statistics [1, 4, 5] and of macroscopical superpositions [6], and the quantum-nondemolition measurement of the photon number [7]. A wider range of nonclassical phenomena and fundamental principles of quantum mechanics can be directly studied by coupling this genuine quantum device to other quantum systems. Important examples of such correlated systems are the recently suggested atomic interferometers to test the principle of complementarity of

quantum mechanics where, in the interferometer arms, micromasers serve as "Welcher Weg" detectors and the interference of the atoms is being observed [8].

It has been shown that pure quantum superpositions of the two macroscopically separated micromaser fields can be generated at steady state in the absence of dissipations [9] and they are experimentally accessible in the transient regime at the presence of losses for several tens of milliseconds [10]. In our present proposal we utilize the correlated fields of two coupled micromasers traversed by two-level atoms consecutively (see cavities *1* and *2*, and the pumping atomic beam depicted in Fig. 1). Employing two atomic beams, one traversing the first and the other traversing the second cavity (see Fig. 1) the correlation between the two nonlocal fields can be translated into a correlation between the two distinct atomic beams. Let us start from the atom-field state given by

$$\left(|n+m,n\rangle \pm |n,n+m\rangle\right)\cdot|b_1',b_1''\rangle \quad , \tag{1}$$

where $|b_i'\rangle$ and $|b_i''\rangle$ are the lower states of the i^{th} atoms in beams *1* and *2*, respectively. (For the sake of simplicity we are going to omit normalization constants throughout this paper.) Apparently, the two atoms are initially uncorrelated, while the state of the two fields exhibits m^{th} order correlation. This field-state can be produced experimentally, as discussed in Ref. [10] in detail. Using the same interaction parameter, $g\tau$, for both cavities satisfying the two equations, $sin\left(g\tau\sqrt{n}\right)=0$ and $cos\left(g\tau\sqrt{n+m}\right)=0$, simultaneously (or at least approximately) the final state after the first pair of atoms reads as

$$|n+m-1,n\rangle\cdot|a_1',b_1''\rangle \pm |n,n+m-1\rangle\cdot|b_1',a_1''\rangle \quad . \tag{2}$$

In the case of $m = 1$ the atoms and the fields disentangle into the EPR-state [11],

$$|a_i',b_i''\rangle \pm |b_i',a_i''\rangle \quad , \tag{3}$$

of the first ($i = 1$) pair of atoms and the number state, $|n,n\rangle$, of the fields. By periodically

reconstructing the $m = 1$ field-state from $|n,n\rangle$ [10], and sending subsequent pairs of lower-state atoms through the cavities two beams can be produced where the atoms are correlated in pairs as shown in Eq. (3) for the i^{th} pair. For higher initial field-correlations, $m > 1$, the atoms and the fields do not disentangle. The subsequent atom-pairs will also become correlated among themselves forming larger clusters of entangled atoms. Various kinds of entangled beams of EPR-pairs or of arbitrarily large clusters of atoms can be engineered by using the proper initial states and interaction parameters. The correlation between the atomic beams can be measured by detecting (anti-) coincidences of atomic states using field ionization detectors.

Several possible applications of these entangled atomic beams can be envisioned such as to study the effect of interatomic correlations on the radiation fields of lasers and micromasers driven by the two beams simultaneously, as depicted in Fig. 2. The singlet states of the atom-pairs (taking the minus sign in Eq. (3)), in particular, play an essential role in the recently suggested teleportation of quantum states [12]. The correlated beams could also be used in fundamental tests of quantum mechanics, as the photon-coincidence experiments [13], experiments challenging local realistic theories [14], and others where the entangled atoms would be employed to substitute for the entangled photons.

In this paper we propose another experimentally feasible application of these correlated atomic beams to test the complementarity principle of quantum mechanics. To this end we are going to use Ramsey's two-field method [15] that, when applying it to a single uncorrelated atomic beam, can be summarized as follows. Starting from a definite atomic state we apply two consecutive $\pi/2$-pulses on the atoms as Ramsey's first and second fields of $\Omega\tau = \pi/2$ in each pulse where Ω, Rabi frequency and τ, interaction time. Between the pulses the relative phase of the atomic levels is shifted by $e^{i\alpha}$ by, e. g., differential Stark shift using a static field. The probabilities of finding the atoms in definite final states display interference fringes. In the case of initial upper state, $|a\rangle$, they are given by

$$P_{\pm} = \frac{1}{2}(1 \pm \cos\alpha) \quad , \tag{4}$$

where + (-) corresponds to the lower (upper) atomic state. The interference is the consequence of the two possible atomic "paths" to reach the same final state, viz., after the first pulse the atom is in a coherent superposition of the two states. The relative phase of the superposition can be varied via $e^{i\alpha}$ in order to display the fringes.

Let us now apply Ramsey's apparatus on one of the two entangled atomic beams discussed above. As a result of the correlation between the atoms "Welcher Weg" information about one of the beams can, in principle, be extracted from its correlated pair and according to complementarity interference fringes are bound to disappear. This can be seen by starting from the symmetric version of the correlated state of Eq. (3) that, after the phase shift of $e^{i\alpha'}$ and the subsequent classical Ramsey-field, R', in beam *1* (Fig. 3), ends up in the final state given by

$$i|a'\rangle \cdot \left(S'|a''\rangle + ie^{i\alpha'}C'|b''\rangle\right) - |b'\rangle \cdot \left(C'|a''\rangle - ie^{i\alpha'}S'|b''\rangle\right) \quad . \tag{5}$$

(Here, the first of the two coupled micromasers serves as Ramsey's first field for beam *1*.) The coefficients, $S' \equiv \sin(\Omega'\tau'/2)$ and $C' \equiv \cos(\Omega'\tau'/2)$, are equal and factor out in the case of a $\pi/2$ - pulse (for $\Omega'\tau' = \pi/2$). The detection probabilities of the individual atomic states and those of the (anti-) coincidences are constants showing no oscillations as functions of α' at all. As a consequence of the strong atom-atom correlation in Eq. (3) the two spatially separated atoms serve as "Welcher Weg" detectors of one another. The atomic state in one beam keeps track of the evolution of that in the other resulting in no indistinguishable paths that could interfere. We want to emphasize that, as in the interferometer schemes of Refs. [8], it is the correlation between the "interference" atom and its "Welcher Weg" detector pair in the other beam that, via making information available, enforces complementarity. There is no added noise in the system of any kind that would lead us to Heisenberg's uncertainty relation.

The information stored in the "Welcher Weg" atoms can, however, be manipulated by applying a phase shift, $e^{i\alpha''}$, and a classical field, R'', on the detector atoms in beam *2* (see Fig. 3). The new state vector starting from Eq. (5) reads as

$$i\left(e^{i\alpha'}C'S'' + e^{i\alpha''}S'C''\right)|a',a''\rangle + i\left(e^{i\alpha'}S'C'' + e^{i\alpha''}C'S''\right)|b',b''\rangle -$$

$$-\left(e^{i\alpha'}C'C'' - e^{i\alpha''}S'S''\right)|a',b''\rangle + \left(e^{i\alpha'}S'S'' - e^{i\alpha''}C'C''\right)|b',a''\rangle \quad , \tag{6}$$

where the coefficients, S', C' and S'', C'' corresponding to R' and R'', respectively, are equal and factor out in the case of $\pi/2$ - pulses ($\Omega'\tau' = \Omega''\tau'' = \pi/2$). The detection probabilities of coincident and anticoincident atomic states in the two beams (first and second two terms in Eq. (6), respectively) can be calculated as

$$P_{\pm} = \frac{1}{4}\left[1 \pm \cos(\alpha' - \alpha'')\right] \quad , \tag{7}$$

where the (lower) upper sign corresponds to the (anti-) coincidences. Apparently, these probabilities show interference (anti-) fringes oscillating as functions of the difference phase, $\alpha' - \alpha''$, similarly to Eq. (4). At the same time the detection of any individual atomic state in any beam disregarding the atomic state in the other beam exhibits constant probabilities ($P_+ + P_- = 1/2$) that are the same as the initial ones in Eq. (5). Consequently, in order to display Ramsey-fringes in, for example, beam *1* one needs to detect the final atomic state on its counterpart in beam *2* thereby undoing the correlation between the atoms and, similarly to the "quantum eraser" in Ref. [8], erasing the stored "Welcher Weg" information. This way, the detections in beam *1* can be separated into two groups: one when the state coincides with the state in beam *2* and another when there is anticoincidence. The coincidence and anticoincidence detection probabilities both exhibit interference fringes which, however, cancel from their sum and add up to the constant detection probability of a given final state in beam *1*. The detections in beam *2* can take

place at any point following the field, R'', even long after the detection event of the atomic state in beam *1*, allowing for a delayed choice as we decide whether to emphasize wave-like (interference) or particle-like ("Welcher Weg") behavior. Together with other similar setups realizing the "quantum eraser" [8] these schemes provide experimentally feasible tests of quantum complementarity.

The interferometer exhibits new features when quantum Ramsey-fields, such as number states, are applied in the apparatus as, for example, in the scheme of Fig. 2. Including the phase shifts, $e^{i\alpha'}$ and $e^{i\alpha''}$, in beams *1* and *2*, respectively, the final state of the system after starting from the symmetric version of the atomic state of Eq. (3) and the photon number state, $|n\rangle$, is given by

$$i\left(e^{i\alpha'}C'_{n+1}S''_n+e^{i\alpha''}S'_nC''_n\right)|a',a'',n-1\rangle+i\left(e^{i\alpha'}S'_{n+1}C''_{n+1}+e^{i\alpha''}C'_nS''_{n+1}\right)|b',b'',n+1\rangle-$$

$$-\left(e^{i\alpha'}C'_{n+1}C''_n-e^{i\alpha''}S'_nS''_n\right)|a',b'',n\rangle+\left(e^{i\alpha'}S'_{n+1}S''_{n+1}-e^{i\alpha''}C'_nC''_{n+1}\right)|b',a'',n\rangle \quad , \qquad (8)$$

provided the atom in beam *1* traversed the cavity first. Here, $C'_n \equiv cos\left(g'\tau'\sqrt{n}\right)$ and $S'_n \equiv sin\left(g'\tau'\sqrt{n}\right)$ correspond to the first while the double-primed ones to the second atom. The differences between this result and its classical counterpart, Eq. (6), lie in the build-up of atoms-field correlations and in the photon number dependence of the coefficients. As a result of the atom-field correlations the cavity field plays a significant role in the present version of the quantum eraser. Considering, for example, beam *1* Ramsey-fringes can be restored from the constant detection probabilities of the individual atomic states by detecting the state of either the beam *2* atoms, as before, or the cavity field. This is similar to the quantum eraser schemes for classical fields with the additional degree of freedom of the quantum field. Another implication of the atom-field correlations is the interference in the photon detection probabilities, where the interfering paths originate from the two-atom interaction of the field. In the case of classical fields the photon numbers cannot be resolved and the probabilities add up to one. On the other hand, the photon number dependence of the coefficients of the atomic paths allows for a continuous adjustment

between two extreme regimes of the system regarding the detection probabilities in beam 2. One, similarly to beam 1, is the quantum eraser when the condition, $|S_n| = |S_{n+1}| \neq 0$, is satisfied (at least approximately) in both beams. The other, however, is given by setting either S_n or S_{n+1} equal to zero. In this regime the probabilities of the individual atomic states in beam 2 are no longer constants as they were in the case of the quantum eraser but exhibit interference fringes themselves. The contrast of these fringes can be enhanced by detecting the quantum state of either beam 1 or in the cavity field. It can also be reduced or left intact as a new quantum feature of the system. Varying the initial photon number, n, in the cavity and/or the interaction parameter, $g\tau$, in the two beams we can adjust the system as we decide whether to emphasize the quantum nature of the field or not. It follows, that this scheme can not only be used to test complementarity but also the quantum nature of the radiation field.

For a possible experiment we consider the case where the cavity field is initially in the vacuum state, $|0\rangle$. The final state of the system can be read out from Eq. (8) for $n = 0$ resulting in zero probability for the first term, constant, $P_{a',b'',0} = C_1^2/2$, for the third, and interferences in the second, $P_{b',b'',1} = \left(S_1^2/2\right)\left[1 + C_1^2 + 2C_1\cos(\alpha' - \alpha'')\right]$, and fourth, $P_{b',a'',0} = 1/2 - \left(S_1^2/2\right)\left[C_1^2 + 2C_1\cos(\alpha' - \alpha'')\right]$. For simplicity we assumed equal velocities in the two beams. These imply that the probabilities of the individual atomic states in beam 1, $P_{a'} = P_{a',b'',0}$ and $P_{b'} = P_{b',a'',0} + P_{b',b'',1}$, are constants, but those of beam 2, $P_{a''} = P_{b',a'',0}$ and $P_{b''} = P_{a',b'',0} + P_{b',b'',1}$, do exhibit interferences. The quantum eraser can be realized in beam 1 using either the other beam or the cavity field to erase information. In this regime, however, this can be done only for the lower state of the atoms, $|b'\rangle$, because due to $S_0 = 0$ the interferometer does not allow for indistinguishable paths for the upper state. On the other hand, a new quantum feature appears in beam 2. The upper state, $|a''\rangle$, exhibits interference fringes that cannot be modified by any subsequent detection on the first atom since, once $|a''\rangle$ is detected, the first atom is in state $|b'\rangle$ with probability 1 and no new information is gained. Furthermore, in the case of the lower state, $|b''\rangle$, the contrast of the preexisting fringes in $P_{b''}$ can be either destroyed or enhanced depending upon whether the atom in beam 1 is detected in its upper or lower

state (*0* resp. *1* photon in the field). This is à manifestation of the quantum nature of the field, markedly absent from the "classical" quantum eraser.

In conclusion, we have proposed experimentally feasible tests of complementarity based upon spatially separated (EPR-) correlated atomic beams. Ramsey interference fringes are detected (or not) in one of the beams, while "Welcher Weg" information (or not) in its correlated pair. There is no added noise in the system that would lead to Heisenberg's uncertainty relation, complementarity is enforced by the correlation between the "interference" atom and its "Welcher Weg" detector pair. The available information and the contrast of the interference fringes can be manipulated using classical and quantum Ramsey fields. The "quantum eraser" can be realized in the former case while it is only a special feature of a more general behavior in the latter one. We end by noting that further applications of entangled atoms can easily be envisioned. For example, quantum optical experiments that, thus far, have been realized with entangled photons only can be redone with entangled atoms. Teleportation of quantum states, EPR-experiments, or the study of collective atomic effects on the radiation field are a few of the many possibilities.

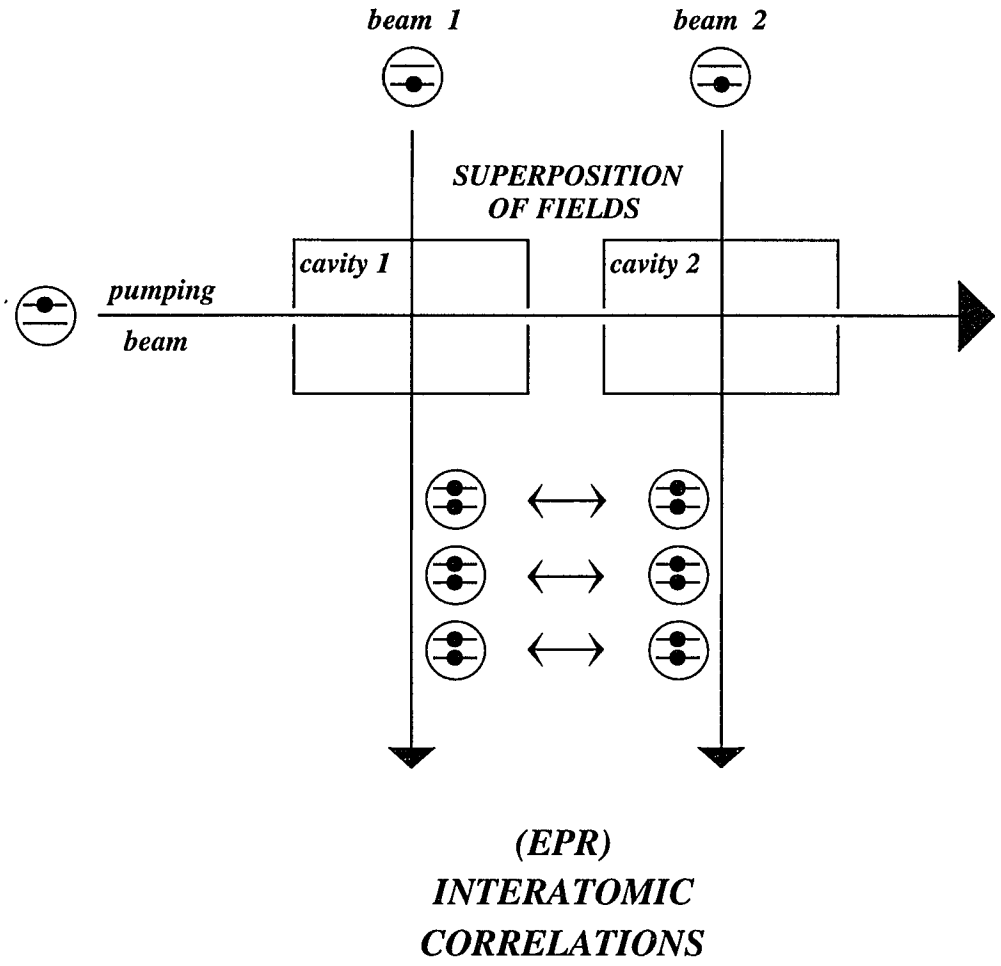

FIG. 1: Schematic arrangement of the production of two (EPR-) entangled atomic beams of macroscopical separation using entangled nonlocal fields of two pump-coupled micromasers.

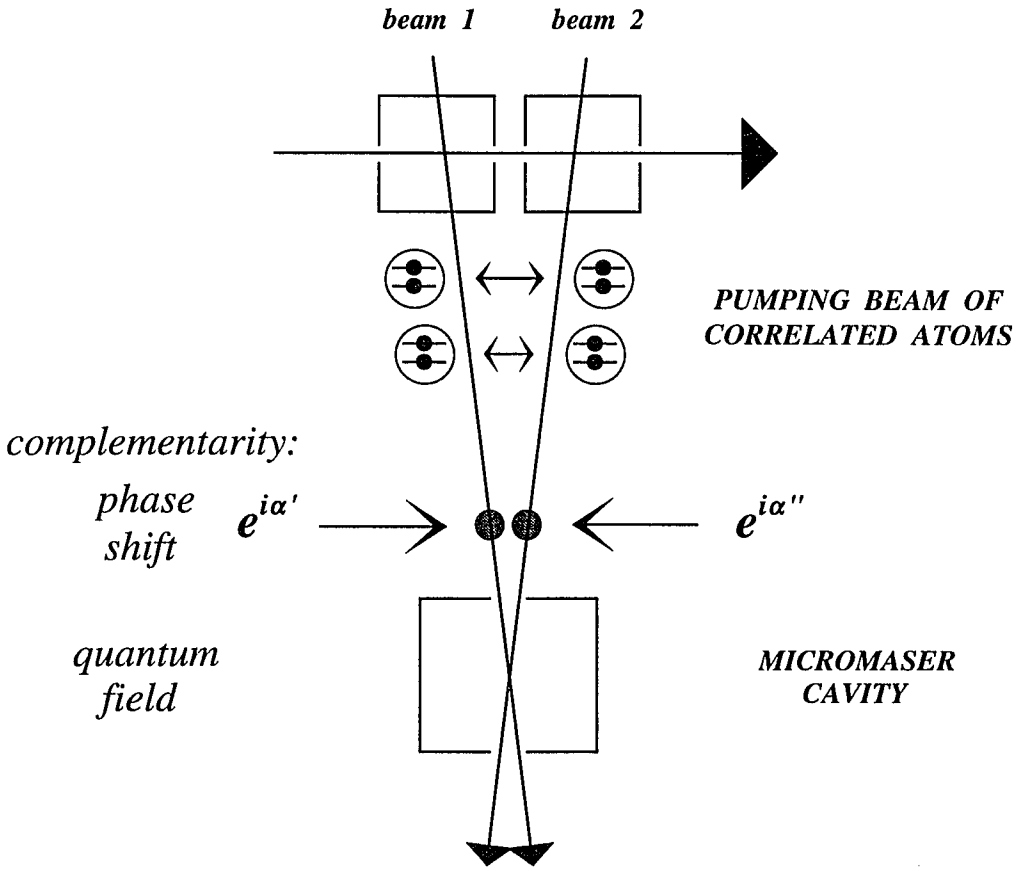

FIG. 2: Schematic arrangement of two entangled atomic beams driving a single micromaser to study the effect of interatomic correlations on its radiation field. Applying phase shifts, $e^{i\alpha'}$ and $e^{i\alpha''}$, on beams *1* and 2, respectively, and a quantum field (e.g. number state) in the cavity this scheme can also be used to generate Ramsey-fringes to test complementarity.

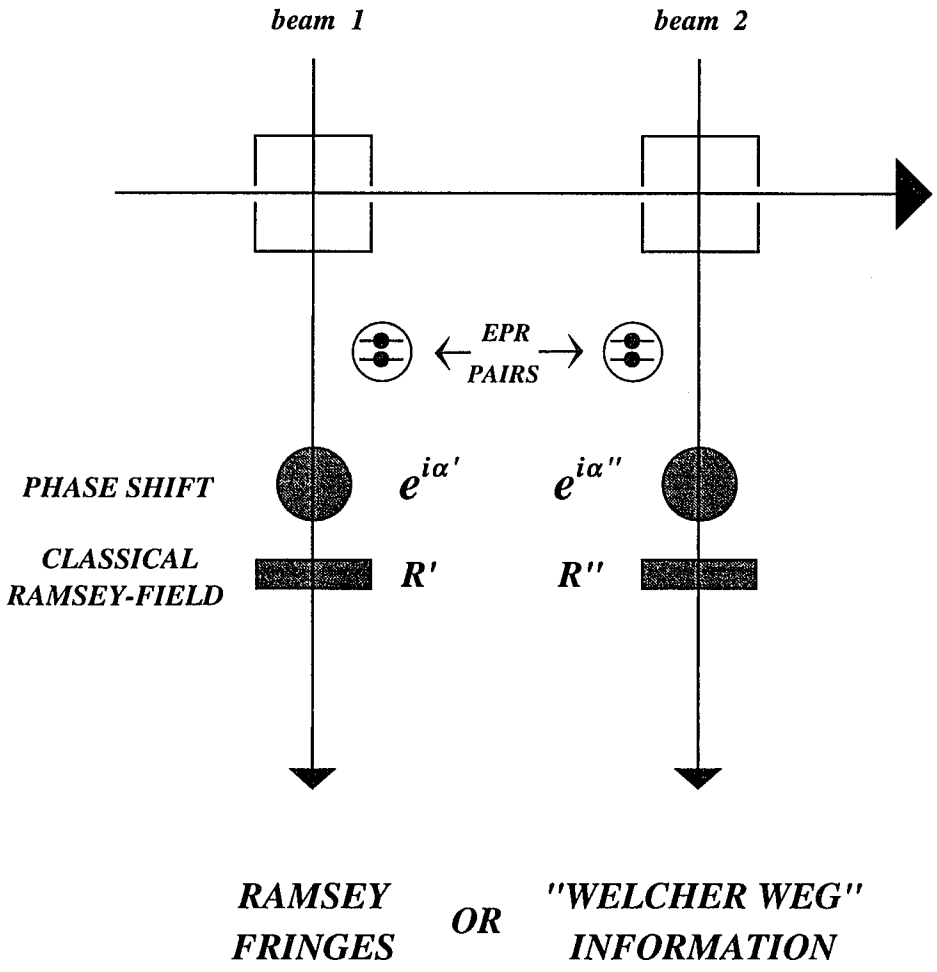

FIG. 3: Schematic arrangement of two entangled atomic beams to test complementarity by detecting Ramsey-fringes (interference) in one and atomic state ("Welcher Weg") in the other beam. First we apply a Ramsey-apparatus including a phase shift, $e^{i\alpha'}$, and a classical field, R', in beam *1* alone, and then together with the second one of $e^{i\alpha''}$ and R'' in beam 2.

4. SUMMARY

Quantum coherence effects in two basic quantum optical systems, lasers and micromasers, were studied theoretically. They arise due to the coherence of the pumping atoms prepared by some external means. In the case of the micromaser, in particular, a preliminary micromaser was applied for this purpose resulting in a system of two pump-coupled micromasers.

First, we investigated the dynamical and noise characteristics of the laser operation when coherences between the various levels of the driving three-level atoms are introduced. In the case when the lower two closely spaced levels (Λ-configuration) are coupled by an external field (quantum-beat laser) we can achieve lasing without inversion between the upper and lower levels. Clearly, this is a result of the coherence induced by the external coupling. At the same time, injecting additional atomic coherences the threshold of the laser can be pushed down to zero pumping and the quantum-noise of the laser field can be reduced significantly to the level of that of the coherent state. The dynamics of this configuration becomes more complicated when two-mode laser operation is considered: various regimes of bistable and tristable operations are found depending on the control parameters of the system.

In the second line of research, we considered two micromasers coupled in series by sharing a common pumping atomic beam. Thus, besides studying the characteristics of the second field we can also consider the complete two-field system in this case and investigate the quantum correlation arising between the two spatially separated fields as atomic coherence is transferred from the first to the second cavity. This is reminiscent of Young's double-slit experiment for having two indistinguishable atomic paths to reach the same final state.

Quantum engineering of entangled states of the two nonlocal micromaser fields was investigated in the two cases when the final states of the atoms are measured conditionally or nonselectively. Various conditional measurement schemes were considered illustrating

the effect of the measurement on the pure evolution of the system. The effect of dissipation was also studied in the case of the nonselective measurement scheme. We found that arbitrary steady state entanglement of the two nonlocal fields can be produced in the form of entangled trapping states. These are experimentally feasible in the short-time transient regime when dissipation does not exceed a certain threshold. It was also shown that correlation between the fields is still a robust effect even when significant losses are present and manifests itself in both the time-dependent and steady-state behavior. In order to see this we compared the two cases of incoherent and coherent coupling, i. e., when the atoms are measured between the cavities or not. Using numerical simulations and analytical techniques we found significant modifications in the average photon number and the photon number noise as a result of the transferred atomic coherence, together with the build-up of correlations and phase locking between the fields.

We also showed that the correlation between the nonlocal fields can be translated into a correlation between spatially separated atomic beams. These entangled atoms can have several applications. Reproducing experiments with correlated photons, studying the effect of interatomic correlations in lasers and micromasers, teleportation, or tests of the local realistic theories are just a few among the many possibilities. However, we specifically discussed here another experimentally feasible application in tests of complementarity using Ramsey's atomic interferometry. It was found that the correlation between the atoms provides us with "Welcher Weg" information resulting in a destruction of the interference fringes without leading to Heisenberg's uncertainty principle. Manipulation of information results in a generalized version of the quantum eraser.

APPENDIX

LIST OF PUBLICATIONS

I. Papers published:

1. Quantum Theory of a Noninversion Laser with Injected Atomic Coherence,
   J. A. Bergou and P. Bogár, Phys.Rev. A **43** (9), 4889-4900 (1 May, 1991).

2. Quantum Island States in the Micromaser,
   P. Bogár, J. A. Bergou, and M. Hillery, Phys. Rev. A **50** (1), 754-762 (1 July, 1994).

3. Pump-Coupled Micromasers: Entangled Trapping States of Nonlocal Fields,
   P. Bogár and J. A. Bergou, Phys. Rev. A **51** (3), 2381-2396 (1 March, 1995).

4. Pump-Coupled High-Q Micromasers with Conditional Measurements of Atoms: Transient and Steady State Entanglement of Nonlocal Fields,
   P. Bogár, J. A. Bergou, and M. Hillery, Phys. Rev. A **51** (3), 2396-2410 (1 March, 1995).

II. Papers submitted:

5. Entanglement of Atomic Beams: Tests of Complementarity and Other Applications,
   P. Bogár and J. A. Bergou, submitted to Phys. Rev. A in November, 1994.

6. Pump-Coupled Micromasers: Coherent and Incoherent Coupling,
   P. Bogár, J. A. Bergou, and M. Hillery, submitted to Phys. Rev. A in July, 1995.

7. Phase Structures in the Micromaser Photon Statistics,
   P. Bogár and J. A. Bergou, submitted to Quantum and Semiclass. Opt. in July, 1995.

8. Two-Mode Lasing Without Inversion with Injected Atomic Coherence,
   P. Bogár, J. A. Bergou, and M. Hillery, submitted to Phys. Rev. A in July, 1995.

III. Invited talks:

1. Quantum State Engineering in Pump-Coupled Micromasers,
   P. Bogár and J. A. Bergou, invited talk at "Fundamental Problems in Quantum Theory" (Baltimore, Maryland, U.S.A., June 18-22, 1994). Published in *Annals of the New York Academy Sciences* **755**, 110-120 (April 22, 1995), ed. by D. Greenberger and A. Zeilinger.

2. Atomic Coherence in Lasers and Masers,
   J. A. Bergou, P. Bogár, invited talk at "International Workshop on Quantum Optics", (Nathiagali, Pakistan, July 9-14, 1994). Published in *Quantum and Semiclass. Opt.* **7** (3), 343-355 (June 1995), ed. by W. P. Schleich, M. O. Scully, and M. S. Zubairy.

3. Micromaser with Atomic Coherence,
   P. Bogár and J. A. Bergou, invited talk at "ONR/Harc Workshop on Quantum Interference Effects in Fundamental and Applied Physics" (Crested Butte, Colorado, U.S.A., August 7-11, 1994). To be published in the *Proceedings*.

4. Pump-Coupled Micromasers,
   M. Hillery, P. Bogár and J. A. Bergou, invited talk at "Lasers '94" (Quebec,

Canada, December 12-16, 1994). Unpublished.

5. Entangled Atomic Beams: a Tool to Test Complementarity,
   J. A. Bergou and P. Bogár, invited talk at "24th Winter Colloqium on Quantum Electronics" (Snowbird, Utah, U.S.A., January 4-7, 1995). Unpublished.

6. Entangled Fields and Entangled Atoms: Tools to Test Fundamentals of Quantum Mechanics,
   J. A. Bergou and P. Bogár, invited talk at "Third Central European Workshop on Quantum Optics" (Budmerice Castle, Slovakia, April 28 - May 1, 1995). Published in *Acta Physica Slovaca* **45** (3), 217-230 (June, 1995), ed. by V. Buzek.

IV. Contributed talks:

1. Nonlinear Refractive Index Change of Saturable Dyes Used for Passive Mode Locking of Solid State Lasers During the Pulse Formation Process,
   P. Bogár, Gy. Farkas and Cs. Tóth, contributed talk at "OPTIKA '88, Third International Symposium on Modern Optics" (Budapest, Hungary, September 13-17, 1988). Published in *OPTIKA '88*, pp. 156-162, ed.: G. Lupkovics, A. Podmaniczky (OPAKFI, Budapest, 1988).

2. Nonlinear Theory of Pump-Coupled Micromasers,
   P. Bogár, J. A. Bergou, and M. Hillery, contributed talk at "OSA Annual Meeting '92" (Albuquerque, New Mexico, U.S.A., September 20-25, 1992). Published in *OSA Annual Meeting Technical Digest, 1992*, **23**, pp. 214-215 FNN5 (Optical Society of America, Washington, D.C., 1992).

3. Two-Mode Lasing Without Inversion,
   P. Bogár, J. A. Bergou and M. Hillery, contributed talk at "OSA Annual Meeting

'93" (Toronto, Canada, October 3-8, 1993). Published in *OSA Annual Meeting Technical Digest, 1993*, **16**, pp. 179 ThQ4 (Optical Society of America, Washington, D.C., 1993).

4. The Effect of Pseudo Trapping States on the Micromaser Dynamics,
   P. Bogár, J. A. Bergou and M. Hillery, contributed talk at "OSA Annual Meeting '93" (Toronto, Canada, October 3-8, 1993). Published in *OSA Annual Meeting Technical Digest, 1993*, **16**, pp. 257 FAA1 (Optical Society of America, Washington, D.C., 1993).

5. Quantum Island States in the Micromaser,
   P. Bogár, J. A. Bergou and M. Hillery, contributed talk at "Winter School on Quantum Optics" (Trieste, Italy, February 14 - March 4, 1994). Unpublished.

V. Posters:

1. Pump-Coupled Micromasers,
   P. Bogár, J. A. Bergou, and M. Hillery, poster presentation at "Fundamental Problems in Quantum Theory" (Baltimore, Maryland, U.S.A., June 18-22, 1994). Published in *Annals of the New York Academy Sciences* **755**, 842-844 (April 22, 1995), ed. by D. Greenberger and A. Zeilinger.

2. Pump-Coupled Micromasers,
   P. Bogár, J. A. Bergou and M. Hillery, poster presentation at "First Annual Science Convocation of GSUC/CUNY" (New York, New York, U.S.A., November 30, 1994). Unpublished.

3. Pump-Coupled Micromasers,

P. Bogár, J. A. Bergou and M. Hillery, contributed paper at "CQO7, Seventh Rochester Conference on Coherence and Quantum Optics" (Rochester, New York, U.S.A, June 7-10, 1995). To be published in *Coherence and Quantum Optics VII*, ed. by J. Eberly, L. Mandel, and E. Wolf

VI. Papers in preparation:

1. Entanglement of Atomic Beams and Their Applications,
   P. Bogár and J. A. Bergou, contributed talk to be given at "OSA Annual Meeting '95" (Portland, Oregon, U.S.A., September 10-15, 1995). To be published in *OSA Annual Meeting Technical Digest, 1995*, **xx**, pp.xxx-xxx (Optical Society of America, Washington, D.C., 1995).

2. A Dressed State Picture of Lasing Without Inversion and Related Phenomena,
   J. A. Bergou and P. Bogár, in preparation.

3. The Effects of Interatomic Correlations on the Micromaser,
   P. Bogár and J. A. Bergou, in preparation.

4. Two-mode Lasing Without Inversion: Correlations and Noise,
   P. Bogár and J. A. Bergou, in preparation.

BIBLIOGRAPHY

Chapter 1

[1] R. Feynman, R. Leighton and M. Sands, *The Feynman Lectures on Physics* Vol. III (Addison Wesley, Reading, 1965).

[2] A. Einstein, B. Podolsky, and N. Rosen, Phys. Rev. **47**, 777 (1935).

Chapter 2.1.1

† Reprinted (abstracted) with permission from J. A. Bergou and P. Bogár, Physical Review A **43**, (9) 4889-4900 (1 May, 1991). Copyright 1991 The American Physical Society.

[1] M. Sargent III, M. O. Scully, and W. E. Lamb, Jr., *Laser Physics* (Addison-Wesley, Reading, MA, 1974).

[2] H. Haken, in *Handbuch der Physik* (Springer-Verlag, New York, 1970), Vol. 25.

[3] W. H. Louisell, *Quantum Statistical Properties of Radiation* (Wiley, New York, 1973).

[4] O. Kocharovskaya and Ya. I. Khanin, Pis'ma Zh. Eksp. Teor. Fiz. **48**, 630 (1988).

[5] V. G. Arkhipkin and Yu. Heller, Phys. Lett. **98A**, 12 (1989).

[6] (a) S. E. Harris, Phys. Rev. Lett. **62**, 1033 (1989); (b) S. E. Harris and J. J. Macklin, Phys. Rev. A **40**, 4135 (1989).

[7] A. Lyras, X. Tang, P. Lambropoulos, and Jian Zhang, Phys. Rev. A **40**, 4131 (1989).

[8] (a) A. Imamoglu, Phys. Rev. A **40**, 2835 (1989); V. R. Blok and G. M. Krochik, *ibid.* **41**, 1517 (1990); G. S. Agarwal, S. Ravi, and J. Cooper, *ibid.* **41**, 4721 (1990); G. S. Agarwal, S. Ravi, and J. Cooper, *ibid.* **41**, 4727 (1990); O. A. Kocharovskaya, R.-D. Li, and P. Mandel, Opt. Commun. **77**, 215 (1990); (b) G. S. Agarwal, Phys. Rev. A **42**, 686 (1990).

[9] M. O. Scully, S.-Y. Zhu, and A. Gavrielides, Phys. Rev. Lett. **62**, 2813 (1989).

[10] R. C. Elton, Opt. Eng. **21**, 307 (1982); H. Holt, Phys. Rev. A **16**, 1136(1976).

[11] N. Lu, Opt. Commun. **73**, 479 (1989); N. Lu, Phys. Lett. A **143**, 457 (1990); N. Lu and C. Benkert, Opt. Commun. **72**, 319 (1990); J. Bergou and P. Bogár (unpublished).

[12] E. E. Fill, M. O. Scully, and S.-Y. Zhu, Opt. Commun. **77**, 36 (1990).

[13] D. F. Walls and P. Zoller, Opt. Commun. **34**, 260 (1980); B. J. Dalton and P. L. Knight, J. Phys. B **15**, 3997 (1982).

[14] E. Arimondo and G. Orriols, Lett. Nuovo Cimento **17**, 333 (1976); G. Orriols, Nuovo Cimento **53B**, 1 (1979).

[15] R. G. Brewer and E. L. Hahn, Phys. Rev. A **11**, 1641 (1975).

[16] G. Alzetta, A. Gozzini, L. Moi, and G. Orriols, Nuovo Cimento **36B**, 5 (1976); H. R. Gray, R. M. Whitley, and C. R. Stroud, Opt. Lett. **3**, 218 (1978); G. Alzetta, L. Moi, and G. Orriols, Nuovo Cimento **52B**, 209 (1979).

[17] M. O. Scully, Phys. Rev. Lett. **55**, 2802 (1985); M. O. Scully and M. S. Zubairy, Phys. Rev. A **35**, 752 (1987); K. Zaheer and M. S. Zubairy, *ibid.* **38**, 227 (1988); J. Bergou, M. Orszag, and M. O. Scully, *ibid.* **38**, 754 (1988).

[18] M. O. Scully, K. Wódkiewicz, M. S. Zubairy, J. Bergou, N. Lu, and J. Meyer ter Vehn, Phys. Rev. Lett. **60**, 1832 (1988).

[19] N. Lu and J. Bergou, Phys. Rev. A **40**, 237 (1989).

[20] U. Fano, Phys. Rev. **124**, 1866 (1961); U. Fano and J. W. Cooper, Rev. Mod. Phys. **40**, 441 (1968).

[21] J Bergou, M. Orszag, M. O. Scully, and K. Wódkiewicz, Phys. Rev. A **39**, 5136 (1989).

Chapter 2.1.2

† Submitted for publication to Physical Review A by P. Bogár and J. A. Bergou.

[1] M. O. Scully, S.-Y. Zhu. and A. Gavrielides, Phys. Rev. Lett. **62**, 2813 (1989); see also about the Λ - system in general, O. Kocharovskaya and Ya. I. Khanin, Pis'ma Zh.

Eksp. teor. Fiz. **48**, 581 (1988) [JETP Lett. **48**, 630 (1988)]; O. Kocharovskaya and P. Mandel, Phys. Rev. A **42**, 523 (1990); E. E. Fill, M. O. Scully, and S.-Y. Zhu, Opt. Commun. **77**, 36 (1990).

[2] S. E. Harris, Phys. Rev. Lett. **62**, 1033 (1989); S. E. Harris and J. J. Macklin, Phys. Rev. A **40**, 4135 (1989); A. Imamoglu and S. E. Harris, Opt. Lett. **14**, 1344 (1989); A. Imamoglu, Phys. Rev. A **40**, 2835 (1989); A. Imamoglu, J. E. Field, S. E. Harris, Phys. Rev. Lett. **66**, 1154 (1991); P. Mandel and O. Kocharovskaya, Phys. Rev. A **46**, 2700 (1992).

[3] L. M. Narducci, H. M. Doss, P. Ru, M. O. Scully, S.-Y. Zhu, and C. Keitel, Opt. Commun. **81**, 379 (1991); M. O. Scully, S.-Y. Zhu, L. M. Narducci, and H. Fearn, Opt. Commun. **81**, 240 (1992); S. Basile and P. Lambropoulos, Opt. Commun. **78**, 163 (1990); P. Mandel and O. Kocharovskaya, Phys. Rev. A **47**, 5003 (1993). For a review see, O. Kocharovskaya, Phys. Rep. **219**, 175 (1992); M. O. Scully, Phys. Rep. **219**, 191 (1991); P. Mandel, Conremp. Phys. **34**, 235 (1994), and references therein

[4] G. Alzetta, A. Gozzini, L. Moi, and G. Orriols, Nuovo Cimento **36B**, 5 (1976); G. Alzetta, L. Moi, and G. Orriols, Nuovo Cimento **52B**, 209 (1979).

[5] J. A. Bergou and P. Bogár, Phys. Rev. A. **43**, 4889 (1991); this is the single-mode version of the system discussed in the present paper.

[6] G. S. Agarwal, Phys. Rev. Lett. **67**, 980 (1991); K. Gheri and D. F. Walls, Phys. Rev. Lett. **68**, 3428 (1992); Phys. Rev. A **45**, 6675 (1992); Y. Zhu, Phys. Rev. A **47**, 495 (1993); Y. Zhu, O. C. Mullins, and M. Xiao, Phys. Rev. A **47**, 602 (1993).

[7] M. O. Scully, Phys. Rev. Lett. **55**, 2802 (1985); M. O. Scully, K. Wódkiewicz, M. S. Zubairy, J. Bergou, N. Lu, and J. Meyer ter Vehn, *ibid.* **60**, 1832 (1988); N. Lu and J. Bergou, Phys. Rev. A **40**, 237 (1989); J. Bergou, J. Zhang, and A. Hourri, Phys. Rev. A **50**, 4188 (1994).

[8] M. O. Scully, Phys. Rev. Lett. **67**, 1855 (1991); M. O. Scully and S.-Y. Zhu, Opt. Commun. **87**, 134 (1992); M. Fleischhauer, C. H. Keitel, M. O. Scully, C. Su, B. T. Ulrich, and S.-Y. Zhu, Phys. Rev. A **46**, 1468 (1992); A. D. Wilson-Gordon and H.

Friedmann, Opt. Commun. **94**, 238 (1992); U. Rathe, M. Fleischhauer, S.-Y. Zhu, T. W. Hänsch, and M. O. Scully, Phys. Rev. A **47**, 4994 (1992); M. O. Scully, Phys. Rev. Lett. **69**, 1360 (1992)

[9] K.-J. Boller, A. Imamoglu, and S. E. Harris, Phys. Rev. Lett. **66**, 2593 (1991); J. E. Field, K. H. Hahn, and S. E. Harris, Phys. Rev. Lett. **67**, 3062 (1991); S. E. Harris, J. E. Field, and A. Kassapi, Phys. Rev. A **46**, R29 (1992); S. E. Harris, Phys. Rev. Lett. **70**, 552 (1993); S. E. Harris, Phys. Rev. Lett. **72**, 52 (1994); J. H. Eberly, M. L. Pons, and H. R. Hag, Phys. Rev. Lett. **72**, 56 (1994); A. Kasapi, Maneesh Jain, G. Y. Yin, and S. E. Harris, Phys. Rev. Lett. **74**, 2447 (1995).

[10] O. Kocharovskaya, P. Mandel, and M. O. Scully, Phys. Rev. Lett. **74**, 2451 (1995).

[11] P. Bogár and J. A. Bergou in preparation.

Chapter 3.1.1

† Submitted for publication to Quantum and Semiclass. Opt. by P. Bogár and J. A. Bergou.

[1] For a recent review, see H. Walther, Phys. Rep. **219**, 201 (1992); also H. Walther, Phys. Scr. **T23**, 165 (1988); F. Diedrich, J. Krause, G. Rempe, M. O. Scully, and H. Walther, IEEE J. Quantum Electron. **QE-24**, 1314 (1988).

[2] E. T. Jaynes and F. W. Cummings, Proc IEEE **51**, 89 (1963).

[3] The quantum theory of the micromaser is given by P. Filipowicz, J. Javanainen, and P. Meystre, Phys. Rev. A **34**, 3077 (1986); L. A. Lugiato, M. O. Scully, and H. Walther, Phys. Rev. A **36**, 740 (1987).

[4] For the semiclassical theory see A. M. Guzman, P. Meystre, and E. W. Wright, Phys. Rev. A **40**, 2471 (1989).

[5] H Paul, Ann. Phys. (Leipzig), **11**, 411 (1963); J. H. Eberly, N. B. Narozhny, and J. J. Sanchez-Mondragon, Phys. Rev. Lett. **23**, 44 (1980); The experimental proof of the quantum collapse and revival predicted by the Jaynes-Cummings model

was reported by G. Rempe, H. Walther, and N. Klein, Phys. Rev. Lett. **58**, 353 (1987).

[6] J. Krause, M. O. Scully, and H. Walther, Phys. Rev. A **36**, 4547 (1987); P. Meystre, Opt. Lett. **12**, 668 (1987); in *Squeezed and Nonclassical Light*, edited by P. Tombesi and E. R. Pike (Plenum, New York, 1988); H. Paul, J. Mod. Opt. **36**, 515 (1989); F. W. Cummings, A. K. Rajagopal, Phys. Rev. A **39**, 3414 (1989).

[7] P. Meystre, G. Rempe, and H. Walther, Opt. Lett. **13**, 1078 (1988).

[8] P. Bogár, J. A. Bergou and M. Hillery, Phys. Rev. A, **50**, 754 (1994).

[9] P. Filipowicz, J. Javanainen, and P. Meystre, J. Opt. Soc. Am. B **3**, 906 (1986); J. J. Slosser, P. Meystre, and S. L. Braunstein, Phys. Rev. Lett. **63**, 934 (1989); J. J. Slosser and P. Meystre, Phys. Rev. A **41**, 3867 (1990); J. J. Slosser, P. Meystre, and E. M. Wright, Opt. Lett. **15**, 233 (1990); P. Meystre, J. Slosser, and M. Wilkens, Phys. Rev. A **43**, 4959 (1991).

[10] L. Davidovich, A. Maali, M. Brune, J. M. Raimond, and S. Haroche, Phys. Rev. Lett. **71**, 2360 (1993); J. A. Bergou and M. Hillery, Phys. Rev. A **44**, 7502, (1991); P. Bogár, J. A. Bergou and M. Hillery, Phys. Rev. A, February, (1995); P. Bogár and J. A. Bergou, accepted for publication in Phys. Rev. A; P. Bogár, J. A. Bergou and M. Hillery, to be published in Phys. Rev. A.

[11] M. O. Scully and H. Walther, Phys. Rev. A **39**, 5229, (1989); M. O. Scully, B.-G. Englert and H. Walther, Nature, **351**, 111 (1991); B.-G. Englert, H. Walther, and M. O. Scully, Appl. Phys. B **54**, 366 (1992); P. Bogár, J. A. Bergou, Phys. Rev. A (to be published).

Chapter 3.1.2

† Reprinted (abstracted) with permission from P. Bogár, J. A. Bergou and M. Hillery, Physical Review A **50**, (1) 754-762 (1 July, 1994). Copyright 1994 The American Physical Society.

[1] The first masing in a single atom micromaser was reported by D. Meschede, H. Walther, and G. Müller, Phys. Rev. Lett. **54**, 551 (1985).

[2] Superradiance in a micromaser cavity was first reported by J. M. Raimond, P. Goi, M. Gross, C. Fabre, and S. Haroche, Phys. Rev. Lett. **49**, 1924 (1982).

[3] The experimental proof of the quantum collapse and revival predicted by the Jaynes-Cummings model (see [23-30] below) was reported by G. Rempe, H. Walther, and N. Klein, Phys. Rev. Lett. **58**, 353 (1987).

[4] On two-photon micromaser, see M. Brune, J. M. Raimond, P. Goy, L. Davidovich, and S. Haroche, Phys. Rev. Lett. **59**, 1899 (1987); and L. Davidovich, J. M. Raimond, M. Brune, and S. Haroche, Phys. Rev. A. **36**, 3771 (1987).

[5] For a review, see H. Walther, Phys. Scr. **T23**, 165 (1988); F. Diedrich, J. Krause, G. Rempe, M. O. Scully, and H. Walther, IEEE J. Quant. El. **QE-24**, 1314 (1988).

[6] More recent results are reported by G. Rempe, F. Schmidt-Kaler, and H. Walther, Phys. Rev. Lett. **64**, 2783 (1990).

[7] See recent review on very high finesse cavities in the optical domain by S. E. Morino, Q. Wu, and T. W. Mossberg, Opt. Photon. News **3**, 8 (1992), and references therein. See also G. Rempe, R. J. Thompson, R. J. Brecha, W. D. Lee, and H. J. Kimble, Phys. Rev. Lett. **67**, 1727 (1991).

[8] For the quantum theory of the micromaser, see P. Filipowicz, J. Javanainen, and P. Meystre, Phys. Rev. A **34**, 3077 (1986); the semiclassical theory is given by A. M. Guzman, P. Meystre, and E. W. Wright, Phys. Rev. A **40**, 2471 (1989).

[9] P. Filipowicz, J. Javanainen, and P. Meystre, Phys. Rev. A **34**, 4547 (1986).

[10] G. Rempe and H. Walther, Phys. Rev. A **42**, 1650 (1990).

[11] L. Lugiato, M. O. Scully, and H. Walther, Phys. Rev. A **36**, 740 (1987).

[12] M. Brune, J. M. Raimond, and S. Haroche, Phys. Rev. A **35**, 154 (1987).

[13] L. Davidovich, J. M. Raimond, M. Brune, and S. Haroche, Phys. Rev. A **36**, 3771 (1987).

[14] L. A. Lugiato, M. O. Scully, and H. Walther, Phys. Rev. A **36**, 740 (1987).

[15] J. Krause, M. O. Scully, and H. Walther, Phys. Rev. A **36**, 4547 (1987).

[16] P. Filipowicz, J. Javanainen, and P. Meystre, J. Opt. Soc. Am. B **3**, 906 (1986).

[17] J. J. Slosser, P. Meystre, and S. L. Braunstein, Phys. Rev. Lett. **63**, 934 (1989).

[18] P. Meystre, G. Rempe, and H. Walther, Opt. Lett. **13**, 1078 (1988).

[19] J. J. Slosser and P. Meystre, Phys. Rev. A **41**, 3867 (1990).

[20] J. J. Slosser, P. Meystre, and E. M. Wright, Opt. Lett. **15**, 233 (1990).

[21] P. Meystre, J. Slosser, and M. Wilkens, Phys. Rev. A **43**, 4959 (1991).

[22] M. O. Scully and H. Walther, Phys. Rev. A **39**, 5229 (1989).

[23] Same result from a different derivation can be found in P. Meystre and M. Sargent III, *Elements of Quantum Optics* (Springer-Verlag, Berlin, 1990).

Chapter 3.2.1

† Submitted for publication to Physical Review A by P. Bogár, J. A. Bergou, and M. Hillery.

[1] For a recent review, see H. Walther, Phys. Rep. **219**, 201 (1992); also H. Walther, Phys. Scr. **T23**, 165 (1988); F. Diedrich, J. Krause, G. Rempe, M. O. Scully, and H. Walther, IEEE J. Quantum Electron. **QE-24**, 1314 (1988).

[2] E. T. Jaynes and F. W. Cummings, Proc IEEE **51**, 89 (1963).

[3] J. H. Eberly, N. B. Narozhny, and J. J. Sanchez-Mondragon, Phys. Rev. Lett. **23**, 44 (1980); The experimental proof of the quantum collapse and revival predicted by the Jaynes-Cummings model was reported by G. Rempe, H. Walther, and N. Klein, Phys. Rev. Lett. **58**, 353 (1987).

[4] For the quantum theory of the micromaser, see P. Filipowicz, J. Javanainen, and P. Meystre, Phys. Rev. A **34**, 3077 (1986); the semiclassical theory is given by A. M. Guzman, P. Meystre, and E. W. Wright, Phys. Rev. A **40**, 2471 (1989).

[5] L. A. Lugiato, M. O. Scully, and H. Walther, Phys. Rev. A **36**, 740 (1987).

[6] P. Filipowicz, J. Javanainen, and P. Meystre, Phys. Rev. A **34**, 4547 (1986).

[7] J. Krause, M. O. Scully, and H. Walther, Phys. Rev. A **36**, 4547 (1987).

[8] Quantum island states have recently been found in the micromaser by P. Bogár, J. A. Bergou and M. Hillery, Phys. Rev. A, **50**, 754 (1994); and Quantum and Semiclass. Opt. (to be published).

[9] J. J. Slosser, P. Meystre, and S. L. Braunstein, Phys. Rev. Lett. **63**, 934 (1989); J. J. Slosser and P. Meystre, Phys. Rev. A **41**, 3867 (1990); J. J. Slosser, P. Meystre, and E. M. Wright, Opt. Lett. **15**, 233 (1990); P. Meystre, J. Slosser, and M. Wilkens, Phys. Rev. A **43**, 4959 (1991).

[10] M. Brune, S. Haroche, V. Lefevre, J. M. Raimond, and N. Zagury, Phys. Rev. Lett. **65**, 976 (1990); M. Brune, S. Haroche, J. M. Raimond, L. Davidovich and N. Zagury, Phys. Rev. A **45**, 5193 (1992).

[11] For the linear theory of pump-coupled micromasers see J. A. Bergou and M. Hillery, Phys. Rev. A **44**, 7502 (1991).

[12] Nonlocal microwave field quantum states have been found in a similar system by L. Davidovich, A. Maali, M. Brune, J. M. Raimond, and S. Haroche, Phys. Rev. Lett. **71**, 2360 (1993).

[13] Pump-coupled lossless micromasers with conditional measurements of atoms have been studied in P. Bogár, J. A. Bergou and M. Hillery, Phys. Rev. A **51**, 2396 (1995).

[14] For generation of entangled trapping states in pump-coupled micromasers see P. Bogár and J. A. Bergou, Phys. Rev. A **51**, 2381 (1995). The effect of cavity losses is also discussed here.

[15] M. O. Scully and K. Drühl, Phys. Rev. A **25**, 2208, (1982); M. O. Scully, B.-G. Englert and H. Walther, Nature, **351**, 111 (1991); M. O. Scully and H. Walther, Phys. Rev. A **39**, 5229, (1989); B.-G. Englert, H. Walther, and M. O. Scully, Appl. Phys. B **54**, 366 (1992); P. Bogár and J. A. Bergou, submitted to Phys. Rev. A.

[16] Same result from a different derivation can be found in P. Meystre and M. Sargent III, *Elements of Quantum Optics* (Springer-Verlag, Berlin, 1990).

[17] M. Hillery, Phys. Rev. A **40**, 3147 (1989).

[18] The problem has been studied in great detail for example in W. H. Louisell, *Quantum Statistical Properties of Radiation* (Wiley, New York, 1973); H. Hake, *Laser Theory* (Springer-Verlag, Berlin, Heidelberg, 1970); for a recent

solution see also A. Mufti, H. A. Scmitt, A. B. Balantekin, M. Sargent III, JOSA **B10**, 2100 (1993).

Chapter 3.2.2

† Reprinted (abstracted) with permission from P. Bogár, J. A. Bergou and M. Hillery, Physical Review A **51**, (3) 2396-2410 (1 March, 1995). Copyright 1995 The American Physical Society.

[1] For a recent review, see H. Walther, Phys. Rep. **219**, 201 (1992); also H. Walther, Phys. Scr. **T23**, 165 (1988); F. Diedrich, J. Krause, G. Rempe, M. O. Scully, and H. Walther, IEEE J. Quantum Electron. **QE-24**, 1314 (1988).

[2] The experimental proof of the quantum collapse and revival predicted by the Jaynes-Cummings model was reported by G. Rempe, H. Walther, and N. Klein, Phys. Rev. Lett. **58**, 353 (1987).

[3] M. O. Scully and H. Walther, Phys. Rev. A **39**, 5229 (1989).

[4] For the quantum theory of the micromaser, see P. Filipowicz, J. Javanainen, and P. Meystre, Phys. Rev. A **34**, 3077 (1986); the semiclassical theory is given by A. M. Guzman, P. Meystre, and E. W. Wright, Phys. Rev. A **40**, 2471 (1989).

[5] L. A. Lugiato, M. O. Scully, and H. Walther, Phys. Rev. A **36**, 740 (1987).

[6] L. Davidovich, J. M. Raimond, M. Brune, and S. Haroche, Phys. Rev. A **36**, 3771 (1987).

[7] About quantum island states see P. Bogár, J. A. Bergou and M. Hillery, Phys. Rev. A **50**, 754 (1994); Quantum and Semiclass. Opt. (to be published).

[8] H. Paul and T. Richter, Opt. Comm. **85**, 508 (1991).

[9] P. Filipowicz, J. Javanainen, and P. Meystre, Phys. Rev. A **34**, 4547 (1986).

[10] M. Brune, J. M. Raimond, and S. Haroche, Phys. Rev. A **35**, 154 (1987).

[11] J. Krause, M. O. Scully, and H. Walther, Phys. Rev. A **36**, 4547 (1987).

[12] P. Filipowicz, J. Javanainen, and P. Meystre, J. Opt. Soc. Am. B **3**, 906 (1986).

[13] J. J. Slosser, P. Meystre, and S. L. Braunstein, Phys. Rev. Lett. **63**, 934 (1989).

[14] P. Meystre, G. Rempe, and H. Walther, Opt. Lett. **13**, 1078 (1988).

[15] J. J. Slosser and P. Meystre, Phys. Rev. A **41**, 3867 (1990).

[16] J. J. Slosser, P. Meystre, and E. M. Wright, Opt. Lett. **15**, 233 (1990).

[17] P. Meystre, J. Slosser, and M. Wilkens, Phys. Rev. A **43**, 4959 (1991).

[18] The first masing in a single atom micromaser was reported by D. Meschede, H. Walther, and G. Müller, Phys. Rev. Lett. **54**, 551 (1985).

[19] More recent results are reported by G. Rempe, F. Schmidt-Kaler, and H. Walther, Phys. Rev. Lett. **64**, 2783 (1990).

[20] Superradiance in a micromaser cavity was first reported by J. M. Raimond, P. Goi, M. Gross, C. Fabre, and S. Haroche, Phys. Rev. Lett. **49**, 1924 (1982).

[21] On the two-photon micromaser, see M. Brune, J. M. Raimond, P. Goy, L. Davidovich, and S. Haroche, Phys. Rev. Lett. **59**, 1899 (1987); and L. Davidovich, J. M. Raimond, M. Brune, and S. Haroche, Phys. Rev. A. **36**, 3771 (1987).

[22] See recent review on very high finesse cavities in the optical domain by S. E. Morino, Q. Wu, and T. W. Mossberg, Opt. Photon. News **3**, 8 (1992), and references therein. See also G. Rempe, R. J. Thompson, R. J. Brecha, W. D. Lee, and H. J. Kimble, Phys. Rev. Lett. **67**, 1727 (1991).

[23] K. Vogel, V. M. Akulin, and W. P. Schleich, Phys. Rev. Lett. **71**, 1816 (1993).

[24] P. Meystre and E. M. Wright, Phys. Rev. A **37**, 2524 (1988).

[25] P. Meystre, Opt. Lett. **12**, 669 (1987).

[26] J. A. Bergou and M. Hillery, Phys. Rev. A **44**, 7502 (1991).

[27] Nonlocal microwave field quantum states has been found in a similar system by L. Davidovich, A. Maali, M. Brune, J. M. Raimond, and S. Haroche, Phys. Rev. Lett. **71**, 2360 (1993).

[28] The production of entangled trapping states has been studied in the same system with nonselective measurements of the atomic states by P. Bogár and J. A. Bergou, Phys. Rev. A **51**, 2381 (1995). There, the fields are started from number states and the effects of dissipations and finite temperature are aslo investigated.

Chapter 3.2.3

† Reprinted (abstracted) with permission from P. Bogár and J. A. Bergou, Physical Review A **51**, (3) 2381-2396 (1 March, 1995). Copyright 1995 The American Physical Society.

[1] Generation of macroscopic superpositions in a micromaser via tangent and cotangent states were suggested by P. Filipowicz, J. Javanainen, and P. Meystre, J. Opt. Soc. Am. B **3**, 906 (1986); J. J. Slosser, P. Meystre, and S. L. Braunstein, Phys. Rev. Lett. **63**, 934 (1989); J. J. Slosser and P. Meystre, Phys. Rev. A **41**, 3867 (1990); J. J. Slosser, P. Meystre, and E. M. Wright, Opt. Lett. **15**, 233 (1990); P. Meystre, J. Slosser, and M. Wilkens, Phys. Rev. A **43**, 4959 (1991).

[2] For a recent review, see H. Walther, Phys. Rep. **219**, 201 (1992); also H. Walther, Phys. Scr. **T23**, 165 (1988); F. Diedrich, J. Krause, G. Rempe, M. O. Scully, and H. Walther, IEEE J. Quantum Electron. **QE-24**, 1314 (1988).

[3] P. Filipowicz, J. Javanainen, and P. Meystre, Phys. Rev. A **34**, 3077 (1986); A. M. Guzman, P. Meystre, and E. W. Wright, Phys. Rev. A **40**, 2471 (1989).

[4] L. A. Lugiato, M. O. Scully, and H. Walther, Phys. Rev. A **36**, 740 (1987).

[5] The first masing in a single atom micromaser was reported by D. Meschede, H. Walther, and G. Müller, Phys. Rev. Lett. **54**, 551 (1985); G. Rempe, F. Schmidt-Kaler, and H. Walther, Phys. Rev. Lett. **64**, 2783 (1990).

[6] Superradiance in a micromaser cavity was first reported by J. M. Raimond, P. Goi, M. Gross, C. Fabre, and S. Haroche, Phys. Rev. Lett. **49**, 1924 (1982); On two-photon micromaser, see M. Brune, J. M. Raimond, P. Goy, L. Davidovich, and S. Haroche, Phys. Rev. Lett. **59**, 1899 (1987); and L. Davidovich, J. M. Raimond, M. Brune, and S. Haroche, Phys. Rev. A. **36**, 3771 (1987).

[7] E. T. Jaynes and F. W. Cummings, Proc IEEE **51**, 89 (1963); H Paul, Ann. Phys. (Leipzig), **11**, 411 (1963); J. H. Eberly, N. B. Narozhny, and J. J. Sanchez-Mondragon, Phys. Rev. Lett. **23**, 44 (1980); The experimental proof of the quantum collapse and revival predicted by the Jaynes-Cummings model was reported by G.

Rempe, H. Walther, and N. Klein, Phys. Rev. Lett. **58**, 353 (1987).

[8] Quantum island states have recently been found in the micromaser by P. Bogár, J. A. Bergou and M. Hillery, Phys. Rev. A, **50**, 754 (1994); Quantum and Semiclass. Opt. (to be published).

[9] J. Krause, M. O. Scully, and H. Walther, Phys. Rev. A **36**, 4547 (1987); P. Meystre, Opt. Lett. **12**, 668 (1987); in *Squeezed and Nonclassical Light*, edited by P. Tombesi and E. R. Pike (Plenum, New York, 1988); H. Paul, J. Mod. Opt. **36**, 515 (1989); F. W. Cummings, A. K. Rajagopal, Phys. Rev. A **39**, 3414 (1989).

[10] P. Meystre, G. Rempe, and H. Walther, Opt. Lett. **13**, 1078 (1988).

[11] For the linear theory of this system see J. A. Bergou and M. Hillery, Phys. Rev. A **44**, 7502 (1991).

[12] The same system with conditional measurements of atoms is studied by P. Bogár, J. A. Bergou and M. Hillery, Phys. Rev. A **51**, 2396 (1995).

[13] Nonlocal microwave field quantum states has been found in a similar system by L. Davidovich, A. Maali, M. Brune, J. M. Raimond, and S. Haroche, Phys. Rev. Lett. **71**, 2360 (1993).

[14] A. O. Caldeira and A. J. Leggett, Phys. Rev. A **31**, 1059 (1985); D. F. Walls and G. J. Milburn, Phys. Rev. A **31**, 2403 (1985); C. M. Savage and D. F. Walls, Phys. Rev. A **32**,2316 (1985).

[15] E. B. Davies, *Quantum Theory of Open Systems* (Academic, London, 1976); K. Krauss, *States, Effects and Operations: Fundamental Notions of Quantum Theory* (Springer-Verlag, Berlin, 1983).

[16] The nonlinear theory and numerical simulations of this system at significant losses are given by P. Bogár, J. A. Bergou and M. Hillery, Phys. Rev. A (to be published).

[17] The problem has been studied in great detail for example in W. H. Louisell, *Quantum Statistical Properties of Radiation* (Wiley, New York, 1973); H. Hake, *Laser Theory* (Springer-Verlag, Berlin, Heidelberg, 1970); for a recent solution see also A. Mufti, H. A. Scmitt, A. B. Balantekin, M. Sargent III, JOSA **B10**, 2100 (1993).

[18] M. Brune, S. Haroche, V. Lefevre, J. M. Raimond, and N. Zagury, Phys. Rev. Lett. **65**, 976 (1990); M. Brune, S. Haroche, J. M. Raimond, L. Davidovich and N. Zagury, Phys. Rev. A **45**, 5193 (1992).

[19] Entangled trapping states of nonlocal fields are applied to generate correlations between two spatially separeted atomic beams in P. Bogár and J. A. Bergou, Phys. Rev. A (to be published).

Chapter 3.2.4

† Submitted for publication to Physical Review A by P. Bogár and J. A. Bergou.

[1] For a review, see H. Walther, Phys. Rep. **219**, 201 (1992) and references therein.

[2] E. T. Jaynes and F. W. Cummings, Proc IEEE **51**, 89 (1963).

[3] J. H. Eberly, N. B. Narozhny, and J. J. Sanchez-Mondragon, Phys. Rev. Lett. **23**, 44 (1980); G. Rempe, H. Walther, and N. Klein, Phys. Rev. Lett. **58**, 353 (1987).

[4] J. Krause, M. O. Scully, and H. Walther, Phys. Rev. A **36**, 4547 (1987); P. Meystre, Opt. Lett. **12**, 668 (1987); P. Meystre, G. Rempe, and H. Walther, Opt. Lett. **13**, 1078 (1988).

[5] P. Bogár, J. A. Bergou and M. Hillery, Phys. Rev. A, **50**, 754 (1994).

[6] J. J. Slosser, P. Meystre, and S. L. Braunstein, Phys. Rev. Lett. **63**, 934 (1989); J. J. Slosser and P. Meystre, Phys. Rev. A **41**, 3867 (1990).

[7] M. Brune, S. Haroche, V. Lefevre, J. M. Raimond, and N. Zagury, Phys. Rev. Lett. **65**, 976 (1990); M. Brune, S. Haroche, J. M. Raimond, L. Davidovich and N. Zagury, Phys. Rev. A **45**, 5193 (1992).

[8] M. O. Scully and K. Drühl, Phys. Rev. A **25**, 2208, (1982); M. O. Scully, B.-G. Englert and H. Walther, Nature, **351**, 111 (1991). M. O. Scully and H. Walther, Phys. Rev. A **39**, 5229, (1989). B.-G. Englert, H. Walther, and M. O. Scully, Appl. Phys. B **54**, 366 (1992).

[9] J. A. Bergou and M. Hillery, Phys. Rev. A **44**, 7502 (1991); L. Davidovich, A. Maali, M. Brune, J. M. Raimond, and S. Haroche, Phys. Rev. Lett. **71**, 2360 (1993); P. Bogár, J. A. Bergou and M. Hillery, Phys. Rev. A **51**, 2396 (1995).

[10] Generation of entangled trapping states of nonlocal fields in the presence of dissipation is studied by P. Bogár, J. A. Bergou and M. Hillery, Phys. Rev. A **51**, 2381 (1995). Particular cases were introduced in Ref. [9] and by P. Meystre in *Progress in Optics XXX*, edited by E. Wolf (North-Holland, Amsterdam, 1992), p. 261.

[11] A. Einstein, B. Podolsky, and N. Rosen, Phys. Rev. **47**, 777 (1935).

[12] C. H. Bennett, G. Brassard, C. Crépeau, R. Jozsa, A. Peres, and W. K. Wooters, Phys. Rev. Lett. **70**, 1895 (1993).

[13] S. Friberg, C. K. Hong, and L. Mandel, Phys. Rev. Lett. **54**, 2011 (1985); Z. Y. Ou and L. Mandel, Phys. Rev. Lett. **61**, 50 (1988).

[14] J. S. Bell, Physics (Long Island City, N.Y.) **1**, 195 (1964); J. F. Clauser, and A. Shimony, Rep. Prog. Phys. **41**, 1881 (1978); A. Aspect in *Atomic Physics 8*, edited by L. Lindgren, A. Rosen, and S. Svanberg (Plenum, New York, 1983), p. 103;

[15] N. F. Ramsey, *Molecular Beams* (Clarendon, Oxford, 1956).